

A Self-Assembly Tale

Collective structural and optical phenomena in supraparticles
of nanocrystals

About the cover: Artistic representation of a supraparticle scattering an X-ray beam (front) and a supraparticles, excited with green light, showing whispering gallery modes and lasing (back). Cover design by Ella Maru Studio.

PhD thesis, Universiteit Utrecht

A Self-Assembly Tale

Collective structural and optical phenomena in supraparticles of nanocrystals

Federico Montanarella, January 2019

Printed by: Ipskamp Printing || proefschriften.net

ISBN: 978-90-9031426-6

A Self-Assembly Tale

Collective structural and optical phenomena in supraparticles
of nanocrystals

Een verhaal over zelf-assemblage

Collectieve structurele en optische fenomenen in supradeeltjes van nano-
kristallen

(met een samenvatting in het Nederlands)

Proefschrift

ter verkrijging van de graad van doctor aan de Universiteit Utrecht op
gezag van de rector magnificus, prof. dr. H.R.B.M. Kummeling, ingevolge
het besluit van het college voor promoties in het openbaar te verdedigen

op maandag 28 januari 2019

des middags te 2.30 uur

door

Federico Montanarella

geboren op 24 september 1990 te Genova, Italië

Promotoren:

Prof. dr. D.A.M. Vanmaekelbergh
Prof. dr. A. van Blaaderen

Copromotor:

Dr. P.J. Baesjou

This thesis was accomplished with financial support from the Marie Skłodowska Curie Action Innovative Training Network PHONSI - Nanophotonics by Nanocrystals and from the European Research Council under the European Union's Seventh Framework Programme (FP-20072013)/ ERC advanced grant agreement 291667: HierarSACol.





Table of Contents

Chapter 1 • Introduction	1
Chapter 2 • Compendium: The shoulders of Giants	9
Chapter 3 • Self-assembly of luminescent CdSe based nanoplatelets in 3D spherical supraparticles	39
Chapter 4 • Crystallization of nanocrystals in spherical confinement probed by <i>in-situ</i> X-ray scattering	55
Chapter 5 • Reversible charge-carrier trapping slows Förster energy transfer in CdSe/CdS quantum-dot solids	87
Chapter 6 • Composite supraparticles with tunable light emission	109
Chapter 7 • Lasing supraparticles self-assembled from nanocrystals	137
Chapter 8 • Summary and Outlook	155
• Samenvatting in het Nederlands	161
• Sommario in Italiano	171
• List of publications and contributions	180
• Acknowledgements	184
• About the Author	194

Chapter 1

Introduction

Abstract

Since the birth of human civilization (since the Romans conquered Western Europe and Egypt), nanomaterials have been part of the technological development of mankind. The last decades of XXth century marked the final ascension of nanomaterials and nanotechnology to a relevant place in our modern society, propelling more and more research in this field and extending the use of nanotechnology to a vast range of applications. We can expect that in the next decades a transition will take place from what has been defined as the Silicon Age, with communication technology being heavily based on (macroscopic) semiconductors, to the Nano Age. In this view, semiconductor nanocrystals, the subject of this work, represent a compelling combination of these two technologies. Thanks to their remarkable size-dependent optical properties, semiconductor nanocrystals are already present in our homes in TV's, displays and lighting. Moreover, their spontaneous organization into superstructures could promote the realization of materials with new intriguing properties. In this thesis we aim to investigate the self-assembly of semiconductor nanocrystals into three dimensional superstructures and the resulting optical properties arising from their interactions in close-packed configurations.

«El sueño de la razón produce monstruos»
[The sleep of Reason produces monsters]
(Francisco Goya)

1.1 The Nano Age

The word Nano, semantically speaking, derives from the Latin word *nanus* which, in turn, derives from the Greek word *νάννος* (= *nannos*), which means dwarf. Since its establishment in 1960 at the General Conference on Weights and Measures, the use of the prefix Nano-, denoting a factor of 10^{-9} or 0.000000001, has spread like wildfire first in the scientific environment and then in daily life. Nanomaterials and nanotechnology are nowadays involved in a wide range of applications in everyday life, from tennis rackets to food industry, and there is a continuous increase of the efforts and fundings in this field of research every year.

Even though nanomaterials are considered as the future for mankind, their actual use started quite back in the past (Fig. 1.1). One of the first documented use of nanomaterials in history is the use of PbS nanoparticles for hair dyeing in the Greco-Roman time, around 2000 years ago (Fig. 1.1a).¹ In fact, PbS nanoparticles, by absorbing a large part of the visible spectrum, appear black to human eye, thus resulting perfect for cosmetic purposes

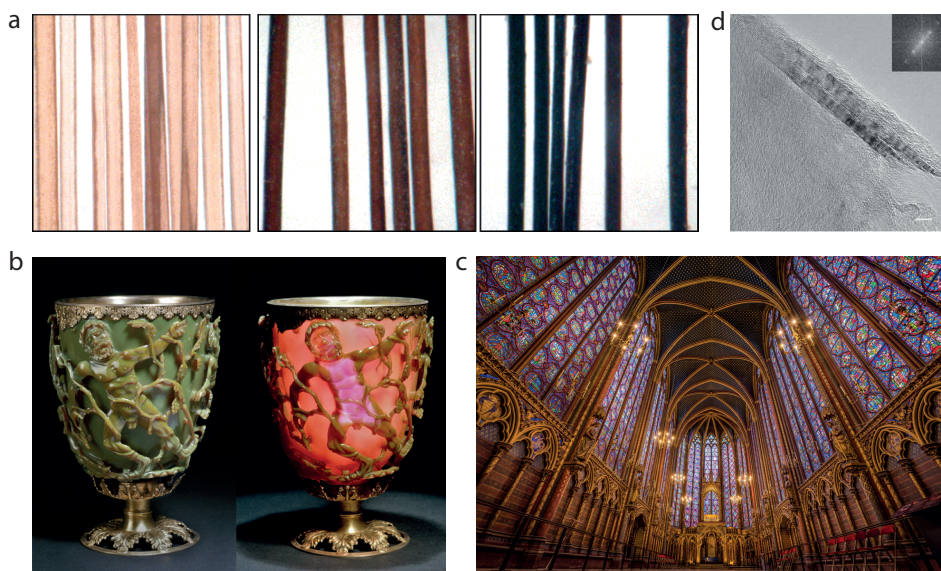


Figure 1.1 • Examples of the use of nanomaterials in history. (a) Since the Greco-Roman time, hair-dyeing recipes based on the use of lead salts were used. These mixtures of lead oxide and lime in water would blacken the hairs over time. These macrographs of human hair after different blackening treatment times show this effect. Reprinted (adapted) with permission from ref ¹. Copyright 2006 American Chemical Society. (b) The famous Lycurgus cup, dated to the fourth century A.D., is made out of a glass with gold and silver nanoparticles embedded in it. This results in a green color in reflection and a red color in transmission. Reproduced with permission from ref ². (c) The stained glasses of the Sainte-Chapelle in Paris, just like many other stained glasses of churches in Europe, are embedded with nanoparticles in order to achieve mesmerizing colors. Reproduced with permission from ref ⁶. (d) Damascus sabers, produced in Middle East during the Middle Age, contained carbon nanotubes which made them more resistant than European blades. This micrograph shows an high-resolution transmission electron microscopy image of a carbon nanotubes in a genuine Damascus saber after dissolution in hydrochloric acid. Reproduced with permission from ref ⁵.

(except for the toxicity of the lead). The most famous Lycurgus cup, also dating back to the same time, is another exquisite example of how our ancestors made unknowingly use of nanomaterials for esthetic purposes.² The dichroic glass of this cup is embedded with gold and silver nanoparticles. As the plasmonic resonance of the nanoparticles matches the bluer region of the visible spectrum, thus preferably absorbing shorter wavelengths rather than longer ones, the cup appears red in transmission and green in reflection (Fig. 1.1b). The same effect was well known to the stained glass maestros of the medieval churches, which used to disperse noble metal nanopowders in the glass in order to obtain particular coloring (Fig. 1.1c).^{3,4} Meanwhile, the crusaders in the Holy Land could not imagine that the secret behind the higher resistance of the Damascus blades of the Moors, compared to their blades, was to be found in the presence of carbon nanotubes embedded in the steel (Fig. 1.1d).⁵ As we can see, the relation between human technological development and use of nanomaterials has been a constant during the history of mankind (even though most of the times it was not a conscious use), to finally flourish in the second half of the XXth century.

Nanomaterials and nanoparticles are nowadays used in various daily applications, ranging from sunscreens and paints to catalytic processes, lighting, TV's and displays, and new applications arise every day, pushing forward the technological development in a virtuous circle. At the same time, companies are increasing the number of transistors in integrated circuits in a trend that has been well described (so far) by the Moore's law.⁷ This results in a constant effort of companies in reducing the size of electronic chips and transistors every year. On the other hand, the development of nanomaterials is also driven by the awareness that their properties depend on their dimensions and size. In addition, the much higher surface to volume ratio in nanomaterials compared to their bulk counterparts results in unmatched catalytic effects in nanoparticles. All these considerations have brought many to the conclusion that the world is now moving towards what can be defined as the Nano Age; an era in which technology will be mainly based on nanomaterials. We can expect that the research efforts of today will blossom in a major role for nanotechnology in our future society, making it more efficient, clean and productive, especially with respect to the new challenges deriving from climate change that mankind is facing.^{8,9}

1.2 The Silicon Age

*“One shouldn't work on semiconductors, that is a filthy mess; who knows whether any semiconductors exist”.*¹⁰ Prof. Wolfgang Pauli probably didn't imagine that semiconductors would have played such an important part in our society, when he wrote this sentence in a letter to his colleague, Sir Rudolf Peierls, in 1931. However modern time technology is heavily based on semiconductors and, among these, silicon in particular, to such an extent that the age of information, in which we are living, has also been named the “Silicon Age”.^{11,12} Each one of us can easily find silicon in our pockets and in our houses in the form of solar cells, electronic chips and transistors in our smartphones, computers and electronic devices.

Semiconductors are materials characterized by a band gap between the valence band and the conduction band roughly between 1 and 2.5 eV. However, an essential difference with insulators is that intrinsic or external generation/switching on/off of movable charge car-

riers is possible. If a semiconductor is properly doped, the local concentration of conduction electrons (or valence holes) can be changed by external illumination or by an external local field. This possibility to turn on and off a photovoltaic (by light) or an electrical (by a local field) conductor forms the basis for the tremendous application range of semiconductors, from solar cells to lasers to transistors, which became the logic units on which computing is based. At the current stage, semiconductors are mainly used in their macroscopic crystalline (bulk) form but, as technology is moving toward the miniaturization of circuits and devices, new horizons are opening. The use of semiconductors on the nanoscale is gaining increasing interest after the discovery of remarkable new properties only existing at these sizes, and a “brave new world” is being shaped by today’s research.

1.3 Semiconductor nanocrystals and superstructures

Colloidal semiconductor nanocrystals, also known as quantum dots, are one of the rising stars in the nanomaterial firmament. They have been extensively studied and developed now for more than 30 years. The scientific interest in them is driven by their remarkable optoelectronic properties which are tightly linked to their sizes. In fact semiconductor nanocrystals are characterized by a very sharp (in terms of linewidth) photoluminescent emission (*e.g.* <100 meV), which can be tuned in the whole visible region of the electromagnetic spectrum just by changing their size, shape and composition (Fig. 1.2a). Because of these properties, semiconductor nanocrystals are nowadays employed in television and computer displays (*e.g.* the first quantum dots televisions were launched on the market in 2014; Fig. 1.2b) and LEDs.

In all these applications, semiconductor nanocrystals are used in close-packed configurations, or in what has also been called quantum dot solids or superstructures. A superstructure is a hierarchical structure composed of individual and distinguishable building blocks, such as for example semiconductor nanocrystals, assembled in a dense and ordered configuration. As nanocrystals also fall with their sizes in the range that defines

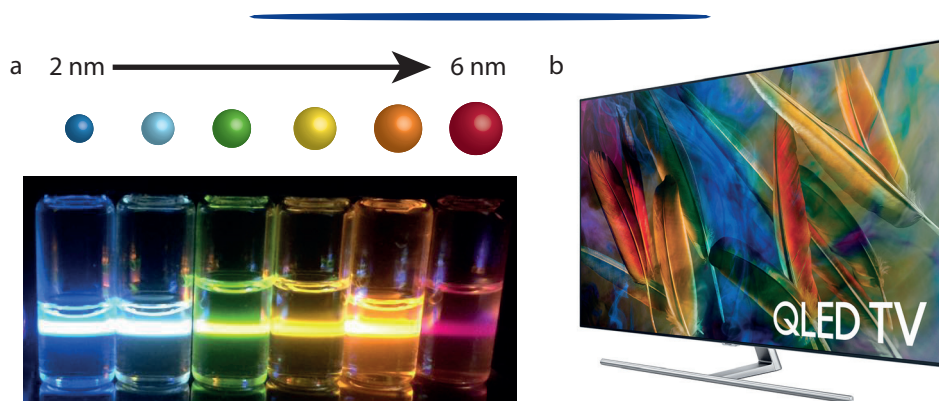


Figure 1.2 • Colloidal semiconductor nanocrystals and their applications. (a) The emission of CdSe nanocrystals can be tuned in the whole visible spectrum by changing their size from 2 nm (blue emission) to 6 nm (red emission). (b) The first LED televisions based on semiconductor nanocrystals recently reached the market, offering unmatched color brightness. Reproduced with permission from ref¹³.

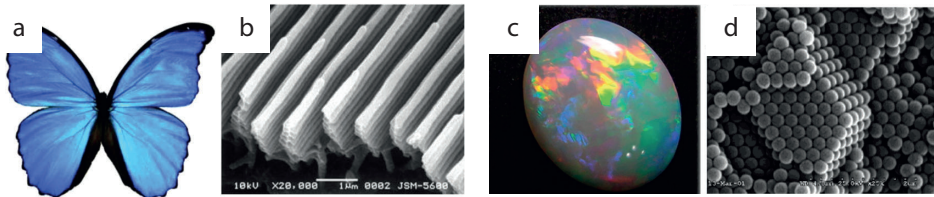


Figure 1.3 • Examples of self-assembly from the natural world. (a-b) *Morpho rhetenor* butterflies have characteristic blue wings, whose color arises from a microstructure with a periodicity comparable to visible light. Reproduced with permission from ref ¹⁷. (c-d) Opals reflect different shades of light depending on the viewing angle; a phenomenon called iridescence. Iridescence arises from the scattering of light with the periodic structure of the silicon dioxide colloidal particles composing the opals. Reproduced with permission from ref ¹⁷.

a colloidal particles, these crystals are therefore also called colloidal crystals. This dense and ordered configuration may lead to the emergence of a new class of properties arising from the interaction between the single building blocks, or simply by the interaction of the superstructure with the surrounding environment. Examples of these properties are the structural colorations in the Morpho butterfly¹⁴, originating from the submicron structure on their wings (Fig. 1.3a-b) and in opals¹⁵⁻¹⁷, arising from the self-assembly of silica spheres with dimensions comparable with those of visible light (Fig. 1.3c-d). The quest for the realization of these superstructures is driven by the will of combining the remarkable properties of the semiconductor nanocrystals with those arising from the structural configuration. In particular, this is sought through the spontaneous assembly (*i.e.* self-assembly) of the composing building blocks. This branch of research could potentially open the door to the realization of materials with properties tailored for specific applications. Even though the research in this field is not completely new, there is still a huge margin for improvement.

Throughout this thesis we investigate semiconductor nanocrystals and their self-assembly into three dimensional supraparticles. Just like following the natural hierarchical structure, we first focus on the individual building blocks (*i.e.* the semiconductor nanocrystals) and then we concentrate on the supraparticles originating from their self-assembly, studying the interactions between the individual nanocrystals and characterizing their optical properties. With this thesis, we wish to contribute to the scientific discussion about superstructures, enriching it with several studies about their formation and their potential applications.

1.4 Outline of this thesis

This thesis is outlined as follow:

In **Chapter 2**, we will provide the theoretical background necessary to understand and follow the development of the thesis. First, the optoelectronic properties of semiconductor nanocrystals will be illustrated, with a particular focus on the origin of the size dependency and the role of their surface. Second, we will present the basic theory behind the synthesis of quantum dots. Subsequently we will illustrate the self-assembly processes and some of the ensemble properties of nanocrystal solids. Finally we will discuss the main

1 characterization techniques, with a particular focus on X-ray scattering.

Chapter 3 describes the synthesis of two dimensional semiconductor nanocrystals, also known as nanoplatelets, and their self-assembly in three dimensional spherical supraparticles. Nanoplatelets with different geometries are synthesized, optically characterized and used as building blocks for the superstructures. We show that the self-assembly in three dimensional superstructures does not alter their optical properties, and we complement our results with electron microscopy measurements.

Chapter 4 presents an *in situ* study of the self-assembly process leading to the crystallization of semiconductor nanocrystals into three dimensional supraparticles through Small Angle X-ray Scattering techniques. The setup geometry with tunable detector distance allowed us to obtain a full picture of the crystallization process, following at the same time the fate of the nanocrystals and of the shrinking droplets which drive the self-assembly. We show that the role of the interparticle interactions is pivotal for the crystallization of the supraparticles, as crystallization starts at particle volume fractions considerably below those required for the crystallization of hard spheres.

In **Chapter 5** the interplay between Förster energy transfer, delayed emission and spontaneous emission is discussed. Through time-resolved emission spectroscopy measurements we unravel the role of reversible charge carrier trapping on the exciton dynamics, showing that the trapping slows down the energy transfer when semiconductor nanocrystals are self-assembled in quantum dots solids. The results are complemented with Monte Carlo simulations, providing us with a more quantitative description of the whole process.

In **Chapter 6** we present three dimensional spherical supraparticles composed of three different types of semiconductor nanocrystals with emission in the red, green and blue. By changing the ratios of the nanocrystals we show that we can tune the emission of the supraparticles in a vast range of the CIE diagram. The dynamics of the interactions between the three populations of nanocrystals is studied through time-resolved emission spectroscopy, while a full structural characterization is performed through scanning transmission electron microscopy.

Chapter 7 describes the use of three dimensional spherical supraparticles composed of semiconductor nanocrystals as microlasers. Through the use of microfluidics, we obtain extremely monodisperse supraparticles in the micrometer range, that can act as lasing cavities. Through photoluminescence microspectroscopy and coherence measurements, we attribute the origin of the lasing to whispering gallery modes arising from the structural geometry of the supraparticles.

In **Chapter 8** we give a short summary of the results obtained in this thesis and we present a short outlook on possible applications and on the further directions that the research in this field may take.

References

1. Walter, P. *et al.* Early use of PbS nanotechnology for an ancient hair dyeing formula. *Nano Lett.* **6**, 2215–2219 (2006).
2. Freestone, I., Meeks, N., Sax, M. & Higgitt, C. The Lycurgus Cup - A Roman nanotechnology. *Gold Bull.* **40**, 270–277 (2008).
3. Colomban, P. The Use of Metal Nanoparticles to Produce Yellow, Red and Iridescent Colour, from Bronze Age to Present Times in Lustre Pottery and Glass: Solid State Chemistry, Spectroscopy and Nanostructure. *J. Nano Res.* **8**, 109–132 (2009).
4. Colomban, P., Tournié, A. & Ricciardi, P. Raman spectroscopy of copper nanoparticle-containing glass matrices: Ancient red stained-glass windows. *J. Raman Spectrosc.* **40**, 1949–1955 (2009).
5. Reibold, M. *et al.* Materials: Carbon nanotubes in an ancient Damascus sabre. *Nature* **444**, 286 (2006).
6. Bricker, T. <https://www.travelcaffeine.com/sainte-chapelle-paris-france-tips/>.
7. Moore, G. E. Cramming more components onto integrated circuits, Reprinted from Electronics, volume 38, number 8, April 19, 1965, pp.114 ff. *IEEE Solid-State Circuits Soc. Newsl.* **11**, 33–35 (2006).
8. Hamilton, A. J., May, R. M. & Waters, E. K. Here be dragons. *Nature* **520**, 42–43 (2015).
9. Mecklin, J. It is 2 minutes to midnight. *Bull. At. Sci.* (2018).
10. Pauli, W. *Wolfgang Pauli – Wissenschaftlicher Briefwechsel mit Bohr, Einstein, Heisenberg u.a. Band II: 1930–1939.* (Springer, 1985).
11. Ross, I. M. The foundation of the silicon age. *Bell Labs Tech. J.* **2**, 3–14 (1997).
12. Castells, M. *Power of Identity: The Information Age: Economy, Society, and Culture.* (Blackwell Publishers, Inc., 1997).
13. <https://www.samsung.com/us/televisions-home-theater/tvs/qled-tvs/>.
14. Kinoshita, S., Yoshioka, S. & Kawagoe, K. Mechanisms of structural colour in the Morpho butterfly: cooperation of regularity and irregularity in an iridescent scale. *Proc. Biol. Sci.* **269**, 1417–1421 (2002).
15. Sanders, J. V. Colour of Precious Opal. *Nature* **204**, 1151–1153 (1964).
16. Darragh, P. J., Gaskin, A. J., Terell, B. C. & Sanders, J. V. Origin of precious opal. *Nature* **209**, 13–16 (1966).
17. Inan, H. *et al.* Photonic crystals: Emerging biosensors and their promise for point-of-care applications. *Chem. Soc. Rev.* **46**, 366–388 (2017).

Chapter 2

Compendium: The shoulders of Giants

Abstract

In 2015 the “30 years of Quantum Dots” conference was held in Paris, celebrating the third decade since the development of semiconductor nanocrystals with a strong “exciton” photoluminescence with a size-dependent energy that could be unambiguously related to quantum confinement. Such colloidal semiconductor nanocrystals, also known as quantum dots (QDs), are nowadays an everyday reality. They are already implemented in commercial television and computer displays, and they are being investigated for further applications such as lasers and solar cells. The interest for QDs arises from their remarkable size-dependent opto-electronic properties, making them one of the most promising nanomaterials in the field of nanoscience. In this chapter, I present a theoretical basis that would allow one to better appreciate the results of my PhD research. After a brief introduction on the synthesis of the QDs and on the origin of their size-dependent opto-electronic properties, we will plunge into the use of the QDs as building blocks for hierarchical superstructures, describing some of the interesting ensemble properties that arise when these semiconductor nanoparticles are in close-packed arrangements.

«If I have seen further it is by standing on the shoulders of Giants»
(Isaac Newton, quoting Bernard of Chartres)

2.1 Colloidal semiconductor nanocrystals: the chemical viewpoint

A nanocrystal, as the name suggests, is a crystalline particle with a size ranging from one to several tens of nanometers. According to this very general classification, we can group under this definition a vast range of particles of different materials and with different geometries. The common denominator to this universe is their very large surface to volume ratio. In particular, if for a bulk material the atoms on the surface account for less than 0.0000001% of the atoms composing it, in a nanoparticle this ratio can go up to tens of percent.¹ As most of the chemical reactions in the world happen at the surface of materials (e.g. reactions catalyzed by heterogeneous catalysts), it is not surprising that the scientific interest for these materials keeps increasing.

Semiconductor nanocrystals, also known as quantum dots (QDs), are a specific class of nanocrystals made of semiconductor material. In general this class can be divided in two subfamilies: epitaxial QDs and colloidal QDs. Epitaxial QDs are grown with gas phase techniques onto substrates, while colloidal QDs are synthesized (and dispersed) in solution starting from organo-metallic precursors.

Colloidal semiconductor nanocrystals are the main subject of this work. QDs have been discovered independently more than 30 years ago, in the early 80's, by Ekimov in glass matrix,²⁻⁴ and by Henglein in colloidal solution.⁵ Only few years later Ekimov⁶ and Brus^{7,8} showed, for the first time, their size dependent opto-electronic properties, while Efros developed the first theoretical model.⁹ It should be noted that the quantum properties of semiconductor nanocrystals could be observed by the experimenters only when the surface of the crystal had been electronically passivated in an appropriate way. Due to progress in this electronic passivation, the research in this field has kept increasing every year, arising to one of the most promising fields of nanoscience.

2.1.1 Nanoscale size effect of semiconductor materials

The unique electronic structure and size-dependent optical properties of semiconductor nanocrystals are due to strong electron (hole) confinement that becomes very clear in well-passivated semiconductors.¹⁰ Following the Drude-Sommerfeld model,¹¹ in a bulk material, the discrete atomic levels of the composing atoms combine to form continuums of states, named bands. Between the bands are forbidden energies which constitute what is called the band gap. In general, the valence band (VB) is defined as the highest energy band occupied by the electrons at absolute zero temperature, while the conduction band (CB) is defined as the lowest energy band composed of unoccupied states at absolute zero temperature. The modern classification of materials is based on the position of the highest filled electron level (the Fermi level) in relation to the band structure of the material. A metal is defined as a material for which the Fermi level lies within the conduction band, while semiconductors and insulators are materials for which the Fermi level lies within the band gap. The energy difference between the highest occupied state (HOMO) and the lowest unoccupied state (LUMO), *i.e.* the band gap energy, is a rough measure to distinguish insulators from semiconductors. However, for crystals with a bandgap above 1 eV, doping or external stimulation is required to obtain a semiconductor ($kT=25.7$ meV at 298 K).

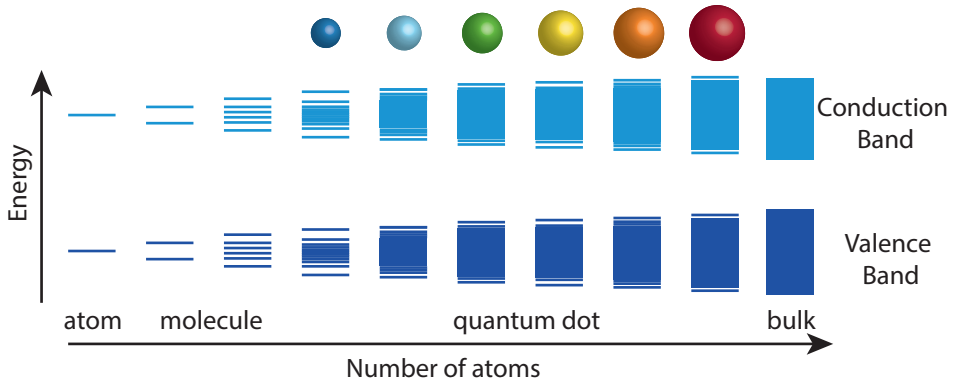


Figure 2.1 • Band structure: from atom to bulk. The combination of atomic orbitals generates, first, molecular orbitals and then, with increasing number of atoms, bands of states. QDs sit in between molecules and bulk: they possess discrete energy levels at the band edge and a continuum of states for higher energies, with a bandgap that decreases with increasing number of atoms. Adapted from ref¹².

Things, however, gets more intriguing when considering materials on the nanoscale. A quantum dot is composed of a variable number of atoms, depending on its size, ranging from 100 to 100 000. This number is enormously tiny compared to bulk materials, which have much bigger volumes ($\sim 10^{22}$ atoms for a cube of 1 cm^3). The huge difference in the number of atoms between a QD and a bulk semiconductor results in properties, for the QD, in between those of an atom and those of the bulk. In Figure 2.1 we can observe a scheme of the relation between the number of atoms and the band structure of the material. Starting from the bulk, characterized by a continuum of states, and decreasing the size of the material (*i.e.* decreasing the number of atoms), the number of atomic states that form the band decreases. Discrete energy levels arise, especially at the band edge. Thus the nanometric size of the QDs results in a band structure composed of discrete levels at the band edge, just like for atoms, and a continuum of states for higher energies; for this reason QDs are also informally called “artificial atoms”.

In semiconductors, by means of an optical transition, an electron can be promoted from a valence to a conduction state, leaving an empty state (hole) behind. The electron in the lowest CB level and the hole in the highest VB level have strongly overlapping wave functions, and form what is called an exciton. The exciton can be considered as a quasi-particle characterized by its own wavefunction, whose spatial extension is defined as the exciton Bohr radius. The wavefunction of the exciton and the exciton Bohr radius are different for each material, as they are related to the intrinsic nature of the band structure of the material. As an example, the exciton Bohr radius of CdSe is 5.4 nm, while for CdTe it is 6.7 nm.¹³ In a QD, the exciton wavefunction is confined in a space which is smaller than its Bohr radius, thus experiencing what is termed quantum confinement. The quantum confinement of the exciton results in an higher interaction energy, which is displayed as an increase in the band gap energy.¹²

The discrete band structure of the QDs and the inter-relation between this and the size of the QDs is manifest in their optical properties. Figure 2.2a shows different solutions

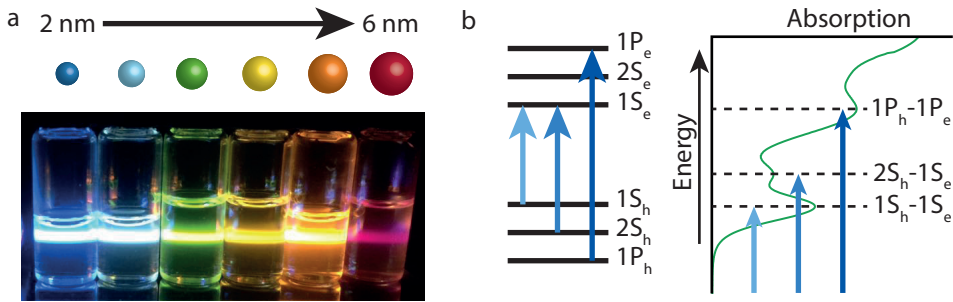


Figure 2.2 • Nanoscale size effect on the optical properties of QDs. (a) The photoluminescent emission of QDs is strongly size dependent. Solutions of CdSe nanocrystals of different sizes, ranging from 2 nm to 6 nm, emit in different regions of the visible spectrum. (b) The discrete energy levels at the band edges in QDs result in peak maxima in the absorption spectrum. Every maximum corresponds to an allowed transition between the energy levels. In the case of CdSe QDs of 3.4 nm, the first three maxima correspond to the $1S_h-1S_e$, $2S_h-2S_e$ and $1P_h-1P_e$ transitions.¹⁴ Adapted from ref¹.

of CdSe QDs with sizes ranging from 2 to 6 nm. The photoluminescent (PL) emission of the QD solutions, directly coupled to the energy of the band gap, shifts towards higher energies when decreasing the size of the nanocrystals. On the other hand, the absorption spectrum of a CdSe QDs solution (Fig. 2.2b) shows local maxima corresponding to the allowed optical transitions between the discrete energy levels.

2.1.2 Dimensionality

Another parameter playing a huge role in the optical properties of semiconductor nanocrystals is the dimensionality of the quantum confinement. For QDs the confinement is in all three directions of space, and for this reason QDs are defined as zero-dimensional nanoparticles. In this sense the French translation of quantum dots, *boîte quantique* (= quantum box), perfectly emphasizes this aspect. However quantum confinement can also be important in two, or only one dimension. In the case of two dimensional confinement the particles are called quantum rods, while in the case of one dimensional confinement they are called quantum wells. The dimensionality of the confinement has an effect on the optical properties of the material in terms of variations in the density of states (DOS). A schematic representation of the relation between the DOS and the dimensionality is shown in Figure 2.3. In the bulk, the DOS has a dependency on the energy as $E^{1/2}$. However, in quantum wells, the DOS evolves in a step-like manner. For quantum rods the DOS assume an $E^{-1/2}$ dependency. Finally, for QDs, the DOS consists of Dirac- δ functions.¹⁵

The manipulation of the opto-electronic properties via the dimensionality of the nanocrystals, has led to a flourishing research on the development of nanoparticles with different geometries. From these efforts, nanoparticles such as nanorods,^{17,18} nanoplatelets,^{19–21} nanowires,^{22,23} tetrapods^{24,25} and nanorings²⁶ have been synthesized. In particular, semiconductor nanoplatelets (NPLs) have been synthesized for the first time few years ago by Ithurria *et al.*^{21,27} The synthesis of NPLs allows an atomic control of the platelet thickness, thus resulting in the absence of inhomogeneous broadening.²⁸ NPLs can now be made with different dimensions,²⁹ geometries^{30–32} and composition,^{33,34} however their formation

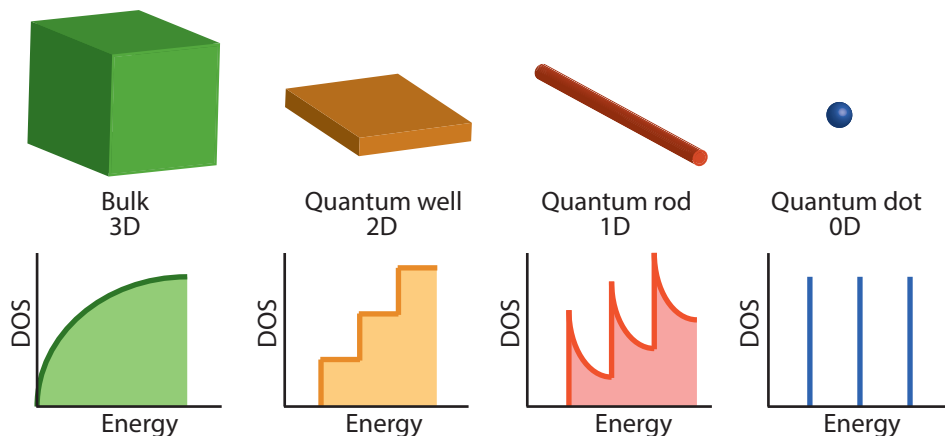


Figure 2.3 • Dimensionality effect on nanomaterials. Going from three-dimensional bulk materials to zero-dimensional quantum dots, the density of states as function of the energy evolves from a square root dependency (bulk, 3D), to a step-like function (quantum well, 2D) to a negative square root dependency (quantum rod, 1D), to a Dirac- δ function (quantum dot, 0D). Adapted from ref ¹⁶.

mechanism is still a matter of debate in the scientific community.^{35,36} In particular, the exact mechanism of symmetry breaking which makes isotropic seeds evolve into anisotropic platelets is, at the moment, the subject of speculation.

2.1.3 Panoramix and the magic potion: synthesis of colloidal QDs

The first protocol for the synthesis of colloidal QDs with low polydispersity in size (<10%) and dissolved in apolar organic solvents was developed in 1993 by Murray, Norris and Bawendi,³⁷ and this is generally considered as one of the most important milestones in the field. Even though the synthesis methods have evolved from that time, allowing the production of even more monodisperse QDs with different compositions and with better optical properties, they are all still mostly based on that work. The key idea behind a low size dispersity is to separate in time the nucleation phase from the growth phase. In order to obtain this, the synthesis is performed through the injection (from which it takes the name of hot injection) of one of the organo-metallic precursors, into a hot solution containing the other precursors. The hot injection synthesis is based on La Mer's theory, who developed a method in order to obtain monodisperse particles in 1950.³⁸

The hot injection synthesis is a kinetically driven method which relies on the variation of the concentration level of the monomers over time in a thermally activated solution. Figure 2.4a is in this sense helpful to follow the three stages in which this synthesis can be divided. In the first stage (I), immediately after the hot injection of the precursor, the concentration of the monomers steadily increases exceeding the supersaturation point (*i.e.* critical level C). This stage is called induction. As the monomer concentration overshoots the critical level, the synthesis enters in the second stage; the nucleation is triggered (II). In this phase, the high concentration of monomers and the high temperatures of the solution (260-350 °C) allow the formation of stable nuclei by consumption of the monomers. During the formation of nuclei, the concentration of monomers reaches a max-

imum and then starts to decrease, quickly passing the critical level and thus concluding the nucleation phase. In the following phase (III), the concentration of monomers is not high enough to form stable nuclei, and the monomers are therefore consumed to grow the QDs. This phase is known as the size focusing phase: as the QDs grow, smaller QDs require less material in order to grow, thus resulting in a fast growth speed compared to bigger QDs. This effects results in the narrowing of the size distribution of the QD product. Typically syntheses are stopped at this stage in order to obtain monodisperse QDs. For much longer time scales, when the growth is depleted by the absence of monomers, the chemical equilibrium between precursors and nanocrystals triggers the dissolution of the smaller QDs to grow the bigger ones, in a process that is generally known as Ostwald ripening. However, the mechanism behind Ostwald ripening in QDs is not fully understood.

The nucleation phase, as we previously explained, is triggered by the high concentration of monomers in the thermally activated solvent. This can be explained more in detail by referring to the classic theory of nucleation.^{39,40} Nucleation is a process where a different phase forms inside another one. Nucleation can be expressed in terms of variation of Gibbs free energy (ΔG) which, in this case, is made by two competing terms (Eq. 2.1): a volume contribution (ΔG_v), associated to the variation of free energy per unit of volume between the liquid phase and the solid phase (negative term); and a surface contribution (ΔG_s), associated to the reversible work associated with creating an interface between the two phases (positive term). The total free energy can, therefore, be expressed as:

$$\Delta G = \Delta G_v + \Delta G_s = -4/3 \pi r^3 \rho \Delta \mu + 4\pi r^2 \gamma \quad (\text{Eq. 2.1})$$

Where r is the radius of the nucleus, ρ is the density of the solid phase, $\Delta \mu$ is the difference in the chemical potential between the nucleus and the monomer solution, and γ is the interfacial energy between the liquid and the solid phases. The competition between

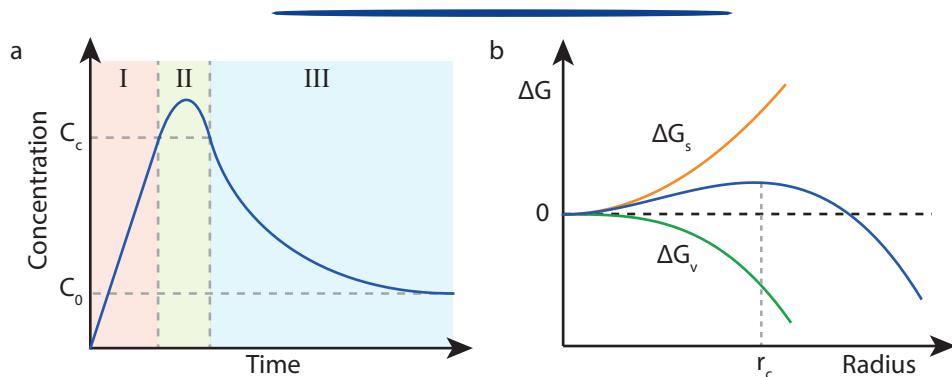


Figure 2.4 • Nucleation and growth of colloidal quantum dots. (a) La Mer³⁸ identified three regions in a typical synthesis: the induction region (I), the nucleation region (II) and the diffusion region (III). The three regions are defined in relation to the concentration level of the monomers with respect to the critical concentration triggering the nucleation (C_c). Adapted from ref³⁸. (b) According to the classic theory of nucleation, a nucleus is considered stable, and its growth thermodynamically favorable, if its radius is bigger than the critical radius (r_c). In this case, the volume contribution to the Gibbs free energy (ΔG_v) is dominant over the surface contribution (ΔG_s).

these two contributions results in a particular trend of the Gibbs free energy as function of the radius of the nucleus which is schematically represented in Figure 2.4b. The curve presents a maximum which corresponds to the so called critical radius. The critical radius (r_c) represents the minimum radius a nucleus should have in order for its growth to be thermodynamically favorable with respect to its dissolution.

Classic nucleation theory has been used to explain the formation of a wide class of QDs, such as CdSe, ZnSe, CdS and CdTe.^{37,41} Although much is known about the formation of QDs, there are still several unresolved debates. For example, several systems don't seem to form according to La Mer theory; and to this class belongs, for example, InP.⁴² Other systems, such as perovskite QDs, nucleate and grow so fast that the kinetics cannot be monitored with conventional investigation methods, and therefore their formation mechanism is still subject of speculation.^{43,44} Even in the most well-known and studied QD system, CdSe, there are still open questions about: the mechanisms that trigger the ripening at long synthesis time,⁴⁵⁻⁴⁷ the effective role of the free and bound ligands with respect to the synthesis chemistry^{48,49} and about the symmetry breaking mechanism that forms nanoplatelets.^{27,35}

2.1.4 Devils and surfaces

*“God made the bulk; surfaces were invented by the devil”.*⁵⁰ Some of the statements underlying this quote from Wolfgang Pauli are debatable, but the general message is quite clear and embraceable: surfaces are different from the bulk from an energetic and electronic perspective. As introduced few pages earlier, surfaces constitute an important part of the entire QD system. They can have, for instance, an important role in determining the optical properties of QDs.⁴⁸ Colloidal QDs are stable in solution thanks to organic ligands (*e.g.* oleic acid, trioctylphosphine, octanethiol) attached to their surface through, more or less (depending on the case), strong chemical (or physical) bonds. The ligands fulfill two functions: (1) they allow the QDs to be colloiddally stable in solution and (2) they passivate their surface bonds. However, the ligands on the surface are in chemical equilibrium with the ligands present in solution, therefore, over time, they undergo attachment and detachment from the surface. In addition, QDs are not perfect, as they are characterized by dangling bonds and, more generally, surface defects which strongly affect their optical properties. In particular these defects create charge accessible trap states in the band gap of the QDs.

Trap states are associated with one of the most important phenomena affecting the optical properties of QDs: non-radiative Auger recombination. Non-radiative Auger recombination is present both in nanocrystals and bulk semiconductors and it occurs when more than one electron-hole pair is present in the material (*e.g.* biexciton, trion). We remark that this may happen for different reasons: charge injection, very high excitation intensities provoking biexciton generation and charge trapping. Figure 2.5 is in this sense helpful to understand the mechanism of Auger recombination for the case of charge trapping. The presence of a trap state with zero oscillatory strength in the band gap may allow one of the charges of the exciton to be trapped, leaving the QD charged. In the meantime, another exciton can be generated in the QD (*e.g.* through absorption of a photon), creating a so-called trion. At this point a non-radiative Auger recombination may take place (process A in Fig. 2.5). As the exciton recombines, it can transfer its energy to the free charge which

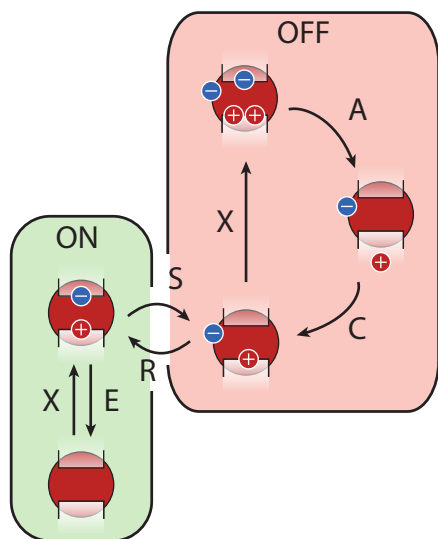


Figure 2.5 • Optical model for blinking in QDs.

When the QD is in the ground state, it can absorb a photon (X) thus generating an exciton. The exciton can recombine radiatively, through the emission of a photon of energy equal to the energy of the bandgap (E). As long as the QD remains in this cycle, it is said to be in an ON state. However, one of the charges of the exciton might get trapped in a surface state with zero-oscillatory strength (S), taking the exciton to the OFF cycle. While in this charged state, the QD can generate another exciton through another absorption event (X). The new exciton will then recombine, transferring its energy to the free charge with an Auger process (A), promoting it to a deep band state. Quick cooling (C) restores the charge at the band edge, where it can undergo other non-radiative cycles, or be restored to the ON state through charge release (R). Adapted with permission from ref.⁵³ Copyright 2015 American Chemical Society.

gets promoted to a hot carrier state and then quickly cools down (fs to ps time scales) to the band edge (process C in Fig. 2.5).^{16,51} Auger recombination is obviously in competition with radiative recombination, but the much quicker time scale of the former (ps to ns time scales) in comparison to the latter (ns to μ s time scales), results in a much higher probability of Auger recombination to happen.¹⁶ While one of the charges is trapped, the QD is said to be in an OFF, or dark, state (in contrast to the ON, or bright, state when no charges are trapped), as there is no radiative emission from it. However, the trapping process is reversible, and the trapped charge can be restored to the band edge, where it can recombine radiatively. The most manifest effect of the reversible charging of the QDs is blinking: random fluctuation of the emission between an “on state”, where there is emission, and an “off state”, where there is no emission.⁵² Observed since the beginning of the research on QDs, blinking has been explained as the direct effect of non-radiative Auger recombination. However it has to be noted that blinking, and its relation to Auger recombination, is one of the most controversial topics in the QD world, and a complete theory that would settle the debate is still to be found.

The emission of photons after the QD has undergone few non-radiative cycles is defined as delayed emission. For many years this contribution to the emission has been overlooked, however new recent studies brought back the attention of the scientific community to this phenomenon.⁵³⁻⁵⁶ In particular, this has been the case since, in some QD systems, delayed emission can account for up to the 50% of the total emission of a QD.⁵⁷ For this reason it does not have to surprise the new reinvigorated interest in this field, especially on the light of its relation to blinking.⁵³ A study on the role of delayed emission in QD solids is presented in chapter 5.

2.1.5 Hetero-nanocrystals: nanocrystals composed of two semiconductor phases

One of the first milestones in the synthesis of optically robust QDs was the development of hetero-nanocrystals, *i.e.* QDs composed of a core nanocrystal, passivated by a shell of a larger band gap semiconductor material. This approach was mainly adopted in order to passivate the surface of the QDs, avoiding charge carrier trapping in the surface trap states and thus obtaining much higher PL quantum yields. For QDs, this approach matured into so called core/shell structures, where QDs are used as template to grow a shell of another semiconductor. The first synthesis procedure in this sense was in 1996 from Guyot-Sionnest.⁵⁸ This work was soon followed by several others^{59–63} until, in 2003, the colloidal atomic layer deposition method was developed by Peng and coworkers. Through the growth of single monolayers of material, the exact thickness of the shell could be controlled with atomic precision.⁶⁴ The introduction of these structures improved enormously the versatility of the QDs, widening the panorama of nanostructures that could be created. The main advantage, as already mentioned, was the reduction of the rate of non-radiative recombination, thus allowing to reach PL quantum yields never obtained before.

The choice of the semiconductor materials used to create the heterostructures has severe consequences on the spatial extensions of the exciton wavefunction, on the exciton dynamics, on the amount of defects (especially in relation to the lattice mismatch) and, more

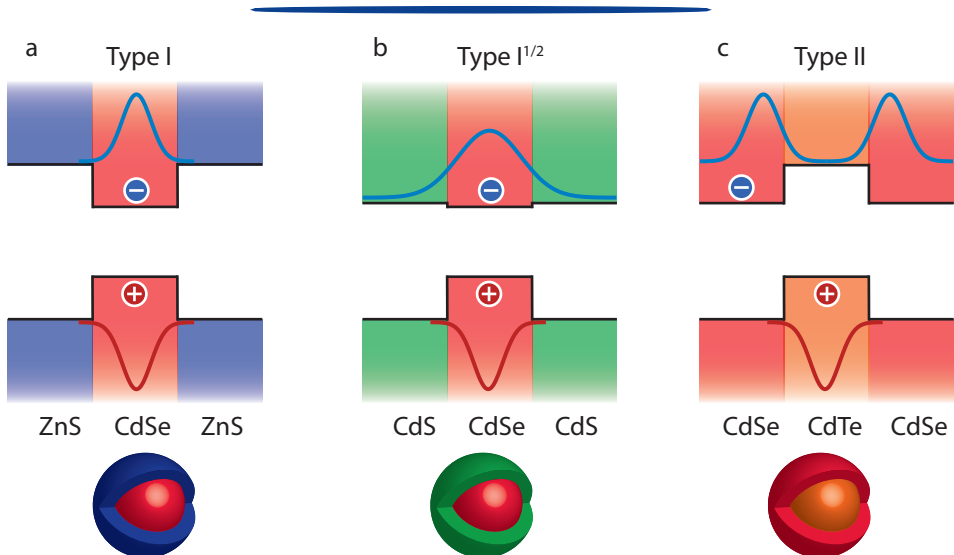


Figure 2.6 • Heteronanocrystals. The choice of the semiconductor materials determines the spatial extension of the electron and hole wavefunctions. (a) For type I heterostructures, both the electron (blue) and hole (red) wavefunctions are confined to the core and only partially to the shell. An example of such an heterostructures is core/shell CdSe/ZnS QDs. (b) For type $I^{1/2}$ heterostructures, the electron wavefunction is extended over the whole heterostructures, while the electron wavefunction is confined to the core. A typical example of this structure is core/shell CdSe/CdS QDs. (c) For type II heterostructures, the electron wavefunction is confined to the shell, and only partially in the core, while the hole wavefunction is confined to the core of the QD. A typical example of this geometry is core/shell CdTe/CdSe QDs. Adapted from ref⁶⁵.

2

in general, on the opto-electronic properties. The modern classification of heterostructures is based on the relative position of the bandgaps of the different materials composing the core and the shell. According to this classification, heteronanocrystals can be classified as: type I, type I^{1/2} and type II. The three possible types of heteronanocrystals are schematically presented in Fig. 2.6. Type I heterostructures are characterized by a core bandgap which lies completely within the shell bandgap (Fig. 2.6a), thus resulting in the confinement of the exciton in the core of the structure, far away from the surface. The exciton in these materials is less prone to be trapped in surface states, thus resulting in typically higher photoluminescence quantum yields (PLQY). A typical example of these kind of structures is core/shell CdSe/ZnS QDs, which, historically, were the first to be synthesized. Type II heteronanocrystals are characterized by a shifted band configuration, resulting in the confinement of one of the charges in the core and of the other in the shell (Fig. 2.6c). This band configuration strongly reduces the wavefunction overlap of the two charges, thus reducing the probability of recombination and extending the exciton lifetime. A common example for this type of heterostructures are core/shell CdSe/CdTe QDs. Finally, the intermediate regime of type I^{1/2} heteronanocrystals consists of a small energy difference in one of the two bands of the materials and of an energetic offset for the other one (Fig. 2.6b). This results in the spatial extension of the wavefunction of one of the charges over the whole QD, while the other one is confined in the a specific region of the heterostructure. The most known example for this band configuration are core/shell CdSe/CdS QDs.

Over the years, the design of heterostructures experienced several innovations involving changes in the shell thickness,^{66,67} and in the realization of multi-shell,⁶⁸ graded⁶⁹ and alloyed⁷⁰ structures in order to reduce the lattice mismatch between the various layers. This enabled the production of robust QDs with near unity PLQY⁷¹⁻⁷³ which opened the door to a deeper investigation of the photo-physical optical properties of nanocrystals and to their use in commercial applications and devices.⁷⁴⁻⁷⁷

2.2 Self-assembly: *E pluribus unum*

As already mentioned in chapter 1, nanoparticles can form complex hierarchical structures.^{78,79} These structures might induce novel properties, arising from the interactions between the building blocks or from those between the building blocks and the surrounding environment. These structures are usually obtained by the spontaneous hierarchical self-organization (*i.e.* self-assembly) of the nanoparticles.⁸⁰ But how does this self-assembly actually work and what are the mechanisms that drive it?

The driving force for the spontaneous organization is the difference in Gibbs free energy between the assembled state and the unassembled state, ΔG , which, for constant temperature, pressure and number of particles during the phase transition, can be expressed as:

$$\Delta G = \Delta H - T\Delta S \quad (\text{Eq. 2.2})$$

Where ΔH is the enthalpic contribution to the free energy, T is the temperature and ΔS is the entropic contribution to the free energy. For the self-assembly to be spontaneous, the difference in the free energy has to be negative; it follows that, depending on the dominant term in the equation above, either the enthalpic contribution is dominant and negative, or

the entropic contribution is dominant and positive.

The enthalpic contribution to the free energy represents the energy decrease by inter-particle attractions in the self-assembled structure. The attractions can be of different nature depending on the nanocrystals involved and on the environmental conditions in which the assembly is performed. For colloidal nanocrystals some of the typical attractive forces in play are: electrostatic, van der Waals or capillary. Electrostatic forces involve interactions between charges on the nanoparticles. This kind of force can be both repulsive or attractive and it has an important role in the self-assembly in polar as well as less polar solvents.⁸¹ A typical system where the self-assembly is driven by electrostatic forces is, for example, silica spheres in water.⁸² Van der Waals forces arise from the interaction between electric dipoles. In particular we can divide van der Waals interactions into three categories related to the nature of the dipoles: Keesom, Debye and London. Keesom interactions are those between permanent dipoles; Debye interactions are those between a permanent dipole and an induced dipole; London interactions are those between two induced dipoles, originating from random fluctuations of charges in the particles. Van der Waals interactions can have a great importance in the self-assembly of nanoparticles, as they strongly depend on the material (polarizability) and on the size of the particles,⁸³ an example will be shown in chapter 4. Finally, capillary forces have great relevance in driving the self-assembly of nanoparticles in 2D geometries. For the self-assembly in these geometries, nanoparticles are typically adsorbed at liquid-liquid or liquid-air interfaces where, by distorting the interface, they can induce attractive capillary forces on neighboring nanoparticles. Capillary forces play a role in determining the geometry of the absorption to the interface (*e.g.* the absorbing facet of a faceted nanocrystal); this can then have consequences on the final result of the self-assembly.⁸⁴ This seems to be the case, for example, in the assembly of PbSe QDs into honeycomb and square superlattices.^{85,86}

When the attractions between the composing nanocrystals can be neglected, they are said to interact as hard particles, and then the entropic contribution to the free energy is the only term in bulk self-assembly. In order for the self-assembly to be spontaneous, it is required that the entropy of the building blocks increases during the process. This counter-intuitive phenomenon can be comprehended if we consider the degree of free volume per particle before and after the self-assembly. Before the organization, the nanocrystals are dispersed in solution in high concentrations and their movements are limited. However, when they are in close-packed configurations, but at non-close packed volume fractions (> 55%), they lose in configurational free volume, but they gain in rotational and translational free volumes.⁸⁷ Hence this results in a general increase of the entropy triggered by an overall increase of the free volume, allowing the spontaneous crystallization.^{83,88}

The formation of superstructures or colloidal crystals can thus be explained in terms of variation of the chemical potential of the dispersed nanocrystals. For crystallization to occur, the chemical potential of the nanocrystals in colloidal liquid or gas phase should be higher than that of the nanocrystals in the colloidal solid. In this sense the chemical potential can be increased either by increasing the standard chemical potential of the solute, for example through the addition of an antisolvent,⁸⁹ or by increasing the concentration of nanoparticles in solution, which is typically obtained by the evaporation of the solvent.

This last technique is consistently used for the self-assembly of particles in 2D geometries, such as at liquid-liquid interfaces. In this way several supercrystals with different geometries and crystal structures have been produced.^{86,90-93} The very same method is also the one used throughout this thesis in order to produce supraparticles (SPs).

2.2.1 Supraparticles

The geometry of the system of dispersed nanocrystals in which the evaporation is performed is crucial in order to determine the final shape of the superstructure. In this sense, the spherical confinement of nanoparticles present in oil droplets, themselves dispersed in a polar solvent, has been recently used to produce three dimensional spherical supraparticles.^{94,95} The self-assembly mechanism can rely on one or more of the contributions described in the paragraph above, but in the course of this thesis we mainly triggered the self-assembly through the increase of the concentration and thus osmotic pressure of the nanoparticles over time. The mechanism used is shown in Figure 2.7. The nanoparticles are usually dispersed in droplets of an apolar solvent with a low boiling point, forming an emulsion with water (Fig. 2.7a). The emulsion is typically produced by applying mechanical stress to the two phase system in various ways, such as with a Couette shear cell,^{96,97} with a microfluidic chip^{98,99} or through sonication (Fig. 2.7b). The so-formed two phase system is stabilized by the presence of organic surfactants (*e.g.* sodium dodecyl sulfate, dodecyltrimethylammonium bromide, Triton-X), while the viscosity of the two systems is tuned through the addition of polymer molecules (*e.g.* dextran), allowing droplet break-

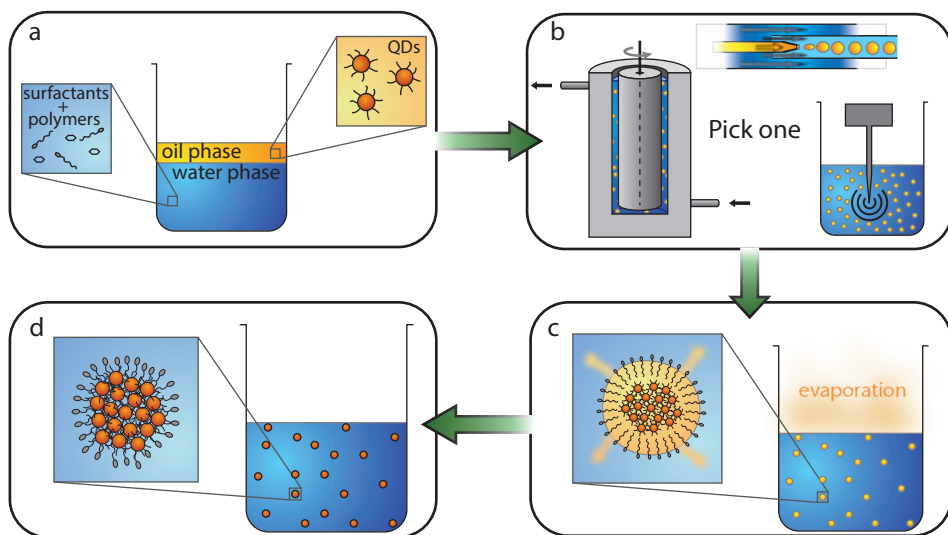


Figure 2.7 • Formation of supraparticles through spherical confinement of an oil-in-water droplet. (a) The apolar phase containing QDs forms a two phase system with the water phase containing surfactants and polymers. (b) The two phase system is emulsified through the application of a mechanical force, either applied with a shear cell, a microfluidic chip or a sonication probe. (c) The resulting two phase system appears as an emulsion of droplets of the apolar solvent containing QDs. During the dissolution and, finally, evaporation of the apolar solvent, the droplets shrink, increasing the concentration of QDs. (d) Upon complete evaporation of the solvent, the formed SPs are covered by a layer of surfactants and dispersed in water.

up to occur in a laminar flow induced by viscoelastic forces, thus producing relatively (e.g. ~10%) monodisperse droplets.¹⁰⁰ Then the low boiling solvent dissolved in the polar phase evaporates from the emulsion system, confining the nanocrystals in a volume which becomes smaller over time. Upon complete evaporation of the oil, spherical superstructures, named supraparticles or supraballs (SPs), are formed. We remark that this is one of the ways of fabricating spherical SPs, and that the literature is rich of creative protocols in order to realize superstructures with different shapes, composition and distribution of the constituting building blocks, and thus resulting in peculiar optical and structural properties.⁹⁴

The key towards the realization of optically active SPs is either in the use of photo-active building blocks, or in the structural motifs of the SPs itself. To the first case belong examples of SPs composed of QDs, or of host nanoparticles filled with dyes. In general the collective optical properties of the SP arise from the combination of the optical properties of the building blocks; an example of this will be shown in chapter 6. To the second case, instead, belong examples of SPs composed of building blocks of sizes comparable to visible light and that, therefore, interact with it. We could say that, in this case, the functionality of the SPs emerges from the hierarchy itself. To this class belong a wide range of examples, also from the natural world,¹⁰¹⁻¹⁰³ of SPs of different composition and structure, all showing structure-dependent optical properties.¹⁰⁴⁻¹⁰⁶ One typical example is the realization of SPs of polymeric spheres showing iridescence and structural coloration.¹⁰⁷⁻¹¹⁰ The composition of the building blocks can also heavily contribute to the emergence of collective properties, as it was shown by the observation of whispering gallery modes (WGMs) in SPs due to the high difference in the refractive index of the SPs and of the surrounding environment.¹¹¹ This result led to the observation of lasing properties in SPs, as it will be shown in chapter 7.

From a more structural point of view, the wide library of self-assembly methods opened the door to the realization of SPs made of building blocks of different shapes, such as cubic,¹¹² rod-like^{113,114} or two-dimensional, as it will be shown in chapter 3 and ref ¹¹⁵. These structures are characterized by their own proper functionalities, which can be tuned even more by combining nanoparticles of different size and composition. This branch of research brought to the realization of SPs with core/shell,¹¹⁶ Janus^{116,117} and binary structures^{116,118} and characterized by multi-modal properties. For example, by combining photo-active with magnetic nanoparticles, Bawendi *et al.* have recently shown that SPs characterized by photonic and magnetic properties could be produced for bio imaging purposes.¹¹⁹ On the other hand, SPs have also been used as a template to realize porous materials for charge storage and catalysis purposes.^{120,121}

2.2.2 QD solids and applications

As already anticipated in chapter 1, in most applications and devices QDs are referred to as QD solids, as they are in close-packed arrangements. The close-packed arrangement has two main reasons, each related to a typical application. On one hand, the close-packing increases the mobility of the electronic charge carriers, and hence their diffusion, for applications like solar cells. The use of QDs for photovoltaic applications is one of the most investigated branches of the research on QD devices, although several doubts still

persist on the negative effects of Auger recombination on charge diffusion, and on the performance *e.g.* compared to silicon solar cells. Nevertheless, the continuous progress in the surface chemistry of QDs, such as the use of short inorganic ligands,¹²² fuels the hopes towards the realization of QD-based photovoltaic cells, which, at the moment of the writing of this thesis, have reached a solar cell efficiency record of 13.4%.¹²³ On the other hand, the high concentration of particles increases the optical output when QDs are used, for example, in LEDs or lasers. This already led to the production of efficient QD-based LEDs which have been implemented in the first computer and television displays.¹²⁴ The main advantages of QD-based LEDs compared to regular phosphors LEDs, which are nowadays largely used in commercial applications, are their higher efficiency and the wider color gamut obtainable.¹²⁵

The QDs self-assembled in SPs are also in close-packed arrangements, and they can be considered as a QD solid model. In the next chapters, several examples of ensemble properties emerging from this configuration will be presented. In order to supply the tools to fully understand those contents, some phenomena emerging from the close-packing will be discussed here; in particular: Förster energy transfer, the additive mixing of colors, whispering gallery modes and lasing.

2.2.2.1 Förster resonant energy transfer

Förster resonant energy transfer (FRET) is a process involving two molecules, or optically active objects (*i.e.* chromophore), which transfer their energy through a far-field dipolar interaction.¹²⁶ One of the two chromophores is called donor, and it's typically in an excited electronic state, while the other chromophore is called acceptor and it's in the ground state. In the case of QDs, the donor QD will have an exciton, while the other one will not.¹²⁷⁻¹²⁹ If the two chromophores are close enough, the donor chromophore can transfer its energy to the acceptor chromophore through dipole-dipole interactions. As this interaction scales inversely with the sixth power of the distance, this process is extremely

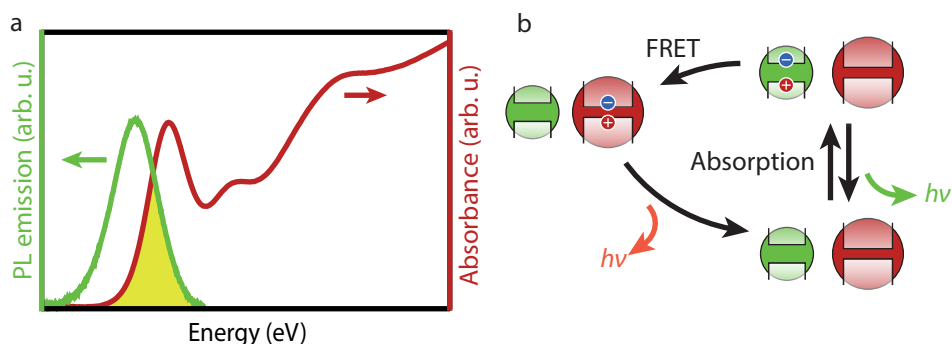


Figure 2.8 • Förster resonant energy transfer in QD solids. (a) The energetic requirement for FRET to happen spontaneously is the overlap (yellow area) between the emission spectrum of the donor chromophore (green) and the absorption spectrum of the acceptor chromophore (red). (b) QDs of different size are characterized by different bandgaps; if a photon gets absorbed in a donor QD, thus generating an exciton, this can either recombine, emitting a photon (green arrow), or transfer its energy to a neighboring acceptor QD with an equal or smaller bandgap (FRET). In the latter case, the exciton will recombine in the acceptor QD, emitting a photon of energy equal to the bandgap (red arrow).

sensitive to the distance between the two chromophores. It is, therefore, only relevant in configurations where the chromophores are very close to each other. Along with the distance, which is the first requirement to observe FRET, the second requirement is the energetic compatibility between the two chromophores. In particular, for the energy transfer to happen spontaneously (*i.e.* without the contribution of additional energy sources), it is necessary that the emission energy of the donor is overlapping with the absorption energy of the acceptor. In other words, if we express this concept in terms of the absorption and the emission of the two compounds, it is necessary that the emission spectrum of the donor and the absorption spectrum of the acceptor overlap (Fig. 2.8a). The bigger the overlap, the higher the chances to observe FRET. For QDs this evolves either in FRET between two different populations of QDs of different size, or in FRET between very similar QDs.^{128,130,131} For the latter case, the important factor driving the FRET is the polydispersity in size of the population. In both cases, the energy transfer will happen from a donor QD with a bigger bandgap, to an acceptor QD with an equal or smaller bandgap (Fig. 2.8b). A study of the interplay between energy transfer, spontaneous radiative emission and delayed emission is the main subject of chapter 5.

2.2.2.2 Color theory and additive mixing of colors

The manipulation of colors has always been, for mankind, one of the most interesting topics over the centuries.¹³² According to the color theory, colors can be divided into primary and secondary colors. By the combination of primary colors through additive or subtractive mixing, it is possible to obtain all shades of secondary colors (*i.e.* all colors). The additive mixing of colors relies on the combination of colored sources of light, *i.e.* the final

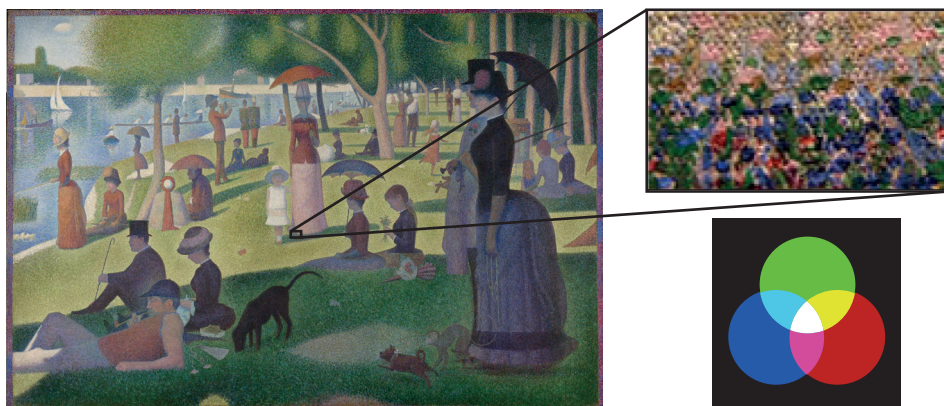


Figure 2.9 • Additive mixing of colors and Pointillism. At the end of the XIXth century, a “subversive” trend of painters named Pointillism (from the French word *point*), inspired by the contemporary emergence of the studies on human eye and human perception of colors, and directly descending from Impressionism, developed a new technique of painting based on little points of colors. One of the most representative examples of this painting technique is the painting “*Un dimanche après-midi à l'Île de la Grande Jatte*” (1894) by George Seurat. From the magnification of the painting, we can observe that the secondary and tertiary colors are generated in the eye of the observer by the vision of points of colors painted next to each other. This process is based on the additive mixing of colors that, by the mixing of three primary colors (red, green and blue), can produce secondary and tertiary colors (cyan, yellow and magenta) in the whole color gamut.

2

color results from the addition of different wavelengths of light, while subtractive mixing of colors relies on the combination of absorbers of light, *i.e.* the final color results from the partial or complete absorption of different wavelengths of light. For the subtractive mixing of colors, the three primary colors are cyan, magenta and yellow, which correspond to three of the four basic components, along with black, of the color series typically used for printing (*i.e.* CMYK). For the additive mixing of colors, the three primary colors are red, green and blue, corresponding to the RGB series. The two techniques of color production are interrelated as the primary colors of the first are the secondary colors of the second, and *vice versa*. The whole color gamut observable by human eye can be produced just by changing the amount of the three primary colors in one of the two techniques. The subtractive mixing of colors is at the base of techniques such as painting, color and photography printing. The additive mixing of colors, instead, is at the base of LEDs, computer and television displays. This technique was also used by Pointillist painters of the XIXth century, which used to paint little points of primary colors next to each other in order to obtain the synthesis of the additive color in the eye of the observer. This technique, and the principle of additive color mixing, can be appreciated in the painting “*Un dimanche après-midi à l’Île de la Grande Jatte*” (1894) from George Seraut in Figure 2.9.

The additive mixture of colors is nowadays at the base of efficient LED displays. Each pixel in an LED display, in fact, is composed of three small LEDs (subpixels) emitting blue, red and green (or emitting blue and coupled to color filters). The electronics in the display controls the amount of light emitted by every LED, thus producing the desired color through additive mixing of the light sources. This technology is already benefiting of the narrow emission linewidth of the QDs with respect to conventional phosphors, by using QD-based LEDs (for liquid crystal displays). However, the manipulation of nanopowders in industrial environment can be an issue, therefore new ways to implement QDs into microscopic platforms for a safer manipulation are under investigation. A potential solution to this problem, relying on the realization of micrometer size SPs composed of QDs emitting in different region of the visible spectrum, is presented in chapter 6.

2.2.2.3 Whispers and lasers

Even though the propagation of acoustic waves with low loss in so-called whispering galleries has been documented throughout history, the first scientific explanation of this phenomenon was proposed only in 1878 by Lord Rayleigh.¹³³ In his study he found the origin of the peculiar effects of sound waves propagating in a whispering gallery at the dome of Saint Paul’s Cathedral, in London, in the specular reflection of the sound waves by the concave surface of the dome (Fig. 2.10a) and the creation of a standing wave of the sound. In this sense, the sound intensity decays as the inverse of the distance, allowing it to be clearly heard in every position of the circumference of the dome. Later, whispering gallery waves were also observed for light, which, as we know, also behaves as a wave.¹³⁴⁻¹³⁶ In this case, the propagation of the wave inside a concave object, such as a sphere or a cylinder, is driven by total internal reflection, which originates from the high difference in the refractive index between the spherical object and the surrounding environment (Fig. 2.10b). The light entrapped inside the concave object, propagates around it, interfering with itself and creating a standing wave whose modes (Fig. 2.10c) take the name of whispering gallery modes (WGMs).¹³⁷

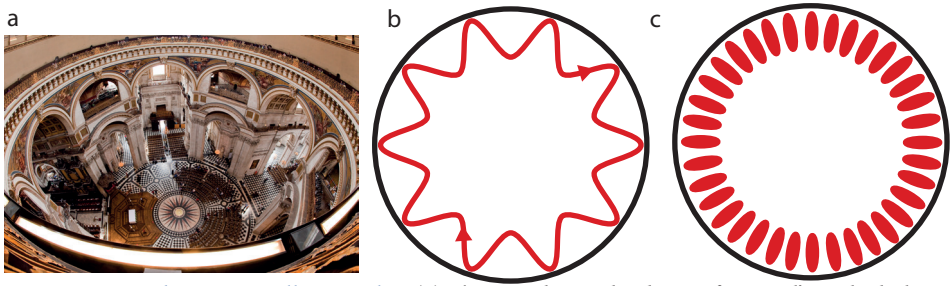


Figure 2.10 • Whispering gallery modes. (a) The corridor in the dome of St. Paul's Cathedral is a famous example of whispering gallery as sound waves travel almost with no losses around its circumference and form a standing wave by interference. (b) Just as sound waves, also light waves can experience a whispering gallery effect. A light wave confined in a sphere propagates in the circumference due to total internal reflection, constructively and destructively interfering with itself, thus generating a standing wave mode pattern (c). Reproduced with permission from ref.¹³⁸

In order to explain the relation between whispering gallery modes and lasers, it is necessary to take a step back and explain first what a laser is. LASER is actually an acronym for Light Amplification by Stimulated Emission of Radiation, so a laser is a device which emits amplified light originating from stimulated emission. In the previous paragraphs we explained that, after an absorption event, an exciton is created. The exciton will spontaneously recombine to emit a photon; this process is named spontaneous emission. Spontaneous emission is characterized by a typical lifetime which depends on the optical environment around it. In the case that an exciton is already present, an additional incoming resonant photon may trigger the recombination of the exciton, thus amplifying the optical output (Fig. 2.11a). This phenomenon takes the name of stimulated emission. Under the condition of population inversion, *i.e.* the excited state is completely filled, the rate of stimulated emission exceeds that of absorption, and a net optical amplification can be achieved, called gain. A laser is usually composed of a lasing medium, which is the source of light through stimulated emission, and of a cavity (Fig. 2.11b). The purpose of the cavity is to confine the light in the region of the space where the lasing medium is. The most simple laser is composed of a lasing medium in between two mirrors facing each other. The light emitted by the lasing medium is reflected back and forth through the lasing medium itself by the mirrors, ensuring the conditions for optical gain. One of the two mirrors is usually only partially reflective, thus allowing part of the coherent lasing light to escape the cavity. This output light, characterized by a specific wavelength and high coherence, is what we commonly call the laser beam. The geometry of the cavity presented above is only the most simple example of a laser device. Several other cavities with different geometries have been built for lasers. Among these, several cavities have been designed as spherical, thus relying on the confinement and propagation of light through WGMs.^{139,140}

QDs have been proposed as a promising candidate for lasing applications.^{141,142} In particular, the main features promoting QDs for lasing applications are their tunable PL emission, coupled with high quantum yields, their excellent photostability compared to commercial dyes, and their nearly temperature-independent gain.¹⁴³ For these reasons, nanoparticles with different dimensionality have already been successfully implemented in several types of cavity.^{144–148} The main drawbacks for the use of QDs as lasing medium are the huge loss-

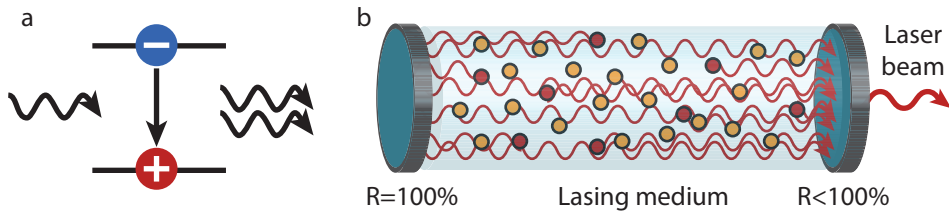


Figure 2.11 • Stimulated emission and lasers. (a) In the case an exciton is already present, an incoming resonant photon might trigger the radiative recombination of the excitons, in a phenomenon called stimulated emission. (b) This process is at the base of lasers. A laser is composed of a lasing medium (e.g. a two-level system; yellow dots are in the ground state, red dots are in the excited state) positioned inside of a cavity. A cavity can be, for example, composed of two mirrors, one fully reflective ($R=100\%$), and the other only partly reflective ($R<100\%$) in order to allow the laser beam to exit the cavity. By excitation of the lasing medium, more and more particles will be in the excited state until reaching the population inversion. Under population inversion, a resonant photon triggers the radiative recombination of one (or more) excitons, resulting in a cascade photon multiplication, called gain.

es deriving from non-radiative Auger recombination. However, in the last years several solutions based on core/multishell QDs with engineered band gap drastically reduced Auger losses in these systems.^{75,149,150} At the same time, electrically pumped QD systems are being investigated to obtain “zero threshold” lasers,^{151,152} and the first reports on continuous-wave excitation lasing are appearing.^{74,153,154} In chapter 7 a new lasing system, based on SPs of QDs, is presented, where the SPs act both as lasing medium and cavity.

2.3 Measuring at the nanoscale: electrons and photons

The characterization of materials typically proceeds through the use of particle-wave probes. Depending on the electron density of the material, as well as on its thickness and on the type of information one is willing to extract, different particle-wave probes can be used. For example, neutrons, electrons and photons at high energy are typically used to probe bulk samples, while low energy photons and electrons at grazing incidence are commonly used to probe the surface of samples. Structures on the nanoscale and, in particular, QDs, are typically probed with electrons and photons.

2.3.1 The amber spyglass

The term electron derives from the Greek word *ἤλεκτρον*, which means amber. Since the VII BC it was known that rubbing an amber piece with fur, this would attract small pieces of dust.¹⁵⁵ Nowadays electrons are a fundamental part of modern day society, and among all, they are heavily used in material science to characterize materials. On the nanoscale, electrons are commonly used to investigate the structure of QDs in scanning electron microscopy (SEM), transmission electron microscopy (TEM) and scanning-transmission electron microscopy (STEM). SEM is a microscopy technique which consists in scanning the sample with a focused electron beam. The electrons are scattered from the sample and they are collected from the detector to acquire information on the topography of the sample. In particular, since the common electron energies for this kind of technique are 10-20 keV, this results in a sensitivity mainly to the surface of the sample. For this reason, TEM is typically preferred to SEM in the analysis of QDs. TEM uses much higher electron energies (120-200 keV), resulting in the transmission of the electron beam through the

sample. As the penetration depth and the scattering intensity of the electrons depends on the electron density of the material, TEM allows to reconstruct the shape and the composition of the scanned sample. Atomic columns of a crystal will then appear as black shapes on a bright background. TEM is nowadays one of the most used techniques to routinely characterize QDs, as it provides direct information on the size, shape and chemical composition of the material. In addition, TEM images can be taken at different tilt angles and used, with the help of dedicated softwares, to reconstruct the 3D shape and position of an imaged object in a technique called electron tomography. STEM can be seen as a combination of SEM and TEM. In this case, the high energy electron beam (120-200 keV) is focused to raster scan the sample (just as for SEM), obtaining atomic resolution imaging of the QDs. This technique can operate both in high-annular dark field (HAADF) mode, where the scattered electrons are collected from an annular detector to create the image (thus obtaining white shapes on a dark background), and in secondary electron (SE) mode, where the detection is directed towards the secondary electrons produced by the surface (thus obtaining an image of the surface of the particle).

2.3.2 «And AC said “Let there be light!”»¹⁵⁶

Photons are one of the most used particle probes to study materials of different dimensions. The wavelength of the used photons needs to be comparable to the size of the object of study in order to overcome the diffraction limit. For objects on the nanoscale, photons with wavelengths around 0.01-10 nm (high energy), *i.e.* X-rays, are used. X-rays were discovered by Wilhelm Röntgen in 1895, and their use for imaging was soon understood as Röntgen used them to image the bones of his wife’s hand.¹⁵⁷ Nowadays X-rays are an important part of our society, as they are used in several bio-imaging and medical applications. For several applications, however, high intensities of X-rays are needed and, for this reason, it is necessary to rely on synchrotron radiation sources.

A synchrotron (Fig. 2.12a) is a facility where X-rays are produced from accelerated electrons. A synchrotron is made of four parts: a linear accelerator, a booster ring, a storage ring and several beamlines. The linear accelerator is the part of the synchrotron where the electrons are produced and inserted in the booster ring. In the booster ring, electrons are accelerated to the required energy (*e.g.* 6 GeV for ESRF in Grenoble) before they can be fi-

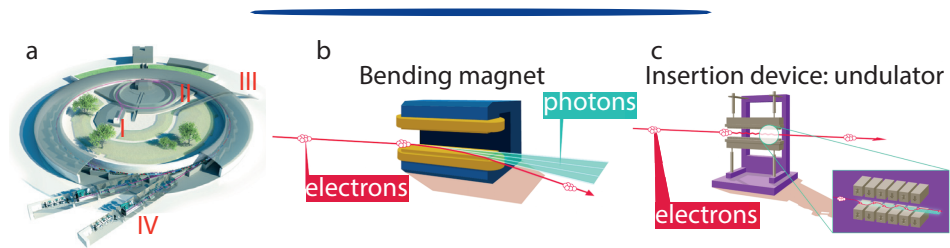


Figure 2.12 • Synchrotron facility. (a) A schematic representation of a synchrotron facility. We can distinguish the linear accelerator (I), the booster ring (II), the storage ring (III) and the beamlines (IV). (b) The main purpose of a bending magnet is to bend the electron beam at the end of every linear segment. The accelerated electrons produce X-rays which are spatially dispersed. (c) An undulator is composed of magnets which bend the electrons, forcing them to produce X-rays. The produced X-rays interfere with each other, producing a much more focused and brilliant beam compared to the one produced by bending magnets. Image courtesy of ESRF.

nally lead into the storage ring. The storage ring is the main component of the synchrotron and most of the time it is depicted as a ring. However it would be more correct to represent it as a sequence of straight segments approximating the shape of a ring. In fact, every time that the electrons are bent, they lose energy in the form of X-ray photons, which are then focused, collimated and directed toward the beamlines, where they are used for different purposes. In order to produce X-rays and keep the electron beam focused, several magnets are used in the storage ring. In particular, we can distinguish three types of magnets: focusing magnets, bending magnets and undulators. The focusing magnets, such as quadrupoles and sextupoles, are used to collimate and focus the electron beam. The bending magnets (Fig. 2.12b) are used to bend the electron beam at the junction of every linear part composing the storage ring. As the main purpose of the bending magnets is to direct the electrons, the X-rays produced by these devices are not very focused. For this reason, several insertion devices (*i.e.* undulators) are placed in the path of the electron beam (Fig. 2.12c). The undulators are composed of an array of magnets with alternated polarity and they have the purpose to accelerate the electrons, making them “wiggle”, thus producing X-rays. The undulators typically produce very focused and brilliant X-ray beams whose energy can be tuned by changing the distance between the single magnets. The last component of a synchrotron are the beamlines, where the brilliant photon beam is focused and collimated in order to be used for a plethora of experiments.

In a variety of experiments and, especially, throughout this thesis, X-rays are used for scattering experiments. The elastic scattering from periodic structures was first described by Bragg:

$$2d\sin(\theta)=n\lambda \quad (\text{Eq. 2.3})$$

Where d is the spacing between the periodic planes, θ is the angle of scattering (angle between the planes and the X-ray), λ is the wavelength of the X-rays and n is an integer number.¹⁵⁸ From equation 2.3 follows that, using X-rays (*e.g.* 0.1 nm of wavelength), atomic planes (0.1-0.2 nm) scatter at large angles (10-20°), while ordered arrangements of nanocrystals (6-10 nm) scatter at small angles (0.1-0.2°), while microstructures scatter at very small angles (0.002-0.003°). Therefore, different X-ray scattering techniques take their name from the size of the scattering object or, more correctly, from the angle at which the photons are scattered: wide-angle X-ray scattering (WAXS) and small-angle X-ray scattering (SAXS). Usually it is easier to reason in terms of reciprocal space (q values) rather than direct space, where the reciprocal space is the Fourier transform of the direct space and it is defined in terms of q vectors.¹¹ The Bragg law can be rewritten, in terms of reciprocal space, as:

$$q=2\pi/d=4\pi\sin(\theta)/\lambda \quad (\text{Eq. 2.4})$$

From equation 2.4 it is clear that small scattering objects (*i.e.* atomic planes) scatter at large q -values, while big scattering objects (*i.e.* nanocrystals) scatter at small q -values. In a typical scattering experiment (Fig. 2.13a), the scattering intensity as a function of the scattering vector q , $I(q)$, is directly proportional to:

$$I(q) \propto F(q)S(q) \quad (\text{Eq. 2.5})$$

Where $F(q)$ is the form factor of the scattering objects and $S(q)$ is the structure factor. The form factor is the Fourier transform of the object shape and dimensionality. For example, for relatively monodispersed (polydispersity < 10%) spherical QDs, the form factor consists of a series of periodic minima (Fig. 2.13b); the position of the minima is determined by the size of the spheres, while the depth of the minima bears information on the polydispersity of the sphere population. The structure factor, instead, emerges from the periodic arrangement of the scattering objects. For example, in SPs the QDs arrange in a face-centered cubic supercrystal;⁹⁵ this is observed in SAXS experiments through the appearance of structure factor peaks on top of the form factor peaks of the QDs (Fig. 2.13c). By analyzing the position of the peaks in the q -space, it is possible to reconstruct the crystal structure of the colloidal or supercrystal.

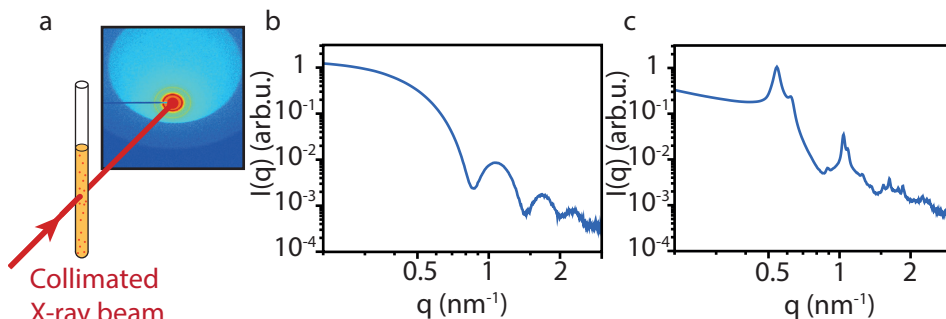


Figure 2.13 • Small-Angle X-ray Scattering experiments. (a) In a typical SAXS experiment, a sample solution is placed inside of a capillary and placed in front of the collimated X-ray beam. The scattering signal is then collected from a detector which can be moved at different distances (*i.e.* 1, 5 or 10 m sample-to-detector distance). By having longer sample-to-detector distances, it is possible to observe the signal scattered at smaller angles, while by having the detector closer to the sample, will allow to detect the scattering signal at bigger angles. (b) The scattering intensity from a solution of monodisperse spherical QDs is modulated by the shape of the scattering objects into a series of minima which bear information about size and shape of the scatterer itself. (c) Ordered arrangements of scattering objects result in the appearance of structure factor peaks on top of the form factor peaks, corresponding to the scattering from the planes of the supercrystal. Data was taken at beamline ID02 of the European Synchrotron Radiation Facility, in Grenoble, France, in march 2017 with an X-ray beam energy of 12.4 keV.

References

1. de Mello Donega, C. *Nanoparticles, Workhorses of Nanoscience*. (Springer, 2014).
2. Ekimov, A. I. & Onushchenko, A. A. Quantum size effect in three-dimensional microscopic semiconductor crystals. *JETPL* **34**, 345 (1982).
3. Ekimov, A. I. & Onushcheko, A. Quantum Size Effect in the Optical-Spectra of Semiconductor Micro-Crystals. *Sov. physics. Semicond.* **16**, 775–778 (1982).
4. I. Ekimov, A. & Onushcheko, A. Size quantization of the electron energy spectrum in a microscopic semiconductor crystal. *Soviet Journal of Experimental and Theoretical Physics Letters* **40**, (1984).
5. Alfassi, Z., Bahnemann, D. & Henglein, A. Photochemistry of colloidal metal sulfides. 3. Photoelectron emission from cadmium sulfide and cadmium sulfide-zinc sulfide cocolloids. *J. Phys. Chem.* **86**, 4656–4657 (1982).
6. Ekimov, A. I., Efros, A. L. & Onushchenko, A. A. Quantum Size Effect in Semiconductor Microcrystals. *Solid State Commun.* **56**, 921–924 (1985).
7. Brus, L. E. Electron–electron and electron–hole interactions in small semiconductor crystallites: The size dependence of the lowest excited electronic state. *J. Chem. Phys.* **80**, 4403–4409 (1984).
8. Brus, L. E. On the development of bulk optical properties in small semiconductor crystallites. *J. Lumin.* **31–32**, 381–384 (1984).
9. Efros, A. & L. Efros, A. Interband Light Absorption in Semiconductor Spheres. *Sov. physics. Semicond.* **16**, 772–775 (1982).
10. Swart, I., Liljeroth, P. & Vanmaekelbergh, D. Scanning probe microscopy and spectroscopy of colloidal semiconductor nanocrystals and assembled structures *Chem. Rev.* **116**, 11181–11219 (2016).
11. Kittel, C. *Introduction to Solid State Physics*. (Wiley, 2005).
12. de Mello Donega, C. Synthesis and properties of colloidal heteronanocrystals. *Chem. Soc. Rev.* **40**, 1512–46 (2011).
13. Fox, M. *Optical Properties of Solids*. (Oxford University Press, 2010).
14. Norris, D. J. & Bawendi, M. G. Measurement and assignment of the size-dependent optical spectrum in CdSe quantum dots. *Phys. Rev. B* **53**, 16338–16346 (1996).
15. Ashcroft, N. W. & Mermin, N. D. *Solid State Physics*. (Brooks and Cole, 1976).
16. Rabouw, F. T. & de Mello Donega, C. Excited-State Dynamics in Colloidal Semiconductor Nanocrystals. *Top. Curr. Chem.* **374**, 1–30 (2016).
17. Peng, X. *et al.* Shape control of CdSe nanocrystals. *Nature* **404**, 59–61 (2000).
18. Carbone, L. *et al.* Synthesis and micrometer-scale assembly of colloidal CdSe/CdS nanorods prepared by a seeded growth approach. *Nano Lett.* **7**, 2942–2950 (2007).
19. Bouet, C. *et al.* Flat colloidal semiconductor nanoplatelets. *Chem. Mater.* **25**, 1262–1271 (2013).
20. Ithurria, S., Bousquet, G. & Dubertret, B. Continuous transition from 3D to 1D confinement observed during the formation of CdSe nanoplatelets. *J. Am. Chem. Soc.* **133**, 3070–3077 (2011).
21. Ithurria, S. & Dubertret, B. Quasi 2D Colloidal CdSe Platelets with Thicknesses Controlled at the Atomic Level. *J. Am. Chem. Soc.* **130**, 16504–16505 (2008).
22. Zhang, D. *et al.* Synthesis of Composition Tunable and Highly Luminescent Cesium Lead Halide Nanowires through Anion-Exchange Reactions. *J. Am. Chem.*

- Soc.* **138**, 7236–7239 (2016).
23. Grebinski, J. W., Hull, K. L., Zhang, J., Kosel, T. H. & Kuno, M. Solution-Based Straight and Branched CdSe Nanowires. *Chem. Mater.* **16**, 5260–5272 (2004).
 24. Manna, L., Scher, E. C. & Alivisatos, P. Synthesis of Soluble and Processable Rod-, Arrow-, Teardrop-, and Tetrapod-Shaped CdSe Nanocrystals. *JACS* **122**, 12700–12706 (2000).
 25. Manna, L., Milliron, D. J., Meisel, A., Scher, E. C. & Alivisatos, A. P. Controlled growth of tetrapod-branched inorganic nanocrystals. *Nat. Mater.* **2**, 382–385 (2003).
 26. Fedin, I. & Talapin, D. V. Colloidal CdSe Quantum Rings. *J. Am. Chem. Soc.* **138**, 9771–9774 (2016).
 27. Ithurria, S. *et al.* Colloidal nanoplatelets with two-dimensional electronic structure. *Nat. Mater.* **10**, 936–941 (2011).
 28. Nasilowski, M., Mahler, B., Lhuillier, E., Ithurria, S. & Dubertret, B. Two-Dimensional Colloidal Nanocrystals. *Chem. Rev.* **116**, 10934–10982 (2016).
 29. Bouet, C. *et al.* Two-dimensional growth of CdSe nanocrystals, from nanoplatelets to nanosheets. *Chem. Mater.* **25**, 639–645 (2013).
 30. Mahler, B., Nadal, B., Bouet, C., Patriarche, G. & Dubertret, B. Core/shell colloidal semiconductor nanoplatelets. *J. Am. Chem. Soc.* **134**, 18591–18598 (2012).
 31. Ithurria, S. & Talapin, D. V. Colloidal Atomic Layer Deposition (c-ALD) using Self-Limiting Reactions at Nanocrystal Surface Coupled to Phase Transfer between Polar and Nonpolar Media. *JACS* **134**, 18585–18590 (2012).
 32. Tessier, M. D. *et al.* Efficient Exciton Concentrators Built from Colloidal Core/Crown CdSe/CdS Semiconductor Nanoplatelets. *Nano Lett.* **14**, 207–213 (2014).
 33. Pedetti, S. *et al.* Optimized synthesis of CdTe nanoplatelets and photoresponse of CdTe nanoplatelets films. *Chem. Mater.* **25**, 2455–2462 (2013).
 34. Bouet, C. *et al.* Synthesis of zinc and lead chalcogenide core and core/shell nanoplatelets using sequential cation exchange reactions. *Chem. Mater.* **26**, 3002–3008 (2014).
 35. Riedinger, A. *et al.* An intrinsic growth instability in isotropic materials leads to quasi-two-dimensional nanoplatelets. *Nat. Mater.* **16**, 743–748 (2017).
 36. Jiang, Y. *et al.* Synthesis of CdSe Nanoplatelets without Short-Chain Ligands: Implication for Their Growth Mechanisms. *ACS Omega* **3**, 6199–6205 (2018).
 37. Murray, C. B., Norris, D. J. & Bawendi, M. G. Synthesis and characterization of nearly monodisperse CdE (E = sulfur, selenium, tellurium) semiconductor nanocrystallites. *J. Am. Chem. Soc.* **115**, 8706–8715 (1993).
 38. Lamer, V. K. & Dinegar, R. H. Theory, Production and Mechanism of Formation of Monodispersed Hydrosols. *J. Am. Chem. Soc.* **72**, 4847–4854 (1950).
 39. de Mello Donega, C., Liljeroth, P. & Vanmaekelbergh, D. Physicochemical evaluation of the hot-injection method, a synthesis route for monodisperse nanocrystals. *Small* **1**, 1152–1162 (2005).
 40. Kumar, S. & Nann, T. Shape control of II-VI semiconductor nanomaterials. *Small* **2**, 316–329 (2006).
 41. Owen, J. & Brus, L. Chemical Synthesis and Luminescence Applications of Colloidal Semiconductor Quantum Dots. *J. Am. Chem. Soc.* **139**, 10939–10943 (2017).
 42. Gary, D. C., Terban, M. W., Billinge, S. J. L. & Cossairt, B. M. Two-step nucleation

- and growth of InP quantum dots via magic-sized cluster intermediates. *Chem. Mater.* **27**, 1432–1441 (2015).
43. Akkerman, Q. A., Rainò, G., Kovalenko, M. V. & Manna, L. Genesis, challenges and opportunities for colloidal lead halide perovskite nanocrystals. *Nat. Mater.* **17**, 394–405 (2018).
 44. Protesescu, L. *et al.* Nanocrystals of Cesium Lead Halide Perovskites (CsPbX₃, X = Cl, Br, and I): Novel Optoelectronic Materials Showing Bright Emission with Wide Color Gamut. *Nano Lett.* **15**, 3692–3696 (2015).
 45. Bullen, C. R. & Mulvaney, P. Nucleation and growth kinetics of CdSe nanocrystals in octadecene. *Nano Lett.* **4**, 2303–2307 (2004).
 46. Rempel, J. Y., Bawendi, M. G. & Jensen, K. F. Insights into the kinetics of semiconductor nanocrystal nucleation and growth. *J. Am. Chem. Soc.* **131**, 4479–4489 (2009).
 47. Abe, S., Čapek, R. K., De Geyter, B. & Hens, Z. Tuning the postfocused size of colloidal nanocrystals by the reaction rate: From theory to application. *ACS Nano* **6**, 42–53 (2012).
 48. Boles, M. A., Ling, D., Hyeon, T. & Talapin, D. V. The surface science of nanocrystals. *Nat. Mater.* **15**, 141–153 (2016).
 49. Razgoniaeva, N. *et al.* Just Add Ligands: Self-Sustained Size Focusing of Colloidal Semiconductor Nanocrystals. *Chem. Mater.* **30**, 1391–1398 (2018).
 50. Jamtveit, B. & Meakin, P. *Growth, Dissolution and Pattern Formation in Geosystems BT - Growth, Dissolution and Pattern Formation in Geosystems*. (Springer Netherlands, 1999).
 51. Rabouw, F. T. *et al.* Dynamics of Intraband and Interband Auger Processes in Colloidal Core-Shell Quantum Dots. *ACS Nano* **9**, 10366–10376 (2015).
 52. Nirmal, M. *et al.* Fluorescence intermittency in single cadmium selenide nanocrystals. *Nature* **383**, 802–804 (1996).
 53. Rabouw, F. *et al.* Delayed Exciton Emission and Its Relation to Blinking in CdSe Quantum Dots. *Nano Lett.* **15**, 7718–7725 (2015).
 54. Whitham, P. J. *et al.* Single-particle photoluminescence spectra, blinking, and delayed luminescence of colloidal CuInS₂ nanocrystals. *J. Phys. Chem. C* **120**, 17136–17142 (2016).
 55. Marchioro, A. *et al.* Strong Dependence of Quantum-Dot Delayed Luminescence on Excitation Pulse Width. *J. Phys. Chem. Lett.* **8**, 3997–4003 (2017).
 56. Marchioro, A. *et al.* Tunneling in the Delayed Luminescence of Colloidal CdSe, Cu⁺-Doped CdSe, and CuInS₂ Semiconductor Nanocrystals and Relationship to Blinking. *J. Phys. Chem. C* **120**, 27040–27049 (2016).
 57. Rabouw, F. T. *et al.* Temporary Charge Carrier Separation Dominates the Photoluminescence Decay Dynamics of Colloidal CdSe Nanoplatelets. *Nano Lett.* **16**, 2047–2053 (2016).
 58. Hines, M. A. & Guyot-Sionnest, P. Synthesis and Characterization of Strongly Luminescing ZnS-Capped CdSe Nanocrystals. *J. Phys. Chem.* **100**, 468–471 (1996).
 59. Dabbousi, B. O. *et al.* (CdSe)ZnS Core-Shell Quantum Dots: Synthesis and Characterization of a Size Series of Highly Luminescent Nanocrystallites. *J. Phys. Chem. B* **101**, 9463–9475 (1997).
 60. Peng, X., Schlamp, M. C., Kadavanich, A. V. & Alivisatos, A. P. Epitaxial growth

- of highly luminescent CdSe/CdS core/shell nanocrystals with photostability and electronic accessibility. *J. Am. Chem. Soc.* **119**, 7019–7029 (1997).
61. Banin, U. *et al.* Evidence for a thermal contribution to emission intermittency in single CdSe/CdS core/shell nanocrystals. *J. Chem. Phys.* **110**, 1195–1201 (1999).
 62. Harrison, M. T. *et al.* Wet Chemical Synthesis of Highly Luminescent HgTe/CdS Core/Shell Nanocrystals. *Adv. Mater.* **12**, 123–125 (2000).
 63. Reiss, P., Bleuse, J. & Pron, A. Highly Luminescent CdSe / ZnSe Core / Shell Nanocrystals of Low Size Dispersion. *Nano* **2**, 781–784 (2002).
 64. Li, J. J. *et al.* Large-Scale Synthesis of Nearly Monodisperse CdSe/CdS Core / Shell Nanocrystals Using Air-Stable Reagents via Successive Ion Layer Adsorption and Reaction. *J. Am. Chem. Soc.* **125**, 12567–12575 (2003).
 65. van der Stam, W. Tailoring on the nanoscale. (Universiteit Utrecht, 2016).
 66. Mahler, B. *et al.* Towards non-blinking colloidal quantum dots. *Nat. Mater.* **7**, 659–664 (2008).
 67. Chen, Y. *et al.* “ Giant ” Multishell CdSe Nanocrystal Quantum Dots with Suppressed Blinking. *J. Am. Chem. Soc.* **130**, 5026–5027 (2008).
 68. Lim, J. *et al.* Preparation of highly luminescent nanocrystals and their application to light-emitting diodes. *Adv. Mater.* **19**, 1927–1932 (2007).
 69. Hadar, I. *et al.* Semiconductor Seeded Nanorods with Graded Composition Exhibiting High Quantum-Yield, High Polarization, and Minimal Blinking. *Nano Lett.* **17**, 2524–2531 (2017).
 70. Bae, W. K. *et al.* Controlled alloying of the core-shell interface in CdSe/CdS quantum dots for suppression of auger recombination. *ACS Nano* **7**, 3411–3419 (2013).
 71. Jeong, B. G. *et al.* Colloidal Spherical Quantum Wells with Near-Unity Photoluminescence Quantum Yield and Suppressed Blinking. *ACS Nano* **10**, 9297–9305 (2016).
 72. Park, Y. S. *et al.* Near-unity quantum yields of biexciton emission from CdSe/CdS nanocrystals measured using single-particle spectroscopy. *Phys. Rev. Lett.* **106**, 6–9 (2011).
 73. Coropceanu, I., Rossinelli, A., Caram, J. R., Freyria, F. S. & Bawendi, M. G. Slow-Injection Growth of Seeded CdSe/CdS Nanorods with Unity Fluorescence Quantum Yield and Complete Shell to Core Energy Transfer. *ACS Nano* **10**, 3295–3301 (2016).
 74. Fan, F. *et al.* Continuous-wave lasing in colloidal quantum dot solids enabled by facet-selective epitaxy. *Nature* **544**, 75–79 (2017).
 75. García-Santamaría, F. *et al.* Suppressed Auger Recombination in ‘Giant’ Nanocrystals Boosts Optical Gain Performance. *Nano Lett.* **9**, 3482–3488 (2009).
 76. Kovalenko, M. V. *et al.* Prospects of Nanoscience with Nanocrystals. *ACS Nano* **9**, 1012–1057 (2015).
 77. Kagan, C. R., Lifshitz, E., Sargent, E. H. & Talapin, D. V. Building devices from colloidal quantum dots. *Science* **353**, (2016).
 78. Glotzer, S. C. & Solomon, M. J. Anisotropy of building blocks and their assembly into complex structures. *Nat. Mater.* **6**, 557–562 (2007).
 79. Damasceno, P. F., Engel, M. & Glotzer, S. C. Predictive Self-Assembly of Polyhedra into Complex Structures. *Science* **337**, 453–457 (2012).
 80. Vanmaekelbergh, D. Self-assembly of colloidal nanocrystals as route to novel

- classes of nanostructured materials. *Nano Today* **6**, 419–437 (2011).
81. Liu, B. *et al.* Switching plastic crystals of colloidal rods with electric fields. *Nat. Commun.* **5**, 3092 (2014).
 82. van Blaaderen, A. *et al.* Manipulating the self assembly of colloids in electric fields. *Eur. Phys. J. Spec. Top.* **222**, 2895–2909 (2013).
 83. Evers, W. H. *et al.* Entropy-driven formation of binary semiconductor-nanocrystal superlattices. *Nano Lett.* **10**, 4235–4241 (2010).
 84. Geuchies, J. J. Connecting the Dots. (Utrecht University, 2017).
 85. Geuchies, J. J. *et al.* In situ study of the formation mechanism of two-dimensional superlattices from PbSe nanocrystals. *Nat. Mater.* **15**, 1248–1254 (2016).
 86. Boneschanscher, M. P. *et al.* Long-range orientation and atomic attachment of nanocrystals in 2D honeycomb superlattices. *Science* **344**, 1377–1380 (2014).
 87. Bodnarchuk, M. I., Kovalenko, M. V., Heiss, W. & Talapin, D. V. Energetic and entropic contributions to self-assembly of binary nanocrystal superlattices: Temperature as the structure-directing factor. *J. Am. Chem. Soc.* **132**, 11967–11977 (2010).
 88. Eldridge, M. D., Madden, P. A. & Frenkel, D. Entropy-driven formation of a superlattice in a hard-sphere binary mixture. *Nature* **365**, 35–37 (1993).
 89. van der Burgt, J. S. *et al.* Cuboidal Supraparticles Self-Assembled from Cubic CsPbBr₃ Perovskite Nanocrystals. *J. Phys. Chem. C* **122**, 15706–15712 (2018).
 90. Redl, F. X., Cho, K.-S., Murray, C. B. & O'Brien, S. Three-dimensional binary superlattices of magnetic nanocrystals and semiconductor quantum dots. *Nature* **423**, 968–971 (2003).
 91. Dong, A., Chen, J., Vora, P. M., Kikkawa, J. M. & Murray, C. B. Binary nanocrystal superlattice membranes self-assembled at the liquid-air interface. *Nature* **466**, 474–7 (2010).
 92. Shevchenko, E. V., Talapin, D. V., Murray, C. B. & O'Brien, S. Structural characterization of self-assembled multifunctional binary nanoparticle superlattices. *J. Am. Chem. Soc.* **128**, 3620–3637 (2006).
 93. Cargnello, M. *et al.* Substitutional doping in nanocrystal superlattices. *Nature* **524**, 450–3 (2015).
 94. Wintzheimer, S. *et al.* Supraparticles : Functionality from Uniform Structural Motifs. *ACS Nano* **12**, 5093–5120 (2018).
 95. de Nijs, B. *et al.* Entropy-driven Formation of Large Icosahedral Colloidal Clusters by Spherical Confinement. *Nat. Mater.* **14**, 56–60 (2015).
 96. Mason, T. & Bibette, J. Emulsification in Viscoelastic Media. *Phys. Rev. Lett.* **77**, 3481–3484 (1996).
 97. Mabile, C. *et al.* Rheological and shearing conditions for the preparation of monodisperse emulsions. *Langmuir* **16**, 422–429 (2000).
 98. Abate, A. R. & Weitz, D. A. High-order multiple emulsions formed in poly(dimethylsiloxane) microfluidics. *Small* **5**, 2030–2032 (2009).
 99. Amstad, E. *et al.* Robust scalable high throughput production of monodisperse drops. *Lab Chip* **16**, 4163–4172 (2016).
 100. Mason, T. G. & Bibette, J. Shear Rupturing of Droplets in Complex Fluids. *Langmuir* **13**, 4600–4613 (1997).
 101. Yin, H. *et al.* Amorphous diamond-structured photonic crystal in the feather

- barbs of the scarlet macaw. *Proc. Natl. Acad. Sci. U. S. A.* **109**, 10798–801 (2012).
102. Sanders, J. V. Colour of Precious Opal. *Nature* **204**, 1151–1153 (1964).
 103. Darragh, P. J., Gaskin, A. J., Terell, B. C. & Sanders, J. V. Origin of precious opal. *Nature* **209**, 13–16 (1966).
 104. Phillips, K. R. *et al.* A colloidoscope of colloid-based porous materials and their uses. *Chem. Soc. Rev.* **45**, 281–322 (2016).
 105. Goerlitzer, E. S. A., Klupp Taylor, R. N. & Vogel, N. Bioinspired Photonic Pigments from Colloidal Self-Assembly. *Adv. Mater.* **30**, 1706654 (2018).
 106. Vogel, N. *et al.* Color from hierarchy: Diverse optical properties of micron-sized spherical colloidal assemblies. *Proc. Natl. Acad. Sci.* **112**, 10845–10850 (2015).
 107. Xiao, M. *et al.* Bioinspired bright noniridescent photonic melanin supraballs. *Sci. Adv.* **3**, 1–8 (2017).
 108. Xiao, M. *et al.* Bio-inspired structural colors produced via self-assembly of synthetic melanin nanoparticles. *ACS Nano* **9**, 5454–5460 (2015).
 109. Lim, C. H., Kang, H. & Kim, S. H. Colloidal assembly in leidenfrost drops for noniridescent structural color pigments. *Langmuir* **30**, 8350–8356 (2014).
 110. Park, J. G. *et al.* Full-spectrum photonic pigments with non-iridescent structural colors through colloidal assembly. *Angew. Chemie - Int. Ed.* **53**, 2899–2903 (2014).
 111. Vanmaekelbergh, D. *et al.* Shape-Dependent Multiexciton Emission and Whispering Gallery Modes in Supraparticles of CdSe / Multishell Quantum Dots. *ACS Nano* **9**, 3942–3950 (2015).
 112. Wang, D. *et al.* Interplay between spherical confinement and particle shape on the self-assembly of rounded cubes. *Nat. Commun.* **9**, (2018).
 113. Wang, T. *et al.* Self-Assembled Colloidal Superparticles from Nanorods. *Science* **338**, 358–363 (2012).
 114. Besseling, T. H. *et al.* Determination of the positions and orientations of concentrated rod-like colloids from 3D microscopy data. *J. Phys. Condens. Matter* **27**, 194109 (2015).
 115. Wang, D. *et al.* Quantitative real space analysis of supraparticles composed of nanoplatelets. *Submitted* (2018).
 116. Kister, T., Mravlak, M., Schilling, T. & Kraus, T. Pressure-controlled formation of crystalline, Janus, and core-shell supraparticles. *Nanoscale* **8**, 13377–13384 (2016).
 117. Yu, Z., Wang, C. F., Ling, L., Chen, L. & Chen, S. Triphase microfluidic-directed self-assembly: Anisotropic colloidal photonic crystal supraparticles and multi-color patterns made easy. *Angew. Chemie - Int. Ed.* **51**, 2375–2378 (2012).
 118. Wang, P., Qiao, Q., Zhu, Y. & Ouyang, M. Colloidal Binary Supracrystals with Tunable Structural Lattices. *J. Am. Chem. Soc.* **140**, 9095–9098 (2018).
 119. Chen, O. *et al.* Magneto-fluorescent core-shell supernanoparticles. *Nat. Commun.* **5**, 5093 (2014).
 120. Jiao, Y. *et al.* Fabrication of three-dimensionally interconnected nanoparticle superlattices and their lithium-ion storage properties. *Nat. Commun.* **6**, 6420 (2015).
 121. Egly, S. *et al.* Bottom-Up Assembly of Silica and Bioactive Glass Supraparticles with Tunable Hierarchical Porosity. *Langmuir* **34**, 2063–2072 (2018).
 122. Kovalenko, M. V., Scheele, M. & Talapin, D. V. Colloidal Nanocrystals with Molecular Metal Chalcogenide Surface Ligands. *Science* **324**, 1417–1421 (2009).

123. Sanehira, E. M. *et al.* Enhanced mobility CsPbI₃ quantum dot arrays for record-efficiency, high-voltage photovoltaic cells. *Sci. Adv.* **3**, 4204 (2017).
124. <https://www.samsung.com/us/televisions-home-theater/tvs/qled-tvs/>.
125. Abe, S., Joos, J. J., Martin, L. I. D. J., Hens, Z. & Smet, P. F. Hybrid remote quantum dot/powder phosphor designs for display backlights. *Light Sci. Appl.* **6**, 1–9 (2017).
126. Forster, T. Energiewanderung und Fluoreszenz. *Naturwissenschaften* **33**, 166–175 (1946).
127. Crooker, S. A., Hollingsworth, J. A., Tretiak, S. & Klimov, V. Spectrally resolved dynamics of energy transfer in quantum-dot assemblies: towards engineered energy flows in artificial materials. *Phys. Rev. Lett.* **89**, 186802 (2002).
128. Kagan, C., Murray, C., Nirmal, M. & Bawendi, M. G. Electronic energy transfer in CdSe quantum dot solids. *Phys. Rev. Lett.* **76**, 1517–1520 (1996).
129. Clapp, A. R., Medintz, I. L. & Mattoussi, H. Forster resonance energy transfer investigations using quantum-dot fluorophores. *ChemPhysChem* **7**, 47–57 (2006).
130. Akselrod, G. M. *et al.* Subdiffusive Exciton Transport in Quantum Dot Solids. *Nano Lett.* **14**, 3556–3562 (2014).
131. Azzaro, M. S., Dodin, A., Zhang, D. Y., Willard, A. P. & Roberts, S. T. Exciton-Delocalizing Ligands Can Speed Energy Migration in Nanocrystal Solids. *Nano Lett.* **18**, 3259–3270 (2018).
132. Frova, A. *Luce Colore Visione - Perché si vede ciò che si vede.* (BUR, 2012).
133. Strutt, John William, B. R. *The theory of sound.* London, MacMillan **2**, (1878).
134. Mie, G. Beiträge zur Optik trüber Medien, speziell kolloidaler Metallösungen. *Ann. Phys.* **330**, 377–445 (1908).
135. Debye, P. Der Lichtdruck auf Kugeln von beliebigem Material. *Ann. Phys.* **335**, 57–136 (1909).
136. Chiasera, A. *et al.* Spherical whispering-gallery-mode microresonators. *Laser Photonics Rev.* **4**, 457–482 (2010).
137. Choi, J. *et al.* Selective pump focusing on individual laser modes in microcavities. *ACS Photonics* **5**, 7, 2791–2798 (2018).
138. Biddulph, M. <https://www.flickr.com/photos/mbiddulph/3730158004>.
139. Tamboli, A. C. *et al.* Room-temperature continuous-wave lasing in GaN/InGaN microdisks. *Nat. Photonics* **1**, 61–64 (2007).
140. Xie, W. *et al.* On-Chip Integrated Quantum-Dot-Silicon-Nitride Microdisk Lasers. *Adv. Mater.* **29**, 2–7 (2017).
141. Klimov, V. I. *et al.* Optical Gain and Stimulated Emission in Nanocrystal Quantum Dots. *Science* **290**, 314–317 (2000).
142. Vandyshv, Y. V., Dneprovskii, V. S., Klimov, V. I. & Okorokov, D. K. Lasing on transition between quantum-well levels in a quantum dot. *Jetp Lett* **54**, 442 (1991).
143. Moreels, I. *et al.* Nearly Temperature-Independent Threshold for Amplified Spontaneous Emission in Colloidal CdSe/CdS Quantum Dot-in-Rods. *Adv. Mater.* **24**, OP231-5 (2012).
144. Gollner, C. *et al.* Random Lasing with Systematic Threshold Behavior in Films of CdSe/CdS Core/Thick-Shell Colloidal Quantum Dots. *ACS Nano* **9**, 9792–9801 (2015).
145. Yakunin, S. *et al.* Low-threshold amplified spontaneous emission and lasing from

- colloidal nanocrystals of caesium lead halide perovskites. *Nat. Commun.* **6**, 1–8 (2015).
146. Di Stasio, F. *et al.* Single-Mode Lasing from Colloidal Water-Soluble CdSe/CdS Quantum Dot-in-Rods. *Small* **11**, 1328–1334 (2014).
 147. Guzelturk, B. *et al.* Stable and Low-Threshold Optical Gain in CdSe/CdS Quantum Dots: An All-Colloidal Frequency Up-Converted Laser. *Adv. Mater.* **27**, 2741–2746 (2015).
 148. Guzelturk, B., Kelestemur, Y., Olutas, M., Delikanli, S. & Demir, H. V. Amplified Spontaneous Emission and lasing in colloidal nanoplatelets. *ACS Nano* **8**, 6599–6605 (2014).
 149. Jung, J. *et al.* Crafting Core / Graded Shell – Shell Quantum Dots with Suppressed Re- absorption and Tunable Stokes Shift as High Optical Gain Materials. *Angew. Chemie* **1–6** (2016).
 150. Klimov, V. *et al.* Single-exciton optical gain in semiconductor nanocrystals. *Nature* **447**, 441–446 (2007).
 151. Wu, K., Park, Y., Lim, J. & Klimov, V. I. Towards zero-threshold optical gain using charged semiconductor quantum dots. *Nat. Nanotechnol.* **12**, 1140–1147 (2017).
 152. Lim, J., Park, Y.-S. & Klimov, V. I. Optical gain in colloidal quantum dots achieved with direct-current electrical pumping. *Nat. Mater.* **17**, 42–49 (2017).
 153. Grim, J. Q. *et al.* Continuous-wave biexciton lasing at room temperature using solution-processed quantum wells. *Nat. Nanotechnol.* **9**, 891–895 (2014).
 154. Yang, Z., Pelton, M., Fedin, I., Talapin, D. V. & Waks, E. A room temperature continuous-wave nanolaser using colloidal quantum wells. *Nat. Commun.* **8**, 143 (2017).
 155. Laertius, D. & Yonge, C. D. *The lives and opinions of eminent philosophers.* (London: H.G. Bohn, 1853).
 156. Asimov, I. *The Last Question.* (Science Fiction Quaterly, 1956).
 157. Röntgen, W. C. On a new kind of rays. *Science* **3**, 227 LP-231 (1896).
 158. Bragg, W. H. & Bragg, W. L. The Reflection of X-rays by Crystals. *Proc. R. Soc. A Math. Phys. Eng. Sci.* **88**, 428–438 (1913).

Chapter 3

Self-assembly of luminescent CdSe based nanoplatelets in 3D spherical supraparticles

Abstract

CdSe-based colloidal semiconductor nanoplatelets are widely known in the field of colloidal nanoparticles for their bright and sharp photoluminescence, directly arising from their (almost) atomically defined 1D confinement. Nanoplatelets have been considered for applications in opto-electronic devices and lasers. Studies of the self-assembly of nanoplatelets were, so far, limited to needle-like structures. Here we report on the formation and the optical properties of spherical supraparticles, made of nanoplatelets through self-assembly in an oil-in-water emulsion. The supraparticles were formed from core-only CdSe nanoplatelets, as well as with core/shell and core/crown CdSe/CdS nanoplatelets, and had a relatively rough surface and only local order in short stacks of the nanoplatelets which, most likely, both originated from attractions between the platelets. The optical properties of the supraparticles composed of nanoplatelets were found to differ only in minor details from those of the corresponding platelets in suspension.

*«I, a universe of atoms, an atom in the universe»
(Richard P. Feynman)*

3.1 Introduction

Colloidal CdSe-based semiconductor nanoplatelets (NPLs) are a relatively new class of colloidal nanocrystals attracting increasing interest since their discovery by Ithurria and coworkers.^{1,2} The NPLs have been reported to exhibit remarkable optical properties different from the ones of the luminescent 0-dimensional nanocrystals synthesized previously. In particular, the atomic control over the NPLs thickness results in narrow (30–40 meV) Lorentzian photoluminescence (PL) emission spectra with no inhomogeneous broadening.³ Viewed in time, the emission consists of fast spontaneous emission,² and delayed emission related to charge carrier trapping.⁴ Thanks to their optical properties, NPLs have been considered as good candidates for several applications, such as spectral converters in light emitting diodes,⁵ as gain materials in lasers^{6,7} and as photodetectors.⁸ The use of NPLs in applications has promoted the demand for more robust NPLs with higher PL quantum yield; this resulted in new designs of heterostructures such as core/shell^{9–11} and core/crown^{12–14} NPLs, with passivation of the top and bottom {001} facets, or the lateral facets, respectively, using a few monolayers (MLs) of a different semiconductor material. More recently, NPLs with different chemical composition and graded structures have also been proposed, thus enriching the current library of two dimensional nanoparticles.^{15–18} More generally, other nanoplatelet systems have been developed and investigated for decades, also in respect of their self-assembly.^{19–26}

Although much is known about NPLs, the actual mechanism of symmetry breaking that leads to their formation still eludes scientists. So far several reports^{27–29} claim to have unraveled their formation mechanism, but a full and complete model that can explain all the experimental observations has yet to be found. This, however, didn't stop scientists from obtaining good control over NPLs thickness and lateral shape.^{2,30} This control promoted the use of NPLs as building blocks for self-assembled superstructures. Notice that the van der Waals binding energy between flat building blocks is considerably larger than between nanospheres, which simply results from the geometry of these nanoparticles with much more atoms being in close proximity when the plates lay on top of each other.³¹ However, it is well known that particles that one wants to use in self-assembly (SA) studies are much harder to control as attractions of just a few kT at contact can already drive system out of equilibrium in more amorphous, or only locally ordered, structures. It has already been reported that NPLs can be assembled in more complex architectures such as liquid crystalline superstructures displaying long-range orientational and positional order.^{21,32} These structures showed interesting collective properties compared to the individual building blocks.³³ However, the self-assembly of NPLs in needle-like superstructures is not ideal due to the ultra-efficient exciton transfer in stacked NPLs, which assists the exciton trapping thus lowering the overall quantum yield of the superstructure.³⁴

Here we report on the synthesis of bright supraparticles^{35,36} (SPs) made of luminescent CdSe NPLs by an oil-in-water emulsion method previously developed in our group.³⁷ The SPs were synthesized with CdSe NPLs as well as with CdSe/CdS core/shell NPLs and CdSe/CdS core/crown NPLs. The general preservation of the optical properties of the individual NPLs when these are self-assembled in the SPs is confirmed by time-resolved emission spectroscopy. SPs of NPLs bear importance for possible applications in *e.g.* lasing and bio-imaging.

3.2 Results and Discussion

3.2.1 Synthesis and optical characterization of SPs made of CdSe NPLs

The CdSe NPLs were synthesized using a protocol present in literature² with some modifications. The synthesized 4 monolayers (ML) CdSe NPLs had a rectangular shape with an average length of 20 ± 2 nm and an average width of 8 ± 1 nm, as estimated from transmission electron microscopy (TEM) (Figure 3.1a). The absorption and photoluminescence (PL) spectra of the NPLs are shown in Figure 3.1d-e. In the absorption spectrum, the lowest-energy absorbance peak (related to the heavy-hole transition^{2,38}) is at 509 nm while the second absorbance peak (related to the light-hole transition^{2,38}) is at 479 nm. These peaks, around 510 nm and around 480 nm, are characteristic for “510 NPLs”, as reported in literature.² The thickness of these NPLs is 4 monolayers (MLs) of CdSe, which is 2 nm.^{2,27} The Lorentzian shaped PL emission peak is centered around 512 nm with a full width half maximum (FWHM) of 44 meV due to pure 1D confinement.

The NPLs were then self-assembled in 3D supraparticles (SPs) using an oil-in-water emulsion method.^{36,37} Slowly evaporating oil droplets, which were dispersed in water them-

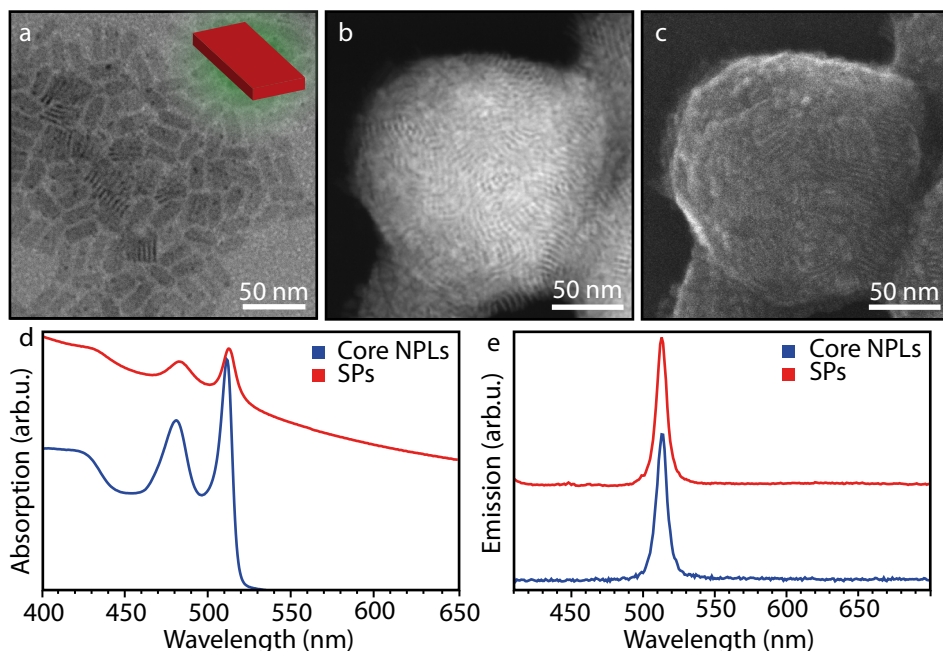


Figure 3.1 • Structural and optical characterization of SPs of CdSe NPLs. (a) Representative TEM picture of 4 ML nanoplatelets; (b) HAADF-STEM image of a SP made of the NPLs showed in panel a. The stacks of NPLs with different orientations are easily recognizable; (c) SE-STEM image of the same SP of panel b; (d) Absorption spectra of the dispersed NPLs and the SPs dispersed in water. The light-hole and heavy-hole transition of the NPLs (480 nm and 510 nm respectively) are still recognizable in the SP spectrum; (e) Emission spectra of the NPLs (blue) and of the SPs (red). The peak position as well as the full width half maximum for the SPs sample are the same as for the NPLs. The gradual increasing onset between 650 and 550 nm is due to light scattering.

selves, containing NPLs provided a spherical confinement for the self-assembly (SA) of the NPLs, eventually resulting in SPs dispersed in water. The SPs were structurally characterized with high angle annular dark-field scanning transmission electron microscopy (HAADF-STEM) and secondary electron scanning transmission electron microscopy (SE-STEM) and characteristic images are shown in Figure 3.1b-c. The average diameter of the SPs was determined to be 165 ± 60 nm (from TEM analysis), with a large polydispersity (PD) of 40%, by averaging over 70 particles. The HAADF-STEM and SE-STEM images both show a spherical but rough SP consisting of small stacks of NPLs. The stacks have different orientations and can also be seen in TEM images of NPLs (Figure 3.5 in Appendix). The stacking of similar NPLs (same ML thickness and ligands) as used in this study in long needle-like structures has been reported in literature.³³ The presence of the stacks is attributed to the presence of several kT of attractive forces between the NPLs “top-on-top”, originating from their flat shape and the high density of ligands on the facets.³⁹ The attractions could not have been too large or otherwise amorphous and/or gel-like, more open systems would have resulted. It is possible that the polydispersity of the stacks already present at lower volume fractions, combined with the system not reaching equilibrium, could have been the reason for the absence of longer ranged order within the SPs. Unfortunately the thickness of the system of NPLs in this work made it not (yet) possible for us to obtain full single NPL positional and orientational order as we recently obtained with other rare-earth based NPL systems.¹⁹ In that study also indications of attractions between the NPLs were found, but the strength of the attractions were probably smaller than in the present study as both perfectly smooth and 3D well-ordered SP were found in that study.¹⁹

In order to investigate the role of nanoplatelet-nanoplatelet interactions on the optical properties of the NPLs, we compared the absorption and emission spectra of the individually suspended NPLs with those of the self-assembled configuration. Figure 3.1d shows the absorption spectra of the SPs (red line) and of the NPLs suspended in hexane (blue line). The NPLs in the SPs exhibit the characteristic absorption peaks of 4 ML CdSe NPLs (around 480 nm and 510 nm), although a small red-shift is observed (9 meV). The increase in the background of the absorption spectra of the SPs can be attributed to scattering. The normalized photoluminescence (PL) spectra of the NPLs (in blue) and SPs (in red) are shown in Figure 3.1e. We observe that the two peaks have the same emission maximum (512 nm) and FWHM (44 meV), thus indicating a general preservation of the optical properties. Concerning the PL quantum yield (QY), for the dispersed NPLs it is 8%, and it decreased to 2% for the NPL SPs. This decrease must be due to energy transfer from platelet-to-platelet in the SPs, enhancing the non-radiative recombination.³⁴ In the present case, all platelets in a SP emit at the same wavelength, which means that energy transfer is not accompanied by a red shift, as observed for QD assemblies (see Chapter 5).⁴⁰ We would also like remark here that PL QY measurements with light scattering samples are not fully trustworthy and should be considered with care.

3.2.2 Synthesis and optical characterization of SPs made of core/shell NPLs

In order to investigate the applicability of the self-assembly method to different kinds of NPL electronic morphologies, we synthesized CdSe/CdS NPLs and we used them as building blocks for SPs. Core/shell NPLs are synthesized by colloidal atomic layer depo-

sition¹⁰ (c-ALD) of semiconductor material to previously synthesized NPLs. Figure 3.2a shows a representative TEM image of core/shell CdSe/CdS NPLs. The NPLs were obtained from previously synthesized 4 ML CdSe NPLs by the growth of 2 ML of CdS on the top and bottom (Cd rich) facets, by means of c-ALD. The final core/shell NPLs are characterized by a rectangular shape with an average length of 21 ± 4 nm, and an average width of 9 ± 5 nm, as determined by TEM.

In Figure 3.2d, the absorption spectra of 4 ML CdSe NPLs (green line) and core/shell CdSe/CdS NPLs (blue line), are compared. The characteristic peaks of 4 ML NPLs (around 508 and 479 nm) are red-shifted to 598 nm and 557 nm after the growth of the CdS shell. The strong red-shift of the absorption peaks is due to partial relaxation of the quantum confinement due to an increase in the vertical thickness through the formation of a type-I^{1/2} heterojunction.¹⁴ The observation of a red-shift after each c-ALD cycle is an indication that the core/shell NPLs were successfully synthesized. Compared to the original CdSe NPLs, the PL spectrum for the CdSe/CdS core/shell NPLs is redshifted by 386 meV, from 512 nm to 609 nm (Figure 3.2e), with an increase in FWHM of 28 meV (from 53 meV to 81 meV). The increase in the FWHM is an intrinsic effect either related to a decrease in the overlap between the electron and the hole wave functions, and/or to local

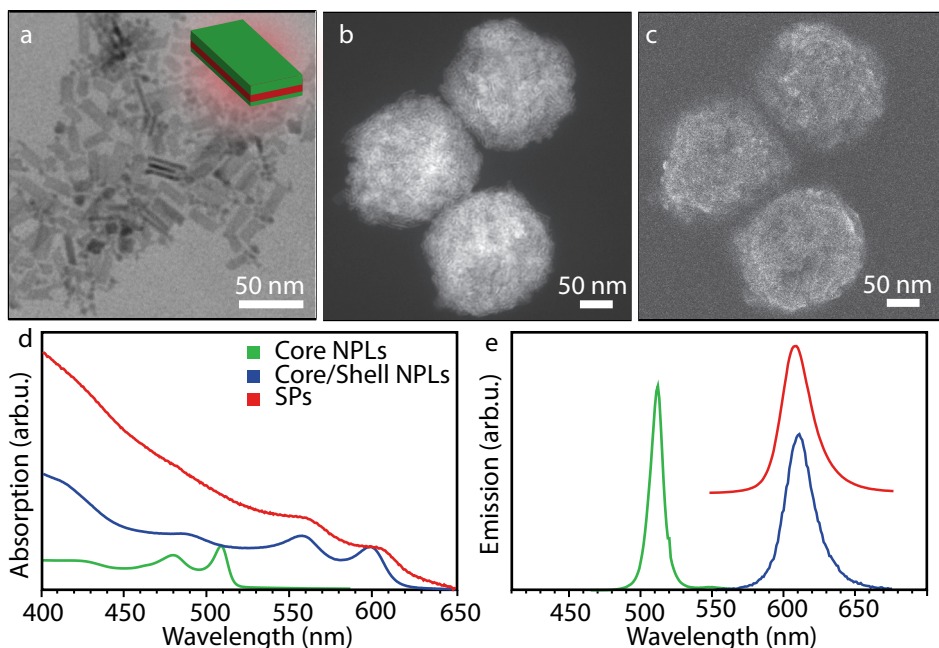


Figure 3.2 • Structural and optical characterization of SPs of CdSe/CdS core/shell NPLs. (a) Representative TEM picture of CdSe/CdS core/shell nanoplatelets; (b) HAADF-STEM image of a SP made of the NPLs shown in panel a; (c) SE-STEM image of the same SP of panel b; (d) Absorption spectra of the core/shell NPLs shown in panel a (blue), the original core NPLs (green) and the SPs presented in panel b and c (red). The light-hole and heavy-hole transition of the NPLs are still recognizable in the SP spectrum; (e) Emission spectra of the core/shell NPLs (blue), of the original core NPLs (green) and of the SPs (red). The peak position as well as the full width half maximum for the SPs sample are the same as for the NPLs.

structure defects and surface disorder, as previously reported.¹⁰

The NPLs were then used as building blocks for the formation of SPs with the same oil-in-water method used for the core NPLs. The resulting SPs were characterized with HAADF-STEM and SE-STEM (Figure 3.2b-c), showing an approximately spherical shape. However, we note that the surface of these SPs is even rougher compared to SPs made out of core CdSe NPLs. We attribute this difference to possibly somewhat larger van der Waals forces between two NPLs laying on top of each other, although it may be that the significantly higher polydispersity may play a role as well. As for the previous case, the single NPLs can still be recognized at the circumference of the SPs, assembled in small stacks with random orientation.

Also in this case, the optical properties of the SPs were compared to those of the composing building blocks (Figure 3.2b-c). The absorption spectrum of the SPs was characterized by two small peaks around 605 and 560 nm, corresponding to the heavy-hole and light-hole transitions previously reported for the dispersed NPLs. The small red shift (27 meV) of the first excitonic peak to 567 nm can be attributed to a change in the refractive index medium when the NPLs are assembled in SPs, or to weak quantum coupling between top-on-top NPLs. The normalized PL spectrum (Figure 3.2e) shows that the emission peak of the SPs is slightly red-shifted (7 meV) compared to the dispersed core/shell NPLs, moving from 609 nm to 611 nm, and we observed a small decrease in the FWHM of the emission peak, from 81 meV to 78 meV. As for the core CdSe NPLs, also for the core/shell CdSe/CdS NPLs the characteristic absorption and emission peaks were retained with no major changes, except for the small redshift. Concerning the PL QY, for the dispersed NPLs it was 6%, and it decreased to 4% for the NPL SPs. The decrease in the PL QY indicates the presence of energy transfer between the NPLs.

3.2.3 Synthesis and optical characterization of SPs made of core/crown NPLs

The third type of NPLs known in literature is core/crown NPL, where the lateral facets of the platelets are passivated with a crown of a different material. For the synthesis of these NPLs we followed the procedure of Tessier *et al.*¹² which consists in the continuous injection of an anisotropic growth mixture during the formation of 4 ML CdSe NPLs, thus obtaining small 4 ML CdSe core NPLs embedded in a big CdS crown. Our 4 ML CdSe/CdS core/crown NPLs were characterized by an average length of 23 ± 3 nm and an average width of 11 ± 1 nm, as deduced from TEM analysis (Figure 3.3a).

The absorption and PL emission of the core/crown NPLs are shown in Figure 3.3d-e. The absorption spectrum shows the characteristic peak at 509 nm, corresponding to the heavy-hole transition of the CdSe core, and another peak at 406 nm, corresponding to the heavy-hole transition of pure CdS NPLs, thus confirming the successful growth of a CdS crown around the core. In particular, the big absorption at 406 nm compared to the absorption peak at 510 nm indicates that we are in the regime of small core/ big crown, as indicated by Tessier.¹² Furthermore we observe the presence of two additional small peaks, at 377 nm and at 448 nm. By comparison to the literature², the peak at 377 nm can be attributed to the heavy hole transition of 3 ML CdS NPLs, suggesting perhaps the pres-

ence of secondary nucleation of 3 ML CdS NPLs during the growth of the crown, while the peak at 448 nm has not been previously observed and it is of unknown origin. The PL emission spectrum of the NPLs shows a maximum at 509 nm with a FWHM of 45 meV. We note that the crown, in this type of NPLs, merely acts as a huge antenna, increasing the absorption of photons, thus not affecting the position and the shape of the PL emission of the core 4 ML CdSe NPLs.

SPs using core/crown NPLs as building blocks were synthesized and representative HAADF-STEM and SE-STEM images are shown in Figure 3.3b-c. The SPs were characterized by a spherical shape with a rough surface; clearly composed of small stacks of NPLs in random orientation. The optical properties of these SPs were compared to those of the corresponding NPL suspension. Similarly to the previous cases, also here the absorption spectrum shows an increased background due to scattering and a slight red-shift (9 meV) of the two characteristic peaks at 408 nm and 512 nm to 411 nm and 514 nm, respectively. The position of the PL emission was, in this case, completely retained as the maximum is still centered at 509 nm and the FWHM is 45 meV (Figure 3.3e). Notice the presence of a second broad peak at 474 nm in the case of NPL SPs. A similar feature in the PL was observed for dispersed CdSe/CdS core/crown platelets by Tessier *et al.*¹², even though with a

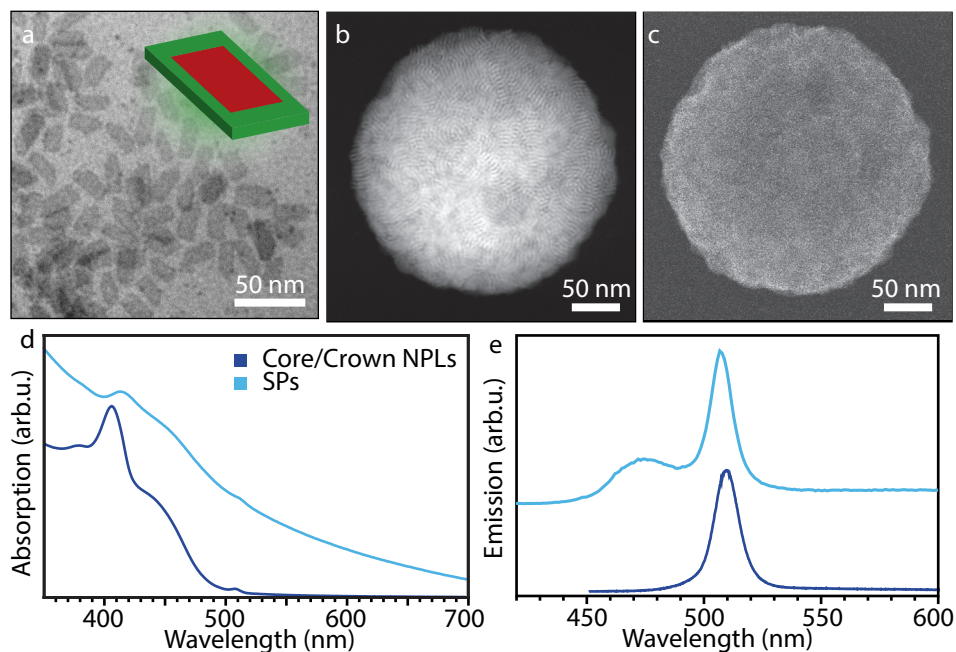


Figure 3.3 • Structural and optical characterization of SPs of CdSe/CdS core/crown NPLs. (a) Representative TEM picture of 4 ML CdSe/CdS core/crown nanoplatelets; (b) HAADF-STEM image of a SP made of the NPLs showed in panel a. The stacks of NPLs with different orientations are easily recognizable; (c) SE-STEM image of the same SP of panel b; (d) Absorption spectra of the NPLs (dark blue) shown in panel a and the SPs (light blue), shown in panel b and c. The heavy-hole transition of the CdSe cores (510 nm) and the CdS shell light-hole transition (410 nm) are still recognizable in the SP spectrum; (e) Emission spectra of the NPLs (blue) and of the SPs (red). The peak position as well as the full width half maximum for the SPs sample are the same as for the NPLs.

much lower intensity, but the authors didn't supply details about it. At the current moment we don't have an explanation for this feature. Concerning the PL quantum yield (QY), we observed a decrease of about 2% (from 4% to 2%) for NPLs assembled in the SPs.

3.2.4 Decay dynamics of NPLs and SPs

In order to get a better insight on the role of the nanoplatelet-nanoplatelet coupling on the dynamics of the excitons, we performed time-resolved emission spectroscopy measurements on the different samples of NPLs in suspension and self-assembled in SPs. Time-resolved emission spectroscopy is a powerful technique to unravel the exciton dynamics in photoluminescent nanocrystals, and it has been previously used, for example, to expand the knowledge about the relation between spontaneous emission, energy transfer and delayed emission in nanocrystalline systems.^{4,41,42} We remark, however, that the relation between delayed emission and spontaneous emission and the role of charge trapping on the exciton dynamics are not fully understood for quantum dots systems. This is even more the case for NPLs, due to the strong non-radiative recombination in these systems, possibly to the large surface area, which increases the chances that chemical changes affect the optical properties of the particles. For these reasons, the following results should be considered as a preliminary study of a much more complex subject, and further investigations are required to fully explain all observations made.

In Figure 3.4a the decay traces of CdSe NPLs dispersed in solution (blue) and assembled in SPs (red) are compared. In both systems the first 20 ns are dominated by a multi-exponential decay with nanosecond and subnanosecond components associated with radiative and non-radiative recombination. After 20 ns the data are plotted in a double logarithmic scale in order to highlight the power-law decay associated with delayed emission.⁴ The general trend is retained and we do not observe any particular difference between the NPLs dispersed in solution and assembled in SP. As for the core/shell CdSe/CdS NPLs (Figure 3.4b), we also observed a strongly multiexponential behavior in the first 20 ns and a power-law trend for longer delay times. The decay is very similar to that observed for core CdSe NPLs (Figure 3.4a), with the only difference being a generally faster decay in the case of NPLs assembled in SPs. Finally, for the core/crown CdSe/CdS NPLs (Figure 3.4c), we observed variations from the previous trends. In the first 20 ns, the decay of the

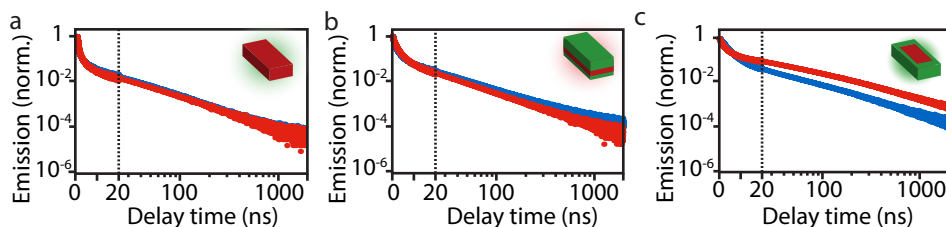


Figure 3.4 • Decay dynamics of NPLs in suspension and self-assembled in SPs. (a) Photoluminescence decay traces of CdSe NPLs freely dispersed in hexane (blue) and assembled in water-dispersed SPs (red). The first 20 ns are plotted in a linear scale, while the following are plotted in a logarithmic scale. (b) Photoluminescence decay traces of CdSe/CdS core/shell NPLs freely dispersed in hexane (blue) and assembled in water-dispersed SPs (red); (c) Photoluminescence decay traces of CdSe/CdS core/crown NPLs freely dispersed in hexane (blue) and assembled in water-dispersed SPs (red).

NPLs assembled in the SPs was faster compared to the dispersed NPLs. In addition, the transition from multiexponential to power-law behavior is observed at earlier delay times, at 10 ns instead of 20 ns. For longer delay times we observe a power-law decay with the same slope in both cases. In all three cases, the faster decay in the early time regime points to energy transfer between the CdSe cores of top-on-top platelets, which is another indication that stacks are present in the NPL solutions as well. Due to this energy transfer, excitons can more easily decay via a defect, resulting in faster non-radiative recombination; this is reflected in the general trend of a lower PL QY for the NPL SPs compared to when the NPLs were separately dispersed in solution.

3.3 Conclusions

In this chapter, we reported on the self-assembly of core, core/shell and core/crown NPLs into SPs. Due to the strong attraction between the facets, the NPLs form small stacks which were randomly oriented in space, giving origin to spherical SPs with a relatively rough (compared to the NPL thickness) surface which we attribute to attractions between the NPLs. The optical properties of the NPLs were generally preserved during the self-assembly process, as supported by emission and absorption measurements. By means of time-resolved emission spectroscopy, we also performed a preliminary study of the changes produced in the exciton dynamic by the self-assembly. It is important for future optical use of SPs build up from NPLs that perfectly ordered and smooth SPs, that could be analyzed on the single NP level, were recently reported on by our group, pointing at the important and subtle role that attractions between NPLs play in SA. This paper focused on what is, as far as we know, the first example of 2D quantum wells self-assembled in spherical confinement, where future optimization of optical properties can be achieved by reducing the attractions between the NPs (*e.g.* by using somewhat longer ligands), thus allowing future analysis of these interesting systems on the single NPL level.

3.4 Methods

Chemicals

1-Butanol anhydrous (BuOH, 99.8%), 1-Octadecene (ODE, 90%), Cadmium acetate dihydrate ($\text{Cd}(\text{Ac})_2 \cdot 2\text{H}_2\text{O}$, 98%), Cadmium nitrate tetrahydrate ($\text{Cd}(\text{NO}_3)_2 \cdot 4\text{H}_2\text{O}$), Cyclohexane, Dextran from *Leuconostoc mesenteroides* (M_w 670000 g/mol), Ethanol (EtOH, 99.8%), Hexane, Methanol (MeOH, anhydrous, 99.8%), N-methylformamide (NMF), Oleic acid (OA, 90%), Oleylamine (OLAM), Sodium acetate (Na(Ac)), Sodium dodecyl sulfate (SDS, $\geq 98.5\%$), Sodium hydrosulfide hydrate (NaSH), Sodium myristate (Na(myristate)), Sulfur (S, 99.998%) and Zinc acetate dihydrate ($\text{Zn}(\text{Ac})_2 \cdot 2\text{H}_2\text{O}$, $\geq 98\%$) were all purchased by Sigma Aldrich and used as received. Se powder (Se, 200 mesh, 99.999%) was purchased from Brunshwig Chemie.

Synthesis of CdSe Nanoplatelets

Precursor Preparation for the Synthesis of 510 Nanoplatelets

In order to prepare the cadmium precursor, cadmium myristate ($\text{Cd}(\text{myr})_2$), 1.23 g cadmium nitrate tetrahydrate ($\text{Cd}(\text{NO}_3)_2 \cdot 4\text{H}_2\text{O}$) was dissolved in 40 mL methanol (MeOH) and 3.13 g sodium myristate (Na(myristate)) was dissolved in 250 mL MeOH. The $\text{Cd}(\text{NO}_3)_2$ solution was then added to the solution of Na(myristate) and stirred vigorously. The cadmium myristate ($\text{Cd}(\text{myr})_2$) precipitates from the solution as a white powder. A Buchner funnel was used to filter the product which was then dried overnight under vacuum.

The selenium precursor was prepared by adding 180 mg selenium (Se) powder to 15 mL octadecene (ODE), this mixture was sonicated until there are no Se traces left on the bottom. As the Se powder tends to precipitate over time, it was sonicated again before addition.

Synthesis of 510 Nanoplatelets

Synthesis of 510 nm NPLs was performed as described in reference¹ with some modifications. In a 100 mL

three neck flask, 170 mg Cd(myristate)₂, 14 mL ODE and 1 mL of the selenium precursor were mixed. This reaction mixture was degassed for 1 hour at room temperature. The mixture was then put under nitrogen flow and heated to 240°C while being stirred at 1000 RPM. The mixture became transparent around 80°C and around 180°C the turned yellow. As the solution started to turn orange at 195°C, a mixture of 40 mg cadmium acetate (Cd(Ac)₂) and 20 mg sodium acetate (Na(Ac)) was quickly added. When the solution reached 240°C a growth time of 5 minutes was allowed, after which the mixture was quickly cooled down. The solution turned orange and then red during the growth time. The turbid, orange product shows green luminescence. 14 mL hexane and 1 mL oleic acid (OA) were added to the mixture and, upon addition of the OA, the product became clear. After the synthesis the NPLs were washed by addition of MeOH and BuOH (1:2) and centrifugation at 1000 RCF for 10 minutes. The precipitate was redispersed in 10 mL hexane. This washing step was repeated twice.

Synthesis of Core/Shell Nanoplatelets using c-ALD

Synthesis of core/shell NPLs was performed using colloidal atomic layer deposition (c-ALD), as described in reference¹⁰. This procedure separates the growth of a CdS shell into two steps. Firstly, the cadmium rich facets react with sulfide ions (S²⁻) forming sulfide rich facets, secondly, the NPLs react with a solution of Cd(Ac)₂ to form cadmium rich facets. While other methods for shell growth have been proposed, this procedure was chosen because it gives a lot of control on the number of layers that are grown on the NPLs.

Precursor Preparation for Colloidal Atomic Layer Deposition

For the synthesis of the sulfide half-monolayer, a 0.10 M solution of sodium hydrosulfide hydrate (NaSH) in N-methylformamide (NMF) was prepared. The solution was prepared by mixing 56.06 mg NaSH in 10 mL NMF and by stirring the mixture inside a glovebox until complete dissolution. The resulting solution was colourless. For the synthesis of the cadmium half-monolayer, a 0.20 M Cd(Ac)₂ stock solution in NMF was prepared by dissolving 533 mg Cd(Ac)₂ dihydrate in 10 mL NMF. The resulting solution was clear and colourless. For the synthesis of a zinc half-monolayer a 0.2 M zinc acetate dihydrate (Zn(Ac)₂·2H₂O) solution in NMF was prepared by dissolving 440 mg Zn(Ac)₂ dihydrate in 10 mL NMF. This resulted in a clear and colourless solution.

Growth of the sulfide half-monolayer

For the synthesis of the sulfide half-monolayer, 3 mL of the 0.10 M NaSH solution was added to 3 mL of CdSe NPLs which had been dispersed in 10 mL hexane after synthesis. This formed a two-phase system with the NPLs in the upper phase and the sulfide ions in the NMF lower phase. The NPLs reacted with the sulfide ions in the lower phase, causing them to slowly transfer to the lower phase. The mixture was stirred at 800 RPM for 5 minutes, after which complete phase transfer of the NPLs from hexane (polar phase) to NMF (the a-polar phase) was observed. During the reaction the colour of the NPLs changed from orange to red.

Washing Step

The upper phase of the two-phase system, was removed with a pipette. The lower phase, containing the NPLs, was rinsed with 2 mL hexane twice, each time removing the upper phase with a pipette. The NPLs were precipitated by addition of 6 mL toluene and 2 mL acetonitrile (3:1) and centrifugation at 1000 RCF for 10 minutes. The precipitate was redispersed in 3 mL NMF. This last washing step was repeated once.

Growth of cadmium or zinc half-monolayer

To the NPL solution 2 mL of the 0.20 M Cd(Ac)₂ solution was added. The NPLs were stirred at 800 RPM for 5 minutes. For a zinc shell a mixture of 0.20 M Cd(Ac)₂ and 0.20 M Zn(Ac)₂ with a total volume of 2 mL was added as reactant. After which the NPLs were stirred at 800 RPM for 5 minutes.

Washing Step

The NPLs were precipitated by the addition of 12 mL toluene and 4 mL acetonitrile (3:1) and centrifugation at 15000 RCF for 15 min. The colourless supernatant was carefully removed with a pipette and the precipitate was redispersed in 3 mL NMF. The washing step was repeated once, the second time the precipitation was performed by adding 9 mL toluene and 3 mL acetonitrile. For additional shell layers the c-ALD procedure was repeated.

Ligand Exchange

After the addition of the desired amount of monolayers a ligand exchange was performed to redisperse the NPLs in hexane. The NPLs were precipitated by addition of 5 mL toluene and 2 mL acetonitrile and centrifugation at 15000 RCF for 15 min. The clear supernatant was carefully removed with a pipette and the precipitate was dried under vacuum (for 15 min). The precipitate was redispersed in 3 mL hexane with 250 µL OA and 150 µL

oleylamine (OLAM). This resulted in a clear solution; in case of a turbid solution an additional 20 μL OA was added to the solution.

Synthesis and Coating of Core/Crown Nanoplatelets

Core/crown NPLs were synthesized with a mixture of $\text{Cd}(\text{Ac})_2$ and sulphur (S), dissolved in ODE for the anisotropic growth of a crown around the lateral facets of the NPLs, while the thickness of the NPLs remains constant. The amount of anisotropic growth mixture used in the core/crown NPL synthesis changes the size of the crown. NPLs were synthesized and directly coated with a CdS crown, as described in reference¹².

Precursor Preparation for Core/Crown Nanoplatelets

The 0.10 M S solution was prepared by heating 50 mL ODE, under nitrogen, in a 100 mL three neck flask to 180 °C. At 180 °C, 160 mg S powder was added to the ODE. The mixture was stirred for 30 minutes, forming a light yellow solution which was degassed at room temperature for 1 hour. In order to prepare 5 mL of anisotropic growth mixture, 480 mg $\text{Cd}(\text{Ac})_2$ dihydrate, 340 μL OA and 2 mL ODE were mixed in a 50 mL three-neck ask. This mixture was heated to 100 °C under ambient atmosphere while stirring vigorously (at 1000 RPM). After 10 minutes at 100 °C the mixture was sonicated for 5 minutes. The mixture was then heated again to 100 °C these steps were repeated until a white/grey homogeneous gel was formed. The homogeneous gel was mixed with 3 mL of the 0.10 M S solution. The anisotropic growth mixture was kept stirring vigorously, until it was used in the core/crown synthesis. The selenium precursor is prepared by adding 180 mg selenium (Se) powder to 15 mL octadecene (ODE), this mixture is sonicated until there are no Se traces left on the bottom. As the Se powder tends to precipitate over time, it is sonicated again before addition.

Synthesis of Core/Crown NPLs

Synthesis of core/crown NPLs was performed as described in reference¹². In a 100 mL three-neck flask, 85 mg $\text{Cd}(\text{myr})_2$ and 7.5 mL ODE were mixed and degassed for 30 minutes. Under nitrogen flow, the mixture was heated to 230 °C. At 230 °C, 1 mL of the Se precursor was quickly injected. Starting 30 seconds after the Se addition, a certain amount of anisotropic growth mixture was continuously injected with a syringe pump into the reaction mixture at a rate of 30 mL/h. A total growth time (counted from the moment the Se precursor was injected) of 5 minutes was allowed, after which the dispersion was quickly cooled down by compressed air. The NPLs were washed by addition of EtOH and centrifugation at 100 RCF for 10 minutes. The precipitate was redispersed in 5 mL hexane.

Synthesis of SPs

Precursor Preparation for Self-Assembly in Supraparticle

The water phase containing surfactants was prepared by adding 4 g dextran to 100 mL milli-Q water. This mixture was stirred until complete dissolution. Then 600 mg sodium dodecyl sulfate (SDS) was added to the mixture. This mixture was stirred for 30 minutes to dissolve the SDS.

Supraparticle Self-Assembly

The SP self-assembly was performed as described in reference.³⁷ For the formation of SPs, a solution of 8-10 mg/mL of NPLs in cyclohexane was prepared. The NPLs dispersed in cyclohexane were then added to 10 mL of the milli-Q water solution containing surfactants and dextran forming a two-phase system. This two-phase system was emulsified using a Couette shear cell. The Couette shear cell uses high shear rates in combination with visco-elastic properties of the dispersion in order to emulsify the two phases and it is a methodology firstly developed by the Bibette group.^{43,44} Thanks to this method, SPs with a precise size, in a size range between 100 nm and 500 nm, can be produced with control over the size by changing the shear rate during the emulsification. The emulsion was then placed in an oil bath at 65 °C and kept stirring at 200 RPM for 4 hours to evaporate the cyclohexane from the oil-in-water droplets. After evaporation, the solution can be slightly turbid depending on the concentration of SPs as they tend to scatter the light. The SPs were washed by centrifuging at 690 RCF for 10 minutes. The clear supernatant was carefully removed with a pipette and the SPs were redispersed in 5 mL milli-Q water.

Optical Measurements

The PL quantum yield (PLQY) measurements were performed on samples consisting of diluted NC or SP solutions (cyclohexane for NCs, Milli-Q water for SPs) in a quartz cuvette using an Edinburgh instruments F900 spectrometer with an integrating sphere and excitation at 420 nm. Confocal images were acquired with a Leica SP8 confocal microscope fitted with a pulsed super continuum light

source (NKT Photonics, 400 nm, 5 ps pulse duration, 78 MHz repetition rate), focusing objective (100x /1.4 NA oil-immersion confocal objective (LEICA)), and PMT detection. The investigated individual supraparticles were lying on a 600 nm SiO₂ covered Si substrate, 0.15 mm thick, and immersed in Leica immersion oil type F. PL emission and decay traces were recorded using an Edinburgh instruments F900 spectrometer, while absorption was measured with a PerkinElmer lambda 950 spectrophotometer.

Definition of polydispersity

All the values of sizes in the article are given with the mean (μ) and the standard deviation (σ) in the form: $\mu \pm \sigma$. Polydispersity of size is defined as PD (%) = $(\sigma/\mu) \cdot 100$.

Electron microscopy

HAADF-STEM images and SE-STEM images of the SPs were acquired using a FEI Tecnai electron microscopes operated at 200 kV.

Acknowledgements

We thank J.D. Meeldijk for his assistance with HAADF and SE-STEM measurements.

References

1. Ithurria, S. & Dubertret, B. Quasi 2D Colloidal CdSe Platelets with Thicknesses Controlled at the Atomic Level. *J. Am. Chem. Soc.* **130**, 16504–16505 (2008).
2. Ithurria, S. *et al.* Colloidal nanoplatelets with two-dimensional electronic structure. *Nat. Mater.* **10**, 936–941 (2011).
3. Tessier, M. D. *et al.* Spectroscopy of colloidal semiconductor core/shell nanoplatelets with high quantum yield. *Nano Lett.* **13**, 3321–3328 (2013).
4. Rabouw, F. T. *et al.* Temporary Charge Carrier Separation Dominates the Photoluminescence Decay Dynamics of Colloidal CdSe Nanoplatelets. *Nano Lett.* **16**, 2047–2053 (2016).
5. Fan, F. *et al.* Colloidal CdSe_{1-x}S_x Nanoplatelets with Narrow and Continuously-Tunable Electroluminescence. *Nano Lett.* **15**, 4611–4615 (2015).
6. Guzelturk, B., Kelestemur, Y., Olutas, M., Delikanli, S. & Demir, H. V. Amplified Spontaneous Emission and lasing in colloidal nanoplatelets. *ACS Nano* **8**, 6599–6605 (2014).
7. She, C. *et al.* Red, Yellow, Green, and Blue Amplified Spontaneous Emission and Lasing Using Colloidal CdSe Nanoplatelets. *ACS Nano* **9**, 9475–9485 (2015).
8. Lhuillier, E. *et al.* Two-Dimensional Colloidal Metal Chalcogenides Semiconductors: Synthesis, Spectroscopy, and Applications. *Acc. Chem. Res.* **48**, 22–30 (2015).
9. Mahler, B., Nadal, B., Bouet, C., Patriarche, G. & Dubertret, B. Core/shell colloidal semiconductor nanoplatelets. *J. Am. Chem. Soc.* **134**, 18591–18598 (2012).
10. Ithurria, S. & Talapin, D. V. Colloidal Atomic Layer Deposition (*c*-ALD) using Self-Limiting Reactions at Nanocrystal Surface Coupled to Phase Transfer between Polar and Nonpolar Media. *JACS* **134**, 18585–18590 (2012).
11. Rossinelli, A. A. *et al.* High-temperature growth of thick-shell CdSe/CdS core/shell nanoplatelets. *Chem. Commun.* **53**, 9938–9941 (2017).
12. Tessier, M. D. *et al.* Efficient Exciton Concentrators Built from Colloidal Core/Crown CdSe/CdS Semiconductor Nanoplatelets. *Nano Lett.* **14**, 207–213 (2014).
13. Kelestemur, Y. *et al.* Type-II Colloidal Quantum Wells: CdSe/CdTe Core/Crown Heteronoplatelets. *J. Phys. Chem. C* **119**, 2177–2185 (2015).
14. Kelestemur, Y. *et al.* Platelet-in-Box Colloidal Quantum Wells: CdSe/CdS@

- CdS Core/Crown@Shell Heteronano-platelets. *Adv. Funct. Mater.* **26**, 3570–3579 (2016).
15. Kelestemur, Y. *et al.* Alloyed Heterostructures of CdSe_xS_{1-x} Nanoplatelets with Highly Tunable Optical Gain Performance. *Chem. Mater.* **29**, 4857–4865 (2017).
 16. Sharma, M. *et al.* Copper-Doped Colloidal Semiconductor Quantum Wells for Luminescent Solar Concentrators. *Adv. Mater.* **1700821**, 1–10 (2017).
 17. Kelestemur, Y. *et al.* CdSe/CdSe_{1-x}Te_x Core/Crown Heteronano-platelets: Tuning the Excitonic Properties without Changing the Thickness. *J. Phys. Chem. C* **121**, 8, 4650–4658 (2017).
 18. Delikanli, S. *et al.* Continuously Tunable Emission in Inverted Type-I CdS/CdSe Core/Crown Semiconductor Nano-platelets. *Adv. Funct. Mater.* **25**, 4282–4289 (2015).
 19. Wang, D. *et al.* Quantitative real space analysis of supraparticles composed of nanoplatelets. *Submitted* (2018).
 20. Paik, T., Diroll, B. T., Kagan, C. R. & Murray, C. B. Binary and Ternary Superlattices Self-Assembled from Colloidal Nanodisks and Nanorods. *J. Am. Chem. Soc.* **137**, 6662–6669 (2015).
 21. Ye, X. *et al.* Competition of shape and interaction patchiness for self-assembling nanoplates. *Nat. Chem.* **5**, 466–473 (2013).
 22. Lekkerkerker, H. N. W. & Vroege, G. J. Liquid crystal phase transitions in suspensions of mineral colloids: new life from old roots. *Philos. Trans. A. Math. Phys. Eng. Sci.* **371**, 20120263 (2013).
 23. Petukhov, A. V. *et al.* Observation of a hexatic columnar liquid crystal of polydisperse colloidal disks. *Phys. Rev. Lett.* **95**, 12–15 (2005).
 24. Vutukuri, H. R., Badaire, S., De Winter, D. A. M., Imhof, A. & van Blaaderen, A. Directed Self-Assembly of Micron-Sized Gold Nanoplatelets into Oriented Flexible Stacks with Tunable Interplate Distance. *Nano Lett.* **15**, 5617–5623 (2015).
 25. Davidson, P. “*Mineral Liquid Crystals: Liquid-Crystalline Suspensions of Mineral Nanoparticles*” in *Handbook of Liquid Crystals* 1–22 (American Cancer Society, 2014).
 26. Sonin, A. S., Churochkina, N. A., Kaznacheev, A. V & Golovanov, A. V. Mineral liquid crystals. *Colloid J.* **79**, 421–450 (2017).
 27. Riedinger, A. *et al.* An intrinsic growth instability in isotropic materials leads to quasi-two-dimensional nanoplatelets. *Nat. Mater.* **16**, 743–748 (2017).
 28. Ithurria, S., Bousquet, G. & Dubertret, B. Continuous transition from 3D to 1D confinement observed during the formation of CdSe nanoplatelets. *J. Am. Chem. Soc.* **133**, 3070–3077 (2011).
 29. Jiang, Y. *et al.* Synthesis of CdSe Nanoplatelets without Short-Chain Ligands: Implication for Their Growth Mechanisms. *ACS Omega* **3**, 6199–6205 (2018).
 30. Bertrand, G. H. V, Polovitsyn, A., Christodoulou, S., Khan, A. H. & Moreels, I. Shape control of zincblende CdSe nanoplatelets. *Chem. Commun.* **52**, 11975–11978 (2016).
 31. Glotzer, S. C. Nanotechnology: Shape matters. *Nature* **481**, 450–452 (2012).
 32. Paik, T., Ko, D.-K., Gordon, T. R., Doan-Nguyen, V. & Murray, C. B. Studies of Liquid Crystalline Self-Assembly of GdF₃ Nanoplates by In-Plane, Out-of-Plane SAXS. *ACS Nano* **5**, 8322–8330 (2011).

33. Abécassis, B., Tessier, M. D., Davidson, P. & Dubertret, B. Self-assembly of CdSe nanoplatelets into giant micrometer-scale needles emitting polarized light. *Nano Lett.* **14**, 710–715 (2014).
34. Guzelturk, B., Erdem, O., Olutas, M., Kelestemur, Y. & Demir, H. V. Stacking in Colloidal Nanoplatelets: Tuning Excitonic Properties. *ACS Nano* **8**, 12524–12533 (2014).
35. Montanarella, F. *et al.* Composite Supraparticles with Tunable Light Emission. *ACS Nano* **11**, 9136–9142 (2017).
36. Montanarella, F. *et al.* Crystallization of nanocrystals in spherical confinement probed by in-situ X-ray scattering. *Nano Lett.* **18**, 3675–3681 (2018).
37. de Nijs, B. *et al.* Entropy-driven Formation of Large Icosahedral Colloidal Clusters by Spherical Confinement. *Nat. Mater.* **14**, 56–60 (2015).
38. Fox, M. *Optical Properties of Solids*. (Oxford University Press, 2010).
39. Antanovich, A., Prudnikau, A., Matsukovich, A., Achtstein, A. & Artemyev, M. Self-Assembly of CdSe Nanoplatelets into Stacks of Controlled Size Induced by Ligand Exchange. *J. Phys. Chem. C* **120**, 5764–5775 (2016).
40. Kagan, C., Murray, C., Nirmal, M. & Bawendi, M. G. Electronic energy transfer in CdSe quantum dot solids. *Phys. Rev. Lett.* **76**, 1517–1520 (1996).
41. Rabouw, F. *et al.* Delayed Exciton Emission and Its Relation to Blinking in CdSe Quantum Dots. *Nano Lett.* **15**, 7718–7725 (2015).
42. Montanarella, F., Biondi, M., Hinterding, S. O. M., Vanmaekelbergh, D. & Rabouw, F. T. Reversible Charge-Carrier Trapping Slows Förster Energy Transfer in CdSe/CdS Quantum-Dot Solids. *Nano Lett.* **18**, 5867–5874 (2018).
43. Mason, T. G. & Bibette, J. Shear Rupturing of Droplets in Complex Fluids. *Langmuir* **13**, 4600–4613 (1997).
44. Mabilie, C. *et al.* Rheological and shearing conditions for the preparation of monodisperse emulsions. *Langmuir* **16**, 422–429 (2000).

Appendix

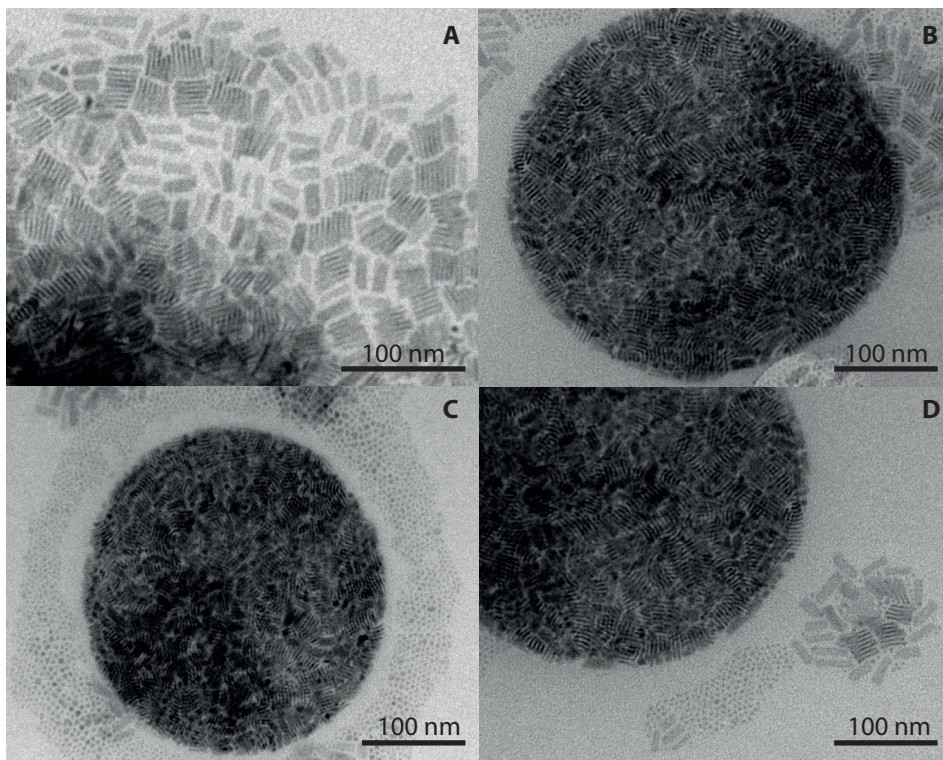


Figure 3.5 • Stacking of NPLs. (a) CdSe NPLs on a TEM grid. NPLs can be found both isolated, laying flat on the grid, or assembled in little stacks. (b-d) During the drying of the CdSe NPL dispersion on TEM grids, NPLs may accidentally deposit in spherical imperfections of the TEM grid, giving origin to what looks like a cut-through of a SP. These figures can give an impression of the random orientation of the stacks inside of a three-dimensional SP. Panel d has been renamed “*Starry Night*”, due to its resemblance to a star with a close comet which reminded us of the famous painting from van Gogh.

Chapter 4

Crystallization of nanocrystals in spherical confinement probed by *in-situ* X-ray scattering

Abstract

We studied the formation of supraparticles from nanocrystals confined in slowly evaporating oil droplets in an oil-in-water emulsion. The nanocrystals consist of an FeO core, a CoFe₂O₄ shell, and oleate capping ligands, with an overall diameter of 12.5 nm. We performed *in situ* small- and wide-angle X-ray scattering experiments during the entire period of solvent evaporation and colloidal crystallization. We observed a slow increase in the volume fraction of nanocrystals inside the oil droplets up to 20%, at which a sudden crystallization occurs. Our computer simulations show that crystallization at such a low volume fraction is only possible if attractive interactions between colloidal nanocrystals are taken into account in the model as well. The spherical supraparticles have a diameter of about 700 nm and consist of a few crystalline face-centered cubic domains. Nanocrystal supraparticles bear importance for magnetic and optoelectronic applications, such as color tunable biolabels, color tunable phosphors in LEDs, and miniaturized lasers.

Based on: Crystallization of nanocrystals in spherical confinement probed by *in-situ* X-ray scattering. Federico Montanarella, Jaco J. Geuchies, Tonnishtha Dasgupta, P. Tim Prins, Carlo van Overbeek, Rajeev Dattani, Patrick Baesjou, Marjolein Dijkstra, Andrei V. Petukhov, Alfons van Blaaderen and Daniel Vanmaekelbergh *Nano Lett.* **18** (6), 3675–3681, (2018)

«Equipped with his five senses, man explores the universe around him and calls the adventure Science»
(Edwin Hubble)

4.1 Introduction

The self-assembly of colloids into larger periodic structures is a phenomenon commonly observed in nature. For example, opals form by colloidal crystallization of highly monodisperse spherical particles with diameters in the 100–1000 nm range.^{1–3} In the last two decades, there has been more and more focus on colloids with sizes in the nanometer range.⁴ Assembly of colloidal nanocrystals (NCs) dispersed in nonpolar solutions has been studied extensively.^{5–9} Single and binary-component NC superlattices have been realized as three-dimensional crystals,^{6,10} thin films,⁹ and in some cases even as two-dimensional sheets with a large variety of NCs.^{8,9,11–15} In this field of nanoscience, there is a quest to design superstructures with tunable optical, magnetic, and electric properties that emerge from the properties of the building blocks, and the quantum mechanical and dipolar interactions between them.^{6,7}

Recently, several groups realized that a versatile route to obtain hierarchical nanocrystal superstructures is through the self-assembly of so-called supraparticles (SPs):¹⁶ particles built up from nanoparticles. Several of us used the slow drying of emulsion droplets as the way to arrive at SPs that are thus self-assembled in a spherical confinement.^{17–19} These supraparticles are nearly spherical with diameters in the 100 to 10000 nm range; they may show a periodic ordering of the NC building blocks and crystalline facets, if the constituent NC building blocks have a sufficiently low polydispersity (<10%). Designer SPs based on CdSe/(Cd,Zn)S core-shell building blocks have attracted interest for their tunable emission, from pure colors to white light,¹⁸ and for the appearance of whispering gallery modes.¹⁹ Despite the broad applicability of NC assembly in spherical confinement and the obvious scientific and technologic interest, the study of the kinetic and mechanistic aspects has been addressed in only a few reports so far.^{17,20–24} However, the growth of nanocrystal superstructures as thin films or even two-dimensional sheets got much more attention with time-resolved, *in situ* synchrotron X-ray scattering methods.^{25–27}

Here, we report a thorough real-time, *in situ* study of the colloidal crystallization of nanocrystals in spherical confinement. Using time-resolved wide-angle and small-angle X-ray scattering data (WAXS and SAXS), we followed the crystallization process over a wave vector (\mathbf{q}) range of 5×10^{-3} to 34 nm^{-1} and thus, in a large spatial domain, obtaining information ranging from the shrinking oil droplets to the position of the NCs inside the droplets. This study allowed us to propose a mechanism for the colloidal crystallization of our NCs in the spherical confinement of an oil droplet. The model system chosen for this study is FeO/CoFe₂O₄ core/shell NCs, as they have been shown to easily form crystalline SPs¹⁷ and because the shape of these NCs can be tuned from spherical to cubic.²⁸ By comparison of our data with simulations on the crystallization mechanism of hard spheres,¹⁷ it is clear that in the confined assembly of FeO/CoFe₂O₄ core/shell NCs of more than 10 nm in diameter, attractions between the NCs must be taken into account.

4.2 Results and Discussion

4.2.1 *In situ* X-ray scattering

We performed *in situ* WAXS and SAXS measurements at the ID02 beamline of ESRF in Grenoble. A scheme of the experimental setup is shown in Figure 4.1. The “oil droplets”

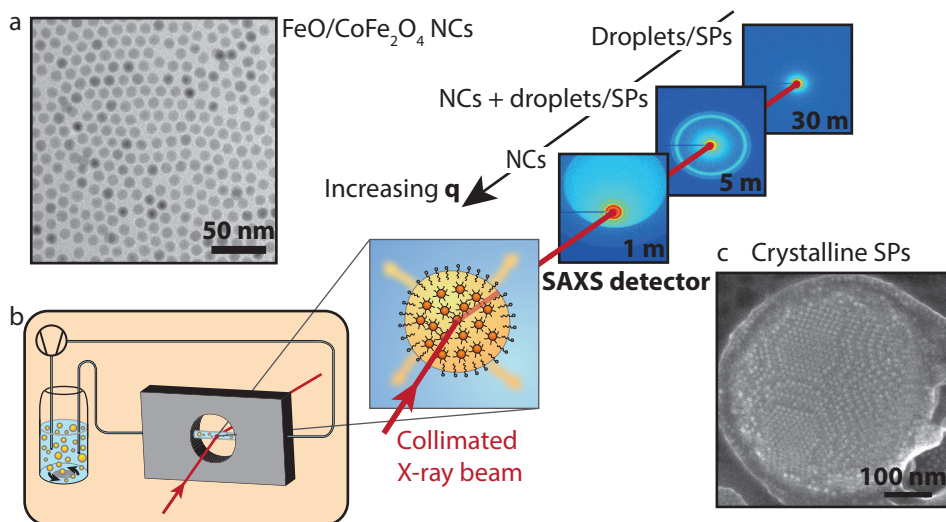


Figure 4.1 • Scheme of the experimental setup and of the experimental conditions in which the self-assembly was investigated. (a) Representative TEM image of FeO/CoFe₂O₄ NCs used in these measurements. (b) Emulsion, while heated and stirred in a vial in order to evaporate the non-polar phase, is pumped through a capillary using a peristaltic pump. The emulsion is then probed, while in the capillary, by X-rays. The experiment has been performed three times with the SAXS detector at three different distances, 1, 5, and 30 m, in order to probe the full q range: from the region where the NCs scatter up to the region where the droplets and, later, the SPs scatter. (c) Representative SE-STEM image of a SP made of FeO/CoFe₂O₄ NCs as obtained from this experiment.

of the oil-in-water emulsion form, in fact, a suspension themselves: they consist of FeO/CoFe₂O₄ core/shell NCs of 10.5 ± 1.2 nm overall diameter (Figures 4.1a, 4.25 and 4.26) dispersed in cyclohexane, the initial NC volume fraction being 0.0077 ± 0.0012 (see Appendix for details about droplets formation). The CoFe₂O₄ shell around the core has a thickness of approximately 1.5 nm.²⁹ Colloidal crystallization and the formation of SPs in the confined volume of the oil droplets were initiated by increasing the NC concentration upon evaporation of the cyclohexane. The emulsion was, therefore, heated to 68 °C in a reaction vessel (left part of Figure 4.1b). During this process, the oil-in-water suspension was pumped through a capillary through which the collimated X-ray beam passed. The scattered beam was detected by a WAXS detector that collected the atomic diffraction from the system. Detection at small angles (SAXS) occurred using three different sample-to-detector distances: 1, 5, and 30 m (see Figure 4.1). In such a way, the scattered signal could be detected over a broad wave vector region (5×10^{-3} to 34 nm^{-1}), and structural information on the nanocrystal organization in the oil droplet was obtained on length scales spanning from $\sim 2.5 \mu\text{m}$ to 0.1 nm. Hence, we were able to follow the fate of the oil droplets and that of the nanocrystals inside each droplet, *in situ*, and in real time (Figure 4.24).

4.2.2 Evolution of the X-ray scattering patterns over a broad wave vector range

The time-resolved X-ray scattering signal during solvent evaporation and NC colloidal

crystallization is presented in Figure 4.2. Panel (a) displays the time-resolved scattering patterns over the entire q range. In the high q range, the signal is modulated by the form factor of the spherical NCs. From the position and the depth of the minima, we can quantify the size of the NCs and their polydispersity: the NCs are 10.7 nm in diameter with a polydispersity of $\sim 9\%$ (Figure 4.2.6). This is in good agreement with the values of 10.5 ± 1.2 nm obtained from transmission electron microscopy (TEM) images (Figures 1a and 4.2.5). In the small q region, the scattering pattern is modulated by the form factor of the cyclohexane/NCs droplets in the water medium (see arrows in Figure 4.2a). We can extract the initial size of the droplets being ~ 3.2 μm , with a polydispersity of $\sim 21\%$, in good agreement with *ex situ* optical microscopy measurements of the oil droplets (Figure 4.2.8).

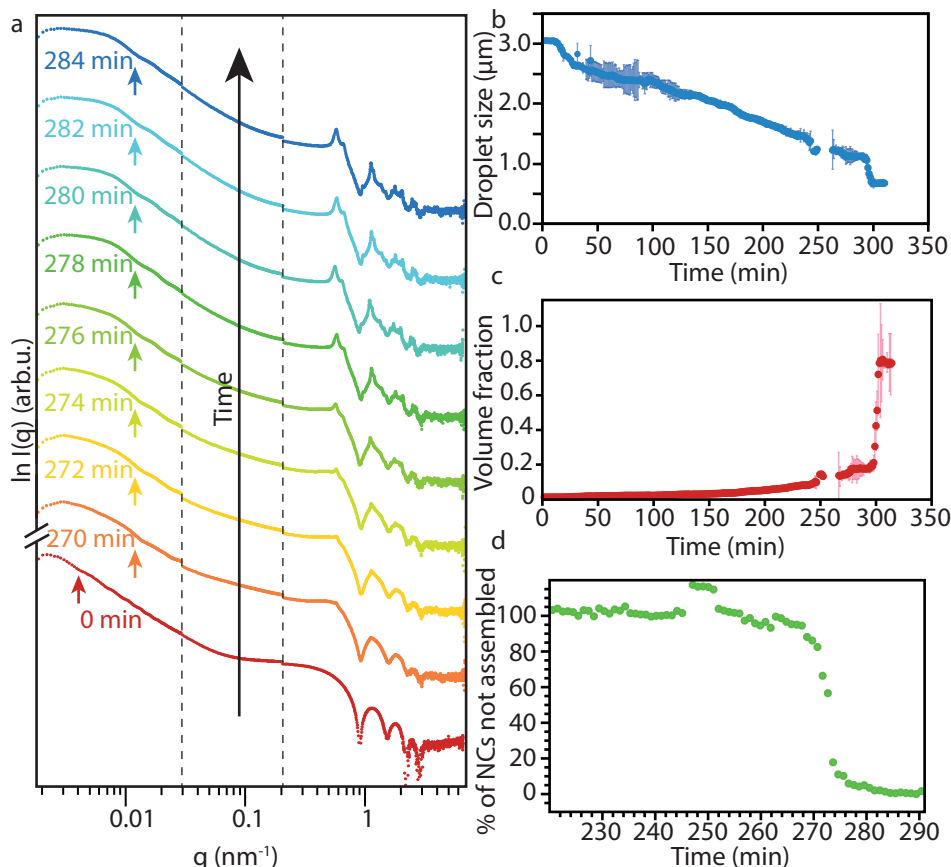


Figure 4.2 • Time-resolved X-ray scattering patterns of the self-assembly. (a) Scattering patterns of the emulsion over time; the crystallization in ordered SPs is confirmed by the appearance of structure factor peaks in the region associated with NC scattering. The arrows indicate the first minima of the form factor relative to the scattering from the droplets/SPs. (b) Droplet size as a function of the reaction time. The error bars in dark blue show the error in the determination of the size relative to each point. (c) Volume fraction of NCs in the droplet as a function of time. The error bars in light red show the error in the determination of the volume fraction relative to each point. (d) Percentage of NCs not assembled in an SP over time; the crystallization is highlighted by the sharp change in the slope of the curve.

During cyclohexane evaporation, taking ~ 4.5 – 5 h, the droplets shrink, increasing the NC concentration. This shrinkage can be followed over time by the change in the position of the form factor minima (see arrows in Figure 4.2a). The diameter of the droplets decreases linearly with time (Figure 4.2b), with an average value of 6.5 nm/min, indicating that the rate of solvent evaporation is determined by the droplet surface area, and that the intrinsic evaporation rate per unit of area is constant, independent of the droplet size (see Appendix for details). After ~ 270 – 290 min, we observe a sudden “apparent” decrease in the droplet size from ~ 1040 to ~ 690 nm, which would correspond to a 70% decrease in the droplet volume. We remark that such a sudden and strong shrinkage of the suspension droplets is unlikely, and therefore, we name this an “apparent” decrease and not a true decrease in droplet size. We believe that the sudden shrinkage is due to X-ray scattering on an object with high electron density, which suddenly emerges from the NC dispersion. The simplest interpretation is that this object is a NC SP with a considerably larger NC density formed by colloidal crystallization (Figures 4.14–4.19). In the Appendix, we show that alternative explanations based on simulated scattering patterns cannot explain the results. In particular, while we cannot fully exclude that a particle monolayer is adsorbed at the interface (as considerable adsorption energies have been predicted) from the scattering pattern (see Figure 4.20), this is clearly not related to the nucleation of the SPs that are observed in our results. Our interpretation that colloidal crystallization has started in the bulk of the droplet is corroborated by the concomitant appearance of structure factor peaks in the high q region of the scattering pattern (Figure 4.2a).

Knowing the size of the droplets and the initial NC volume fraction in the dispersion, we quantified the NC volume fraction in the dispersion in the droplets during solvent evaporation (Figure 4.2c). The NC volume fraction steadily increases over time from the initial value of 0.0077 ± 0.0012 . At the moment of the crystallization, the volume fraction has a value of 0.20 , and we observe an apparent increase in the volume fraction up to the value of 0.74 , typical for a colloidal crystal with a face-centered-cubic (FCC) packing. According to the crystallization model for hard spheres, crystallization should occur at ~ 0.5 NC volume fraction.³⁰ In our case, crystallization occurs at a much lower volume fraction, indicating the existence of attractive forces between the NCs (further discussion follows below).

The WAXS signal shows reflections of the atomic planes of the FeO and CoFe_2O_4 crystals (Figure 4.21), in agreement with the TEM data (Figure 4.25). Since we are sampling over many SPs we have no information on possible alignment of the NCs in one SP (see Appendix for details).

4.2.3 Analysis of the structure factor peaks

By integration of the scattering intensity of the structure factor peaks (see Appendix for details) in the high q range (5×10^{-1} to 6 nm $^{-1}$), we are able to estimate the percentage of NCs dispersed, compared to those present in the SPs, over time during oil evaporation (Figure 4.2d). We assume that at time zero all the NCs were dispersed, and that, upon the shrinkage of the droplets indicating the crystallization, all the NCs are present in the SPs. We can then fit the data in Figure 4.2d (for $t > 270$ min) with a single exponential (see Figure 4.10), yielding an average time constant for the NC crystallization process in

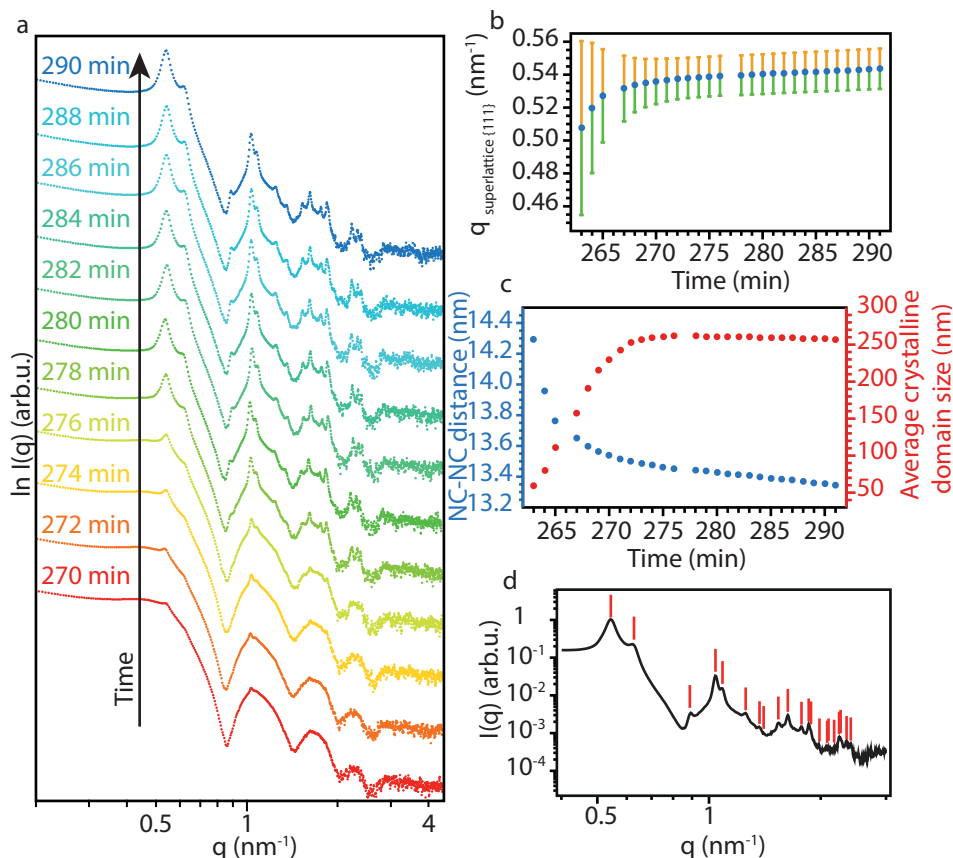


Figure 4.3 • Crystallization of the NCs in FCC SPs. (a) SAXS patterns at high q at different times during the crystallization. (b) Variation of the peak position (dots) and relative peak width (lines) of the first structure factor peak (0.5 nm^{-1}) over time. (c) Variation of the NC-NC distance (blue) and average crystalline domain size (red) over time. (d) Indexing of the first 21 reflections of an FCC lattice in the scattering pattern of the SPs.

a droplet of 7.5 min (see Appendix for details). Now, we focus on the mechanism of NC crystallization into SPs by the analysis of the evolution of the structure factor peaks over time (Figure 4.3a). The first peak arises at 0.51 nm^{-1} , corresponding to the reflection of the $\{111\}$ planes in an FCC NC lattice. The peak can be fitted with a Lorentzian (Figure 4.7). The distance between adjacent NCs in the SP can be obtained from the position of the peak (Figure 4.3b,c), and the spatial extent of the periodic order from the full-width at half maximum (fwhm) (Figure 4.3b,c and see Appendix for details on the methods). After a sharp change in the initial stage of the crystallization, the fwhm stabilizes to a constant value. We derive that the average crystalline domain size increases to a value of 260 nm, *i.e.*, roughly 2.5 times smaller than the average SP size observed from the form factor scattering of the SP. Hence, each SP consists of 10–15 crystalline domains on average. The peak position shifts steadily toward higher q values (Figure 4.3b). The derived average distance between adjacent NCs in the SP is initially 14.3 nm, roughly corresponding to

the size of two NCs with extended ligands (oleate) around them. This distance steadily decreases to 13.6 nm and then slowly to 13.3 nm. This decrease in the NC–NC distance must reflect interpenetration of the oleate ligands of the two adjacent ligand shells.

All structure factor peaks originate from reflections from different crystal planes in the NC superlattice, which allowed us to identify the crystal structure of the SP as FCC (Figure 4.3d). We were able to index as many as 21 reflections, which landmarks the excellent crystallinity of our SPs. The position of the structure factor peaks was also compared to those of the random hexagonal-close-packed (RHCP) and hexagonal-close-packed (HCP) structures (Figure 4.27). Our analysis, however, unambiguously showed that the structure factor peaks can only be indexed as originating from an FCC colloidal crystal.

4.2.4 Mechanism of colloidal crystallization in spherical confinement

Recently, the colloidal crystallization of nanocrystals in spherical confinement has been simulated by assuming that the nanocolloids act as hard spheres.¹⁷ It was found that crystallization sets in at a NC volume fraction of ~ 0.5 ; crystal nuclei that have a NC volume fraction of 0.55 are formed by heterogeneous nucleation at the surface of the oil droplets. In our case, crystallization starts at a much lower volume fraction of ~ 0.20 . This suggests that NC–NC attractions should be incorporated in the model, as also supported by computer simulations presented below. It has been previously shown that in nearly ideal dispersions, the crystallization of small (< 8 nm in diameter) semiconductor NCs can be seen as hard-sphere crystallization.^{14,31} However, in many other cases the formation of NC superlattices by self-assembly was understood on the basis of a subtle balance of entropy arguments and NC–NC attractions.^{7,9} Analysis of the state of a dispersion of nanocrystals in organic solvents indicated that the NC–NC attraction corresponds to a pair potential of a few times the thermal energy at room temperature, increasing with the size of the nanocrystals.^{32,33} This was also corroborated by calculations of the effective NC interactions (see Appendix).¹⁴

We propose a mechanism of crystallization that is schematically shown in Figure 4.4. In

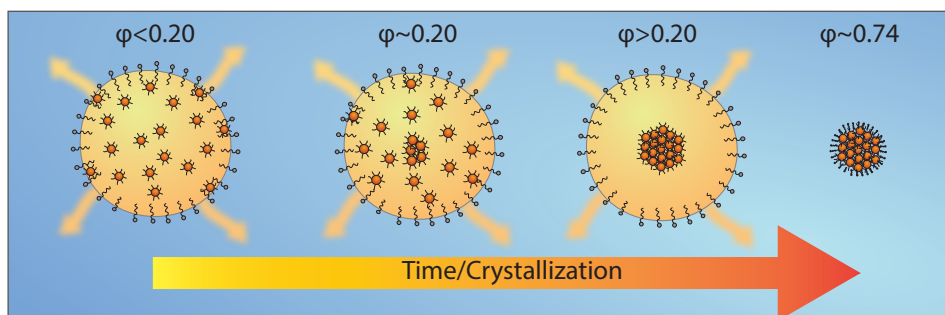


Figure 4.4 • Crystallization mechanism. In the initial state (volume fraction, $\phi < 0.20$), the NCs are homogeneously distributed in the droplet; when the volume fraction of NCs becomes critical ($\phi \approx 0.20$), a nucleation event starts inside the droplet. After a certain time, the NCs are nearly all assembled in the SP, which is still inside the droplet. Upon complete evaporation of the cyclohexane, the SP is covered by a layer of surfactants and suspended in water.

the initial stage, the NCs are homogeneously distributed in the oil droplets. Regarding the X-ray scattering, such NC/oil droplets can be assumed as having a homogeneous electron density, with a scattering length density somewhere between that of the cyclohexane and the NC solid. Over time the scattering contrast increases due to the densification of the NCs in the oil droplets. This temporal regime shows a gradual and constant decrease in the droplet size with time. We then observe a critical time regime of a few minutes in which the scattering pattern changes dramatically. This is attributed to the NC crystallization in the oil droplets occurring at a volume fraction of ~ 0.20 , which is corroborated by the sudden appearance of FCC structure factor peaks. One or more crystalline SP(s) start(s) to form via homogeneous nucleation inside each oil droplet, growing by NC addition and, possibly, aggregation of smaller SPs into a larger one. The scattered X-ray photons in the low- q region are now mainly due to the growing SP, the SP being considerably smaller than the oil droplet itself. In fact, the droplets can be seen as consisting of a strongly scattering core (the NC SP) and a weakly scattering shell of the remaining cyclohexane. The scattering length density difference, *i.e.*, the contrast, of the SP compared to the cyclohexane is ~ 350 times stronger. This explains the sudden “apparent” decrease of the size of the oil droplet. In the final stage, the remaining cyclohexane evaporates, leaving the SP covered by a layer of surfactants, which will enable its dispersion in water.

4.2.5 Computer simulations

In order to support our hypothesis on the crystallization mechanism, we perform event-driven Brownian dynamics (EDBD) simulations of 100 000 NCs interacting with an attractive square-well potential in a slowly shrinking droplet as modeled by a spherical hard wall (see Appendix for details). As the confinement shrinks, the volume fraction of the nanoparticles in the droplet increases. At volume fraction (η) ≈ 0.11 , we observe the formation of multiple crystalline nuclei (Figure 4.5a), which are identified using a bond-orientational order parameter and a cluster criterion (see Appendix for further details). We clearly observe from Figure 4.5a that the crystallization proceeds via homogeneous nucleation of multiple crystallites in the bulk and is not induced by crystallization at the wall as in the case of pure hard spheres.¹⁷ With further increase in volume fraction, we observe that the nuclei merge and form a single crystalline domain that becomes eventually spherical due to the shrinking confinement. Remarkably, we observe that the surface of our SP assembled from attractive NCs shows ledges and facets indicating that the crystallization is not surface-induced. This should be contrasted to the case of SPs formed from hard spheres, which show a much smoother surface (Figure 4.29). In order to investigate the evolution of the crystallization mechanism, we plot in Figure 4.5b the fraction of the crystalline particles as a function of the volume fraction (time) for attractive NCs and for pure hard spheres. Figure 4.5b shows that (i) the onset of the crystallization for attractive NCs is at a much lower volume fraction ($\eta \approx 0.11$) than for hard-sphere NCs ($\eta \approx 0.5$) and that (ii) the crystallization of attractive NCs occurs via homogeneous nucleation, while it proceeds through heterogeneous nucleation for hard-sphere NCs, which can also be appreciated from the corresponding thumbnails of Figure 4.5b, showing a cross-section of the attractive and hard-sphere NC SPs after crystallization has set in. We remark that a more quantitative agreement, between simulations and experiments, in the estimated volume fraction at which there is an onset of crystallization, could be obtained by tuning the strength of the attraction between the NCs. Furthermore, the increase in the fraction

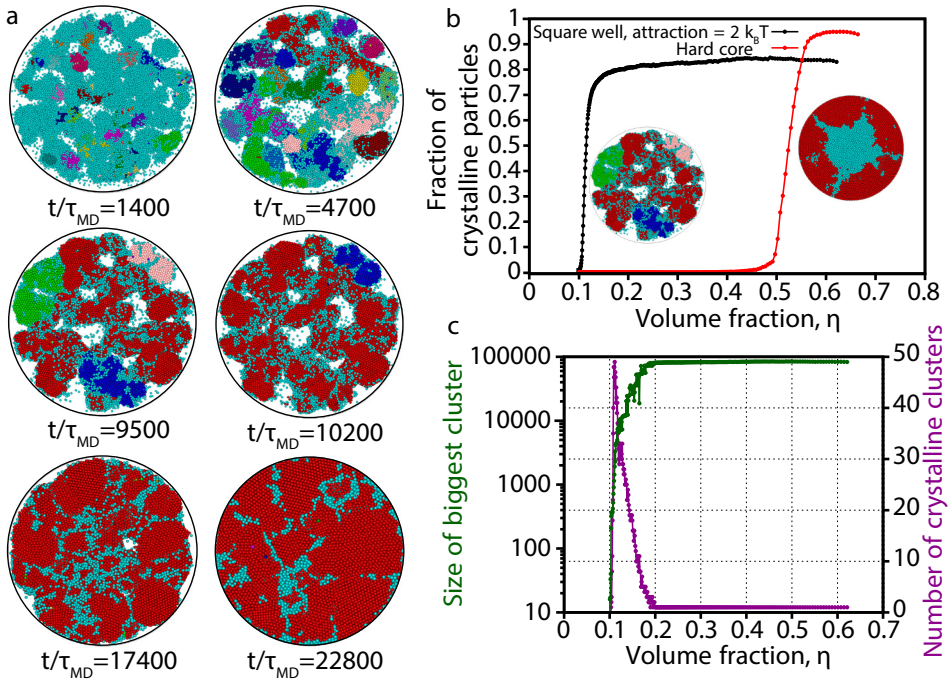


Figure 4.5 • Computer simulations. (a) Cross-section (through the center) of the SP at different times (t/τ_{MD}) in a slowly shrinking spherical confinement. The crystallization proceeds through homogeneous nucleation of multiple crystal nuclei, which merge together at long simulation times to form a single crystalline domain. Colors are assigned randomly to distinct different nuclei in every time snapshot (cyan always denotes disordered particles). (b) Number of crystalline particles as a function of volume fraction for attractive NCs and hard-sphere NCs in a shrinking spherical confinement. The onset of the crystallization for attractive NCs is at a much lower volume fraction ($\eta \approx 0.11$) than for hard-sphere NCs ($\eta \approx 0.5$). The thumbnails show a cross-section of the attractive and hard-sphere NC SPs after crystallization has set in, thereby demonstrating that the crystallization of attractive NCs occurs via homogeneous nucleation, while it proceeds through heterogeneous nucleation for hard-sphere NCs. (c) Size of the largest cluster and the number of differently oriented clusters as a function of volume fraction (time). Eventually there is only one main crystalline domain.

of crystalline particles with volume fraction is very steep, indicating a very rapid crystallization process, which is in qualitative agreement with the experimental observations.

Finally, we show in Figure 4.5c (i) the number of crystalline particles in the largest crystal domain as a function of volume fraction (time) (in green), which increases in time until $\sim 83\%$ of the NCs constitute the main crystal, and (ii) the number of crystal nuclei (in purple), which shows a peak during the shrinking process and finally decays to one corresponding to the formation of a single cluster. Both trends support our proposed crystallization mechanism.

4.3 Conclusions

We studied the mechanism of the self-assembly of colloidal NCs into NC SPs in a NC

dispersion being confined to an oil droplet dispersed in water. We performed *in situ* small- and wide-angle X-ray scattering experiments at the ID02 beamline at ESRF, Grenoble. Our results showed that colloidal crystallization sets in at a NC volume fraction of ~ 0.20 ; this indicates that attractive interactions between the NCs are important as a driving force for the self-assembly. The completion of the crystallization of the SPs takes on average about 7.5 min to incorporate all NCs. The SPs themselves consist of a few FCC crystalline domains. SPs bear importance for optoelectronic applications, as color tunable biolabels, phosphors in LEDs, and possibly also miniaturized lasers.

4.4 Methods

Chemicals

Sodium dodecyl sulfate (SDS, $\geq 98.5\%$), Dextran from *Leuconostoc mesenteroides* (M_w 670000 g/mol), Iron (II) chloride tetrahydrate ($\text{FeCl}_3 \cdot 4\text{H}_2\text{O}$, 99.99%), Cobalt (II) chloride (CoCl_2 , 99.9%), Sodium hydroxide (NaOH, $\geq 97\%$), Hexane (anhydrous, 95%), Cyclohexane (anhydrous, 99.5%), Oleic acid (OA, 90%), Ethanol (EtOH, 99.8%), 1-Butanol anhydrous (BuOH, 99.8%), Methanol (MeOH, anhydrous, 99.8%) and Toluene (anhydrous, 99.8%) were all purchased by Sigma Aldrich and used as received. 1-Hexadecene (92%) was purchased from Antonides CV.

Synthesis of FeO/CoFe₂O₄ NCs

The synthesis of the FeO/CoFe₂O₄ NCs was performed according to the literature.²⁹ For this synthesis we first prepared the iron-cobalt oleate precursor; for this 8.66 g (32 mmol) of $\text{FeCl}_3 \cdot 4\text{H}_2\text{O}$ were dissolved in 80 mL of MeOH, and 2.08 g (16 mmol) of CoCl_2 in 40 mL of MeOH. The two solutions were mixed together and with 40.2 g of OA in a three neck flask. A solution of 5.12 g of NaOH dissolved in 320 mL of MeOH was added to the previous mixture over 30 min, resulting in a quite viscous dark-brown solution. The viscous liquid was separated by decanting and the precipitate was washed multiple times (>3) with MeOH. The final precipitate was dissolved in 80 mL of hexane. The hexane phase was washed twice with warm (50 °C) deionized water and separated using a separatory funnel. The hexane was finally removed by putting the solution under vacuum overnight. A precursor solution with a concentration of 0.50 mol/kg was prepared by adding 1.48 g 1-hexadecene per each gram of mixed oleate precursor. The precursor solution was stored under nitrogen in a glovebox.

For the synthesis of the NCs we mixed 9.60 g of iron-cobalt oleate solution, 0.76 g of OA and 13.72 g of 1-hexadecene in a three-neck flask. The mixture was stirred for 1 hour at 110 °C under vacuum. The mixture was then put under nitrogen and the temperature was raised to 290 °C at a speed of 2-3 °C/min. The mixture was then left refluxing at 290 °C for 35 min, then it was cooled to room temperature. The particles were diluted with 1 volume equivalent of hexane and washed through precipitation upon addition of 1 volume equivalent of EtOH, the non-solvent. This washing procedure was repeated twice and in the end the particles were redispersed in cyclohexane in a concentration of ~ 10 mg/mL.

Synthesis of SPs

The synthesis was performed in open air following a procedure from literature.¹⁷ First of all, the FeO/CoFe₂O₄ solution of the NCs in cyclohexane was emulsified with a water solution made of 10.0 mL of milli-Q water containing 60 mg of sodiumdodecylsulfate (SDS), the surfactant, and 0.40 g of dextran. Dextran acts as steric stabilizer, but is also added as well to bring the solution in a visco-elastic regime necessary for creating relatively monodisperse droplets under high shear rates.³⁴ The emulsification, together with the initial volume fraction of particles, is important, since it will determine the size of the droplets and consequently, after the evaporation of the oil phase, the mean size and size distribution of the resulting SPs. The emulsification was performed following a methodology developed by the Bibette group that uses high shear rates generated in a home-built Couette shear cell.³⁵ In particular, the two phase system, composed of the water phase and the oil phase (with particles dispersed inside), was pushed through the 0.1 mm gap between the stator and the rotor (rotational speed of 7500 rpm) of the shear cell. The high shear rates produced by the shear cell induce a rupture of the two phase system into small and relatively monodisperse (10-15%) droplets.¹⁷ After the emulsification, the emulsion was then collected and stirred for 6 hours at 68 °C, in order to evaporate the oil phase (=cyclohexane). The resulting dispersion was centrifuged at 3000 rpm for 10 min, and the precipitated SPs were finally redispersed in distilled water.

Experimental setup

The emulsion was put in an open vial (57.5 mm of height x 27.3 mm of radius) placed over a heating/stirring

plate set at 68 °C and stirred at ~300 rpm. The vial was enveloped by two thermoelectric heating foils (Peltier elements), also set at 68 °C, in order to obtain a better thermal homogeneity. The vial and the foils were also enveloped in aluminum foil, in order to guarantee a better thermal contact. The temperature of the emulsion was probed by a thermocouple and constantly monitored to remain at 68 ± 2 °C. Part of the emulsion was also pumped, via tubing (containing ~4 mL of liquid), through a quartz capillary, where the emulsion was probed by the X-rays, and then back inside the vial. The pumping was performed with the aid of a peristaltic pump. The SAXS/WAXS experiments were performed on the ID02 beamline of the ESRF (European Synchrotron Radiation Facility) at an energy of 12.4 keV. The experiment was performed three times, each with a different detector distance, 1 m, 5 m and 30 m, in order to probe the full q range, from the NCs to the droplets/SPs. For each data point, the acquisition time was 30 ms, the acquisition was repeated 10 times and the resulting data points were obtained from an average of the acquisitions. We acquired one of these averaged SAXS patterns every minute. In principle the time resolution could be easily increased, but the kinetics during our experiments allowed for this lower time resolution.

Acknowledgements

The author thanks Freddy Rabouw and Ward van der Stam for very fruitful discussion, Jan Ilavsky for support in the use of IRENA, Jacques Gorini for assistance during the scattering measurements and Giulia Fiorucci, Massimiliano Chiappini and Gabriele Coli for support in calculating crystal reflections.

References

1. Sanders, J. V. Colour of Precious Opal. *Nature* **204**, 1151–1153 (1964).
2. Iler, R. K. Formation of Precious Opal. *Nature* **207**, 472–473 (1965).
3. Darragh, P. J., Gaskin, A. J., Terell, B. C. & Sanders, J. V. Origin of precious opal. *Nature* **209**, 13–16 (1966).
4. Cheng, Z. *Colloidal crystallization. Fluids, Colloids Soft Mater. An Introd. to Soft Matter Phys.* **203–248** (2016).
5. Murray, C. B., Kagan, C. R. & Bawendi, M. G. Self-Organization of CdSe Nanocrystallites into Three-Dimensional Quantum Dot Superlattices. *Science* **270**, 1335–1338 (1995).
6. Vanmaekelbergh, D. Self-assembly of colloidal nanocrystals as route to novel classes of nanostructured materials. *Nano Today* **6**, 419–437 (2011).
7. Talapin, D. V., Lee, J. S., Kovalenko, M. V. & Shevchenko, E. V. Prospects of colloidal nanocrystals for electronic and optoelectronic applications. *Chem. Rev.* **110**, 389–458 (2010).
8. Redl, F. X., Cho, K.-S., Murray, C. B. & O'Brien, S. Three-dimensional binary superlattices of magnetic nanocrystals and semiconductor quantum dots. *Nature* **423**, 968–971 (2003).
9. Dong, A., Chen, J., Vora, P. M., Kikkawa, J. M. & Murray, C. B. Binary nanocrystal superlattice membranes self-assembled at the liquid-air interface. *Nature* **466**, 474–7 (2010).
10. Yang, Z. *et al.* Supracrystalline Colloidal Eggs: Epitaxial Growth and Freestanding Three-Dimensional Supracrystals in Nanoscaled Colloidosomes. *J. Am. Chem. Soc.* **138**, 3493–3500 (2016).
11. Ye, X. *et al.* Competition of shape and interaction patchiness for self-assembling nanoplates. *Nat. Chem.* **5**, 466–473 (2013).
12. Bodnarchuk, M. I. *et al.* Three-dimensional nanocrystal superlattices grown in

- nanoliter microfluidic plugs. *J. Am. Chem. Soc.* **133**, 8956–8960 (2011).
13. Cargnello, M. *et al.* Substitutional doping in nanocrystal superlattices. *Nature* **524**, 450–3 (2015).
 14. Evers, W. H. *et al.* Entropy-driven formation of binary semiconductor-nanocrystal superlattices. *Nano Lett.* **10**, 4235–4241 (2010).
 15. Boneschanscher, M. P. *et al.* Long-range orientation and atomic attachment of nanocrystals in 2D honeycomb superlattices. *Science* **344**, 1377–1380 (2014).
 16. Wang, T., LaMontagne, D., Lynch, J., Zhuang, J. & Cao, Y. C. Colloidal superparticles from nanoparticle assembly. *Chem. Soc. Rev.* **42**, 2804–2823 (2013).
 17. de Nijs, B. *et al.* Entropy-driven Formation of Large Icosahedral Colloidal Clusters by Spherical Confinement. *Nat. Mater.* **14**, 56–60 (2015).
 18. Montanarella, F. *et al.* Composite Supraparticles with Tunable Light Emission. *ACS Nano* **11**, 9136–9142 (2017).
 19. Vanmaekelbergh, D. *et al.* Shape-Dependent Multiexciton Emission and Whispering Gallery Modes in Supraparticles of CdSe / Multishell Quantum Dots. *ACS Nano* **9**, 3942–3950 (2015).
 20. Lacava, J., Ouali, A.A., Raillard, B. & Kraus, T. On the behaviour of nanoparticles in oil-in-water emulsions with different surfactants. *Soft Matter* **10**, 1696 (2014).
 21. Lacava, J., Born, P. & Kraus, T. Nanoparticle clusters with Lennard-Jones geometries. *Nano Lett.* **12**, 3279–3282 (2012).
 22. Schmitt, J. *et al.* Formation of Superlattices of Gold Nanoparticles Using Ostwald Ripening in Emulsions: Transition from fcc to bcc Structure. *J. Phys. Chem. B* **120**, 5759–5766 (2016).
 23. Kister, T., Mravlak, M., Schilling, T. & Kraus, T. Pressure-controlled formation of crystalline, Janus, and core-shell supraparticles. *Nanoscale* **8**, 13377–13384 (2016).
 24. Yang, P. W. *et al.* Tracing the Surfactant-Mediated Nucleation, Growth, and Superpacking of Gold Supercrystals Using Time and Spatially Resolved X-ray Scattering. *Langmuir* **33**, 3253–3261 (2017).
 25. Weidman, M. C., Smilgies, D.-M. & Tisdale, W. A. Kinetics of the self-assembly of nanocrystal superlattices measured by real-time *in situ* X-ray scattering. *Nat. Mater.* **15**, 775–781 (2016).
 26. Geuchies, J. J. *et al.* In situ study of the formation mechanism of two-dimensional superlattices from PbSe nanocrystals. *Nat. Mater.* **15**, 1248–1254 (2016).
 27. Wu, L. *et al.* High-temperature crystallization of nanocrystals into three-dimensional superlattices. *Nature* **548**, 197–201 (2017).
 28. Wang, D. *et al.* Interplay between spherical confinement and particle shape on the self-assembly of rounded cubes. *Nat. Commun.* **9**, (2018).
 29. Bodnarchuk, M. I. *et al.* Exchange-coupled bimagnetic wustite/metal ferrite core/shell nanocrystals: Size, shape, and compositional control. *Small* **5**, 2247–2252 (2009).
 30. Hoover, W. G. & Ree, F. H. Melting Transition and Communal Entropy for Hard Spheres. *J. Chem. Phys.* **49**, 3609–3617 (1968).
 31. Bodnarchuk, M. I., Kovalenko, M. V., Heiss, W. & Talapin, D. V. Energetic and entropic contributions to self-assembly of binary nanocrystal superlattices: Temperature as the structure-directing factor. *J. Am. Chem. Soc.* **132**, 11967–11977

- (2010).
32. Klokkenburg, M., Dullens, R. P. A., Kegel, W. K., Ern , B. H. & Philipse, A. P. Quantitative real-space analysis of self-assembled structures of magnetic dipolar colloids. *Phys. Rev. Lett.* **96**, 1–4 (2006).
 33. van Rijssel, J. *et al.* Enthalpy and entropy of nanoparticle association from temperature-dependent cryo-TEM. *Phys. Chem. Chem. Phys.* **13**, 12770–12774 (2011).
 34. Mason, T. G. & Bibette, J. Shear Rupturing of Droplets in Complex Fluids. *Langmuir* **13**, 4600–4613 (1997).
 35. Mabille, C. *et al.* Rheological and shearing conditions for the preparation of monodisperse emulsions. *Langmuir* **16**, 422–429 (2000).
 36. Ilavsky, J. & Jemian, P. R. Irena: Tool suite for modeling and analysis of small-angle scattering. *J. Appl. Crystallogr.* **42**, 347–353 (2009).
 37. Byelov, D. V. *et al.* Diffuse scattering in random-stacking hexagonal close-packed crystals of colloidal hard spheres. *Phase Transitions* **83**, 107–114 (2010).
 38. Dolbnya, I. P., Petukhov, A. V, Aarts, D. G. A. L., Vroege, G. J. & Lekkerkerker, H. N. W. Coexistence of rhcp and fcc phases in hard-sphere colloidal crystals. *EPL (Europhysics Lett.)* **72**, 962 (2005).
 39. Petukhov, A. V, Dolbnya, I. P., Aarts, D. G. A. L., Vroege, G. J. & Lekkerkerker, H. N. W. Bragg Rods and Multiple X-Ray Scattering in Random-Stacking Colloidal Crystals. *Phys. Rev. Lett.* **90**, 28304 (2003).
 40. Pusey, P. N. & van Megen, W. Observation of a glass transition in suspensions of spherical colloidal particles. *Phys. Rev. Lett.* **54**, 3–6 (1985).
 41. Poon, W. C. K., Weeks, E. R. & Royall, C. P. On measuring colloidal volume fractions. *Soft Matter* **8**, 21–30 (2012).
 42. Royall, C. P., Poon, W. C. K. & Weeks, E. R. In Search of Colloidal Hard Spheres. *Soft Matter* **9**, 17–27 (2013).
 43. Pusey, P. N. & van Megen, W. Phase behaviour of concentrated suspensions of nearly hard colloidal spheres. *Nature* **320**, 340–342 (1986).
 44. Shevchenko, E. V., Talapin, D. V., Murray, C. B. & O’Brien, S. Structural characterization of self-assembled multifunctional binary nanoparticle superlattices. *J. Am. Chem. Soc.* **128**, 3620–3637 (2006).
 45. Ohara, P. C., Leff, D. V, Heath, J. R. & Gelbart, W. M. Crystallization of Opals from Polydisperse Nanoparticles. *Phys. Rev. Lett.* **75**, 3466–3469 (1995).
 46. Israelachvili, J. N. *Intermolecular and Surface Forces* (Third Edition). Elsevier (Academic Press, 2011).
 47. Faure, B., Salazar-Alvarez, G. & Bergstr m, L. Hamaker Constants of Iron Oxide Nanoparticles. *Langmuir* **27**, 8659–8664 (2011).
 48. Marechal, M., Hermes, M. & Dijkstra, M. Stacking in sediments of colloidal hard spheres. *J. Chem. Phys.* **135**, 34510 (2011).
 49. Dasgupta, T., Edison, J. R. & Dijkstra, M. Growth of defect-free colloidal hard-sphere crystals using colloidal epitaxy. *J. Chem. Phys.* **146**, 74903 (2017).
 50. Scala, A., Voigtmann, T. & Michele, C. De. Event-driven Brownian dynamics for hard spheres. *J. Chem. Phys.* **126**, 134109 (2007).
 51. Steinhardt, P. J., Nelson, D. R. & Ronchetti, M. Bond-orientational order in liquids and glasses. *Phys. Rev. B* **28**, 784–805 (1983).

Appendix

Analysis of the SAXS data

The analysis of the SAXS data was performed using the Irena package v2.64 (available at <http://usaxs.xray.aps.anl.gov/staff/ilavsky/irena.html> from the APS).³⁶ The size and size distribution of disperse NCs and SPs were modeled using the Modelling II module of the IRENA package. We found that a spherical form factor and Gaussian size distributions were the best fit to our data; in addition, they were chosen because they corroborated the data extracted from transmission electron microscopy analysis.

In the case of the form factor fitting, the scattering intensity is expressed by the formula:

$$I(q) = |\Delta\rho|^2 \int_0^\infty |F(q, r)|^2 V(r)^2 NP(r) dr$$

where $\Delta\rho$ is the scattering contrast, $F(q, r)$ is the scattering form factor, $V(r)$ is the nanocrystal volume, N is the total number of nanocrystals, and $P(r)$ is the probability of the nanocrystal at size of r . Since the NCs are spherical, their form factor is:

$$F(q, r) = \frac{3[\sin(qr) - qr\cos(qr)]}{(qr)^3}$$

For the particles we assumed a Gaussian size distribution of particle sizes, as also confirmed by TEM analysis (Figure 4.24).

For the calculations of Figure 4.6 we modeled the form factor of a core/shell particle with the formula:

$$F(q, r) = [V_c^2(\rho_c - \rho_s)^2\Psi_c^2 + 2V_cV_s(\rho_c - \rho_s)(\rho_s - \rho_{solv})\Psi_c\Psi_s + V_s^2(\rho_s - \rho_{solv})^2\Psi_s^2]$$

where

$$\Psi_x = \frac{3[\sin(qr_x) - qr_x\cos(qr_x)]}{(qr_x)^3} \quad (1)$$

V_c and V_s are the volume of the core and the total volume of the particle, ρ_c and ρ_s are the scattering length density of the core and of the shell, and where the total particle is defined by a radius r_s with a core radius r_c and a shell thickness $r_s - r_c$.

The scattering contrast between two different media was obtained by calculating the difference in scattering length density (SLD) between the medium one and medium two (scattering contrast = ΔSLD), where the SLD of a material is calculated with the following equation:

$$SLD = \frac{\delta 2\pi}{\lambda^2} \quad (2)$$

Where λ is the wavelength of the X-photons (1 Å) and δ is the real part of refractive index of the material, which is expressed as $n = 1 + \delta - i\beta$. Since the imaginary part of the refractive index β is orders of magnitude smaller than the real part (since we do not work in the vicinity of an X-ray absorption edge), we neglect this part in the calculation for the

scattering contrast. Note that the contrast value is valid for amplitudes, and hence should be squared for intensity contrast differences.

System	δ	β	Re(SLD) (\AA^{-2})	Im(SLD) (\AA^{-2})
FeO	7.41E-06	3.42E-07	4.66E-05	2.15E-06
CoFe ₂ O ₄	6.82E-06	3.03E-07	4.29E-05	1.90E-06
Cyclohexane	1.20E-06	6.47E-10	7.54E-06	4.07E-09
Water	1.50E-06	2.10E-09	9.42E-06	1.32E-08
Oleic acid	1.35E-06	8.99E-10	8.50E-06	5.65E-09

System	Contrast (\AA^{-2})
NCs-cyclohexane	3.51E-05
Cyclohexane-water	1.88E-06
NCs-water	3.32E-05
Oleic acid-cyclohexane	9.64E-07

The values for δ can be calculated based on the density of a material and were obtained from http://henke.lbl.gov/optical_constants/getdb2.html.

Concerning the form factor of the NCs, we evaluated the contribution of the ligands on the final scattering power of the NCs. We compared the form factor of the NCs made of CoFe₂O₄ (for simplicity we assumed the particles as homogeneous, and made of CoFe₂O₄, and we neglected the small difference between the epitaxial FeO core and the CoFe₂O₄ shell since the scattering power of the two media is similar; see Figure 4.6a) with the form factor of a core/shell NCs where the core is CoFe₂O₄ and the shell is oleic acid. The results

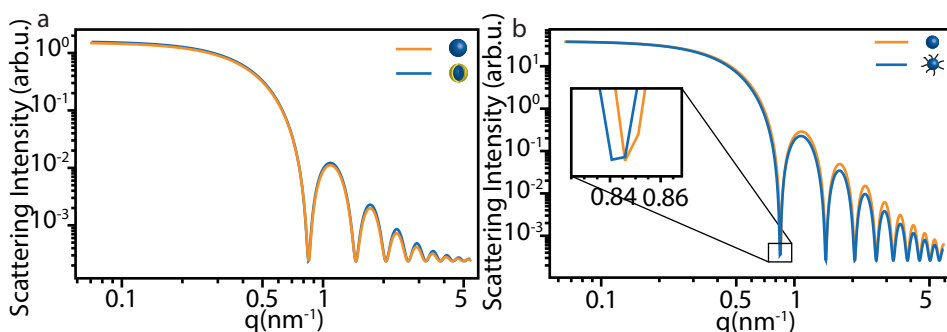


Figure 4.6 • Modeling of the form factor of spherical NCs. (a) We modeled the form factor of homogeneous CoFe₂O₄ NCs with a radius of 5.3 nm (in orange) in comparison to the form factor of FeO/CoFe₂O₄ core/shell NCs composed of 4.6 nm in radius FeO core and 0.75 nm thick CoFe₂O₄ shell (in blue); (b) We modeled the form factor of homogeneous CoFe₂O₄ NCs with a radius of 5.3 nm (in orange) in comparison to the form factor of the same NCs covered by a shell of ligands (oleic acid) 2 nm thick (in blue). In the inset is a magnification of the first minimum.

are shown in Figure 4.6b. It is clear that the ligands around the NCs brings an extremely small contribution to the final scattering power, therefore, for simplicity, as model for further calculations we considered a NC with homogeneous composition of CoFe_2O_4 and no ligands around.

Analysis of the crystalline structure

We use the symmetry of an FCC lattice to calculate the expected positions of the structure factor (SF) reflections. For any cubic crystal with lattice constant a and Miller indices $\{hkl\}$ we can write:

$$d_{hkl} = \frac{a}{\sqrt{h^2 + k^2 + l^2}} \quad (3)$$

where d_{hkl} is a plane through the lattice. Since the scattering vector $q_{hkl} = 2\pi/d_{hkl}$, we can write the expected peak positions for an FCC lattice:

$$\mathbf{q}_{hkl} = \frac{2\pi}{a} \sqrt{h^2 + k^2 + l^2} \quad (4)$$

For an FCC lattice, all miller indices must be either all even or all odd for constructive interference (which is described by the structure factor of the FCC lattice). This means the first allowed reflection is the $\{111\}$ reflection. From the peak position of the $\{111\}$ reflection, which we determine by a Lorentzian fit plus linear background, we can calculate the expected position of all other FCC reflections by simply plugging in the consecutive Miller indices. In this way we were able to index up to 21 reflections for lattice planes from an FCC lattice: $\{111\}$, $\{200\}$, $\{220\}$, $\{311\}$, $\{222\}$, $\{400\}$, $\{331\}$, $\{420\}$, $\{422\}$, $\{511\}$, $\{440\}$, $\{531\}$, $\{600\}$, $\{620\}$, $\{622\}$, $\{353\}$, $\{444\}$, $\{711\}$, $\{640\}$, $\{642\}$, $\{731\}$.

Concerning the selection rules for Figure 4.17, for an FCC lattice the allowed reflections are those for which the Miller indices $\{hkl\}$ are all odd or all even, for an HCP lattice all the reflections are allowed but those for which l is odd and $h-k=3n$, where n is an integer number, while for an RHCP lattice the sharp reflections are those for which $h-k=3n$, where

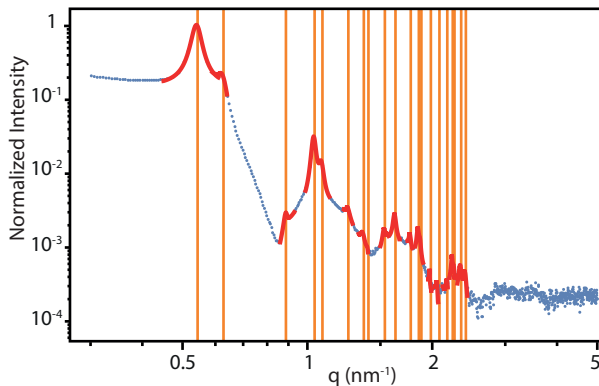


Figure 4.7 • Analysis of the structure factor peaks. The data of the SAXS pattern in the high q region after 290 min after the beginning of the measurement are shown in blue, while the fitting with a double Lorentzian function are shown in red. The orange lines indicates the position of the reflections for lattice planes from an FCC lattice.

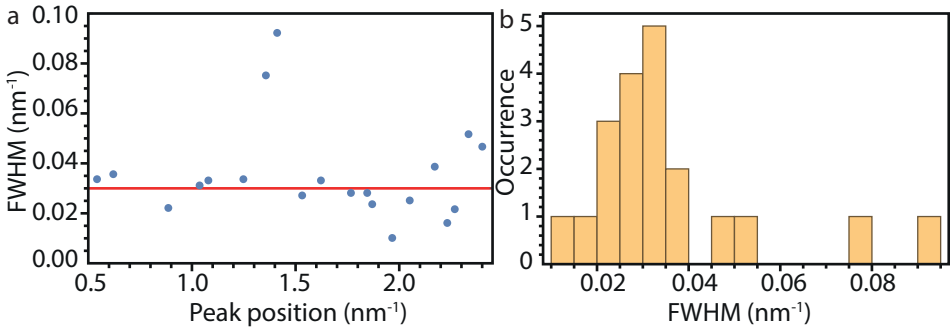


Figure 4.8 • Analysis of the FWHM of the structure factor peaks. (a) FWHM of each peak as function of its peak position. The red line indicates the average FWHM, corresponding to 0.03 nm⁻¹, which is clearly independent on the peak position; (b) Distribution of the FWHM plotted in panel (a) showing that the FWHM is centered around the average value.

n is an integer number, and l is even.³⁷⁻³⁹

From the change in the peak position (PP) and full width at half maximum (FWHM) of the structure factor peak of the {111} reflection we determined the NC-NC distance with the following formula:

$$NC - NC \text{ distance} = \frac{4\pi}{\sqrt{h^2 + k^2 + l^2} PP} \quad (5)$$

At the same time, we evaluated the average crystalline domain size (ACDS) with the following equation:

$$ACDS = \frac{2\pi}{FWHM} \quad (6)$$

The analysis of the peak position and the FWHM of the structure factor peaks was performed by fitting the peaks with a double Lorentzian function. The double Lorentzian was chosen because some of the peaks are very close to each other. The data, with the corresponding fittings, are shown in Figure 4.7.

From the fittings we could extract the FWHM for each peak. Since the polydispersity of a sample might have an influence over the FWHM of a single peak, thus deviating from the behavior described by equation (6), we plotted the FWHM of the peaks in Figure 4.7 as function of their peak position.

The polydispersity of the sample influences the order of the crystal at long distances, contributing stronger for higher index reflections. However, since the FWHM of the peaks seems to be independent of the peak position, we can conclude that, in our case, there is no effect of the strain (induced by polydispersity or defects) on the peak width. The inverse peak width (equation 6) is therefore a measure of the typical size of periodically-ordered domains.

Determination of the percentage of assembled NCs

In order to determine the percentage of NCs assembled in the SP over time we modeled the form factor of polydisperse spheres for the SAXS pattern at different times. Then we divided the modeled form factor from the scattered intensity, thus obtaining the structure factor. At any time, the integral of the structure factor in the considered q range is proportional to the amount of NCs assembled in the SPs. We calculated the amount of NCs assembled in the SP with this method for every scattering pattern, obtaining the evolution in time of this amount. Finally, the graph was normalized to 0 and 1 assuming two conditions: that at the measurement before the appearance of any structure factor peaks all the NCs are unassembled; and that at the measurement for which the integral of the structure factor remains unchanged compared to the previous measurement, all the NCs are assembled in the SPs. The second assumption is corroborated by the absence of residual NCs in the supernatant obtained after washing the SPs.

The average crystallization time has been obtained by fitting the curve in figure 2d of the main text with a monoexponential function with formula $NC_{\%} = Ae^{-\alpha t}$, where A is the maximum percentage of unassembled NCs, α is the crystallization rate and t is the time. The best fitting parameters for our data are 98.68 and 0.302, respectively for A and α . The average crystallization time is the value of t for which only 10% of the NCs are not in the SP (*i.e.* 90% of the NCs are in assembled in the SP). This gives an average crystallization time of 7.5 min.

Determination of the volume fraction

The volume fraction of NCs in cyclohexane was determined by the same method used by Pusey and van Megen.⁴⁰ A dispersion of the NCs in cyclohexane with unknown concentration is destabilized by the addition of anti-solvent (ethanol) and subsequently precipitated by centrifugation. The supernatant is discarded while the pellet is dried under vacuum for two hours, in order to remove all the solvent. The pellet is then weighted and subsequently redispersed in a certain amount of cyclohexane in order to obtain a dispersion with a concentration of 10 mg/mL. By knowing the size of the NCs, from transmission electron

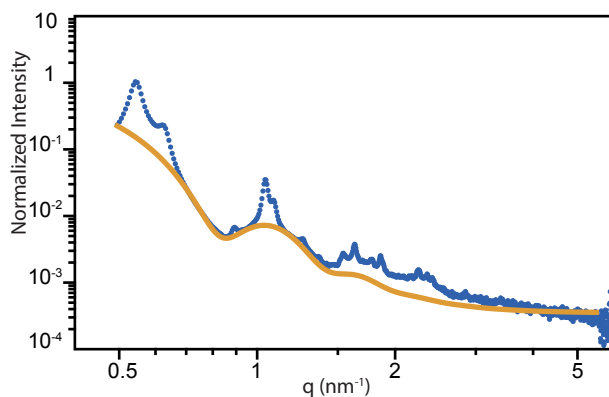


Figure 4.9 • Fitting the form factor to extract the percentage of NCs assembled in the crystal. In blue is shown the SAXS pattern in the high q region after 290 min after the beginning of the measurement. In yellow is shown the fitting of the form factor of the NCs.

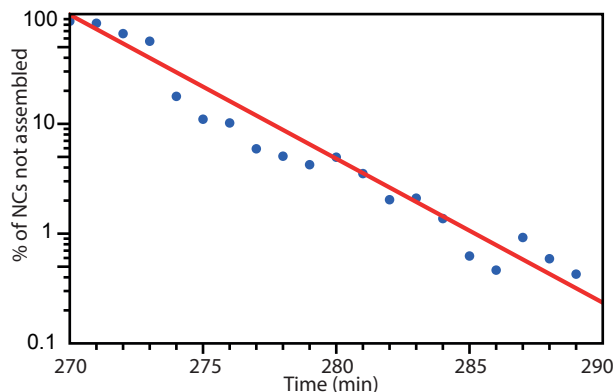


Figure 4.10 • Fitting of the percentage of NCs not assembled in the crystal over time. In blue are shown the experimental data, while the monoexponential fit of equation $NC_{\%} = Ae^{-\alpha t}$ is shown in red. The best fitting parameters for our data are 98.68 and 0.302, respectively for A and α . The plot is in log-lin scale.

microscopy (TEM) analysis (Figure 4.24) corroborated by small angle X-ray scattering data (Figure 4.25), the size of the ligands (oleate) and the density of all the components, we calculate the weight of a single NC and, therefore, the number of NCs in the dispersion. By calculating the total volume occupied by the NCs, we are able to obtain the initial volume fraction of the NCs in the dispersion: 0.0077.

This procedure is intrinsically corrupted by errors:^{41,42} (a) error in weighting the pellet, and (b) error assuming the ligands fully extended (as our particles are not truly “hard” since they are covered by a shell of ligands). Concerning the first error, we have a 5% relative error to the weight of the pellet, while concerning the second error, if we assume fully extended ligands (1.8 nm) against partially interpenetrated ligands (1.3 nm as derived from the peak position of the structure factor peaks in the SAXS data, Figure 4.3c in the main text) we might commit a relative error of 14%. By combining these two errors, we obtain a general error of 15% in the determination of the initial volume fraction. Following from the theory of propagation of the error, this means that we have a relative error of 20% on the determination of the critical volume fraction at which crystallization occurs.

Furthermore, the volume fraction over time has been calculated by assuming conservation of the material (NCs) during the evaporation of the cyclohexane, therefore: $V_i\theta_i = V_f\theta_f$, where V_i and V_f are, respectively, the initial and the final volume of the droplets, while θ_i and θ_f are, respectively, the initial and the final volume fractions. The initial and the final volumes are known from the fitting of the form factors of the droplets at the beginning and at the end of the measurement, while the initial volume fraction has been calculated from the amount of NCs present in the emulsion (see above). The error in the determination of the volume fraction at each moment in time is therefore also related to the error in the determination of the size of the droplets for each measurement. This results in a relative error on the volume fraction ranging from 15% to 32%, and this error is plotted as error bars in Figure 4.2c in the main text.

Analysis of the SAXS data in the small q range

Concerning the analysis of the form factor related to the droplets and the SPs, we fitted this part of the data with a power law of equation $I=Aq^{-\alpha}$, where I is the scattered intensity, A is a scaling parameter, α is the slope of the curve and q is the scattering vector. For every scattering pattern we fitted the data with the best fitting parameters and we analyzed the residuals of the fit.

In this way we were able to highlight the modulation related to the form factor of our particles. In this way we were able to determine the position of the first minimum with an error ranging from $\sim 1\%$ to $\sim 13\%$, depending on the quality of the data. The position of the first minimum gives an indication of the size of the droplets/particles following the relation:

$$\text{Radius droplet [nm]} = \frac{4.42}{\text{first minima [nm}^{-1}\text{]}} \quad (7)$$

In order to take in account the deviation induced by the polydispersity of the droplets, we used the droplet size evaluated in this way as a starting fit parameter for the Modeling II function of the IRENA package and extracting the real droplet size and polydispersity from the best fitting model. We therefore obtained an average polydispersity of $\sim 19\%$, in accordance with our previous findings.¹⁸ We also notice that the first estimation of the droplet size, from the position of the first minimum without taking into account the effect of the polydispersity, is very similar ($<10\%$ difference) to the droplet size as extracted from the IRENA modeling.

Concerning the determination of the droplet size, after 51 min after the beginning of the measurement, as the position of the minimum moves towards higher q values (as expected for droplets growing smaller), we see the appearance of another minimum on the left side (at smaller q values) of the original first minimum. We therefore assume this minimum as the true first minimum, while the first minimum observed for the first 51 min is therefore assumed as the second minimum. We monitor the distance in q between the first

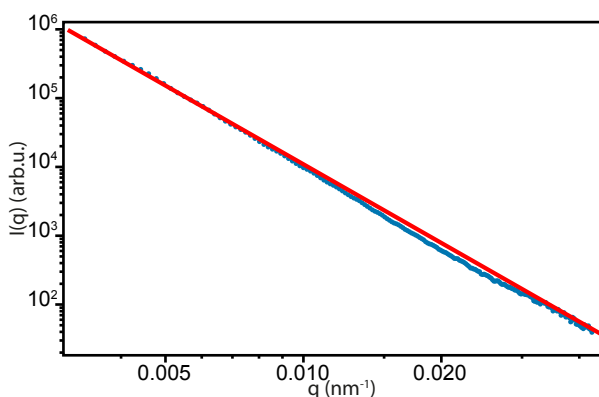


Figure 4.11 • Scattering pattern at $t=0s$ in the small q range, in blue, with power law fit to the best fit parameters, in red.

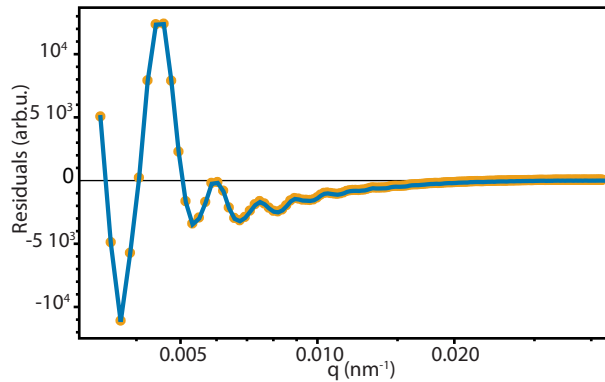


Figure 4.12 • Residuals of the fit of Figure 4.11, in yellow, and corresponding interpolation of the points for a better visualization of the minima, in blue.

and the second minimum for the course of the measurement and we calculate the average distance between the two minima. This value is then used to extract the position of the first minimum for the first 51 min starting from the position of the second minimum. In this way we extract an original size of the droplets at the beginning of our measurement of ~ 3150 nm, which is in agreement with optical microscopy observations (see Figure 4.27) and with our expectations for droplet size in the current experimental conditions: volume fraction of the liquids 10%, gap of 0.1 mm between rotor and stator during the emulsification and rotation speed of 7500 rpm for the rotor. We think that the first minimum is not observed in the first 51 min of the measurement because the droplet size is over the limit of the detection range of our detector, when positioned at 30 m (maximum detectable particle size ~ 2500 nm).

Evaporation rate

The evaporation rate has been calculated by fitting the data relative to the size of the SPs with a linear equation: $S = -mt + q$, where S is the diameter of the droplet, t is the time in minutes, m is the evaporation speed in nm/min and q is the initial droplet size in nm. The so calculated evaporation rate is ~ 6.5 nm/min. The constant evaporation rate shows that it is proportional to the droplet surface, and hence that the evaporation rate per unit area is a constant, independent of the size of the droplet:

$$\frac{dV}{dt} = -kA \rightarrow \frac{4}{3}\pi \frac{dr^3}{dt} = -k4\pi r^2 \rightarrow r^2 \frac{dr}{dt} = -kr^2 \rightarrow \frac{dr}{dt} = -k \rightarrow v = -k \quad (8)$$

Where V is the volume of the droplet, t is the time, k is a constant, r is the radius of the droplet, A is the surface area of the droplet and v is the evaporation rate. As it can be seen from the development of the equation, the evaporation rate is independent from the size of the droplet, confirming that the evaporation rate per unit area is constant.

Crystallization mechanism

A general scheme of the crystallization mechanism proposed in the article and of the general hard spheres crystallization mechanism is shown in Figure 4.14.

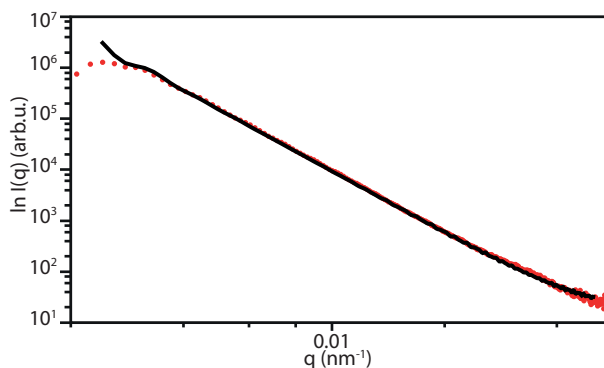


Figure 4.13 • Fitting of the SAXS scattering pattern in the small q region. The data, corresponding to the measurement at $t = 0$ s, are shown in red while the fitting is shown in black.

At the beginning of the crystallization the NCs are homogeneously distributed in the droplet, composing a homogeneous scattering medium. The crystallization can either go through the blue path, representing the model that is proposed in this article, or through the red path, representing the model based on hard spheres crystallization.⁴³ In order to discern between these two models, we analyzed the data relative to the form factor of the SPs at the end of the crystallization and we compared it to the modeled scattering pattern for the different crystallization paths.

First, we modeled the form factor of a SP with 0.74 volume fraction and diameter of ~ 710 nm, observing that the position of the minima fits well the data (Figure 4.15).

Then we modeled the case for a SP with the same characteristic as for the previous case, but inside of a cyclohexane droplet of 1000 nm in diameter (Figure 4.16).

As it can be seen from Figure 4.16, the position of the minima is very similar to the one observed for the scattering pattern of Figure 4.15; this is mainly due to the fact that the scattering contrast SP-cyclohexane is ~ 350 times stronger than the scattering contrast cyclohexane-water, therefore the droplet has a negligible contribution to the overall scattering power. This fact proves that the model that we propose in the article is compatible with our experimental observations.

As countercheck, we also modeled the case for a SP crystallizing through the hard spheres model. According to this model, the crystallization happens through the formation of a crystalline phase of 0.55 volume fraction at the surface of the droplet, in constant equilibrium with the liquid phase of 0.50 volume fraction present inside the droplet. This equilibrium is maintained during the shrinkage of the droplet, until the crystalline phase propagates inside the droplet to form the SP. To model this, in Figure 4.17 is shown the case of a core/shell structure of an overall diameter of 1000 nm composed by a core of 680 nm in diameter and a volume fraction of 0.50, and a shell with a volume fraction of 0.55, in agreement with hard spheres crystallization proposed in literature.¹⁷

In the modeled pattern, however, the position of the minima does not correspond to the

ones of the data. In order to keep the same geometry and have a correspondence between model and data, the particle should have an overall diameter of 710 nm and a core of 400 nm (Figure 4.18).

The same result is obtained if we assume an inverse structure, with the same overall size and core/shell geometry, but with inverted volume fractions: 0.55 for the core, which is, in this case, the crystalline phase, and 0.50 for the shell, which is, in this case, the liquid phase (Figure 4.19).

This must mean that if we would assume the hard sphere model to explain the crystallization in our system, we would have to conclude that the sudden decrease in the droplet size observed in Figure 4.2 in the main text is real. This would mean that in 3 min the droplets shrink of 300 nm in diameter, at a speed of ~ 100 nm/min, and losing 70 % of their volume. We believe that this is highly unlikely, and that, therefore, the crystallization according to hard spheres model does not apply to our case.

Furthermore, in Figure 4.20, we investigated the effect of a monolayer of NCs adsorbed at the interface of the droplet on the scattering pattern. The model system is a droplet of 1000 nm with homogeneous distribution of NCs and a volume fraction of 0.20 (before crystallization). We then compared the modeled scattering patterns of the droplet with (green line) and without (black line) a monolayer of NCs (10 nm thickness) with a volume fraction of 0.74 adsorbed at the interface. The two modeled scattering patterns are very similar, and therefore we are unable to clearly resolve whether NCs are adsorbed at the

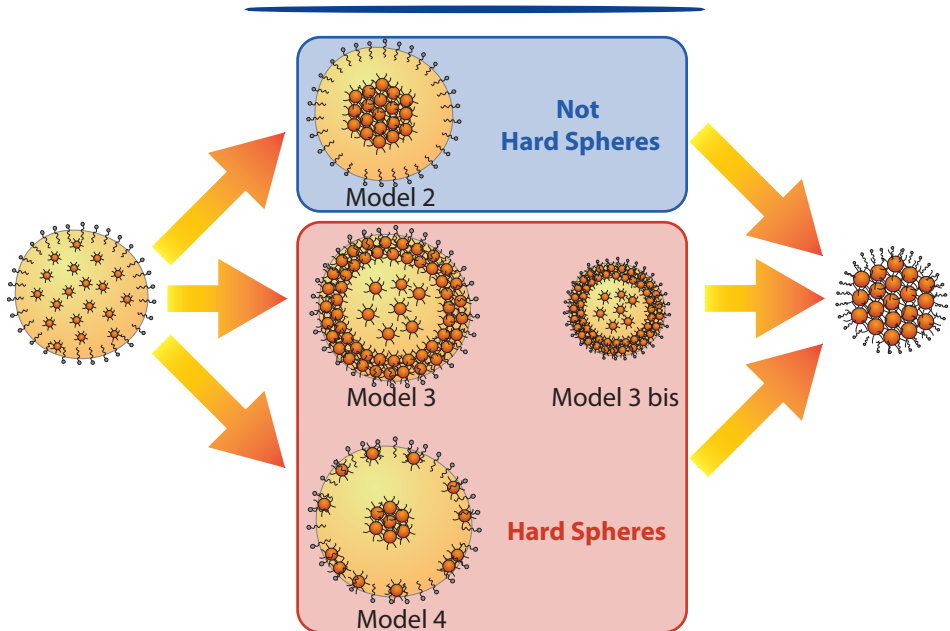


Figure 4.14 • Scheme of the different crystallization mechanisms. In the blue box is schematized the model that we propose, based on the presence of attractions between the NCs, while in the red box is presented the model based on hard sphere crystallization proposed in literature.¹⁷

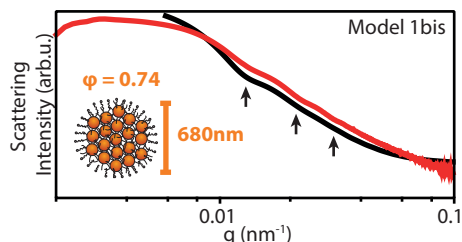


Figure 4.15 • Modeled scattering pattern for a SP with volume fraction 0.74, diameter of 680 nm and polydispersity of 20%. The data are shown in red, while the modeled scattering pattern is shown in black. The arrows indicate the position of the minima of the form factor.

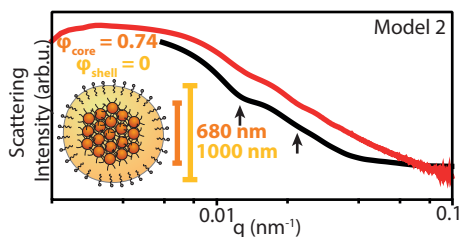


Figure 4.16 • Modeled scattering pattern for a SP with volume fraction 0.74, diameter of 680 nm and polydispersity of 20%, included in a cyclohexane droplet. Data are shown in red, while the modeled scattering pattern is in black. The arrows indicate the position of the minima of the form factor.

interface.

Wide angle X-ray scattering (WAXS) data

The wide angle X-ray scattering pattern of the concentrated solution of NCs is presented in Figure 4.21. We observe a very prominent peak at 13 nm^{-1} , corresponding to the scattering of the solvent (*i.e.* water, SDS and dextran), and three small peaks at very big scattering vectors. By comparing the position of these peaks with the values found in literature²⁹ for the reflections from the atomic planes of $\text{FeO}/\text{CoFe}_2\text{O}_4$ NCs, it is possible to index these peaks. In particular we distinguish the reflection from the (311) plane of bulk FeO , and the reflections from the (111) and (200) planes of the bulk CoFe_2O_4 . Unfortunately we were not able to extract information on the crystallographic alignment of the NCs inside the SPs in this manner, since the signal is averaged out over multiple SPs which are freely moving throughout the solution.

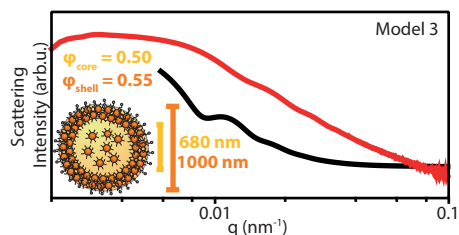


Figure 4.17 • Modeled scattering pattern for a SP crystallizing according to the hard sphere model. The particle is modeled with a core/shell geometry, composed by a core of 680 nm and a volume fraction of 0.50 (the liquid phase), and a shell with volume fraction of 0.55 (the crystalline phase), with an overall shape of 1000 nm. Data are shown in red, while the modeled scattering pattern is in black.

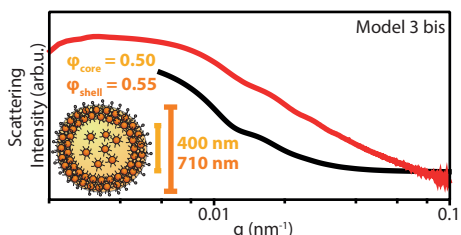


Figure 4.18 • Modeled scattering pattern for a SP crystallizing according to the hard sphere model. The particle is modeled with a core/shell geometry, composed by a core of 400 nm and a volume fraction of 0.50 (the liquid phase), and a shell with volume fraction of 0.55 (the crystalline phase), with an overall shape of 710 nm. Data are shown in red, while the modeled scattering pattern is in black.

Definition of polydispersity

All the values of sizes in the article are given with the mean (μ) and the standard deviation (σ) in the form: $\mu \pm \sigma$. Only exceptions are the values of volume fraction, which are given with the mean and the relative error. Polydispersity of size is defined as $PD (\%) = (\sigma/\mu) \cdot 100$.

Electron microscopy

HAADF-STEM images, SE-STEM images and TEM images were acquired using a FEI Tecnai electron microscope operated at 200 kV.

Computer simulations

Model: The effective pair potential $\beta U_{\text{eff}}(r_{ij}, \sigma_c)$ between two colloidal NCs with diameter σ_c depends predominantly on the van der Waals interactions $\beta U_{\text{vdW}}(r_{ij}, \sigma_c)$ originating from the NCs¹⁴ and the steric repulsive interaction $\beta U_{\text{steric}}(r_{ij}, \sigma_c)$ between the capping ligands. The center-of-mass distance between the two NCs, labelled i and j , is denoted by r_{ij} .

The van der Waals interaction $\beta U_{\text{vdW}}(r_{ij}, \sigma_c)$ between two spherical NCs is given by:^{44,45}

$$\beta U_{\text{vdW}}(r_{ij}, \sigma_c) = -\frac{\beta A}{12} \left[\frac{\sigma_c}{2D_{ij} \left(1 + \frac{D_{ij}}{2\sigma_c}\right)} + \frac{1}{1 + \frac{2D_{ij}}{\sigma_c} + \frac{D_{ij}^2}{\sigma_c^2}} + 2 \ln \left(\frac{2D_{ij} \left(1 + \frac{D_{ij}}{2\sigma_c}\right)}{\sigma_c \left(1 + \frac{2D_{ij}}{\sigma_c} + \frac{D_{ij}^2}{\sigma_c^2}\right)} \right) \right] \quad (9)$$

with $D_{ij} = r_{ij} - \sigma_c$, A the Hamaker constant, $\beta = 1/k_B T$ the inverse temperature, and k_B the Boltzmann constant.

We use the Alexander-de Gennes model to describe the steric repulsive interaction between two plates with a densely adsorbed polymer layer in a good solvent,⁴⁶ and we use the Derjaguin approximation⁴⁶ to convert the interaction between two plates to that between two spherical NCs with a high density of capping ligands. The steric repulsive interaction due to the ligands is given by:

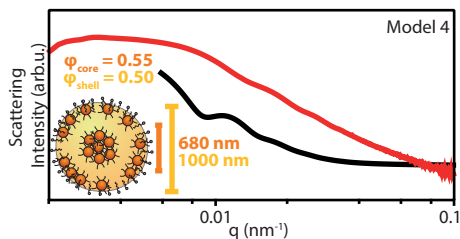


Figure 4.19 • Modeled scattering pattern for a SP crystallizing according to the hard sphere model. The particle is modeled with a core/shell geometry, composed by a core of 680 nm and a volume fraction of 0.55 (the crystalline phase), and a shell with volume fraction of 0.50 (the liquid phase), with an overall shape of 1000 nm. Data are shown in red, while the modeled scattering pattern is in black.

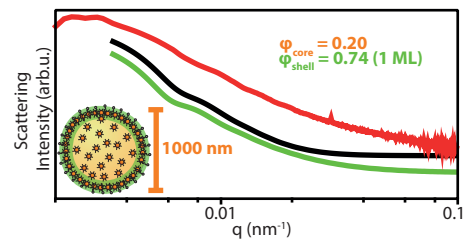


Figure 4.20 • Modeled scattering pattern for a droplet before crystallization with and without NCs adsorbed at the interface. The data (red line) are compared to a modeled particle with a core of 1000 nm in diameter and a volume fraction of 0.20 (black line), and to the same particle but covered by a shell of 1 monolayer (10 nm) of NCs with volume fraction of 0.74 (green line).

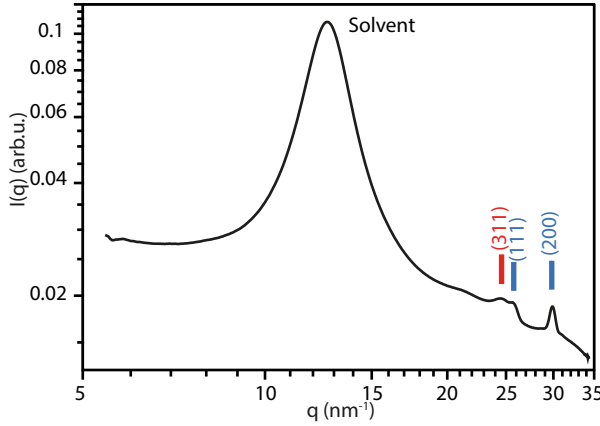


Figure 4.21 • WAXS pattern of a dispersion of NCs. The main peak at 13 nm^{-1} is due to the scattering from the continuous phase (*i.e.* water, SDS and dextran), while the peaks at higher q values are related to scattering from the atomic planes of $\text{FeO}/\text{CoFe}_2\text{O}_4$ NCs; in particular in blue are the reflections associated to bulk FeO , and in red are the reflections associated to bulk CoFe_2O_4 .

$$\beta U_{steric}(r_{ij}, \sigma_c) = \begin{cases} \frac{32\pi\sigma_c L^2}{140s^3} \left[28 \left(x_{ij}^{-\frac{1}{4}} - 1 \right) + \frac{20}{11} \left(1 - x_{ij}^{\frac{11}{4}} \right) + 12(x_{ij} - 1) \right] & \sigma_c < r_{ij} < \sigma_c + 2L \\ 0 & \text{otherwise} \end{cases} \quad (10)$$

where $x_{ij} = D_{ij}/(2L)$, s represents the mean distance between the attachment points of the capping ligands (also referred to as the mean ligand distance), and L is the thickness of the capping layer.

We plot the effective pairwise interaction potential $\beta U_{eff}(r_{ij}, \sigma_c) = \beta U_{vdW}(r_{ij}, \sigma_c) + \beta U_{steric}(r_{ij}, \sigma_c)$ for our $\text{FeO}/\text{CoFe}_2\text{O}_4$ core-shell NCs with oleate as capping ligands in comparison with the interaction potential for a similar NC system reported by De Nijs and Dussi¹⁷ in Figure 4.22. The only difference between these two model systems is the overall core-shell NC diameter, which for the system of Ref.² is $\sigma_c = 6.0 \pm 0.3 \text{ nm}$, and for the system employed in this work is $\sigma_c = 10.6 \pm 0.1 \text{ nm}$. For both systems, the NC-NC Hamaker constant A across a hydrocarbon medium is approximately 2.5 eV ,⁴⁷ the capping ligand length $L = 1.5 \text{ nm}$,¹⁷ mean ligand distance $s = 0.43 \text{ nm}$ ¹⁴ and temperature $T = 341 \text{ K}$. Figure 4.22 shows that the effective pair potential is repulsive at short distances due to the steric interactions between the ligands and attractive at intermediate distances due to the van der Waals interactions, and approaches zero at sufficiently large distances. The attractive interaction decreases with NC size. We find that NCs used in the present work are attractive, whereas the smaller NCs of Ref.¹⁷ are hard-sphere-like as already anticipated in that work.

In Figure 4.23a we replot the effective interaction potential $\beta U_{eff}(r_{ij}, \sigma_c)$ for our core-shell NCs. In order to speed up equilibration, we approximate this interaction potential with a hard-core attractive square-well potential $U_{HCSW}(r_{ij})$ in our event-driven Brownian Dynamics (EDBD) simulations:

$$\beta U_{HCSW}(r_{ij}) = \beta U_{HS}(r_{ij}) + \beta U_{SW}(r_{ij}), \quad (11)$$

where

$$\beta U_{HS}(r_{ij}) = \begin{cases} \infty, & r_{ij} \leq \sigma \\ 0, & r_{ij} > \sigma \end{cases}$$

and

$$\beta U_{SW}(r_{ij}) = \begin{cases} -\beta\varepsilon, & r_{ij} \leq \delta \\ 0, & r_{ij} > \delta \end{cases}$$

with σ the hard-core diameter, and $\delta > 0$ and $\varepsilon > 0$ the range and the strength of the attractive square well, respectively.

As shown in Figure 4.23b, the effective pair potential of our core-shell NCs can be approximated by a hard-core attractive square-well potential with an effective hard-core diameter $\sigma = 12.8$ nm, an attraction strength $\varepsilon = 2 k_B T$ and range of attraction $\delta = 1.2$, $\sigma = 15.36$ nm as indicated by the dashed lines in Figure 4.23b.

EDBD simulations: The simulation method detects particle collisions (with the wall and with each other) as discrete events and calculates an event tree of collision time intervals to each event as obtained from the Newtonian equations of motion. The dynamics evolves through a sequence of (varying) time intervals depending on the nearest event. In order to mimic a colloidal dispersion, particle velocities are stochastically adjusted at a regular interval of Δt to simulate Brownian “kicks” from the surrounding solvent.

$$v(t + \Delta t) = \alpha_t v(t) + \beta v_R(t) \quad (12)$$

where $v(t + \Delta t)$, $v(t)$ are the particle velocities before and after the Brownian adjustment, $v_R(t)$ is a variable calculated from a 3D Gaussian distribution with zero mean and variance $k_B T/m$ with mass m . We set $\alpha_t = 1/\sqrt{2}$ with a probability $\nu \Delta t$ and 1 otherwise. We set $\beta_t = \sqrt{(1 - \alpha_t^2)}$ in order to keep the temperature constant. In addition, we employ $\nu = 10\tau_{MD}^{-1}$ and $\Delta t = 0.01\tau_{MD}$ in all our simulations and use $\tau_{MD} = \sqrt{(m/k_B T)}$ as the unit of time in our

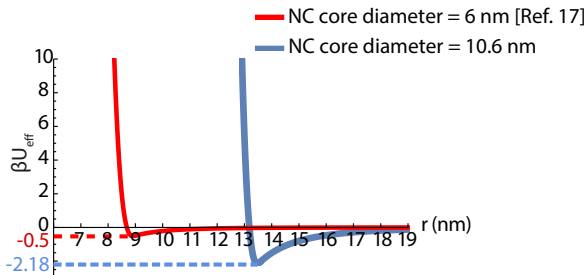


Figure 4.22 • The effective pair potential between two spherical FeO/CoFe₂O₄ core-shell NCs for the system employed in the present work and for a similar system as used in Ref.¹⁷ The NC core-shell diameters σ_c are 10.6 nm and 6 nm, respectively.

EDBD simulations.^{48,49}

We perform EDBD simulations⁵⁰ on a system of 100000 NCs interacting with each other via a $U_{\text{HCSW}}(r_{ij})$ potential with $\beta\epsilon=2$ and $\delta=1.2\sigma$ inside a slowly shrinking hard spherical confinement. The spherical confinement shrinks at a constant compression rate $\gamma=10^{-3} \sigma/\tau_{\text{MD}}$.

Cluster criterion: In order to determine if a particle is crystalline we investigate its local symmetry using bond-orientational order parameters.⁵¹ The (un-normalized) 3D bond order parameter of particle i is defined as:⁵¹

$$q_{l,m}(i) = \frac{1}{N_{\text{nb}}(i)} \sum_{j=1}^{N_{\text{nb}}(i)} Y_{l,m}(\theta_{ij}, \phi_{ij}) \quad (13)$$

where $N_{\text{nb}}(i)$ denotes the number of neighbors of particle i which we define as the particles that lie within a center-of-mass distance of 1.2σ of particle i , θ_{ij} and ϕ_{ij} are the polar and azimuthal angles, respectively, of the center-of-mass distance vector $\mathbf{r}_{ij} = \mathbf{r}_j - \mathbf{r}_i$ the position of particle i . $Y_{l,m}(\theta, \phi)$ are the spherical harmonics for m ranging from $[-l, l]$. Additionally, neighbor j of particle i forms a “solid-like” bond if $d_1(i, j) > d_c$ with:

$$d_1(i, j) = \frac{\sum_{m=-l}^l q_{l,m}(i) q_{l,m}^*(j)}{\left(\sum_{m=-l}^l |q_{l,m}(i)|^2\right)^{1/2} \left(\sum_{m=-l}^l |q_{l,m}(j)|^2\right)^{1/2}} \quad (14)$$

Crystalline particles are defined as particles for which the number of solid-like bonds exceeds a critical value n_c . As the crystal of NCs is expected to exhibit hexagonal order, we choose the symmetry index $l=6$. We set the cut-off values defined above as $n_c=6$ and $d_c=0.6$. In order to further distinguish crystal domains from one another, we calculate $d_1(i, j)^d$ of a crystalline particle with its crystalline neighbours. We contend that two crystalline neighbours belong to the same cluster if $d_1(i, j)^d > 0.7$, where the cut-off value signifies the degree of order in a similarly oriented crystal domain.

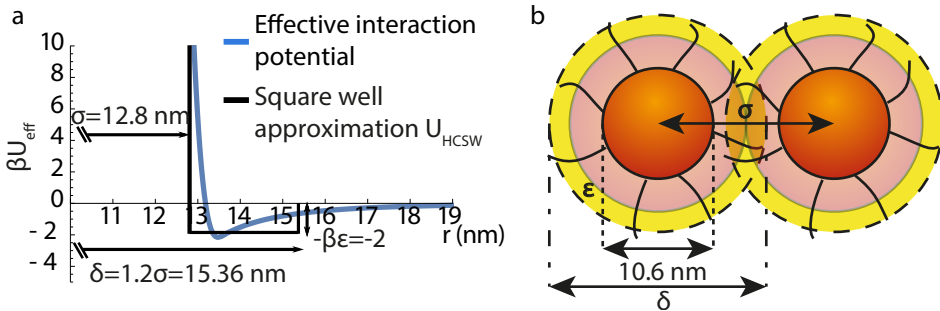


Figure 4.23 • Model of the system. (a) The effective pair potential $\beta U_{\text{eff}}(r_{ij}, \sigma_c)$ between two spherical FeO/CoFe₂O₄ core-shell NCs with diameter 10.6 nm along with the hard-core attractive square-well potential $U_{\text{HCSW}}(r_{ij})$ potential for comparison with $-\beta\epsilon=-2$ the strength of attraction, $\delta=1.2\sigma$ the range of the attraction, and $\sigma=12.8$ nm the effective hard-sphere diameter; (b) model of the system with the relevant length scales labelled.

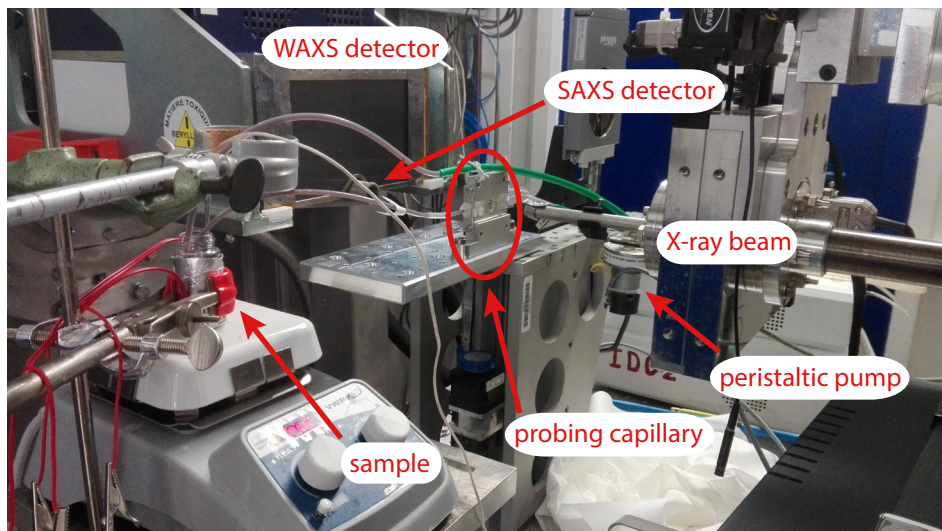


Figure 4.24 • Experimental setup used for these measurements. As also schematized in Figure 4.1, the sample is kept at 68 ± 2 °C through the aid of a heating plate and few peltier heating elements. Part of the sample is pumped through the probing capillary and then back in the containing vial through the aid of tubing connected with a peristaltic pump. The X-ray beam probes the sample and the scattered rays are collected by the SAXS and the WAXS detectors.

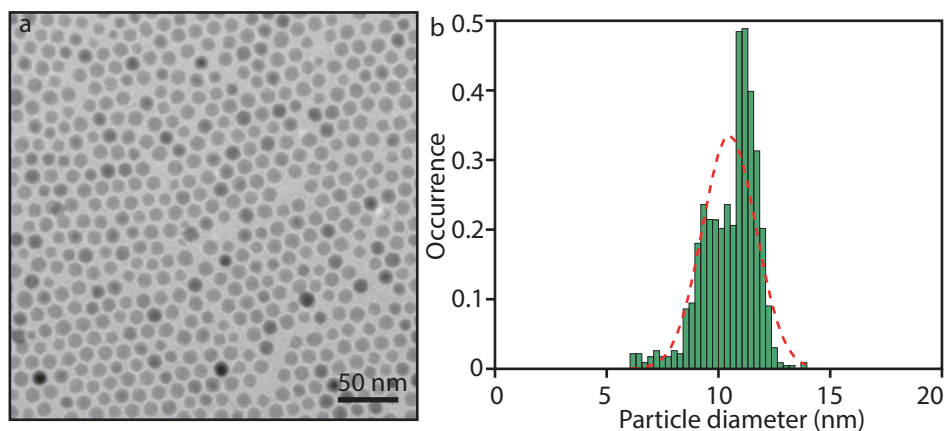


Figure 4.25 • Representative bright field TEM image of FeO/CoFe₂O₄ NCs and relative size analysis. (a) Bright field TEM image of the NCs; (b) Histogram of the sizes extracted from the image in panel a. The average diameter is 10.5 ± 1.2 nm.

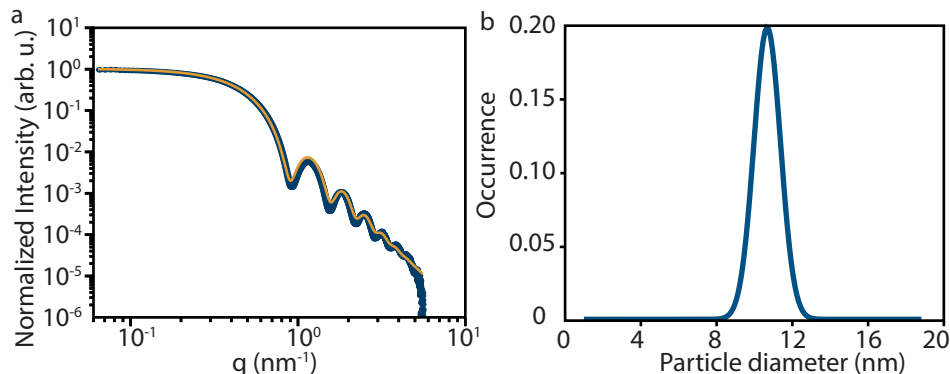


Figure 4.26 • SAXS pattern and relative analysis of the dispersion of NCs. (a) SAXS pattern of a dispersion of FeO/CoFe₂O₄ NCs in cyclohexane after background (cyclohexane) subtraction (blue) and relative fit (yellow); (b) Distribution of sizes as extracted from the fit of the pattern in panel a; the extracted average diameter is 10.7 ± 1.0 nm.

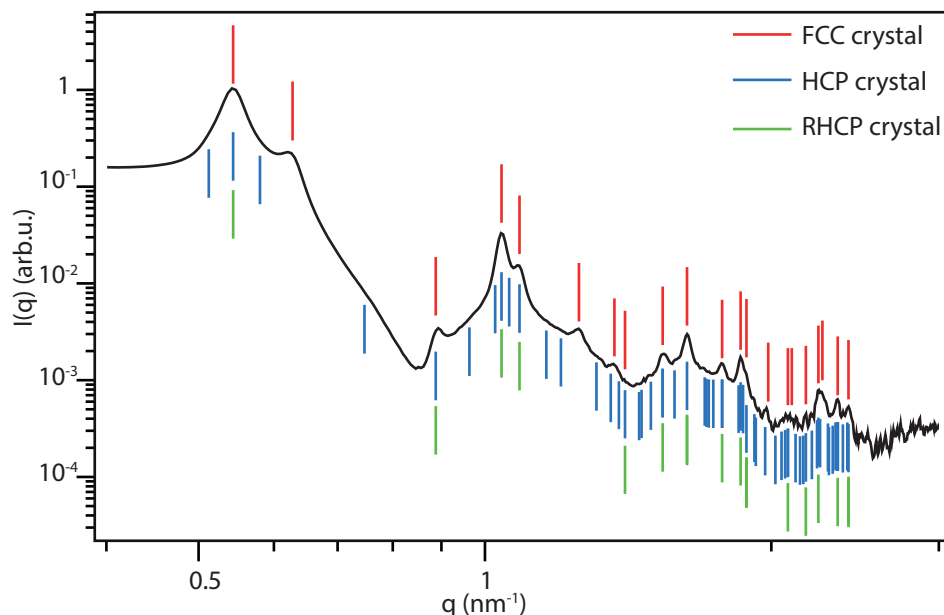


Figure 4.27 • Analysis of the crystal structure of the SPs. In black is the SAXS pattern of the solution of SPs at the end of the experiment. In red are highlighted the allowed reflections for a face centered cubic (FCC) crystal, in blue are highlighted the allowed reflections for an hexagonal close-packed (HCP) crystal and in green are highlighted the allowed reflections for a random hexagonal close-packed (RHCP) crystal. We can conclude that our SPs undoubtedly have a FCC crystal structure.

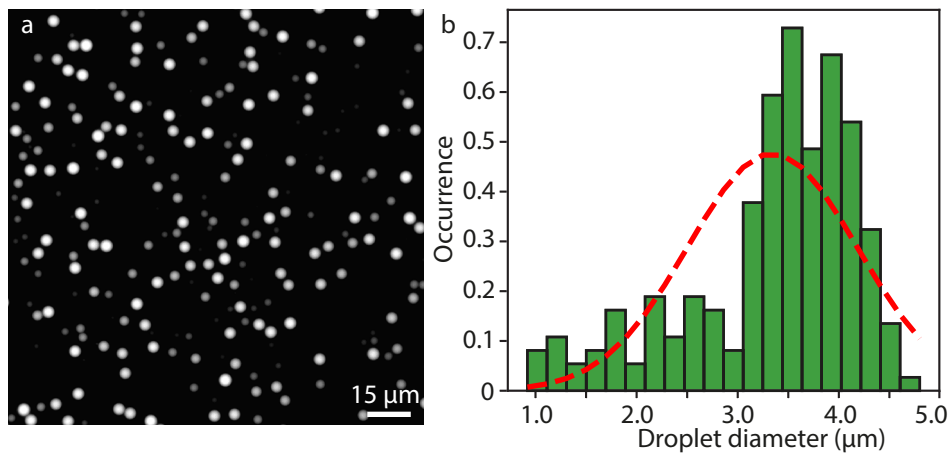


Figure 4.28 • Representative fluorescence optical image of droplets and relative size analysis. (a) Fluorescent optical image of droplets of cyclohexane containing a dye, Pyromethene 546, and formed with the same procedure used to emulsify the two phase system in our experiment; (b) histogram of the diameters of the droplets shown in panel a. The average size of the droplets is $3.3 \pm 0.8 \mu\text{m}$, in qualitative agreement with the initial diameter extracted from SAXS experiments.

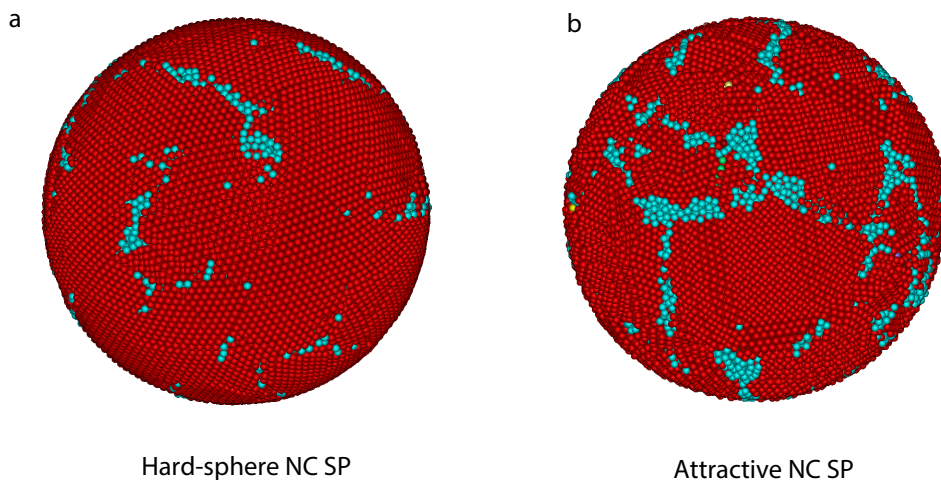


Figure 4.29 • Visual comparison of the outer surfaces of two SP systems. SP composed of hard-sphere NCs (a), and SP composed of hard-core attractive square well NCs (b). The hard-sphere NC SP has a smooth outer shell, while the attractive NC SP surface shows visible ledges.

Chapter 5

Reversible charge-carrier trapping slows Förster energy transfer in CdSe/CdS quantum-dot solids

Abstract

The dynamics of photoluminescence (PL) from nanocrystal quantum dots (QDs) is significantly affected by the reversible trapping of photoexcited charge carriers. This process occurs after up to 50% of the absorption events, depending on the type of QD considered, and can extend the time between the photoexcitation and relaxation of the QD by orders of magnitude. Although many optoelectronic applications require QDs assembled into a QD solid, until now, reversible trapping has been studied only in (ensembles of) spatially separated QDs. Here, we study the influence of reversible trapping on the excited-state dynamics of CdSe/CdS core/shell QDs when they are assembled into close-packed “supraparticles”. Time- and spectrally resolved photoluminescence (PL) measurements reveal competition among spontaneous emission, reversible charge-carrier trapping, and Förster resonance energy transfer between the QDs. While Förster transfer causes the PL to red-shift over the first 20–50 ns after excitation, reversible trapping stops and even reverses this trend at later times. We can model this behavior with a simple kinetic Monte Carlo simulation by considering that charge-carrier trapping leaves the QDs in a state with zero oscillator strength in which no energy transfer can occur. Our results highlight that reversible trapping significantly affects the energy and charge-carrier dynamics for applications in which QDs are assembled into a QD solid.

Based on: Reversible Charge-Carrier Trapping Slows Förster Energy Transfer in CdSe/CdS Quantum-Dot Solids. Federico Montanarella, Margherita Biondi, Stijn O.M. Hinterding, Daniel Vanmaekelbergh and Freddy T. Rabouw
Nano Lett. **18** (9), 5867–5874, (2018)

«If we knew what we were doing, it wouldn't be called research»
(Albert Einstein)

5.1 Introduction

The most-ancient application of quantum dots (QDs) reported in human history is their use for hair dyeing in ancient Greco-Roman times.¹ Since that time, significant progress has been made on the synthesis of bright and monodispersed QDs² as well as on the fundamental understanding of their remarkable size-dependent optoelectronic properties.³ Nowadays QDs are used in various optoelectronic applications,^{4–9} while more are still under development.^{10–13} For commercial applications, QDs are usually assembled into QD solids, *i.e.* close-packed structures. In contrast, fundamental studies on the photophysical properties of QDs are usually performed on spatially separated QDs (for example, dispersed in solution). More in-depth studies are necessary on QDs in close-packed conditions^{14–17}, and on the differences in properties between spatially separated and close-packed configuration, to fully understand their behavior.

It was recently shown that, upon pulsed excitation of an ensemble of separated QDs, spontaneous emission on nanosecond time scales is followed by strongly delayed emission at the same photon energies up to milliseconds after photoexcitation.^{18–24} The amplitude of delayed emission in a photoluminescence (PL) decay experiment is often low, and its existence has been overlooked. However, the time-integrated delayed emission accounts for more than 10% of the overall emission for many types of QDs.^{18–24} The current understanding is that the recombination of an electron–hole pair is delayed because one (or both) charge carrier is temporarily stored in a trap state. The original exciton state is restored after some time by release of the trapped charge carrier. The implications of temporary charge carrier storage on optoelectronic applications of QDs have not been addressed until now. In particular, QDs interact through charge and Förster resonance energy transfer (FRET) when assembled into a QD solid.^{14–17,25} Because reversible charge-carrier trapping has such a pronounced effect on the dynamics of spontaneous emission from spatially separated QDs, a significant influence on FRET and charge transfer in QD solids can be anticipated as well.

Here, we study the effect of reversible charge-carrier trapping on the excited-state dynamics in assemblies of interacting CdSe/CdS core/shell QDs. The dynamics, and thereby the PL properties, are determined by the interplay between three processes: spontaneous emission, FRET, and temporary storage of the exciton. We use QDs with a constant CdSe core size while varying the shell thickness from 1 to 4 CdS monolayers. The QDs are assembled into supraparticles (SPs) presenting a model system of a QD solid.^{26–29} The shell thickness allows us to control the FRET rate between QDs. Our key observation is the time evolution of the PL spectrum upon pulsed excitation, recorded from the nanosecond to the microsecond time scale. We observe that the spectrum redshifts over the first 20–50 ns after excitation, as expected for exciton diffusion by FRET, but that subsequently, this evolution stops and even reverses to a blue shift. This demonstrates the effect of reversible charge carrier storage, which temporarily freezes a QD in a state from which no FRET can occur. The release of trapped charge carrier(s) restores the exciton state. We model and reproduce the emission dynamics of our QD assemblies using kinetic Monte Carlo simulations, which we then use to track each FRET event and more quantitatively illustrate the effect of temporary charge-carrier trapping on FRET.

5.2 Results and Discussion

We synthesized QDs consisting of CdSe cores with a fixed diameter of 3.4 ± 0.3 nm (mean \pm standard deviation, as determined from electron microscopy) and different CdS shell thicknesses ranging from 1 to 4 monolayers (ML). The resulting core/shell QDs have overall diameters of 3.8 ± 0.6 , 4.6 ± 0.5 , 5.0 ± 0.6 , and 5.5 ± 0.6 nm (Figures 5.1a and 5.5). The QDs were assembled in nearly spherical supraparticles (SPs) through an oil-in-water emulsion synthesis (Figures 5.1b, 5.7 and 5.8).²⁶ Basic optical characterization of the QDs

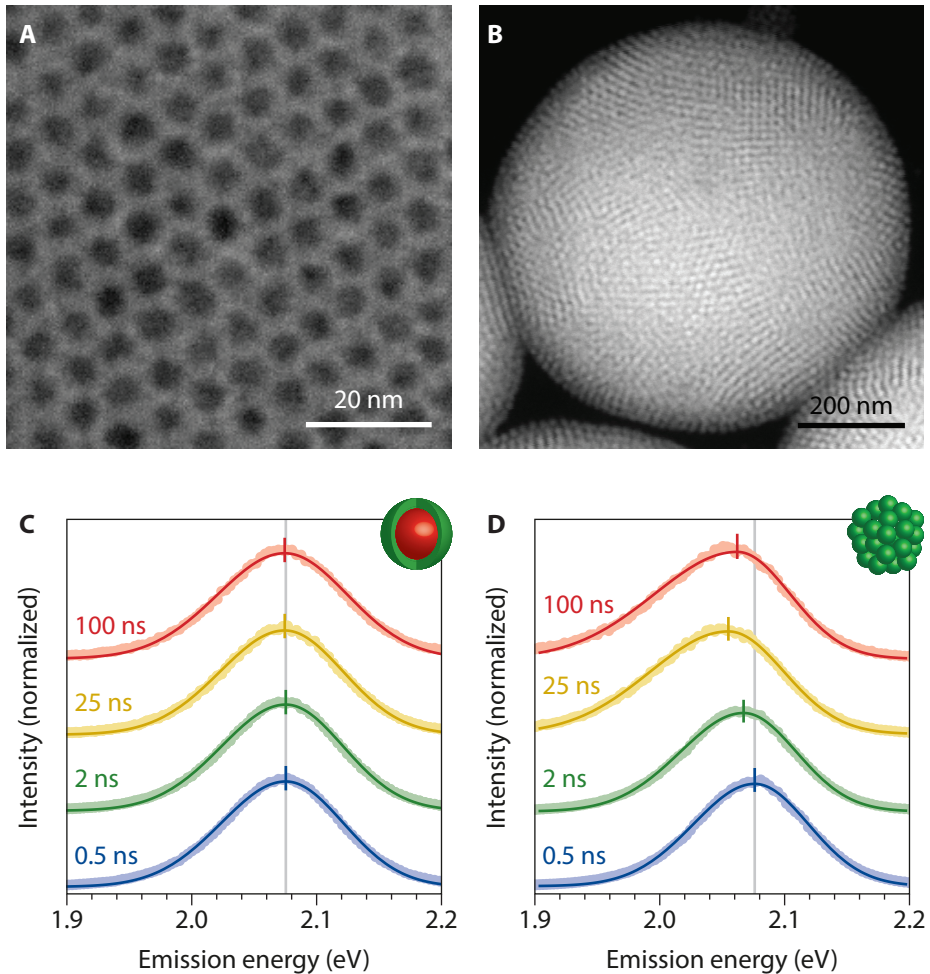


Figure 5.1 • Energy transfer in supraparticles of quantum dots. (a) Representative transmission electron microscopy (TEM) image of the CdSe/CdS QDs. (b) Representative high-angle annular dark field scanning transmission electron microscopy (HAADF-STEM) image of a SP. (c) Emission spectra of CdSe/CdS 2 ML QDs in toluene dispersion at 0.5 ns (blue), 2 ns (green), 25 ns (yellow), and 100 ns (red) delay time after an excitation pulse. The solid lines are fits to a two-sided Gaussian (see the Methods section for details). The short vertical bars are the peak energies obtained. The gray vertical line is the PL peak energy of the first spectrum at 0.5 ns. (d) The same for CdSe/CdS 2 ML QDs assembled in SPs.

in the two configurations (freely dispersed and assembled) is shown in Figure 5.8. The absorption and emission spectra show a clear red shift of the first ($1S_{3/2}-1S_c$) exciton resonance with increasing shell thickness due to reduced quantum confinement.³⁰ The full width at half-maximum (fwhm) of the emission peaks is approximately 110 meV. This is wider than the line widths of 50–80 meV fwhm that have been reported for similar QDs examined at the single-QD level,^{31,32} indicating some spectral broadening due to size in-

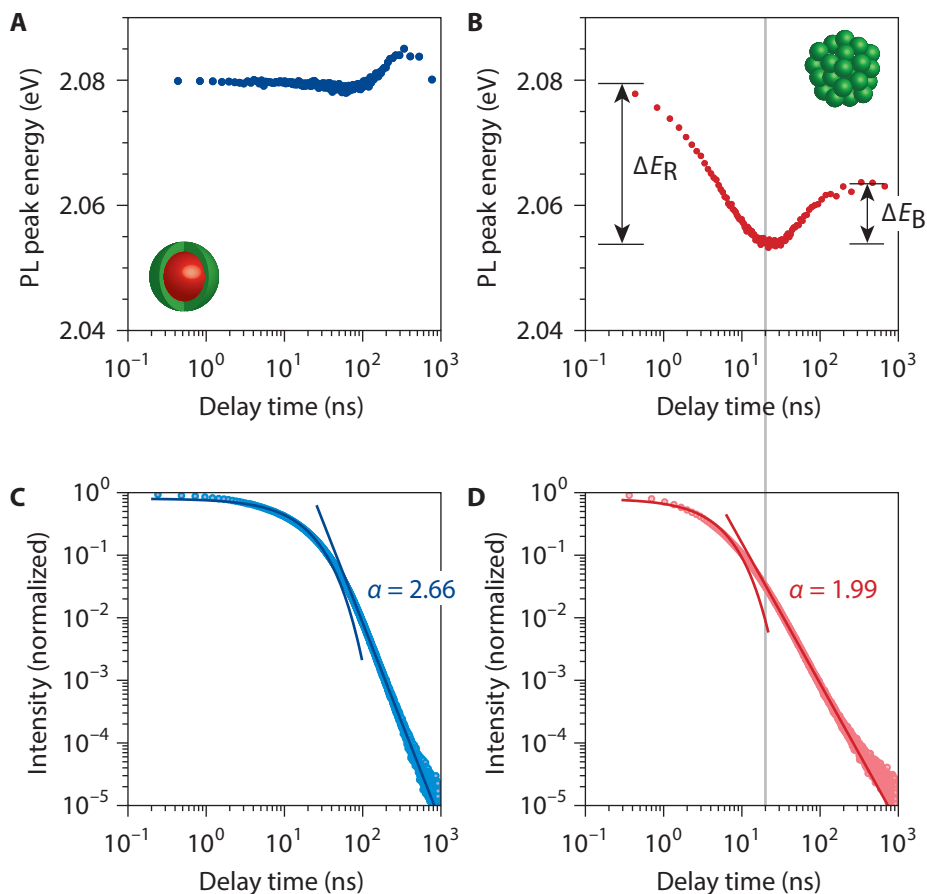


Figure 5.2 • Time-resolved PL emission of CdSe/CdS QDs in solution and assembled in SPs. (a) PL peak energy of the CdSe/CdS 2 ML QDs dispersed in toluene as a function of delay time after the excitation pulse as obtained from two-sided Gaussian fits to the emission spectra (see the Methods section for details). (b) The same but for CdSe/CdS 2 ML QDs assembled in SPs. The maximum red shift, ΔE_R , and blue shift, ΔE_B , are indicated by black arrows. (c) PL decay trace of CdSe/CdS 2 ML QDs dispersed in toluene as a function of delay time after the excitation pulse, spectrally integrated over the entire emission band, and plotted on a double-logarithmic scale. The solid lines are an exponential fit to the first part of the decay curve and the power-law fit to the later part. The delayed component has a power-law exponent of $\alpha = 2.66$. (d) Same for CdSe/CdS 2 ML QDs assembled in SPs. The power-law decay has an exponent of $\alpha = 1.99$. The dashed line highlights the moment when the contribution of the delayed emission becomes predominant over the prompt emission, which coincides with the reversal of the red shift in panel b.

homogeneity.

Following pulsed excitation of CdSe/CdS QDs with 2 ML shell thickness, we measure the time evolution of the photoluminescence (PL) spectrum over a time scale of 1 μ s (Figure 5.1c,d). The PL spectrum shows a time-independent peak energy and line width when the QDs are dispersed in toluene (Figure 5.1c). In contrast, the spectra obtained for QDs assembled into SPs (Figure 5.1d) first shift toward lower energies (red shift) over the first 25 ns after excitation, followed by a shift toward higher energies (blue shift) at later times.

To unravel the origin of the shifts in the PL spectra of assembled QDs, we analyze the time-resolved PL measurements in more detail. In Figure 5.2a,b the energy of the PL emission peak is plotted as a function of delay time after excitation. The results confirm what we concluded from inspecting the PL spectra in Figure 5.1c,d. For the QDs dispersed in toluene (Figure 5.2a) the emission energy is nearly constant in time. The delayed emission at times longer than 200 ns is at slightly higher energy than the prompt emission. In contrast, in our previous experiments with another batch of QDs the delayed emission was at slightly lower energy than the prompt emission.²⁰ This indicates slight variations in the probability of temporary carrier trapping among the QDs in ensemble. For the samples in this work, the smaller QDs may exhibit slightly more temporary trapping. The spectral dynamics are markedly different when QDs are in a close-packed configuration (Figure 5.2b). First, we observe a gradual redshift of the PL over the first 20 ns. This has previously been observed and studied in similar QD solids,^{14–17} and can be ascribed to Förster energy transfer between adjacent QDs interacting through dipole–dipole coupling. The initial red shift is followed by a clear blue shift over 10 meV from 20 to 200 ns after excitation (Figure 5.2b). This blue shift has not previously been reported, although we find here that it occurs in all four QD samples under study. It reflects a likely general aspect of the excited-state dynamics in QD solids that has so far been overlooked.

To understand the PL blue shift observed for QDs assembled into SPs, we consider the (spectrally integrated) PL decay traces. For both the QDs in dispersion (Figure 5.2c) and for those assembled in SPs (Figure 5.2d), the PL decay is approximately exponential over the first tens of nanoseconds, characteristic for the “normal” spontaneous emission of excitons. The decay statistics change to power-law (straight line on a double-logarithmic scale) after the intensity drops to a few percent of the initial intensity. This power-law emission has been termed “delayed emission” and attributed to emission after temporary exciton storage by reversible trapping of charge carriers.^{18–20,23} The power-law statistics (intensity proportional to $t^{-\alpha}$) reflect the wide distribution of the release times of the charge carriers from the trap states. Previous studies have demonstrated that the state with a trapped charge carrier can persist for up to milliseconds before the carrier is released,^{18–20,23} the exciton state is restored, and a delayed photon is emitted. The charge-separated state (with one or both of the charge carriers localized on a trap) must have an oscillator strength orders of magnitude lower than that of the exciton state. Indeed, radiative decay, which scales linearly with oscillator strength, would otherwise limit the lifetime of the charge-separated state to much shorter than a millisecond. Interestingly, the rate of exciton diffusion by FRET scales with oscillator strength as well.³³ Hence, just as temporary charge-carrier trapping stores the exciton in separated QDs by preventing radiative

recombination, so too does it prevent FRET in QD solids.

By comparing the PL decay curve of the QDs in SPs (Figure 5.2d) with the evolution of the PL peak position (Figure 5.2b), it is evident that the onset of the spectral blue shift coincides with the moment when the power-law decay component becomes dominant over the exponential component. Clearly, the delayed photons (those emitted following charge-carrier trapping and release) are less red-shifted than “normal” photons due to prompt spontaneous emission. The initial red shift and subsequent blues shift in PL energy from SPs reflects a competition between spontaneous emission, FRET, and reversible charge-carrier trapping. On the first ~ 20 ns after excitation, FRET gradually red shifts the PL as excitons hop from smaller QDs (with larger bandgap) to larger QDs (with smaller bandgap).^{14–17} Simultaneously, charge carriers have a finite probability to be trapped in temporary traps before spontaneous emission and/or FRET can occur. Once a charge carrier is trapped, the transfer of the exciton by means of FRET is temporarily prevented. At later times, distributed from ~ 20 ns to at least a $1 \mu\text{s}$ after excitation (Figure 5.2d), the charge carrier is released, and the exciton state in the QD is restored. If temporary charge-carrier trapping had not occurred, the exciton could in the meantime have hopped to other larger QDs with red-shifted exciton energy. Reversible trapping prevents this red shift. In the experiment, this effect manifests itself in a partial reversal of the PL red shift when around ~ 20 ns delayed emission becomes dominant over prompt emission (Figure 5.2b).

The strong distance dependence of FRET (which is inversely proportional to the sixth power of the center-to-center distance) allows us to tune its interplay with spontaneous emission and reversible trapping. In Figure 5.3, we measure the excited-state dynamics in SPs while varying the CdS shell thickness of the constituent QDs from 1 to 4 ML. Figure 5.3a shows the rate of red shift of the PL, *i.e.*, the energy red shift per unit of time ($|dE/dt|$) over the first few nanoseconds after excitation. We observe a lower rate of red shift as the shell thickness increases. Indeed, because of the strong distance dependence of FRET, we expect a lower exciton-diffusion rate¹⁵ for increasing shell thickness. Also, the value of the red-shift ΔE_r at the moment when it reaches its maximum (around 20 ns; highlighted in Figure 5.2b) decreases with increasing shell thickness (Figure 5.3b). This is a necessary consequence of the decreasing rate of red shift with increasing shell thickness. Delayed emission becomes the dominant emission component at approximately 20 ns for all shell thicknesses (Figure 5.9), so the final red-shift ΔE_r at that moment scales with the rate of red-shift $|dE/dt|$. This trend still holds if we normalize the maximum red shift to the ensemble line width of the QD batch (Table 1), indicating that slight differences in the ensemble line widths of our QD batches (Table 2) do not influence the trends observed. Interestingly, the shell thickness also affects the dynamics at times beyond 20 ns in the time regime of delayed emission due to the release of previously trapped charge carriers. The PL blue-shift ΔE_b between 20 and 200 ns shows a slight decrease with increasing shell thickness (Figure 5.3c). We can understand this if we realize that the blue shift reflects the energy difference between excitons that were protected from FRET by temporary storage and excitons that were free to diffuse. If diffusion is slower because of thicker shells, then the difference that temporary storage can make to the PL color is also lower.

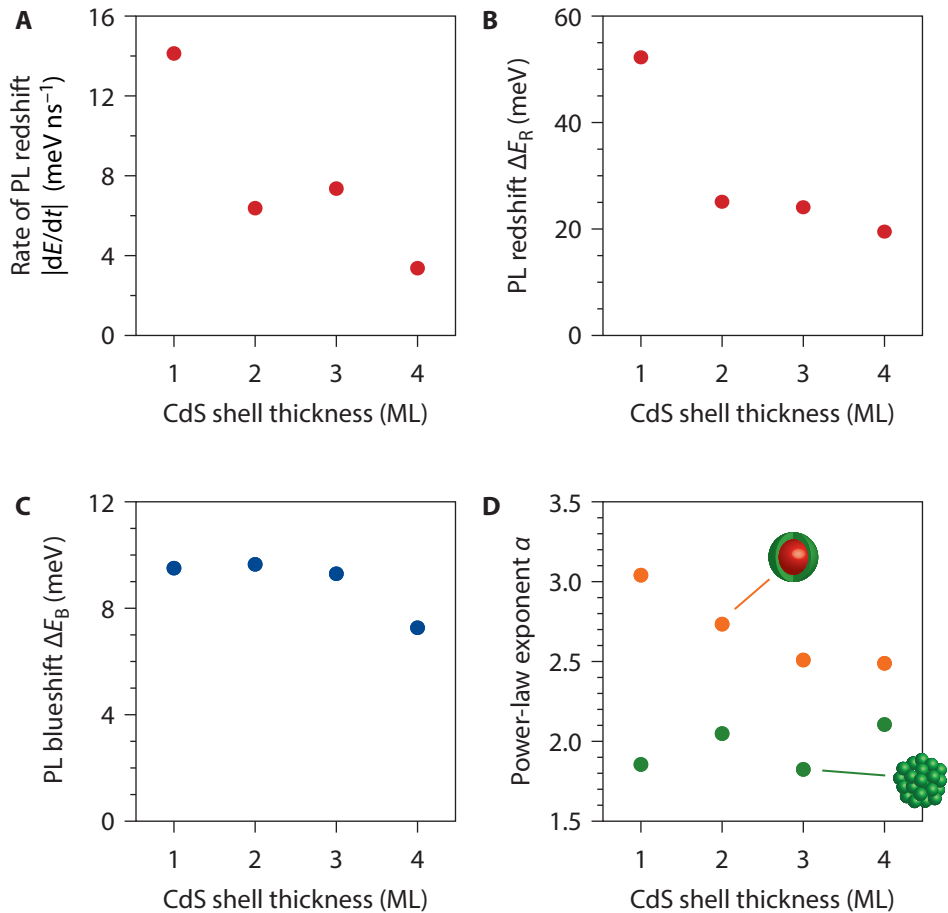


Figure 5.3 • Analysis of the spectral dynamics as a function of shell thickness. (a) The rate of PL red shift directly after the photoexcitation of SPs as a function of the shell thickness of the constituent QDs. (b) The maximum extent of the PL red shift compared to the SP emission spectrum directly after excitation (indicated ΔE_R in Figure 2b) as a function of shell thickness. (c) The PL blue shift observed from the moment that delayed emission takes over (ΔE_B in Figure 2b) as a function of shell thickness. (d) Power-law exponent α of the delayed emission dynamics for QDs dispersed in toluene (orange) and QDs assembled in SPs (green) as a function of shell thickness.

Finally, we observe that the power-law exponent α (describing the delayed emission dynamics $I \propto t^{-\alpha}$) is affected by assembly of the QDs in SPs as well as by the shell thickness of the QDs (Figure 5.3d). More specifically, α is always larger for QDs freely dispersed in solution (orange) than for QDs in SPs (green). This corresponds to a wider distribution of storage times for QDs in SPs. In other words, it takes longer for the exciton state to be restored after charge-carrier trapping in SPs compared to individual QDs. Additionally, the delayed emission dynamics are more affected by QD assembly for thin-shell QDs than for those with thick shells.

We can speculate about two possible origins for the slowing of exciton restoration when

5

QDs are assembled into SPs. First, the dielectric surrounding of QDs is different in SPs than when they are free in dispersion. In SPs, trapped charges on the surface of a QD may be stabilized by polarization of the surrounding semiconductor particles (dielectric constant of $\epsilon \approx 10$) or water molecules ($\epsilon = 80$) more effectively than individual QDs that are surrounded by toluene molecules ($\epsilon = 2.4$). The improved stabilization of trapped charges will lead to a slowing of their release. This can affect the statistics of delayed emission, making late emission more likely and therefore decreasing the power-law slope α . Previous studies have indeed reported influences of the polarizability of the surrounding on the trapping dynamics of QDs.²⁴ Second, although exciton hopping by FRET is inhibited in the charge-separated state, charge hopping may still be possible. Exciton hopping relies on near-field electromagnetic coupling between QDs, which scales with the oscillator strength of the excited QD.³³ Charge hopping, however, is a single-carrier tunneling process, which depends, for example, on the conductivity of ligands³⁴ and on the Auger excitation of carriers.³⁵ Even if one charge carrier is (reversibly) trapped, the other carrier can still hop from QD to QD. This could affect the dynamics of delayed emission in a QD solid. For recombination of photoexcited charges, not only must the trapped charge be released but the hopping charge must also return to the QD from which it came. This effect may contribute to a broadening of the distribution of exciton restoration times, consistent with what we observe by comparing the dynamics in SPs with those in individual QDs (Figure 5.3d).

Based on our experimental results, we set up a simple kinetic Monte Carlo model to understand the competition between spontaneous emission, FRET, and reversible trapping in more detail. We simulate the dynamics in a QD solid upon pulsed excitation. The processes included in the model are schematically depicted in Figure 5.4a for a pair of one small (green sphere) and one large QD (red sphere). The simulations are, however, done on a QD solid consisting of 864 QDs with a distribution of sizes. Following the photoexcitation of a small QD, it enters the excited state (state 2) and may directly emit (green arrow). The small QD may also transfer its energy to a larger QD by FRET (state 3), exciting the large QD and bringing the small QD back to its ground state, which eventually leads to red-shifted emission (red arrow). Alternatively, a charge carrier may be trapped, resulting in a stored-exciton state with zero oscillator strength (state 4). The trapped charge is eventually released, restoring the exciton state in the small QD, after which it can again take one of the three possible pathways (*viz.*, spontaneous emission, energy transfer, or charge-carrier trapping). In practice, the rate of temporary charge-carrier trapping may vary among the QDs in the sample, trapping may occur not only from the emitting exciton state but also from hot-carrier states,^{36,37} or some QDs in the ensemble may exhibit non-radiative recombination. We make some simplifying assumptions for our Monte Carlo model: we assign the same radiative decay rate and the same rate of temporary charge-carrier trapping to all QDs, we do not consider hot-carrier trapping,²¹ and we do not include non-radiative recombination pathways. In this way, our model remains basic yet captures the relevant physics of the competition between reversible trapping, FRET, and spontaneous emission. More details of the model can be found in the caption of Figure 5.4a and in the Methods section.

The Monte Carlo model reproduces the red shift of PL on the first tens of nanoseconds fol-

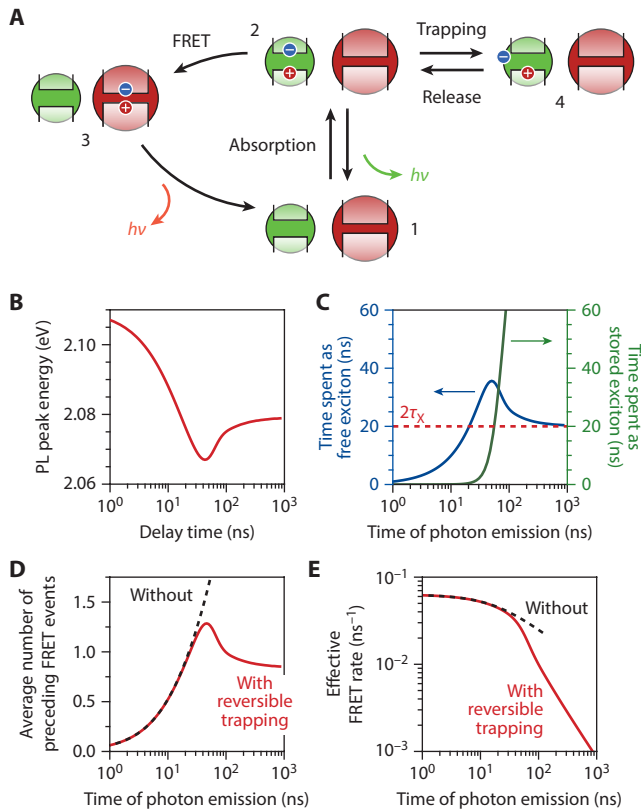


Figure 5.4 • Kinetic Monte Carlo simulations of the excited-state dynamics in a QD solid. (a) The excited-state pathways in a QD solid considered in our model. The size inhomogeneity in a QD solid is depicted as a pair of one smaller and one bigger QD. Absorption of a photon brings the system from its ground state (state 1) into a “free-exciton” state (state 2), in which both charge carriers occupy a quantum-confined energy level. State 2 can relax back to the ground state by spontaneous emission (green arrow), the excited QD can transfer its energy to a larger neighbor by means of FRET (state 3), or one charge carrier can be trapped temporarily (state 4). State 3 may then relax by the emission of a lower-energy photon (red arrow), make a further FRET step (not depicted), or undergo temporary charge-carrier trapping (not depicted), *etc.* From the “stored-exciton” state (state 4), the free exciton is restored after some time by charge carrier release. More details of the model and the rates we put in are provided in the Methods section. (b) The simulated shifts in PL peak energy from a QD solid as a function of delay time after photoexcitation. (c) For photons emitted at time t after excitation, we track how much preceding time was spent as a free exciton (state 2 or 3 in panel a; blue) and how much time as a stored exciton (state 4; green). The dashed red line lies at twice the exciton lifetime. (d) For photons emitted at time t after excitation, we plot the number of FRET events N_{FRET} that preceded emission (red line). The black dashed line is a reference simulation without temporary trapping. (e) For photons emitted at time t after excitation, we plot the effective FRET rate $k_{\text{FRET}}^{\text{eff}} \equiv N_{\text{FRET}}/t$ during the preceding time. The black dashed line is a reference simulation without temporary trapping.

lowed by a blue shift at later times (compare Figure 5.4b to Figure 5.2b). As in the experiment, the transition from a red shift to a blue shift coincides with the moment that delayed emission becomes the dominant contribution to the PL. This confirms our interpretation

that the spectral dynamics in SPs are a manifestation of the intricate competition between spontaneous emission, FRET, and reversible trapping.

In our Monte Carlo model, we can follow the fate of each simulated exciton in the SPs as it undergoes FRET, trapping, release, and eventually recombination by spontaneous emission. This yields insights into the competition between the different excited-state processes that are not obtainable from the experiment alone. More specifically, for the photons emitted at delay time t after photoexcitation, we can track all the steps (FRET, reversible trapping, or both) that preceded emission.

Figure 5.4c shows, for charge carriers recombining by photon emission at time t , how much preceding time they spent as “free exciton” (with both carriers in the quantum-confined levels of a QDs; blue) and how much was “stored exciton” (with one carrier trapped; green). The transition from prompt emission to delayed emission is clearly visible as the moment at $t = 30\text{--}100$ ns when the time spent as stored exciton increases from none (prompt emission) to tens of nanoseconds and further (delayed emission). Across the transition from prompt to delayed emission the time spent as free exciton first peaks at 36 ns and then levels off to 20 ns. The value of 20 ns equals twice the lifetime, τ_x , of the free-exciton state in our simulation (red dashed line). We can understand why the curve levels off to this value by considering the pathway to delayed emission, in which the system goes from the free exciton (state 2 in Figure 5.4a) to a stored-exciton state (state 4) back to the free-exciton state (state 2) that then decays to the ground state (state 1). The simulation also allows for the possibility of multiple reversible-trapping events, but these are relatively rare until very long delay times ($t \sim \mu\text{s}$) for the trapping probabilities relevant to our system. Each time the system is in the free-exciton state, it stays there for on average $\tau_x = 10$ ns. Overall the system is therefore in the free-exciton state for on average twice the exciton lifetime $2\tau_x = 20$ ns. Hence, a delayed photon emitted at time t originates from charge carriers that were free for on average a period $2\tau_x$ and stored for a period $t - 2\tau_x$.

In Figure 5.4d, we plot the average number of FRET events preceding emission at time t . The number of FRET events (red) peaks at 1.3 at $t \approx 40$ ns and then levels off to a value of 0.9. Clearly, the number of FRET events (Figure 5.4d) scales with the time that the system spends as free exciton (Figure 5.4c). This simply reflects that the longer the exciton is free, the more hops it makes from QD to QD. In a reference simulation without reversible trapping (black dashed line), the number of FRET events keeps increasing with time. This continuous increase is slowed and even reversed by reversible trapping (red) because this limits the time spent as free excitons. To quantify the inhibition of FRET by reversible charge-carrier trapping, we define the “effective FRET rate” that preceded emission at time t (Figure 5.4e), *i.e.*, the number of FRET events per unit of time preceding emission. The effective FRET rate slowly decreases with time t over the first 40 ns in simulations both with (red) and without (dashed line) reversible trapping. This is the result of energy disorder in a QD solid, which slows FRET as the exciton population redshifts.¹⁵ In addition, a pronounced effect of temporary exciton storage is observable in the delayed-emission regime ($t > 40$ ns): the effective FRET rate in the simulation with reversible trapping rapidly drops to a few percent of the initial rate. Hence, temporary charge-carrier trapping can slow FRET in QD solids considerably. It is this slowing of the effective FRET rate that

causes the PL blue shift observed on the time scales associated with delayed emission.

5.3 Conclusions

In summary, we have studied the PL dynamics of QDs assembled in supraparticles on long time scales up to a microsecond. Exciton storage by reversible charge-carrier trapping is found to slow the effective rate of FRET in this system. More specifically, storage temporarily “freezes” the exciton in a state with zero oscillator strength, in which it cannot hop from QD to QD by means of FRET. For PL applications, this manifests as an effective PL blue shift at tens of nanoseconds after excitation when temporarily trapped charges are released. More generally, our work highlights that temporary charge-carrier trapping significantly affects the relaxation pathways of excited QDs. This process should be taken into account to understand the excited-state dynamics of QDs, especially when, in QD solids, it competes with various other processes such as FRET or charge extraction.

5.4 Methods

Chemicals

Sodium dodecyl sulfate (SDS, $\geq 98.5\%$), dextran from *Leuconostoc mesenteroides* ($M_w = 670000$ g/mol), trioctylphosphine oxide (TOPO, 90%), octadecylamine (ODA, 90%), oleic acid (OA, 90%), 1-octadecene (ODE, 90%), cadmium acetate dihydrate ($\text{Cd}(\text{Ac})_2 \cdot 2\text{H}_2\text{O}$, 98%), trioctylphosphine (TOP, 90%), sulfur (S, 99.998%), ethanol (EtOH, 99.8%), 1-butanol anhydrous (BuOH, 99.8%), methanol (MeOH, anhydrous, 99.8%), and toluene (anhydrous, 99.8%) were all purchased from Sigma Aldrich and used as received. Se powder (Se, 200 mesh, 99.999%) was purchased from Brunschwig Chemie.

Synthesis of CdSe QDs

Precursor synthesis. For the Cd-precursor, 1.28 g $\text{Cd}(\text{Ac})_2 \cdot 2\text{H}_2\text{O}$, 51.84 g ODE and 7.36 g OA were mixed and degassed at 150°C for two hours to form $\text{Cd}(\text{OA})_2$ with 0.1 M concentration. For the Se-precursor, 4.25 g Se powder, 22.5 g TOP and 35.7 g ODE (previously degassed) were heated to 50°C and stirred until complete dissolution of the Se powder.

QD synthesis

The synthesis of CdSe QDs was done following a procedure from literature.³⁸ 3.2 g ODA, 1.11 g TOPO (previously degassed) and 5.2 g of Se-precursor were placed in a 100 mL three-neck flask. The content of the flask was heated to 300°C under nitrogen. At 300°C, 4.9 g Cd-precursor was rapidly injected. The temperature was decreased to 280°C and the solution was kept at this temperature for 7 minutes while stirring. Then, the reaction was rapidly cooled down to room temperature by flowing compressed air on the outside of the flask, after which 10 mL of toluene was added into the flask. The color of the solution went from yellow to orange and then to red within one minute. The solution was then washed by addition of a mixture of MeOH and BuOH (1:3) and centrifuged at 2500 rpm for 10 minutes. After centrifugation the supernatant was discarded and the precipitate was redispersed in 6 mL of toluene. The resulting QD solution was red and clear. It was stored in a glovebox under nitrogen atmosphere.

Growth of CdS shells

Precursor synthesis

To obtain a Cd-precursor solution at 0.1 M concentration, 5.5 g $\text{Cd}(\text{Ac})_2 \cdot 2\text{H}_2\text{O}$, 54.15 g OA, and 216 mL ODE were mixed in a three-neck flask and then kept at 120°C under vacuum for at least two hours. The S-precursor solution at 0.1 M concentration was prepared by putting 0.320 g S and 100 mL ODE in a three-neck flask, heating the mixture to 180°C and keeping it at this temperature until the S was completely dissolved.

Shell growth

The growth of the CdS shell was performed using the “Successive ionic layer adsorption and reaction” (SILAR) method, following the procedure from ref³⁹. Four different samples of core/shell NCs were prepared, with one, two, three, and four monolayers of CdS. For each of these, the procedure started with 10–7 mol of CdSe QDs

in 5 g ODE and 1.5 g ODA in a three-neck flask in a glovebox under nitrogen atmosphere. First, the solution was heated to 150°C and kept at this temperature for one hour in order to evaporate the toluene. Then the temperature was raised to 240°C. The growth of the shell was performed by dropwise addition of precursors. The amount of precursor necessary for the addition of a monolayer increases as the QDs grow, since this increases their surface area. The procedure for each monolayer growth was to add Cd-precursor, wait for 10 minutes, add S-precursor, and wait for another 15 min. These four steps were repeated depending on the number of monolayers desired. The amount of precursor solution used for each monolayer is listed in the table below.

Monolayer #	Precursor added (mL)	
	S	Cd
1	0.199	0.199
2	0.244	0.244
3	0.293	0.293
4	0.346	0.346

After the synthesis the solutions were washed using a 1:3 mixture of MeOH and BuOH, and centrifuged at 2750 rpm for 10 minutes. The supernatant was discarded and the precipitate was redispersed in 6 mL of toluene. The resulting CdSe/CdS QD solutions were red and clear.

Assembly of QDs into SPs

The assembly of QDs into SPs was performed in open air following a procedure from literature.²⁶ First of all, a solution of QDs in cyclohexane was prepared with a QD concentration of around 10 mg/mL. It was emulsified with 10 mL milli-Q water containing 60 mg of sodiumdodecylsulfate (SDS) surfactant and 0.4 g of dextran. The emulsification was performed following a methodology developed by the Bibette group that uses high shear rates generated in a Couette shear cell.⁴⁰ Dextran acts as steric stabilizer, but also serves to bring the solution in the visco-elastic regime necessary to create relatively monodisperse droplets under high shear rates.⁴¹ The emulsification process is important in determining the size of the droplets. In combination with the initial volume fraction of QDs, this sets the mean size and size distribution of the resulting SPs after evaporation of the oil phase. After emulsification, the emulsion was collected and stirred for 6 hours at 68°C in order to evaporate the cyclohexane. The resulting dispersion was centrifuged at 3000 rpm for 10 min, and the sedimented SPs were finally redispersed in distilled water. The resulting SPs have a diameter of 185 ± 40 nm for 1 ML core/shell QDs, 202 ± 89 nm for 2 ML QDs, 297 ± 131 nm for 3 ML QDs and 264 ± 57 nm for 4 ML QDs. The SPs have a nearly spherical shape.

Optical measurements

For optical measurements the individual QDs were dispersed in toluene, while the SPs of QDs were dispersed in deionized water. During measurements on SPs, continuously stirring the dispersion prevented sedimentation and photocharging in the focal volume. (Time-resolved) PL emission measurements were performed using an Edinburgh Instruments F900 spectrometer exciting at 375 nm with an Edinburgh EPL-375 picosecond pulsed diode laser. Spectra as a function of time delay after excitation were reconstructed from a large set of PL decay traces measured at energies covering the entire emission spectrum. Absorption was measured with a PerkinElmer lambda 950 spectrophotometer.

Analysis of time-resolved emission dynamics

The peak positions E_0 of the time-resolved emission spectra (Figures 1c, 1d, 2a, 2b in the main text) were determined by fitting the PL spectrum on energy scale to a two-sided Gaussian fit function:

$$I(E) = \begin{cases} Ae^{-\frac{(E-E_0)^2}{2\sigma_1^2}} & E < E_0 \\ Ae^{-\frac{(E-E_0)^2}{2\sigma_2^2}} & E > E_0 \end{cases}$$

where A is the amplitude, E_0 is the peak energy, σ_1 is the width on the red side, and σ_2 is the width on the blue side of the spectrum. The spectra were reconstructed from a set of PL decay traces measured at intervals of 1 nm and with a time resolution of 250 ps. At long delay times we rebinned the time axis to obtain a better signal-to-

noise ratio.

Electron microscopy

HAADF-STEM images, SE-STEM images and TEM images were acquired using a FEI Osiris and a FEI Tecnai electron microscopes operated at 200 kV.

Kinetic Monte Carlo simulations

We used kinetic Monte Carlo simulations to study the competition between spontaneous emission, FRET, and reversible charge carrier trapping. To simulate a QD solid, we constructed a geometry wherein the QDs are arranged in a face-centered cubic (fcc) crystal lattice. The QDs are placed in a cubic simulation box with periodic boundary conditions. To simulate inhomogeneous spectral broadening, each QD i is assigned a PL peak energy $E_{\text{PL},i}$ from a Gaussian distribution with mean $\langle E_{\text{PL}} \rangle$ and standard deviation σ_{inh} . The corresponding $1S_{3/2}-1S_e$ absorption peak energy of QD i is at $E_{\text{abs},i} = E_{\text{PL},i} + \Delta E_S$, where ΔE_S is the Stokes shift, which we assume equal for all QDs in the simulation. All QDs have an equal radiative decay rate k_{rad} and charge carrier trapping rate k_{T} . The rate of FRET from QD i to QD j depends on their separation r_{ij} and the normalized spectral overlap integral J_{ij} as

$$k_{\text{FRET},ij} = k_{\text{FRET},0} \left(\frac{r_{ij}}{r_{\text{NN}}} \right)^{-6} J_{ij}$$

where $k_{\text{FRET},0}$ is the FRET rate for a reference QD pair ij at nearest-neighbor distance r_{NN} and with perfect spectral overlap. Perfect spectral overlap is the situation where $E_{\text{abs},j} = E_{\text{PL},i}$, *i.e.* the emission of donor QD i overlaps exactly with the absorption of QD j . For any other pair ij the normalized spectral overlap is

$$J_{ij} = \begin{cases} \exp \left[-\frac{1}{4} \left(\frac{E_{\text{PL},i} - E_{\text{abs},j}}{\sigma_{\text{1QD}}} \right)^2 \right] & ; E_{\text{PL},i} > E_{\text{abs},j} \\ 1 & ; E_{\text{PL},i} \leq E_{\text{abs},j} \end{cases}$$

where σ_{1QD} is the linewidth of the single-QD $1S_{3/2}-1S_e$ PL and absorption peaks. Here we approximate that the normalized spectral overlap is always 1, *i.e.* perfect, if the emission energy of the donor i is higher than the absorption energy of acceptor j .

The fate of an excitation in the QD solid is simulated by initiating a free exciton on QD i . From this state, QD i can decay to the ground state by photon emission with rate k_{rad} , transfer its energy to any of the other QDs $\{j, k, \dots\}$ in the solid with rate $\{k_{\text{FRET},ij}, k_{\text{FRET},ik}, \dots\}$, or go into the 'stored-exciton' state by charge carrier trapping with rate k_{T} . The time between initial excitation and a next event is drawn from an exponential distribution with decay constant $k_{\text{tot}} = k_{\text{rad}} + k_{\text{T}} + \sum_j k_{\text{FRET},ij}$. The nature of the event (radiative decay, charge carrier trapping, or FRET to some QD j) is then chosen randomly, where the probability for a particular event to occur is proportional to the rate associated. In case of FRET to QD j , the system has three possible subsequent steps: radiative decay from QD j , a next FRET event to QDs $\{i, k, \dots\}$ or charge carrier trapping. This continues until radiative decay takes place from some QD in the solid. The simulation is then finished and we store the emission time and emission color of the emitted photon. If charge carrier trapping takes place on some QD i , the system is frozen in a state from which no FRET nor radiative decay can occur. The only possible process is restoration of the free-exciton state of QD i , which occurs after a time generated from a power-law distribution with exponent $-\alpha$ and minimum time t_{min} . After restoration, the free exciton on QD i has all the excited-state pathways available described before. See Figure 4a in the main text for a schematic illustration of the excited-state processes considered in the simulation.

For the results presented in the main text (Figure 4b–e), the simulations were performed in a box with a size of $6 \times 6 \times 6$ fcc unit cells. Each of the 864 QDs in the box were excited 9000 times (or 100000 times for the reference simulations without FRET; Figure 4d,e), after which the fate of the excitation was followed as described above. This procedure was repeated 350 times for different realizations of the QD solid, with different PL energies $E_{\text{PL},i}$ randomly assigned to each of the QDs for each realization. We used the following parameters for the results in the main text: $\langle E_{\text{PL}} \rangle = 2.11$ eV; $\sigma_{\text{inh}} = 43$ meV; $\Delta E_S = 43.2$ meV; $k_{\text{rad}} = 0.1$ ns $^{-1}$; $k_{\text{T}} = 0.0062$ ns $^{-1}$; $k_{\text{FRET},0} = 0.0091$ ns $^{-1}$; $\sigma_{\text{1QD}} = 23$ meV; $\alpha = 1.8$; $t_{\text{min}} = 17$ ns. The same qualitative trends, *e.g.* an initial PL redshift followed by a blueshift, were obtained for a wide range of parameter values.

References

1. Walter, P. *et al.* Early use of PbS nanotechnology for an ancient hair dyeing formula. *Nano Lett.* **6**, 2215–2219 (2006).
2. Murray, C. B., Norris, D. J. & Bawendi, M. G. Synthesis and characterization of nearly monodisperse CdE (E = sulfur, selenium, tellurium) semiconductor nanocrystallites. *J. Am. Chem. Soc.* **115**, 8706–8715 (1993).
3. Norris, D. J. & Bawendi, M. G. Measurement and assignment of the size-dependent optical spectrum in CdSe quantum dots. *Phys. Rev. B* **53**, 16338–16346 (1996).
4. Talapin, D. V., Lee, J. S., Kovalenko, M. V. & Shevchenko, E. V. Prospects of colloidal nanocrystals for electronic and optoelectronic applications. *Chem. Rev.* **110**, 389–458 (2010).
5. Shirasaki, Y., Supran, G. J., Bawendi, M. G. & Bulović, V. Emergence of colloidal quantum-dot light-emitting technologies. *Nat. Photonics* **7**, 13–23 (2013).
6. Sun, Q. *et al.* Bright, multicoloured light-emitting diodes based on quantum dots. *Nat. Photonics* **1**, 717–722 (2007).
7. Sukhovatkin, V., Hinds, S., Brzozowski, L. & Sargent, E. H. Colloidal Quantum-Dot Photodetectors Exploiting Multiexciton Generation. *Science* **324**, 1542–1544 (2009).
8. McDonald, S., Konstantatos, G. & Zhang, S. Solution-processed PbS quantum dot infrared photodetectors and photovoltaics. *Nat. Mater.* **4**, 138–42 (2005).
9. Konstantatos, G. *et al.* Ultrasensitive solution-cast quantum dot photodetectors. *Nature* **442**, 180–183 (2006).
10. Grivas, C. *et al.* Single-mode tunable laser emission in the single-exciton regime from colloidal nanocrystals. *Nat. Commun.* **4**, 1–9 (2013).
11. Klimov, V. I. *et al.* Optical Gain and Stimulated Emission in Nanocrystal Quantum Dots. *Science* **290**, 314–317 (2000).
12. Meinardi, F. *et al.* Large-area luminescent solar concentrators based on ‘Stokes-shift-engineered’ nanocrystals in a mass-polymerized PMMA matrix. *Nat. Photonics* **8**, 392–399 (2014).
13. Meinardi, F. *et al.* Highly efficient large-area colourless luminescent solar concentrators using heavy-metal-free colloidal quantum dots. *Nat. Nanotechnol.* **10**, 878–885 (2015).
14. Kagan, C., Murray, C., Nirmal, M. & Bawendi, M. G. Electronic energy transfer in CdSe quantum dot solids. *Phys. Rev. Lett.* **76**, 1517–1520 (1996).
15. Akselrod, G. M. *et al.* Subdiffusive Exciton Transport in Quantum Dot Solids. *Nano Lett.* **14**, 3556–3562 (2014).
16. Crooker, S. A., Hollingsworth, J. A., Tretiak, S. & Klimov, V. Spectrally resolved dynamics of energy transfer in quantum-dot assemblies: towards engineered energy flows in artificial materials. *Phys. Rev. Lett.* **89**, 186802 (2002).
17. Azzaro, M. S., Dodin, A., Zhang, D. Y., Willard, A. P. & Roberts, S. T. Exciton-Delocalizing Ligands Can Speed Energy Migration in Nanocrystal Solids. *Nano Lett.* **18**, 3259–3270 (2018).
18. Whitham, P. J. *et al.* Single-particle photoluminescence spectra, blinking, and delayed luminescence of colloidal CuInS₂ nanocrystals. *J. Phys. Chem. C* **120**, 17136–17142 (2016).
19. Marchioro, A. *et al.* Tunneling in the Delayed Luminescence of Colloidal CdSe,

- Cu⁺-Doped CdSe, and CuInS₂ Semiconductor Nanocrystals and Relationship to Blinking. *J. Phys. Chem. C* **120**, 27040–27049 (2016).
20. Rabouw, F. *et al.* Delayed Exciton Emission and Its Relation to Blinking in CdSe Quantum Dots. *Nano Lett.* **15**, 7718–7725 (2015).
 21. Rabouw, F. T. *et al.* Temporary Charge Carrier Separation Dominates the Photoluminescence Decay Dynamics of Colloidal CdSe Nanoplatelets. *Nano Lett.* **16**, 2047–2053 (2016).
 22. Sher, P. H. *et al.* Power law carrier dynamics in semiconductor nanocrystals at nanosecond timescales. *Appl. Phys. Lett.* **92**, 9–11 (2008).
 23. Marchioro, A. *et al.* Strong Dependence of Quantum-Dot Delayed Luminescence on Excitation Pulse Width. *J. Phys. Chem. Lett.* **8**, 3997–4003 (2017).
 24. Jones, M., Lo, S. S. & Scholes, G. D. Quantitative modeling of the role of surface traps in CdSe/CdS/ZnS nanocrystal photoluminescence decay dynamics. *Proc. Natl. Acad. Sci.* **106**, 3011–3016 (2009).
 25. Förster, T. Energiewanderung und Fluoreszenz. *Naturwissenschaften* **33**, 166–175 (1946).
 26. de Nijs, B. *et al.* Entropy-driven Formation of Large Icosahedral Colloidal Clusters by Spherical Confinement. *Nat. Mater.* **14**, 56–60 (2015).
 27. Vanmaekelbergh, D. *et al.* Shape-Dependent Multiexciton Emission and Whispering Gallery Modes in Supraparticles of CdSe / Multishell Quantum Dots. *ACS Nano* **9**, 3942–3950 (2015).
 28. Montanarella, F. *et al.* Composite Supraparticles with Tunable Light Emission. *ACS Nano* **11**, 9136–9142 (2017).
 29. Montanarella, F. *et al.* Crystallization of nanocrystals in spherical confinement probed by in-situ X-ray scattering. *Nano Lett.* **18**, 3675–3681 (2018).
 30. de Mello Donega, C. Synthesis and properties of colloidal heteronanocrystals. *Chem. Soc. Rev.* **40**, 1512–46 (2011).
 31. Cui, J. *et al.* Direct probe of spectral inhomogeneity reveals synthetic tunability of single-nanocrystal spectral linewidths. *Nat. Chem.* **5**, 602–6 (2013).
 32. Cui, J. *et al.* Evolution of the Single-Nanocrystal Photoluminescence Linewidth with Size and Shell: Implications for Exciton-Phonon Coupling and the Optimization of Spectral Linewidths. *Nano Lett.* **16**, 289–296 (2016).
 33. Henderson, B. & Imbusch, G. F. *Optical Spectroscopy of Inorganic Solids*. (Clarendon Press, 2006).
 34. Kovalenko, M. V, Scheele, M. & Talapin, D. V. Colloidal Nanocrystals with Molecular Metal Chalcogenide Surface Ligands. *Science* **324**, 1417–1421 (2009).
 35. Shabaev, A., Efros, A. L. & Efros, A. L. Dark and Photo-Conductivity in Ordered Array of Nanocrystals. *Nano Lett.* **13**, 5454–5461 (2013).
 36. McGuire, J. A. *et al.* Spectroscopic Signatures of Photocharging due to Hot-Carrier Transfer in Solutions of Semiconductor Nanocrystals under Low-Intensity Ultraviolet Excitation. *ACS Nano* **4**, 6087–6097 (2010).
 37. Galland, C. *et al.* Two types of luminescence blinking revealed by spectroelectrochemistry of single quantum dots. *Nature* **479**, 203–207 (2011).
 38. Qu, L., Peng, Z. & Peng, X. Alternative routes toward high quality CdSe nanocrystals. *Nano Lett.* **1**, 333–337 (2001).
 39. Li, J. J. *et al.* Large-Scale Synthesis of Nearly Monodisperse CdSe / CdS Core /

- Shell Nanocrystals Using Air-Stable Reagents via Successive Ion Layer Adsorption and Reaction. *J. Am. Chem. Soc.* **125**, 12567–12575 (2003).
40. Mabile, C. *et al.* Rheological and shearing conditions for the preparation of monodisperse emulsions. *Langmuir* **16**, 422–429 (2000).
 41. Mason, T. G. & Bibette, J. Shear Rupturing of Droplets in Complex Fluids. *Langmuir* **13**, 4600–4613 (1997).

Appendix

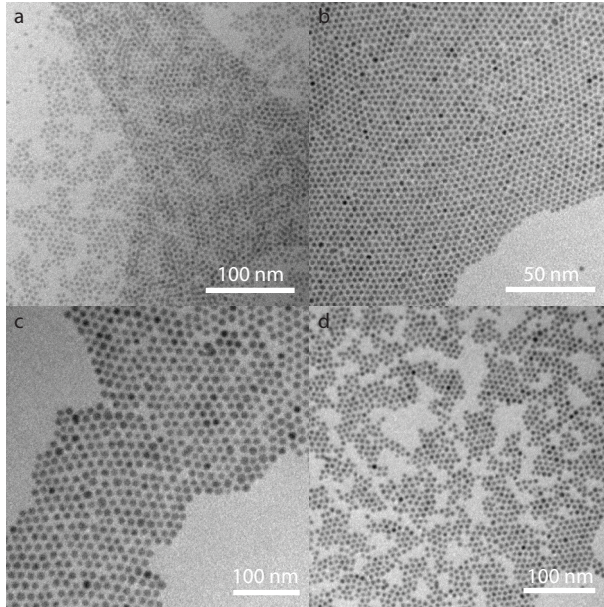


Figure 5.5 • Representative bright-field TEM images of the CdSe/CdS core/shell QDs. (a) CdSe/CdS 1 ML, (b) CdSe/CdS 2 ML, (c) CdSe/CdS 3 ML, and (d) CdSe/CdS 4 ML.

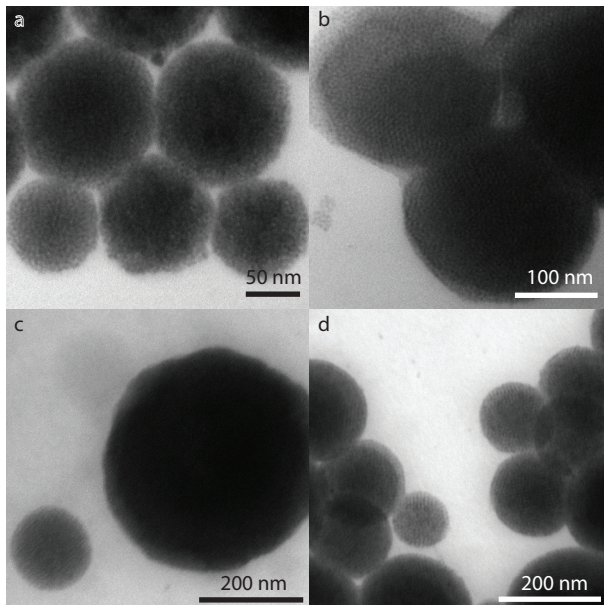


Figure 5.6 • Representative bright-field TEM images of the SPs made with (a) CdSe/CdS 1 ML, (b) CdSe/CdS 2 ML, (c) CdSe/CdS 3 ML, (d) CdSe/CdS 4 ML.

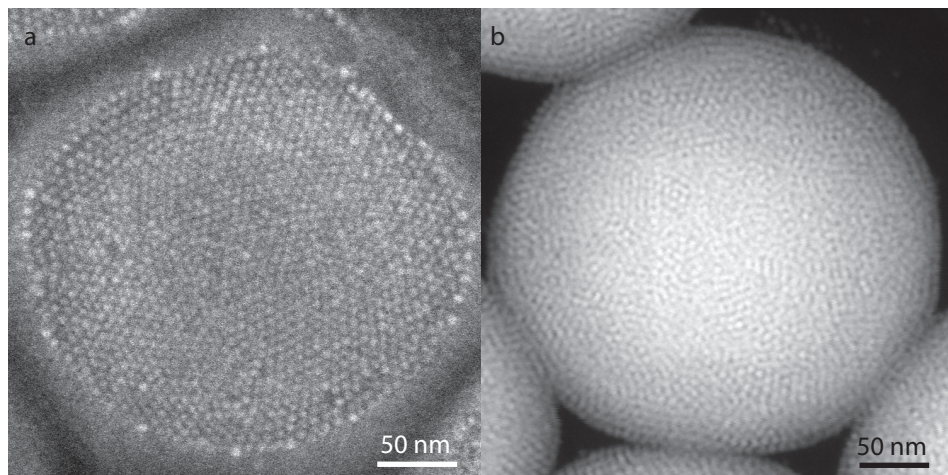


Figure 5.7 • Scanning Transmission Electron Microscopy (STEM) images of a SP made of CdSe/CdS 4 ML QDs in (a) Secondary Electron (SE) mode and (b) High Angle Annular Dark Field (HAADF) mode.

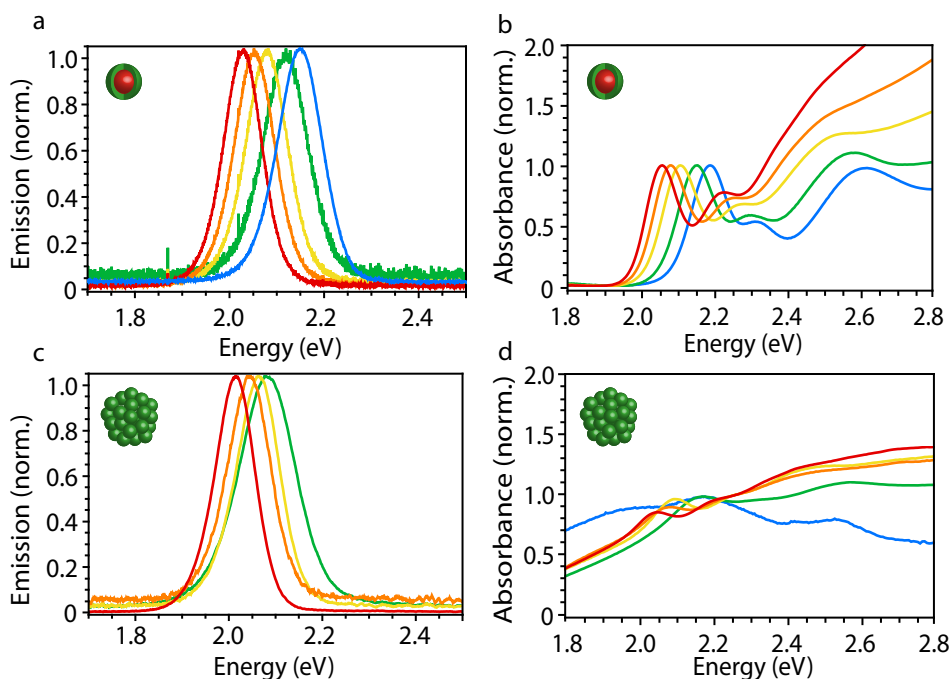


Figure 5.8 • Characterization of CdSe/CdS QDs in solution and in SPs. (a) Emission spectra of the CdSe cores (blue), CdSe/CdS 1 ML core/shell QDs (green), CdSe/CdS 2 ML (yellow), CdSe/CdS 3 ML (orange), and CdSe/CdS 4 ML (red) in toluene dispersion. **(b)** Absorption spectra of the different QDs samples, using the same color coding. **(c)** Emission spectra of SPs made of the QDs presented in panels a,b, using the same color coding. The emission from CdSe cores is quenched after SP formation, so no spectrum is presented for this sample. **(d)** Extinction spectra of SPs made of the same QDs presented in panels a,b, using the same color coding. The extinction spectra are dominated by strong scattering of the SPs.

Sample	Ensemble PL linewidth of QDs in dispersion (meV)	Maximum redshift (meV)	Maximum redshift normalized to ensemble PL linewidth
CdSe/CdS 1 ML	49	52	106%
CdSe/CdS 2 ML	46	25	54%
CdSe/CdS 3 ML	45	24	53%
CdSe/CdS 4 ML	42	19	45%

Table 1 • The PL redshift due to FRET in SPs compared to the ensemble linewidth of the QDs. We define the ensemble PL linewidth of the QDs in dispersion as the standard deviation of a Gaussian fit to their PL spectrum.

Sample	Emission Energy Peak (eV)	σ_{ens} (meV)	σ_{1QD} (meV) from ref ^{31,32}	σ_{inh} (meV)
Cores	2.14	49	27	41
QD 1 ML	2.11	49	23	43
QD 2 ML	2.08	46	23	40
QD 3 ML	2.05	45	25	37
QD 4 ML	2.03	42	28	31
SP 1 ML	2.08	62		
SP 2 ML	2.06	49		
SP 3 ML	2.04	48		
SP 4 ML	2.01	44		

Table 2 • Contributions to the ensemble emission linewidths from the intrinsic single-particle linewidth and from ensemble broadening. The ensemble emission spectrum in dispersion is a convolution of the single-QD spectrum and the inhomogeneous distribution of peak energies due to size dispersion. Approximating all distributions as Gaussian, the ensemble linewidth σ_{ens} is related to the single-QD linewidth σ_{1QD} and the standard deviation of the peak energies σ_{inh} as $\sigma_{\text{ens}}^2 = \sigma_{\text{1QD}}^2 + \sigma_{\text{inh}}^2$. We measure the ensemble linewidths, estimate the single-QD linewidths from a literature comparison,^{31,32} and then calculate the inhomogeneous broadening. The full width at half maximum (FWHM) mentioned in the main text is related to the ensemble emission linewidth as $\text{FWHM} = 2.35\sigma_{\text{ens}}$. This analysis cannot be done on the spectra from SPs, because their spectra are not only broadened (see table) because of the QD size distribution but are also affected by FRET.

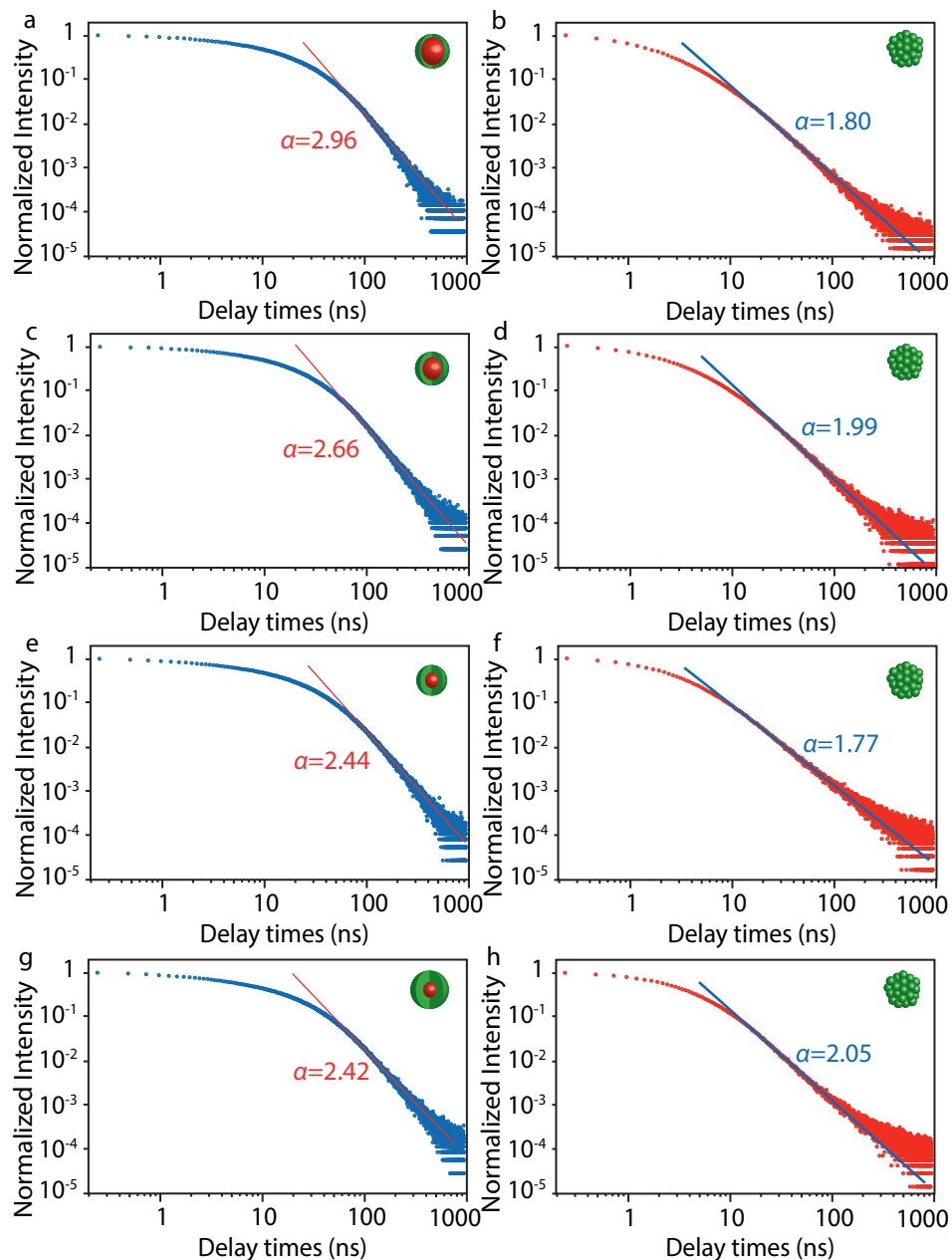


Figure 5.9 • Decay traces of QDs plotted on a double logarithmic scale for (a) CdSe/CdS 1 ML dispersed in toluene and (b) assembled in supraparticles, for (c) CdSe/CdS 2 ML dispersed in solution and (d) assembled in supraparticles, for (e) CdSe/CdS 3 ML dispersed in solution and (f) assembled in supraparticles, and (g) CdSe/CdS 4 ML dispersed in solution and (h) assembled in supraparticles.

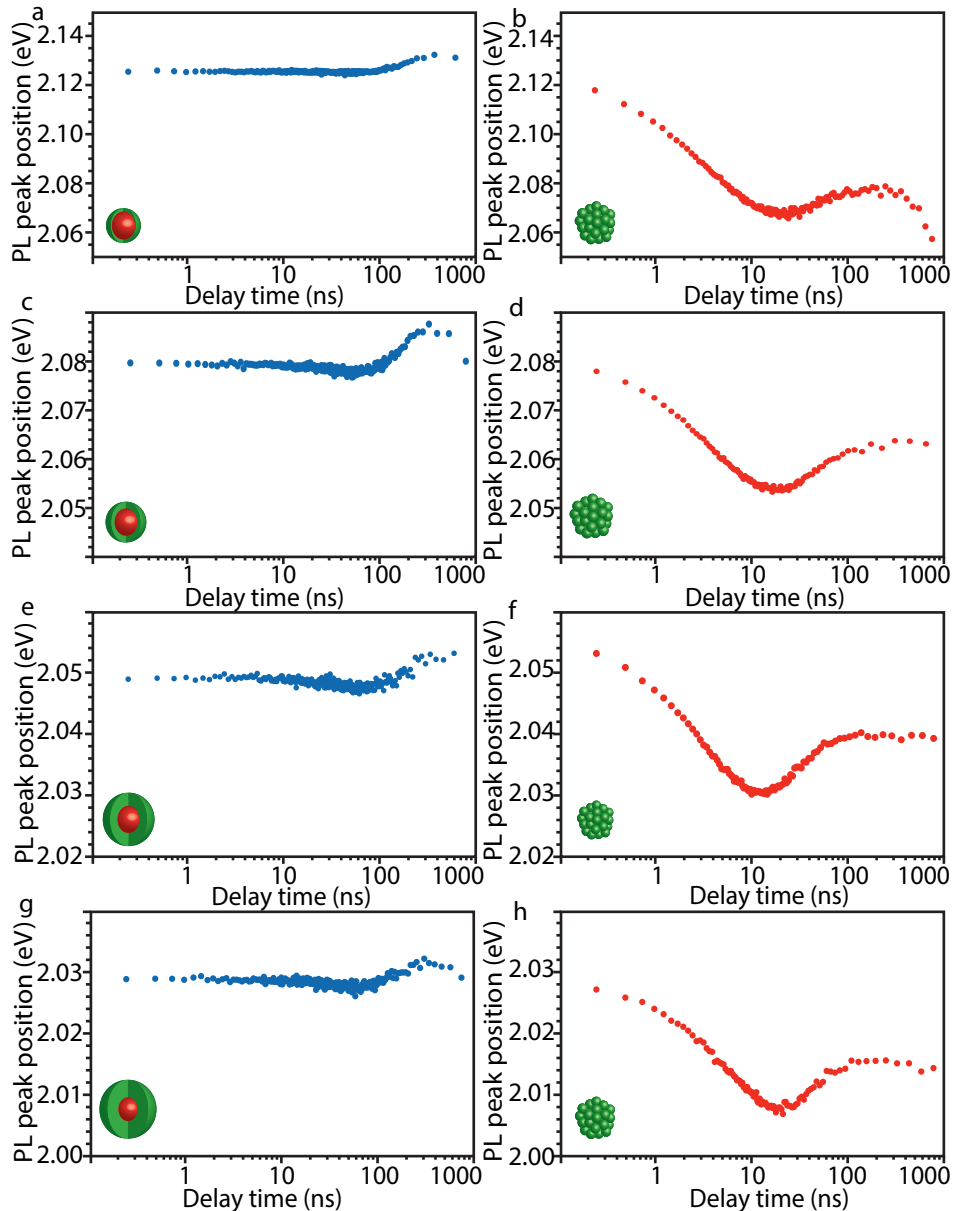


Figure 5.10 • Time-resolved PL emission of CdSe/CdS QDs in solution and assembled in SPs for different shell thicknesses. Emission energy of the CdSe/CdS 1 ML QDs (a) dispersed in solution or (b) assembled in SPs as a function of delay time after the excitation pulse, as obtained from two-sided Gaussian fits to the emission spectra. (c, d) Same, but for CdSe/CdS 2 ML QDs. (e, f) Same, but for CdSe/CdS 3 ML QDs. (g, h) Same but for CdSe/CdS 4 ML QDs.

Chapter 6

Composite supraparticles with tunable light emission

Abstract

Robust luminophores emitting light with broadly tunable colors are desirable in many applications such as light-emitting diode (LED)-based lighting, displays, integrated optoelectronics and biology. Nanocrystalline quantum dots with multicolor emission, from core- and shell-localized excitons, as well as solid layers of mixed quantum dots that emit different colors have been proposed. Here, we report on colloidal supraparticles that are composed of three types of Cd(Se,ZnS) core/(Cd,Zn)S shell nanocrystals with emission in the red, green, and blue. The emission of the supraparticles can be varied from pure to composite colors over the entire visible region and fine-tuned into variable shades of white light by mixing the nanocrystals in controlled proportions. Our approach results in supraparticles with sizes spanning the colloidal domain and beyond that combine versatility and processability with a broad, stable, and tunable emission, promising applications in lighting devices and biological research.

Based on: Composite Supraparticles with Tunable Light Emission. Federico Montanarella, Thomas Altantzis, Daniele Zanaga, Freddy T. Rabouw, Sara Bals, Patrick Baesjou, Daniel Vanmaekelbergh and Alfons van Blaaderen

ACS Nano, **11** (9), 9136–9142, (2017)

«The most exciting phrase to hear in science, the one that heralds new discoveries, is not 'Eureka!' but 'That's funny...'»

(Isaac Asimov)

6.1 Introduction

Even after more than two decades of extensive research, the optical properties of colloidal semiconductor nanocrystals, also known as quantum dots (QDs),¹ continue to intrigue researchers in nanophotonics, materials science and biology. Compared to solid-state QDs, colloidal QDs have a smaller and more easily tunable size.² This means that, due to strong exciton confinement, the light emission is tunable over a wide wavelength range in the visible or near-IR. Moreover, epitaxial engineering in core–shell systems has advanced remarkably over the past decade. This resulted in photochemically stable QDs with photoluminescence (PL) quantum yield close to unity.^{3,4} Furthermore, the control over epitaxial core–shell synthesis enabled the community to explore new degrees of freedom brought by engineering of the exciton wave functions,⁵ resulting in reduced Auger recombination,^{6–8} brighter multiexciton emission, and lower lasing thresholds.^{9–11} There is no doubt that following these recent advances, colloidal QDs will be used in a wide variety of applications, ranging from biological research^{12–14} to luminescent light concentrators^{15–17} and displays.¹⁸

Nowadays, two of the most important applications of colloidal QDs are their use as spectral conversion phosphors in light-emitting diodes (LEDs) and in (the backlight of) liquid crystal (LC) displays. In LEDs aimed at general lighting applications, the main role of QDs is to partially convert the primary blue light from the LEDs into multicolored light, with a spectrum matching human needs. In LED technology, where a high power efficiency is paramount, QDs have shown to be valuable for two different reasons: (i) they have a high quantum yield, and (ii) they are narrow band emitters. When QDs are used as a red phosphor instead of traditional wide-band red emitters, the red emission of an LED lamp is possible without losing photons in the near-IR, thereby significantly boosting the power efficacy (lumen/watt) of the lamp. Additionally, by using mixtures of differently colored QDs, it is relatively easy to achieve a high color rendering index lamp (CRI > 90), compared to traditional phosphors. Regarding display technology, QDs have shown to be valuable for their size-dependent tunable, narrow-band emission, which enables a strong matching of the backlight emission with the color filters of the display, thereby enhancing brightness and color saturation. In displays, QDs are already applied commercially. In order to strengthen these properties and enhance the suitability of QDs for industrial applications, especially for white light emission, several approaches have been proposed: QDs doped with metal ions,^{19,20} ultrasmall CdSe QDs,^{21,22} or QDs that show a relatively broad spectrum due to multiexciton emission²³ or shell emission.²⁴ All of these materials show only partially tunable emission spectra. Moreover, the spectra change with the intensity of the excitation, thus hampering several applications. A simple approach would be to mix three types of colloidal semiconductor QDs with emission in the red, green, and blue, respectively. In this respect, attempts based on mixed thin films of QDs have been reported.²⁵

Here, we report an approach that results in spherical supraparticles (SPs) that are composed of QDs emitting in the red, green, and blue. By controlling the ratios of QDs per SP, we can easily and rationally tune the spectrum of the SPs, and the emission spectrum is independent of the excitation intensity in a wide range. The SPs are charge- and sterically stabilized colloids themselves and can be dispersed in many industrially relevant polar

solvents, including water. In addition, their much larger size as compared to individual QDs also makes them easier to process in an industrial setting. Our work presents a platform for easily processable colloidal particles with a bright and stable (non-blinking) emission of pure or composite color, tunable in the entire visible range. Such a platform holds promise for displays as well as optoelectrical and biological applications.

6.2 Results and Discussion

6.2.1 Synthesis and composition of the tunable emitting SPs

The first step in the realization of SPs is to synthesize the constituent QDs. For this, we adapted existing protocols for stable red, green, and blue emitting Cd(Se,ZnS) core/(Cd,Zn)S shell QDs (Figure 6.1) (see the Methods section for further information).

Our general approach for the self-assembly of the SPs is based on the drying of an oil-in-water emulsion at elevated temperatures (68 °C) as described previously^{26,27} (details given in the Methods section). In Figure 6.6 the synthesis procedure is schematically presented. The emulsification is performed through a methodology developed by the Bibette group that uses high shear rates generated in a Couette shear cell²⁸ combined with the viscoelasticity of a concentrated emulsion; this leads to fairly monodisperse breakup of the drop-

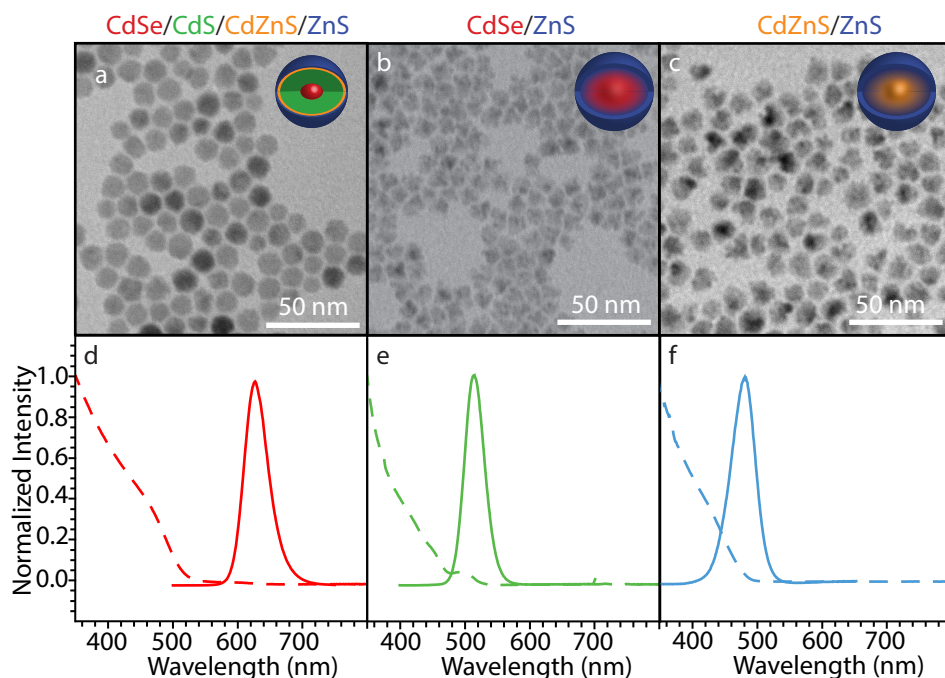


Figure 6.1 • TEM images and optical properties of the original QDs. (a–c) Representative transmission electron micrographs of (a) the red emitting QDs (diameter: 10.3 ± 1.0 nm), (b) the green emitting QDs (diameter: 11.0 ± 1.1 nm), and (c) the blue emitting QDs (diameter: 10.5 ± 1.3 nm). Insets are models of the QDs. (d–f) Absorption (dashed lines) and emission (solid lines) spectra of three different populations of QDs used for the self-assembly.

lets. In this manner, SPs with a precise size can be produced in a size range between 100 nm and several micrometers (Figure 6.7).

The three types of QDs that are incorporated in the SP are of similar size, and they have the same inorganic outer shell (ZnS) and organic ligands (oleic acid). However, the sizes are different enough that the effective polydispersity of the mixture is above 10%, which should prevent crystallization of the QDs into a long-range ordered superstructure. We therefore expect that the three types of QDs will be randomly packed and homogeneously distributed in the SPs in proportion to their concentration in the precursor suspension of mixed QDs.

6.2.2 Structural characterization of the SPs

The surface structure of the as-prepared SPs can be studied by detection of secondary electrons (SE) in a scanning transmission electron microscope (STEM) (Figures 6.2a and 6.8). To investigate the inner structure of the SPs, high-angle annular dark-field scanning transmission electron microscopy (HAADF-STEM) is combined with electron tomogra-

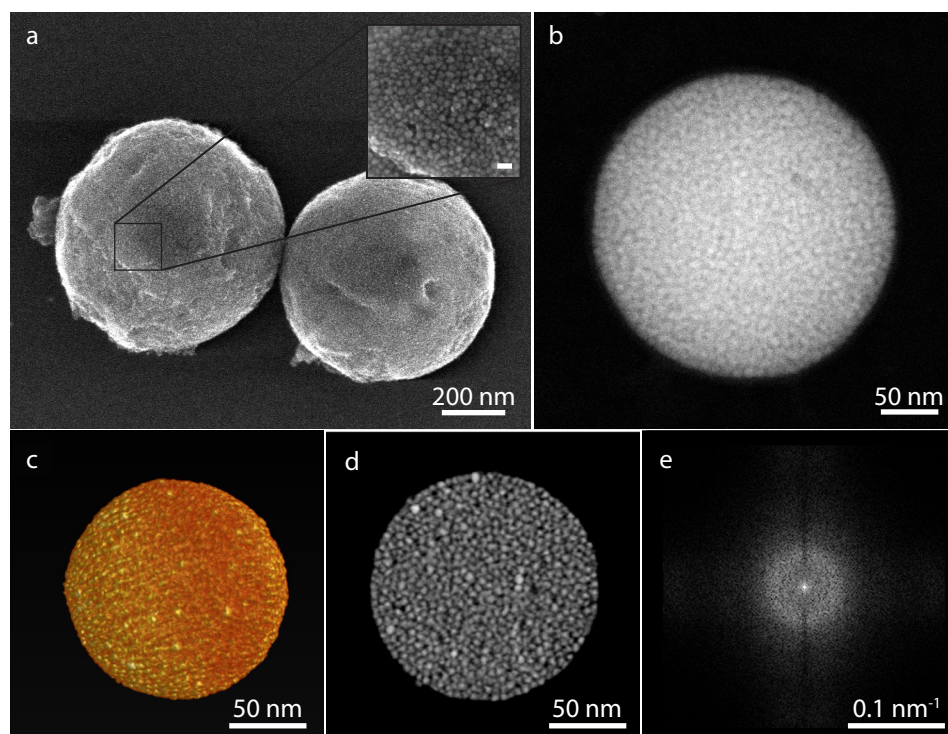


Figure 6.2 • Structural characterization of the SPs. (a) SE-STEM image of two SPs. The inset shows a magnification of one of the particles (scale bar 20 nm). Individual QDs can be clearly distinguished. (b, c) 2D HAADF-STEM images of a small SP for which electron tomography has been performed (b), and a 3D visualization of the 3D tomographic reconstruction of the same SP (c). (d) Slice through the center of the 3D reconstruction of the SP. Individual QDs can be clearly recognized as well as their relative position, showing the irregular inner structure. (e) Fast Fourier transform of the slice of panel d.

phy^{29,30} (Figure 6.2b–e). Hereby, a tilt series of HAADF-STEM images (Figure 6.2b) is acquired along different viewing directions and is combined into a three-dimensional (3D) reconstruction (Figure 6.2c) using a mathematical algorithm (see Methods). In Figure 6.2d we present a slice through the 3D reconstruction yielding the internal structure. This image as well as the fast Fourier transform in Figure 6.2e clearly show that the QDs are not ordered in the SPs, thus forming an amorphous glassy structure, as expected. In order to investigate the type of packing in the assemblies in more detail, the coordinates extracted from the tomography reconstruction were used to calculate bond order parameters.^{31,32} The analysis excluded the presence of periodic arrangements of particles. It was shown previously²⁶ that if the composing QDs have the same size and a regular spherical shape and their interactions can be approximated well with that of a hard-sphere potential, then the SPs form crystalline structures with an icosahedral or face-centered cubic structure. In our case, the composing QDs mixtures are characterized by a relatively high polydispersity and an irregular shape; this leads to a random arrangement of the QDs inside the SPs with a high packing fraction. This is confirmed by the radial distribution function (RDF) (Figure 6.9), which is calculated through the identification of the single QDs inside a SP (Figure 6.10). The RDF shows an average distance between nearest neighbors of 10.9 nm, which is in agreement with the particle size derived from TEM images.

The 3D analysis of the SPs by electron tomography also enables us to verify whether the QDs are homogeneously mixed in each of the SPs. In Figure 6.11a–c, HAADF-STEM images acquired from the individual red, green, and blue population are presented. The shape of the red emitting QDs is more spherical in comparison to the other types. The intensity in HAADF-STEM images depends on the atomic number Z . Energy dispersive X-ray spectroscopy (EDS) measurements on the individual QDs (Figures 6.12–6.15) show that the red emitting particles contain a higher amount of Cd in their structure compared to the green and blue ones (Table 1). In this manner, we conclude that the high intensity particles in the orthoslices correspond to red emitting particles. Visual inspection of the QDs in the orthoslices in Figure 6.2d shows that the different QDs are homogeneously mixed in each SP.

The homogeneous distribution of the QDs in the SPs was further confirmed by EDS measurements (Figure 6.16). From Figure 6.16 it is clear that all the elements, and in particular Se (which is not present in the blue emitting QDs), were found to be homogeneously distributed inside the SP, thus supporting our statements about the homogeneous distribution of the QDs inside the SPs.

6.2.3 Optical characterization of individual SPs and ensembles

We use confocal microspectroscopy to study the optical properties of our SPs (Figure 6.3). Microscopy of individual micron-sized SPs, larger than the diffraction limit, demonstrates that the emission of the red, blue, and green light does not vary spatially within a SP (Figures 6.3a–b and 6.17). This agrees with the homogeneous mixing of the QDs in each SP as derived from electron tomography measurements (see above). Confocal microscopy also confirms uniform emission spectra among all SPs in one batch. Even SPs from one synthesis batch but with different sizes show similar PL emission spectra (Figures 6.3c–e and 6.18).

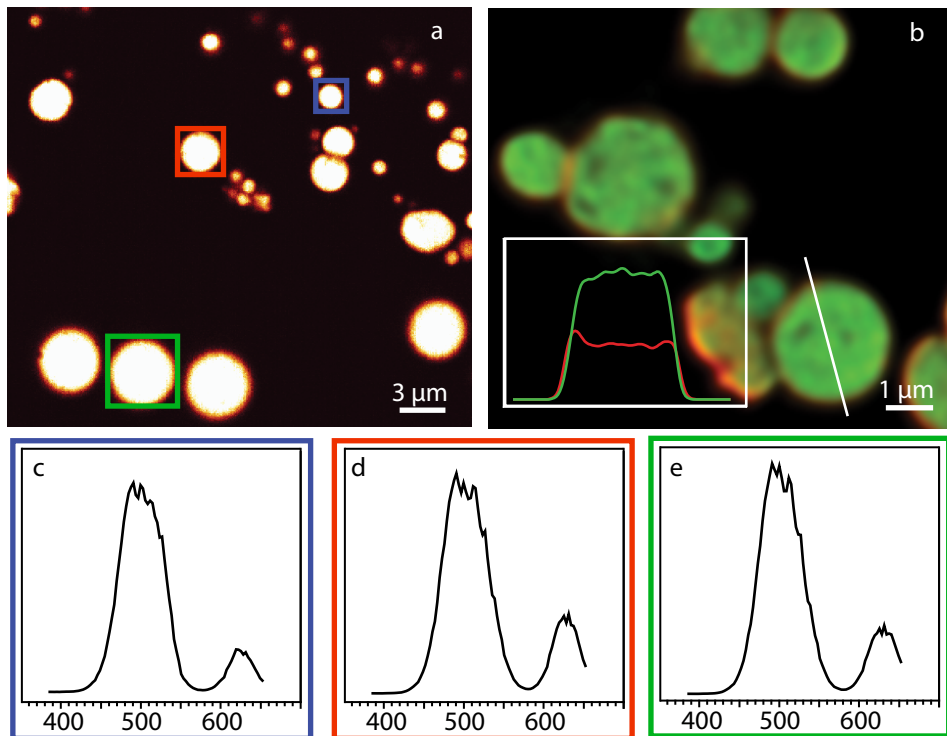


Figure 6.3 • Optical characterization of the SPs. (a) Confocal microscopy image of a set of SPs drop-casted and dried on a glass slide and excited with UV excitation. (b) Confocal fluorescence image of different SPs. The blue-green emission (450–550 nm) is shown in green, while the red emission (600–700 nm) is shown in red; the image is deconvolved through the modeling of the point spread function of the microscope. The inset shows the signal collected along the white line drawn in the figure coming from the two detectors. (c–e) Emission spectra of some of the SPs presented in panel a, indicated with the green, red, or blue frame.

Using (time-resolved) PL spectroscopy, we study in more detail how the ensemble-averaged optical properties of the SPs relate to those of the separate constituent QDs (Figure 6.4). In Figure 6.4a the emission spectra are compared. The contributions from the separate NC populations (colored lines) are clearly distinguished in the composite emission spectrum of the SP (black). This is to be expected because (i) the constituent QDs are too far apart to exhibit quantum mechanical coupling that could otherwise change the energy levels and (ii) the SPs are too polydisperse for whispering gallery modes²⁷ to appear in the ensemble emission spectrum. Nevertheless, the peak position of the blue contribution to the SP emission (black line) is slightly red-shifted from the peak position of the dispersion of blue QDs (blue). This indicates energy transfer among blue QDs in the SP and/or from blue QDs to the green and red QDs. Most likely, both Förster-type energy transfer (*i.e.* by dipole–dipole coupling) and photon reabsorption contribute to this. We wish to remark that the emission spectrum of the composed SPs is independent of the excitation intensity in the broad range of single exciton excitation (up to 14 mW) (Figure 6.19). This is an important asset compared to previous proposals in which a broad emission was reached

by simultaneous exciton and biexciton emission²³ or shell emission.²⁴

In Figure 6.4b–d we show the PL decay dynamics of the three batches of QDs freely dispersed in toluene (closed circles) compared to QDs assembled into a SP (open circles). The suspension of the red emitting QDs shows the slowest PL decay, followed by the green and the blue emitting QDs, qualitatively in agreement with the frequency dependence of the optical transition strengths.³³ The decay dynamics of the same batches of QDs assembled in water-dispersed SPs are consistently faster. More precisely, the PL of SPs consisting purely of red QDs (red open circles) decays 66% faster than that of freely dispersed QDs in toluene (see Methods section for a description of our analysis procedure). The decay of the red component in mixed white light-emitting SPs (black open circles) is 33% faster than the red NC dispersion. For the green emission, these acceleration factors are 41% for the purely green SPs and 32% for the mixed SPs; for the blue emission 29% and 211%.

Multiple collective effects simultaneously affect the decay dynamics in the SPs. For example, the local density of optical states (LDOS), which determines the rate of radiative decay, is higher for QDs in a SP than for those freely dispersed in toluene. We estimate the LDOS in a SP using a simplified model, where the SP is assumed to be a perfect sphere with a homogeneous refractive index, which can support Mie resonances (Figure 6.20).

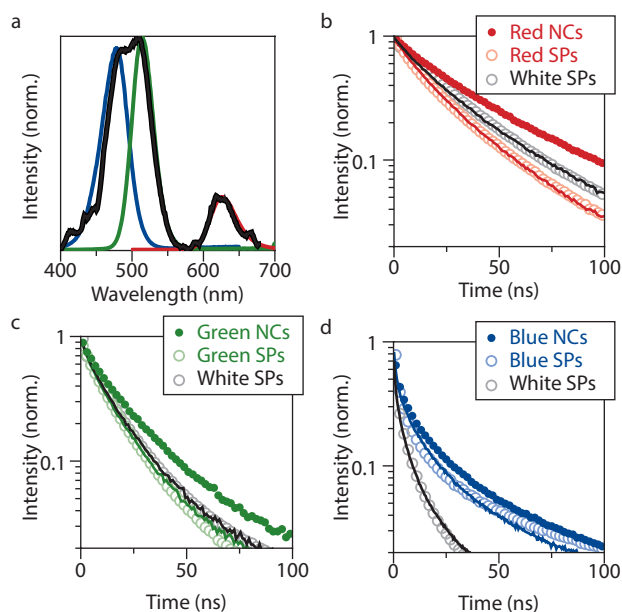


Figure 6.4 • Optical properties of SPs compared to suspensions of the constituent QDs. (a) Emission spectrum of an ensemble of white light-emitting SPs (black) and of the three separate dispersions of the constituent QDs (colored; each scaled to match the maximum intensity of the corresponding peak in the composite spectrum). (b) PL decay traces of red QDs freely dispersed in toluene (red closed circles), assembled in water-dispersed SPs of red QDs (red open circles), and assembled in a white light-emitting SPs (gray open circles). The red line is a fit to the PL decay of red SPs, and the black line to the decay of white-light emitting SPs (see Methods section for an explanation of the fitting procedure). Same for (c) green QDs and (d) blue QDs.

This model predicts that the LDOS, averaged over the volume of the SP and orientation of the transition dipole moments, is approximately two times larger in a SP than for free QDs (Figure 6.20). Indeed, the PL decay in SPs is always faster than for dispersed QDs (Figure 6.4b–d). However, the acceleration is less pronounced than the simplified Mie model predicts, which can in part be due to damping of the Mie resonances by refractive index inhomogeneities and absorption in the SP. Moreover, the PL decay dynamics observed can be affected by Förster energy transfer among QDs and reabsorption of emitted light.

We can get some insight into the occurrence of Förster energy transfer in the SPs by comparing the PL decay dynamics in pure-color SPs (colored open circles in Figure 4b–d) and mixed white light SPs (gray open circles). In pure-color SPs energy transfer can occur only among QDs from the same (inhomogeneously broadened) color population. Mixed SPs enable additional transfer between populations from blue to green, blue to red, and green to red. Indeed, the blue PL decay (Figure 6.4d) is faster in mixed SPs than in pure SPs because of these additional decay channels. The red PL (Figure 6.4b) is slower in mixed SPs, because the red QDs are fed through energy transfer from the blue and green populations. The green PL decay is approximately equally fast in pure and mixed SPs, which indicates that the effects of feeding from the blue population and transfer to the red compensate each other. Detailed modeling of these energy-transfer processes and their effect on the color output depends on many factors (*e.g.* the degree of inhomogeneous broadening and the separations and relative orientations of the QDs in the SP). This is beyond the scope of the current work. Nevertheless, these effects must be taken into account in the composition of the SPs if a certain desired shade of white light is targeted (see below), and in our case this was done empirically.

Lighting applications require photochemically stable SPs, while many biolabeling applications require time-constant emission from individual SPs, without blinking or dark periods. Our SPs show bright, non-blinking, and non-bleaching emission on the single-SP level over a time period of at least 3000 s (Figure 6.21). This stability is an important asset compared to conventional optical labels, for example, silica particles filled with organic dyes such as rhodamine isothiocyanate (RITC).³⁴

Concerning the non-blinking feature, we remark that this is due to the concomitant emission of many QDs in each SP. We also remark that the size of the SPs can be tuned up to 100 nm, that they can be dispersed in water, if needed, coated by a thin silica layer, and that the surface can be bio-functionalized at will. Thus, the NC SPs presented here, emitting one color or a combination of two or three fundamental colors, are suitable as biological labels.

For application of the SPs as spectral conversion phosphors in lighting, the precise tunability of the white light spectrum is of great importance. To study this, we convert the pure spectra of the constituent QDs and the composite spectra of the SPs to coordinates of the Commission Internationale de l'Éclairage (CIE) chromaticity space (Figure 6.5). The vertices of the triangle are the coordinates of the three QDs components. The better the color purity of the single NC components, the larger the area of the triangle in the CIE space. The area inside the triangle represents all the colors that can be achieved by composing

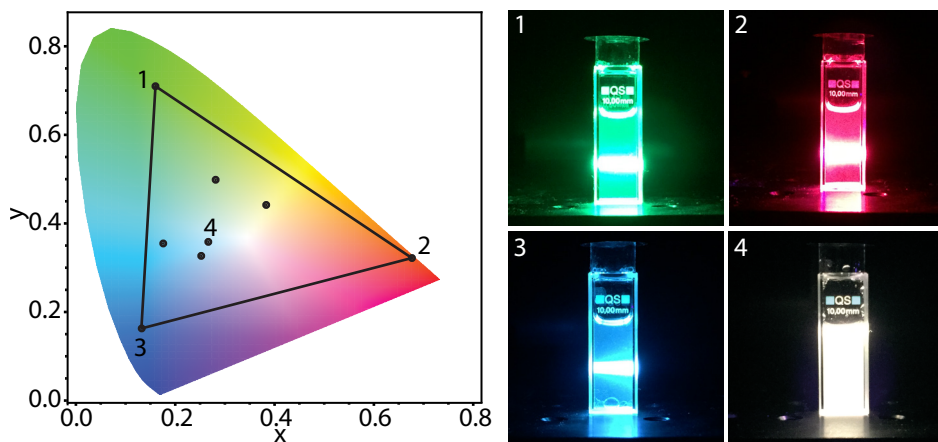


Figure 6.5 • CIE chromaticity diagram of the QDs and the SPs. Left: CIE diagram representing different SP batches as obtained by changing the ratio between the three QDs populations. The vertices of the triangle represent the coordinates of the three types of QDs. Therefore, the area of the triangle represents all the possible colors SPs can have. Right (1–3): Digital true-color photographs of the QDs dispersed in solution when illuminated with a UV laser. (4) Digital photograph of a dispersion of the SPs, composed of the three types of QDs, emitting white light.

SPs from the three different QDs used here. The color purity of the QDs, as used here, is another important advantage of NC SPs over regular phosphors that usually have a broad emission spectrum. The black dots within the triangle in Figure 6.5 represent color points that we obtained by assembling our QDs into SPs. A given broad SP emission spectrum can be achieved and fine-tuned if one knows the emissive strength of the red, green, and blue emitting QDs and takes the lower effective emission yield from the blue-emitting particles into account, in a few experimental iterations (see Figure 6.22). We remark that a targeted composite emission spectrum will remain independent of excitation intensity over a broad excitation regime as long as the steady-state exciton population remains below unity.

6.3 Conclusions

We have reported the synthesis and structural and optical characterization of colloidal water-soluble SPs composed of three types of QDs. The SPs can be fabricated to emit pure colors as well as a broad white light spectrum (or anything in between) that can be fine-tuned via the NC composition of the SPs. The bright emission from individual SPs is stable over time and does not blink. Such SPs hold promise as phosphors in LEDs for lighting, opto-electrical integration in semiconductor chips and as biological labels.

6.4 Methods

Chemicals

Sodium dodecyl sulfate (SDS, $\geq 98.5\%$), Dextran from *Leuconostoc mesenteroides* (M_w 670000 g/mol), Trioctylphosphine oxide (TOPO, 90%), Octadecylamine (ODA, 90%), Oleic acid (OA, 90%), 1-Octadecene (ODE, 90%), Cadmium acetate dihydrate ($\text{Cd}(\text{Ac})_2 \cdot 2\text{H}_2\text{O}$, 98%), Trioctylphosphine (TOP, 90%), Sulfur (S, 99.998%), Ethanol (EtOH, 99.8%), 1-Butanol anhydrous (BuOH, 99.8%), Methanol (MeOH, anhydrous, 99.8%), Toluene (anhydrous, 99.8%), Cadmium oxide (CdO , 99.99%), Zinc acetate dihydrate ($\text{Zn}(\text{Ac})_2$, $\geq 98\%$), 1-octanethiol

($\geq 98.5\%$), Chloroform ($\geq 99\%$) were all purchased by Sigma Aldrich and used as received. Se powder (Se, 200 mesh, 99.999%) and Diethylzinc (95%) were purchased from Brunschwig Chemie. Acetone (dried) was purchased by VWR International.

Synthesis of red emitting QDs

Synthesis of the precursors

Prior to the synthesis, different precursors were prepared. The Cd- and Se- precursors for the synthesis of the cores were prepared as follows. For the Cd- precursor, 51.84 g of ODE were mixed in a 100 mL Erlenmeyer with 7.36 g of OA and 1.28 g of $\text{Cd}(\text{Ac})_2 \cdot 2\text{H}_2\text{O}$. This solution was stirred at 150°C under vacuum in a schlenkline for two hours. For the Se- precursor, 4.25 g of Se were mixed with 22.5 g of TOP and 35.7 g of ODE in a 50 mL Erlenmeyer. The solution was stirred at 50°C until complete dissolution of the Se.

Synthesis of the cores

The synthesis was performed in a schlenkline under nitrogen atmosphere. In a 50 mL three neck flask, 2.22 g of TOPO, 6.40 g of ODA and 9.8 g of Cd precursor solution were mixed, and the temperature was increased to 300°C. When this temperature was reached, 10.4 g of Se precursor solution was quickly injected in the mixture. The nanocrystals were allowed to grow for 30 s, after which the solution was rapidly cooled down to room temperature with the aid of compressed air. The particles were diluted by adding 1 equivalent of hexane. The NCs were then washed by adding 2 equivalents of MeOH and collecting the upper colored layer of the resulting two-phase system. The NCs were then precipitated by adding 1 equivalent of acetone and centrifuging at 2500 rpm for 5 min. The NCs were finally redispersed in 10 mL of toluene and stored inside the glovebox.

Growth of CdS shells

This synthesis was adapted from another procedure³⁵ from literature. Prior to the synthesis, the Cd-, S- and Zn-precursors were prepared. For the Cd- precursors, 5.5 g of $\text{Cd}(\text{Ac})_2 \cdot 2\text{H}_2\text{O}$ were mixed with 54.15 g of OA and 216 mL of ODE in a 500 mL Erlenmeyer. The mixture was stirred for 2 hours at 120 °C under vacuum. For the S- precursor, 0.320 g of S was mixed with 100 mL of ODE in a 250 mL Erlenmeyer and heavily stirred at 180 °C until complete dissolution of the S. For the Zn- precursor, 0.988 g of diethylzinc was mixed with 40 mL of ODE in a 100 mL Erlenmeyer in a glovebox. The mixture was stirred at room temperature while 10.10 mL of OA was added dropwise. The solution started foaming and was kept stirring until complete stabilization; at that point the temperature was increased to 310 °C and the solution was further stirred for 5 min.

For the growth of CdS shells, 10^{-7} M of NCs (3.1 nm in diameter) in toluene solution were combined with 5 g of ODE and 1.5 g of ODA. The solution was stirred at 150 °C for 1 hour in order to let all the toluene evaporate. The reaction temperature was then increased to 240 °C and, in steps with reaction periods of 30 min, the precursors were added slowly to grow the shell layer by layer. In total, 10 monolayers of CdS, 2 monolayer of CdZnS and 2 monolayer of ZnS were grown.

Monolayer #	Precursor to add (mL)		
	S	Cd/Zn	
0	-	-	-
1	0.143	0.143	Cd
2	0.181	0.181	Cd
3	0.223	0.223	Cd
4	0.270	0.270	Cd
5	0.321	0.321	Cd
6	0.377	0.377	Cd
7	0.438	0.438	Cd
8	0.502	0.502	Cd
9	0.572	0.572	Cd
10	0.645	0.645	Cd

11	0.723	0.723	Cd/Zn
12	0.806	0.806	Cd/Zn
13	0.893	0.893	Zn
14	0.895	0.895	Zn

After the growth, the reaction mixture was cooled down to room temperature and diluted by adding 1 equivalent of toluene. The NCs were washed by adding 2 equivalents of a 1:2 v/v BuOH:MeOH mixture, then centrifuging at 2500 rpm in order to precipitate the NCs, and then redispersing the pellet in 10 mL of toluene. The NCs were stored in the glovebox under nitrogen atmosphere.

Synthesis of green emitting QDs

The synthesis procedure was adapted by a protocol present in literature.³⁶ For the synthesis, 0.2 mmol (2.7 mg) of CdO, 4 mmol (878.0 mg) of Zn(Ac)₂ and 5 mL of OA were mixed in a 100 mL three neck bottle in a schlenkline. The mixture was stirred for 30 min under vacuum at 150 °C in order to degas. Then 15 mL of ODE was added. The temperature was then increased to 310°C under nitrogen, thus obtaining clear solution. Then a solution composed of 0.2 mmol (15.8 mg) of Se, 4 mmol (128.3 mg) of S and 2 mL of TOP, previously stirred at 70°C until complete dissolution, was rapidly injected in the reaction bath. The solution quickly changed color to orange and the NCs were allowed to grow for 10 min at 300 °C. After this time, 0.5 mL of 1-octanethiol were added in order to passivate the surfaces of the NCs. The solution was further stirred for 5 min, then it was let cool down to room temperature, where it looked yellow. The NCs were finally washed twice by adding 1 equivalent of chloroform, precipitating by adding 2 equivalents of acetone and then centrifuging at 2500 rpm. The NCs were finally redispersed in 5 mL of toluene.

Synthesis of blue emitting QDs

The procedure was adapted from a protocol present in literature.³⁷ The synthesis was performed in a schlenkline in nitrogen atmosphere. For the synthesis, 1 mmol (128.4 mg) of CdO, 10 mmol (1.83 g) of Zn(Ac)₂ and 7.0 mL of OA were mixed and stirred in a three neck bottle at 150 °C, under vacuum, for 40 min, obtaining a pale yellow solution. Then 15 mL of ODE was added and the mixture was heated up at 310 °C under nitrogen atmosphere. When the temperature was reached, a solution made of 1.6 mmol (51 mg) of S and 2.4 mL of ODE, previously mixed at 70 °C to complete dissolution, was quickly injected in the reaction bath, obtaining a vivid yellow solution. The mixture was left to react for 12 min, after which another solution, made of 4 mmol (128.1 mg) of S and 5 mL of OA, previously mixed at 70°C upon complete dissolution, was injected at a speed of 0.5 mL/min in the reaction bath, obtaining a dark orange solution. The mixture was left to react for 3 hours, after which it was cooled down to room temperature by removing the heating source. The solution was washed by adding 2 equivalents of EtOH and centrifuging at 2500 rpm, in order to precipitate the NCs. The NCs were then redispersed in toluene and washed another time with a 1:1 v/v BuOH:MeOH solution, centrifuging at 2500 rpm and redispersing the pellet in 10 mL of toluene.

Synthesis of SPs

The synthesis was performed in open air. First of all, the three different populations of NCs, dispersed in cyclohexane, were premixed in the desired ratios forming 1 mL of mixed solution. The solution, with a NC concentration of ~ 10 mg/mL, was emulsified with a water solution made of 10 mL of milli-Q water containing 60mg of sodiumdodecylsulfate (SDS), the surfactant, and 0.4 g of dextran. Dextran acts as steric stabilizer, but is also added as well to bring the solution in a visco-elastic regime necessary for creating relatively monodisperse droplets under high shear rates.³⁸ Then, the water solution and the oil solution were brought in contact, thus forming a two phase system. This system was then emulsified. The emulsification, together with the initial volume fraction of particles, is important, since it will determine the size of the droplets and consequently, after the evaporation of the oil phase, the mean size and size distribution of the resulting SPs. We used two methods to realize our emulsions, both allowing relatively easy scaling up: sonication and a methodology developed by the Bibette group that uses high shear rates generated in a Couette shear cell.²⁸ In the sonication process, ultrasonic waves were used in order to break the two phase system in an emulsion. This method resulted in a relatively polydisperse emulsion (PD ~ 20%) consisting of medium-size SPs with diameters in a size range between 500 nm (size distribution: ± 100 nm) and 2 µm (size distribution: ± 400 nm). SPs in Figure 6.3 in the main text and 6.14 of the Appendix were made using this method. Using the shear method developed by Bibette et al. control over the average size of the particles and the resulting polydispersity are better. In fact SPs with a precise size, in

a size range between 100 nm and 500 nm, can be produced with control over the size (Figure 6.7) by changing the shear rate during the emulsification. These values for the size range are more restrictive compared to the ones cited by Bibette et al., but in our case we limited ourselves to these sizes by using an initial volume fraction of 10% and, thus, an initial droplet size of 2-3 μm . As mentioned, the shear procedure gave better results in terms of polydispersity (PD \sim 15%) and, as sonication, it is also quite rapid, taking just few minutes, and for this reason it was the most used in our experiments. SPs in Figure 6.2 in the main text and 6.7, 6.8, 6.9, 6.10 and 6.13 of the Appendix were made using this method. After the emulsification, the emulsion was then collected and stirred for 4 hours at 68°C, in order to evaporate the oil phase (=cyclohexane). The resulting dispersion was centrifuged at 2000 rpm for 10 min, and the sedimented SPs were finally redispersed in distilled water.

Optical Measurements

The PL quantum yield (PLQY) measurements were performed on samples consisting of diluted NC or SP solutions (cyclohexane for NCs, Milli-Q water for SPs) in a quartz cuvette using an Edinburgh instruments F900 spectrometer with an integrating sphere and excitation at 420 nm. The measured PLQY for our composed SPs is up to 25%. When going from solution of NCs in toluene to SPs of one single population of NCs, the measured PLQY changes as follow: for SPs composed of only red emitting NCs the PLQY remains stable at 75%, for SPs composed of only green NCs the PLQY goes from 81% to 40%, and for SPs composed of only blue emitting NCs the PLQY goes from 12% to 2%.

Confocal images were acquired with a Leica SP8 confocal microscope fitted with a pulsed super continuum source (NKT Photonics, 400 nm, 5 ps pulse duration, 78 MHz repetition rate), focusing objective (100x /1.4 NA oil-immersion confocal objective (LEICA), and PMT detection. The investigated individual supraparticles were lying on a 600 nm SiO₂ covered Si substrate, 0,15 mm thick, and immersed in Leica immersion oil type F.

The images taken with the confocal microscope were processed by deconvolution using the point spread function (PSF) of the microscope, which was recently determined experimentally (width 190 nm in the x-y imaging plane and 490 nm along the optical z-axis³⁹), and were deconvolved afterwards. We note, however, that the images might be slightly distorted by the large refractive index contrast between the SPs and the surrounding environment.

PL emission and decay traces were recorded using an Edinburgh instruments F900 spectrometer, while absorption was measured with a PerkinElmer lambda 950 spectrophotometer.

Analysis of photoluminescence decay dynamics

The photoluminescence decay curves of Figure 6.4b-d in the main text were measured after spectrally selecting the relevant emission using a grating and slit. From the often multi-exponential curves we fitted the acceleration of decay upon assembly of the NCs into a SP without assuming any particular functional form for the curves (e.g. mono-exponential, bi-exponential, stretched exponential, or a log-normal rate distribution). Instead, we determined the optimal acceleration factor x that could shift the decay curve of the individual NCs onto those of the SPs through a transformation $t \rightarrow t/x$ of the time coordinates of the data points. This yields an acceleration of 66% upon going from individual red NCs to SPs purely consisting of red NCs, and an acceleration of 34% upon going to mixed (white-light emitting) SPs. For green NCs these numbers are 41% and 32%, and for blue NCs 29% and 211%. To benchmark this analysis method, we can compare it to more conventional single-exponential fitting on the data of the red NCs. (Note however that such fits match the data poorly in case of multi-exponential decay curves). Using single-exponential fitting on the first 100 ns, the accelerations would be estimated as $(39 \text{ ns} / 24 \text{ ns} - 1) = 63\%$ and $(39 \text{ ns} / 31 \text{ ns} - 1) = 23\%$ for the red NCs; $(20 \text{ ns} / 31 \text{ ns} - 1) = 40\%$ and $(20 \text{ ns} / 16 \text{ ns} - 1) = 21\%$ for the green NCs; and $(14 \text{ ns} / 8 \text{ ns} - 1) = 68\%$ and $(14 \text{ ns} / 5 \text{ ns} - 1) = 197\%$ for the blue NCs. The results of the two methods are qualitatively the same.

Definition of polydispersity

All the values of sizes in the article are given with the mean (μ) and the standard deviation (σ) in the form: $\mu \pm \sigma$. Polydispersity of size is defined as PD (%) = $(\sigma/\mu) \cdot 100$.

Hydrodynamic diameter

The hydrodynamic diameter (i.e. the diameter of the semiconductor material plus the ligand shell) of the particles has been precisely measured for the red population of NCs, characterized by a spherical shape and therefore easier to analyze, from visual analysis of the TEM images. From those images we extracted the mean length of

the ligands (oleic acid) and, since the ligands are the same for all the nanocrystals, we assumed it the same also for the green and the blue population. The as measured hydrodynamic diameters are: 11.8 ± 1.7 nm (red), 12.5 ± 1.8 nm (green) and 12.0 ± 1.9 nm.

Electron microscopy

HAADF-STEM images, SE-STEM images, EDS maps and electron tomography series of the SPs were acquired using a FEI Osiris and a FEI Tecnai electron microscopes operated at 200 kV. Electron tomography series were acquired using a Fischione model 2020 single tilt tomography holder and the series were acquired within the tilt ranges from -64° to $+74^\circ$, from -76° to $+64^\circ$ and a tilt increment of 2° . Alignment of the tilt series was performed through cross-correlation routines⁴⁰ implemented in Matlab. For the reconstruction of the series, the simultaneous iterative reconstruction technique (SIRT) was used, implemented in the ASTRA toolbox.⁴¹⁻⁴³ HAADF-STEM images of the NCs were acquired using an aberration-corrected 'cubed' FEI Titan 60-300 electron microscope operated at 120 kV, equipped with a ChemiSTEM44 system.

Radial distribution function

The radial distribution function of NC centers of mass in a SP was calculated from the reconstructed SP obtained from tomographic analysis. The individual NCs were automatically detected, and the center-of-mass coordinates extracted. Then the histogram of center-to-center distances was normalized to the distances in an ideal gas with the same density. In order to minimize the shape effects of the supraparticle, the volume of the droplet is approximated by the convex hull around all particle coordinates in the data set. The normalization factor is then calculated from the distances between centers-of-mass of an ideal gas in this volume, thus minimizing shape effects.

CIE diagram

The CIE coordinates of the different emitters were obtained firstly by multiplying the emission spectra with the standard color matching functions (CIE standard 1964). Then the tristimulus values (X, Y and Z) were obtained by integrating the previously calculated values over the entire visible spectrum. Finally, the CIE coordinates (x, y and z) were calculated from the tristimulus values using the following formulas:

$$x = \frac{X}{X + Y + Z} ; y = \frac{Y}{X + Y + Z} ; z = \frac{Z}{X + Y + Z}$$

The CIE coordinates, calculated in this way, and corresponding to the numbers in Figure 6.5 of the main text, are as follow:

(0.1602; 0.7126; 0.1272)

(0.6767; 0.3233; 0.0001)

(0.1319; 0.1639; 0.7042)

(0.2666; 0.3599; 0.3735)

Packing fraction

The packing fraction of NCs in the SPs was determined by performing a thresholding of the reconstructed electron-density map of the SP through the Otsu method,⁴⁵ and comparing the thresholded volume with the overall volume of the assembly. This approach was chosen since no order of the single NCs was detected and since the particles do not have a spherical shape. The packing fraction measured this way was 0.8.

Acknowledgements

We thank Jaco Geuchies for help with the optical analysis, Wessel Vlug for providing silica particles filled with RITC, Hans Meeldijk for his assistance with SE-STEM measurements, Ernest van der Wee for help with the calculation of the radial distribution functions and Marijn van Huis and Simone Dussi for very fruitful discussions.

References

1. Murray, C. B., Norris, D. J. & Bawendi, M. G. Synthesis and characterization of nearly monodisperse CdE (E = sulfur, selenium, tellurium) semiconductor nanocrystallites. *J. Am. Chem. Soc.* **115**, 8706–8715 (1993).
2. Talapin, D. V., Lee, J. S., Kovalenko, M. V. & Shevchenko, E. V. Prospects of colloidal nanocrystals for electronic and optoelectronic applications. *Chem. Rev.* **110**, 389–458 (2010).
3. Chen, O. *et al.* Compact high-quality CdSe-CdS core-shell nanocrystals with narrow emission linewidths and suppressed blinking. *Nat. Mater.* **12**, 445–51 (2013).
4. Christodoulou, S. *et al.* Synthesis of highly luminescent wurtzite CdSe/CdS giant-shell nanocrystals using a fast continuous injection route. *J. Mater. Chem. C* **2**, 3439 (2014).
5. de Mello Donega, C. Synthesis and properties of colloidal heteronanocrystals. *Chem. Soc. Rev.* **40**, 1512–46 (2011).
6. García-Santamaría, F. *et al.* Suppressed Auger Recombination in ‘Giant’ Nanocrystals Boosts Optical Gain Performance. *Nano Lett.* **9**, 3482–3488 (2009).
7. Mahler, B. *et al.* Towards non-blinking colloidal quantum dots. *Nat. Mater.* **7**, 659–664 (2008).
8. Hollingsworth, J. A. Heterostructuring nanocrystal quantum dots toward intentional suppression of blinking and auger recombination. *Chem. Mater.* **25**, 1318–1331 (2013).
9. Park, Y.S., Bae, W. K., Baker, T., Lim, J. & Klimov, V. I. Effect of Auger Recombination on Lasing in Heterostructured Quantum Dots with Engineered Core/Shell Interfaces. *Nano Lett.* **15**, 7319–7328 (2015).
10. Klimov, V. I. *et al.* Optical Gain and Stimulated Emission in Nanocrystal Quantum Dots. *Science* **290**, 314–317 (2000).
11. Klimov, V. Spectral and dynamical properties of multiexcitons in semiconductor nanocrystals. *Annu. Rev. Phys. Chem.* **58**, 635–673 (2007).
12. Alivisatos, P. The use of nanocrystals in biological detection. *Nat. Biotechnol.* **22**, 47–52 (2004).
13. Bruchez Jr., M., Moronne, M., Gin, P., Weiss, S. & Alivisatos, A. P. Semiconductor Nanocrystals as Fluorescent Biological Labels. *Science* **281**, 2013–2016 (1998).
14. Michalet, X. *et al.* Quantum Dots for Live Cells, in Vivo Imaging, and Diagnostics. *Science* **538**, 538–545 (2013).
15. Meinardi, F. *et al.* Highly efficient large-area colourless luminescent solar concentrators using heavy-metal-free colloidal quantum dots. *Nat. Nanotechnol.* **10**, 878–885 (2015).
16. Meinardi, F. *et al.* Large-area luminescent solar concentrators based on ‘Stokes-shift-engineered’ nanocrystals in a mass-polymerized PMMA matrix. *Nat. Photonics* **8**, 392–399 (2014).
17. Bradshaw, L. R., Knowles, K. E., McDowall, S. & Gamelin, D. R. Nanocrystals for luminescent solar concentrators. *Nano Lett.* **15**, 1315–1323 (2015).
18. Shirasaki, Y., Supran, G. J., Bawendi, M. G. & Bulović, V. Emergence of colloidal quantum-dot light-emitting technologies. *Nat. Photonics* **7**, 13–23 (2013).
19. Kim, J.-H. *et al.* White Electroluminescent Lighting Device Based on a Single Quantum Dot Emitter. *Adv. Mater.* **28**, 5093–5098 (2016).

20. Panda, S. K., Hickey, S. G., Demir, H. V. & Eychmüller, A. Bright White-Light Emitting Manganese and Copper Co-Doped ZnSe Quantum Dots. *Angew. Chemie* **123**, 4524–4528 (2011).
21. Schreuder, M. A., Xiao, K., Ivanov, I. N., Weiss, S. M. & Rosenthal, S. J. White light-emitting diodes based on ultrasmall CdSe nanocrystal electroluminescence. *Nano Lett.* **10**, 573–576 (2010).
22. Bowers, M. M. J., Ii, M. J. B., McBride, J. R. & Rosenthal, S. J. White-light emission from magic-sized cadmium selenide nanocrystals. *J. Am. Chem. Soc.* **127**, 15378–15379 (2005).
23. Nasilowski, M., Spinicelli, P., Patriarche, G. & Dubertret, B. Gradient CdSe/CdS Quantum Dots with room temperature biexciton unity quantum yield. *Nano Lett.* **15**, 3953–3958 (2015).
24. Brovelli, S. *et al.* Dual-color electroluminescence from dot-in-bulk nanocrystals. *Nano Lett.* **14**, 486–494 (2014).
25. Lee, K. *et al.* Highly Efficient, Color-Reproducible Full-Color Electroluminescent Devices Based on Red/Green/Blue Quantum Dot-Mixed Multilayer. *ACS Nano* **9**, 10941–10949 (2015).
26. de Nijs, B. *et al.* Entropy-driven Formation of Large Icosahedral Colloidal Clusters by Spherical Confinement. *Nat. Mater.* **14**, 56–60 (2015).
27. Vanmaekelbergh, D. *et al.* Shape-Dependent Multiexciton Emission and Whispering Gallery Modes in Supraparticles of CdSe / Multishell Quantum Dots. *ACS Nano* **9**, 3942–3950 (2015).
28. Mabile, C. *et al.* Rheological and shearing conditions for the preparation of monodisperse emulsions. *Langmuir* **16**, 422–429 (2000).
29. Midgley, P. a. & Weyland, M. 3D electron microscopy in the physical sciences: The development of Z-contrast and EFTEM tomography. *Ultramicroscopy* **96**, 413–431 (2003).
30. Altantzis, T. *et al.* Quantitative structure determination of large three-dimensional nanoparticle assemblies. *Part. Part. Syst. Charact.* **30**, 84–88 (2013).
31. Steinhardt, P. J., Nelson, D. R. & Ronchetti, M. Bond-orientational order in liquids and glasses. *Phys. Rev. B* **28**, 784–805 (1983).
32. Wang, Y., Teitel, S. & Dellago, C. Melting of icosahedral gold nanoclusters from molecular dynamics simulations. *J. Chem. Phys.* **122**, 1–16 (2005).
33. van Driel, A. F. *et al.* Frequency-dependent spontaneous emission rate from CdSe and CdTe nanocrystals: Influence of dark states. *Phys. Rev. Lett.* **95**, 1–4 (2005).
34. Verhaegh, N. A. M. & van Blaaderen, A. Dispersions of Rhodamine-Labeled Silica Spheres: Synthesis, Characterization, and Fluorescence Confocal Scanning Laser Microscopy. *Langmuir* **10**, 1427–1438 (1994).
35. Li, J. J. *et al.* Large-Scale Synthesis of Nearly Monodisperse CdSe / CdS Core / Shell Nanocrystals Using Air-Stable Reagents via Successive Ion Layer Adsorption and Reaction. *J. Am. Chem. Soc.* **125**, 12567–12575 (2003).
36. Bae, W. K. *et al.* Highly Efficient Green-Light-Emitting Diodes Based on CdSe@ZnS Quantum Dots with a Chemical-Composition Gradient. *Adv. Mater.* **21**, 1690–1694 (2009).
37. Lee, K. *et al.* Highly efficient, Color-pure, Color-Stable Blue Quantum Dot Light-Emitting Devices. *ACS Nano* **7**, 7295–7302 (2013).

38. Mason, T. G. & Bibette, J. Shear Rupturing of Droplets in Complex Fluids. *Langmuir* **13**, 4600–4613 (1997).
39. Besseling, T. H., Jose, J. & van Blaaderen, A. Methods to calibrate and scale axial distances in confocal microscopy as a function of refractive index. *J. Microsc.* **257**, 142–150 (2015).
40. Guizar-Sicairos, M., Thurman, S. T. & Fienup, J. R. Efficient subpixel image registration algorithms. *Opt. Lett.* **33**, 156–158 (2008).
41. van Aarle, W. *et al.* Fast and Flexible X-ray Tomography Using the ASTRA Toolbox. *Opt. Express* **24**, 25129–25147 (2016).
42. van Aarle, W. *et al.* The ASTRA Toolbox: A platform for advanced algorithm development in electron tomography. *Ultramicroscopy* **157**, 35–47 (2015).
43. Palenstijn, W. J., Batenburg, K. J. & Sijbers, J. Performance improvements for iterative electron tomography reconstruction using graphics processing units (GPUs). *J. Struct. Biol.* **176**, 250–253 (2011).
44. Schlossmacher, P., Klenov, D. O., Freitag, B. & von Harrach, H. S. Enhanced Detection Sensitivity with a New Windowless XEDS System for AEM Based on Silicon Drift Detector Technology. *Microsc. Today* **18**, 14–20 (2010).
45. Otsu, N. A threshold selection method from gray-level histograms. *IEEE Trans. Syst. Man. Cybern.* **9**, 62–66 (1979).
46. Chew, H. Radiation and lifetimes of atoms inside dielectric particles. *Phys. Rev. A* **38**, 3410–3416 (1988).

Appendix

Characterization of the separate NC batches

The red emitting NCs consist of a 3.1 nm CdSe core with 5 monolayers (ML) of CdS, 1 ML of CdZnS and 1 ML of ZnS. These core/multi-shell NCs are nearly spherical with a diameter of 10.3 ± 1.0 nm, and the PL emission is centered at 627 nm. The measured photoluminescence quantum yield (QY) is 75 %. The green emitting NCs were obtained by a single-step synthesis and consist of an alloyed core-shell structure of CdSe at the center and ZnS at the surface with a graded interface. The NCs have a diameter of 11.0 ± 1.1 nm, the PL emission is centered around 512 nm and the QY was measured to be 81%. The blue emitting NCs were also synthesized using a single-step method and consist of an alloyed structure with a CdZnS core and a ZnS shell with a graded interface. The final NCs have an irregular shape with a size of 10.5 ± 1.3 nm. The PL emission is centered at 477 nm with a QY of 12%. The synthesis procedure of the three NC components has been adjusted in order to get a thick shell around the core. This results not only in excellent photochemical stability, but also in a pronounced separation in energy between the dominant absorption feature coming from the massive NC shell and the luminescence from the core. In such a way, reabsorption of the red and green emission, and also partially of the blue emission can be largely reduced when the different NCs are present in mixed suspensions or in the SPs.

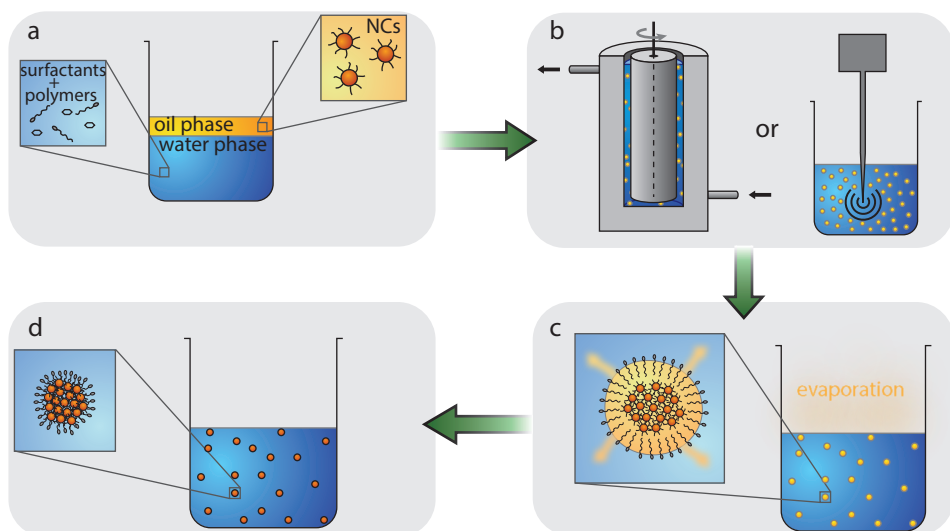


Figure 6.6 • Schematic representation of the self-assembly procedure. (a) The oil phase containing the NCs and the water phase containing surfactants, to stabilize the droplets, and polymers, to achieve a viscoelastic medium, are in contact forming a two phase system; (b) the emulsification process can be performed in a Couette shear cell or via sonication; (c) the oil phase of the droplets evaporates, thus forcing the contained NCs to self-assemble and form the SP; (d) when all the oil phase is evaporated, the SPs are suspended in water due to a layer of surfactants.

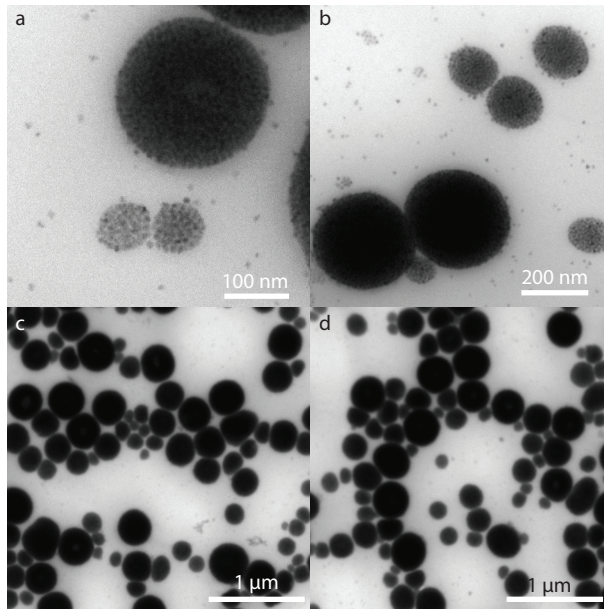


Figure 6.7 • Representative bright field TEM images of different SPs. The non-spherical shape of some of the SPs in the image can be explained by an effect of the capillary forces during the drying process of the SPs from water on the TEM grid.

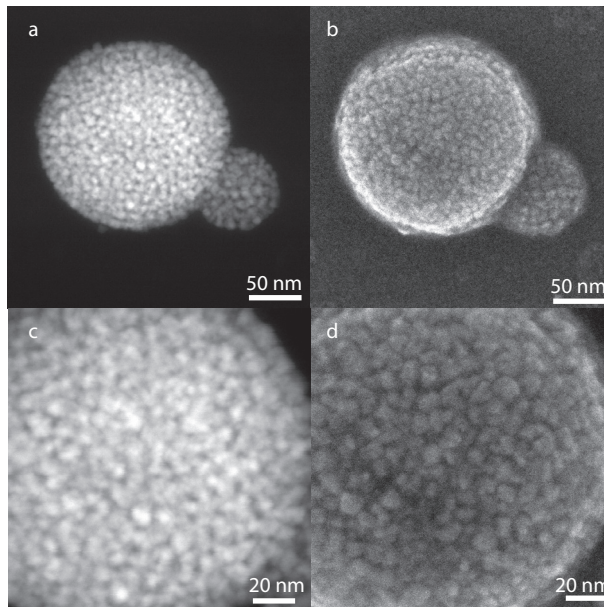


Figure 6.8 • Representative SE-STEM and HAADF-STEM images of SPs. (a) HAADF-STEM image of two SPs of different sizes. The small size is ideal to appreciate the inner structure of the SP and the arrangement of the NCs; (b) SE-STEM of the same SPs of panel a. Thanks to the secondary electron detection, it is possible to observe the surface structure more in detail, such as the amorphous arrangement of the NCs; (c) magnification of panel a; (d) magnification of panel b.

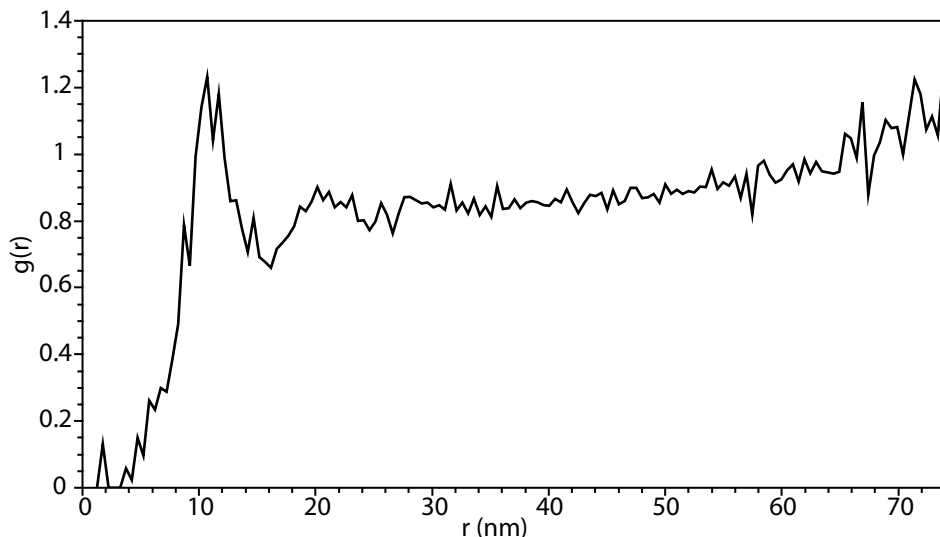


Figure 6.9 • Radial distribution function calculated for the NC position in mixed SPs. The function shows an average distance between nearest neighbors of 10.9 nm, which is approximately equal to the average diameter of the NCs.

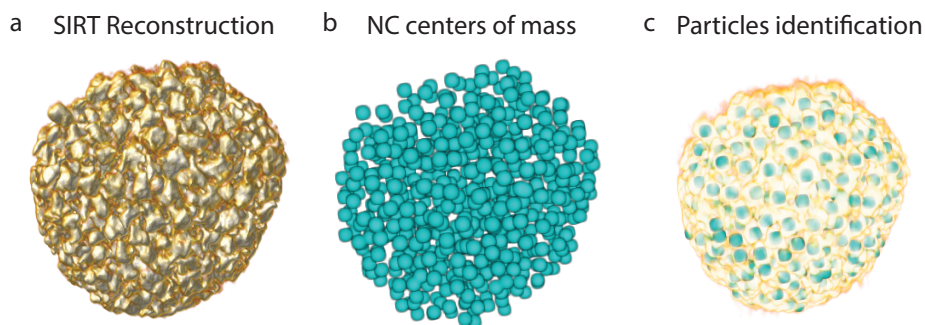


Figure 6.10 • Obtaining the NC coordinates inside a SP. From HAADF-STEM imaging of the same SP under different tilt angles it is possible to reconstruct the inner structure of the SP. (a) Volume rendering of the tomographic reconstruction obtained using the Simultaneous Iterative Reconstruction Technique (SIRT); (b–c) Using the morphologies of individual NCs known from separate TEM images (e.g. Figure 6.11a–c), automatic segmentation can identify the centers of mass (b) and packing (c) of individual NCs in the SP.

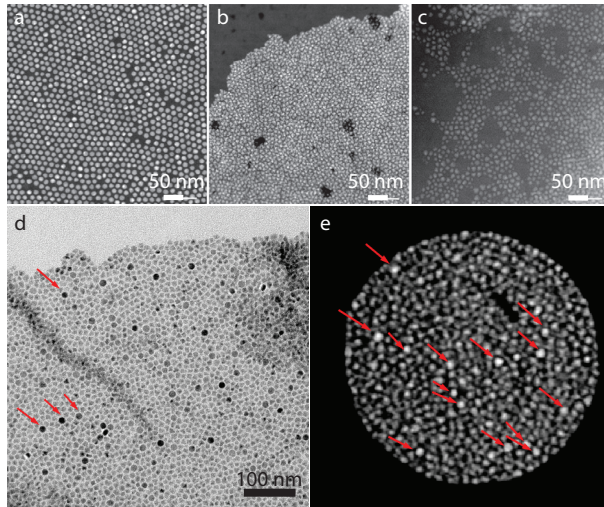


Figure 6.11 • Identification of NCs inside the SP. (a) HAADF-STEM image of the red population of NCs; (b) HAADF-STEM image of the green population of NCs; (c) HAADF-STEM image of the blue population of NCs; (d) TEM image of the mixture of NCs used to make the SP on panel e, self-assembled on a liquid-air interface; some of the red NCs are highlighted with red arrows. Their regular and spherical morphology enables their identification over the irregularly branched green and blue NCs. The image clearly shows that the mixing of the different populations of NCs is homogeneous and no phase separation occurs in 2D; (e) Orthoslice through one of the reconstructed SPs where it is possible to recognize some of the red NCs, indicated by red arrows. Also in 3D the NC populations mix homogeneously and no phase separation is observed.

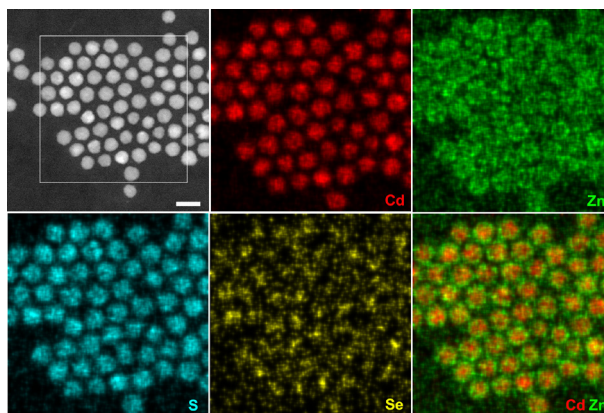


Figure 6.12 • Energy-Dispersive X-ray (EDS) maps of red emitting NCs, together with the corresponding HAADF-STEM image of the region used for the acquisition, revealing the distribution of the elements in the NCs.

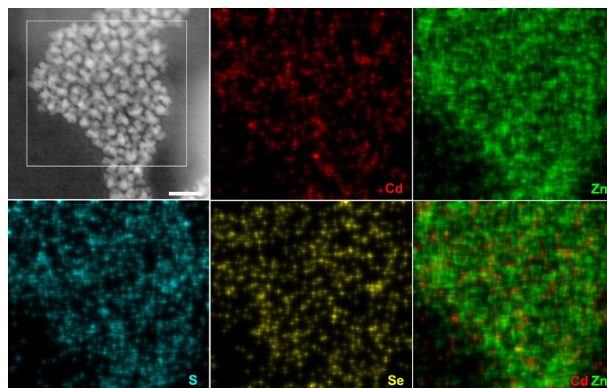


Figure 6.13 • Energy-Dispersive X-ray (EDS) maps of green emitting NCs, together with the corresponding HAADF-STEM image of the region used for the acquisition, revealing the distribution of the elements in the NCs.

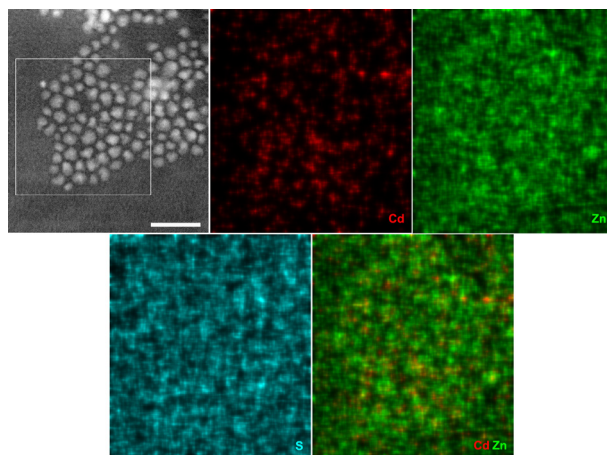


Figure 6.14 • Energy-Dispersive X-ray (EDS) maps of blue emitting NCs, together with the corresponding HAADF-STEM image of the region used for the acquisition. Instability of the sample under the electron beam hampered the acquisition of EDS maps with longer exposure time, therefore limiting the spatial resolution. In this case the maps were averaged to produce an overall composition measurement (Figure 6.15c).

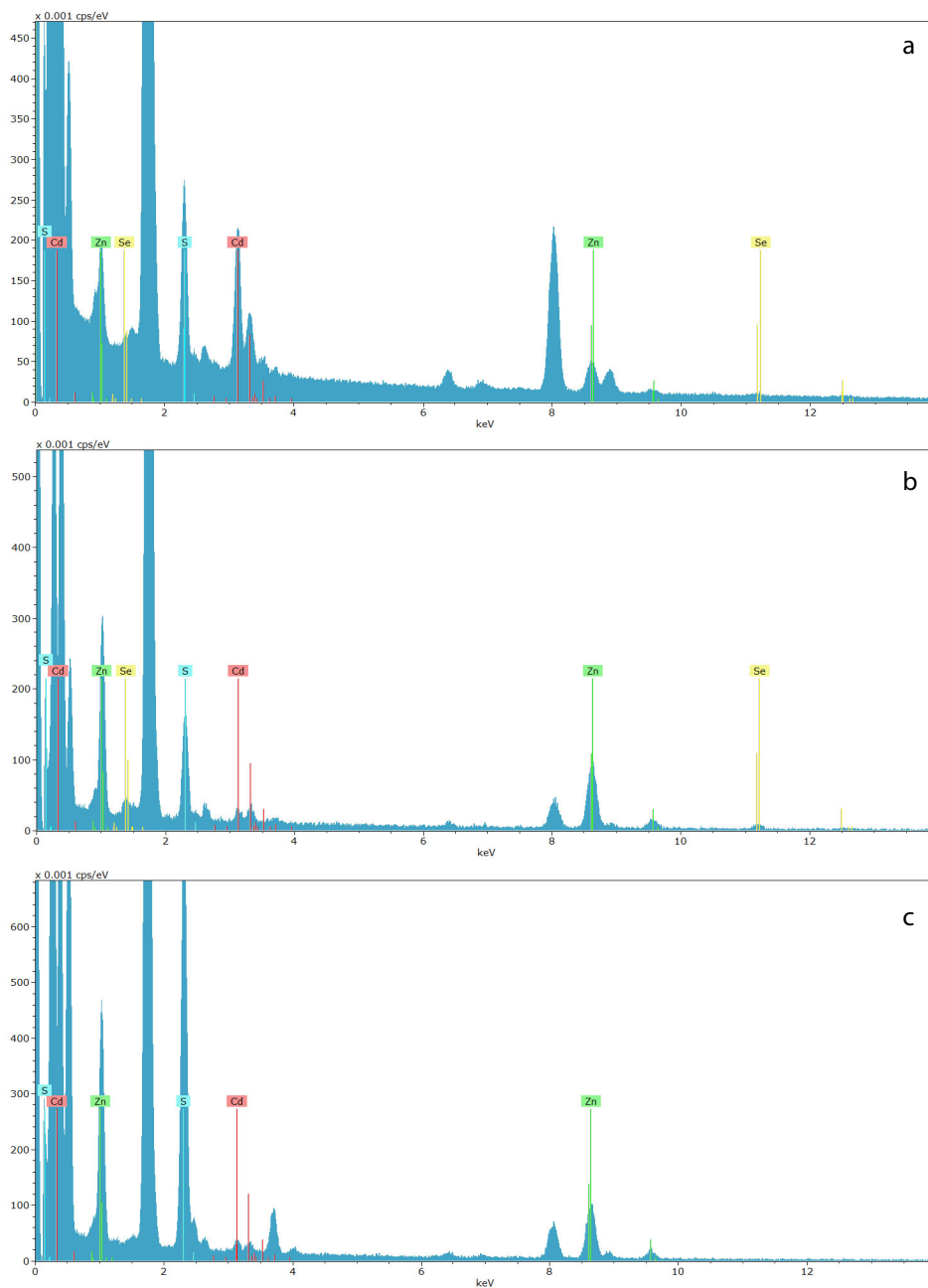


Figure 6.15 • Energy-Dispersive X-ray (EDS) spectra from the (a) red, (b) green and (c) blue NCs. The spectra were obtained by averaging the signal from the STEM-EDS maps shown in Figures 6.12-6.14. It is clear that Cd concentration is a lot higher in the red crystals compared to the green and blue ones. The peaks at 1.7 keV and 8.1 keV which are not indicated correspond to Si and Cu originating from the SiN grid and the holder respectively.

	Red NCs	Green NCs	Blue NCs
Cd	63.7	13.9	8.2
Zn	13	53.7	27
S	22	26.5	64.8
Se	1.3	5.9	0

Table 1 • Energy-Dispersive X-ray (EDS) quantification results. The mass % values of Cd, Zn, S and Se for the three different NCs are presented, as obtained from the spectra shown in Figure 6.15.

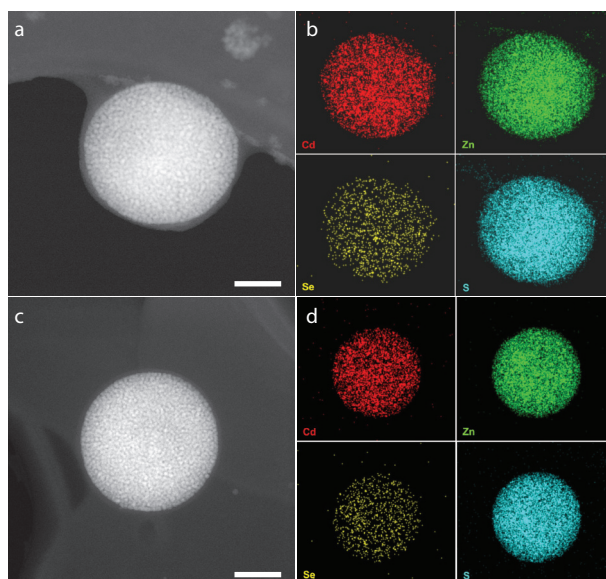


Figure 6.16 • Energy-Dispersive X-ray (EDS) images of different SPs. (a,c) HAADF-STEM images of two different SP (scale bars 100 nm) composed of red, green, and blue emitting NCs, and (b,d) the corresponding energy-dispersive X-ray (EDS) maps for the elements Cd (red), Zn (green), Se (yellow), and S (blue). The EDS maps show that all elements are homogeneously distributed over the volume of the SPs, indicating homogeneous mixing of the NCs.

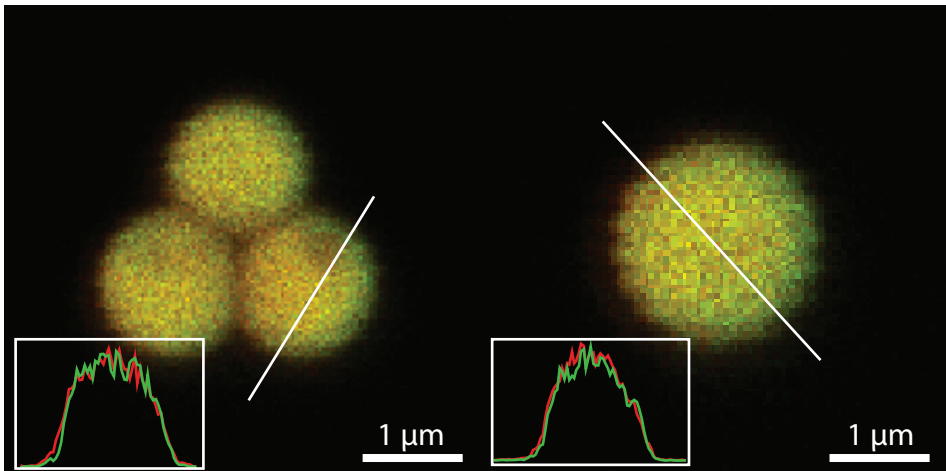


Figure 6.17 • Confocal images showing the recorded emission of monodisperse SPs made of red, green and blue emitting NCs, deposited on a silicon wafer. The insets show the intensity profile of the emission in the blue/green spectral range (450-550 nm; green line) and in the red (600-700 nm; red line). Line profiles were taken over the straight lines indicated in the main images. Both color channels show similar emission profiles in terms of intensity and shape, indicating homogeneous mixing of the NCs in the SPs.

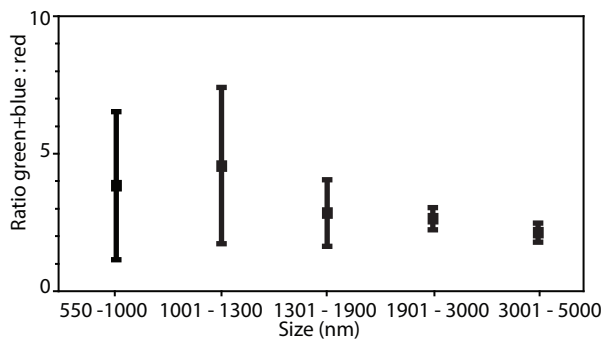


Figure 6.18 • Analysis of the optical properties of single SPs through confocal imaging. The plot shows the ratio between the maximum of the green+blue peak and the maximum of the red peak in the emission spectra of the single SPs plotted versus their size. This plot supports the statement that the optical properties SPs are homogeneous throughout the synthesis batch, as the intensity ratio is similar for the different SP sizes. The relatively large error bars for sizes below 1300 nm are due to the close proximity between the volume of the SP and the volume of the PSF of the confocal microscope.

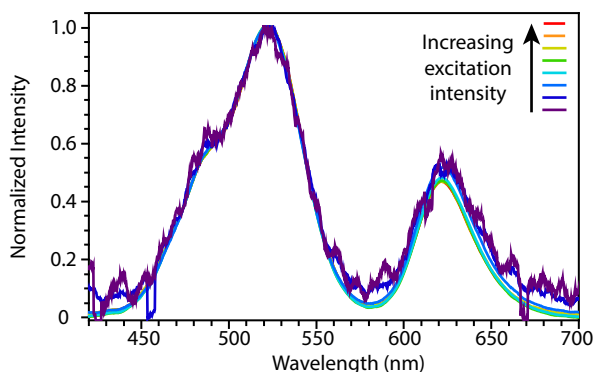


Figure 6.19 • Emission spectra of a dispersion of SPs in function of the excitation power. Emission spectra of a suspension of SPs in water excited with a diode laser at 405 nm at different excitation powers: 104.5 mW/cm² (red), 81.0 mW/cm² (orange), 62.1 mW/cm² (yellow), 42.4 mW/cm² (green), 18.9 mW/cm² (cyan), 1.7 mW/cm² (blue), 0.61 mW/cm² (dark blue), 0.036 mW/cm² (purple).

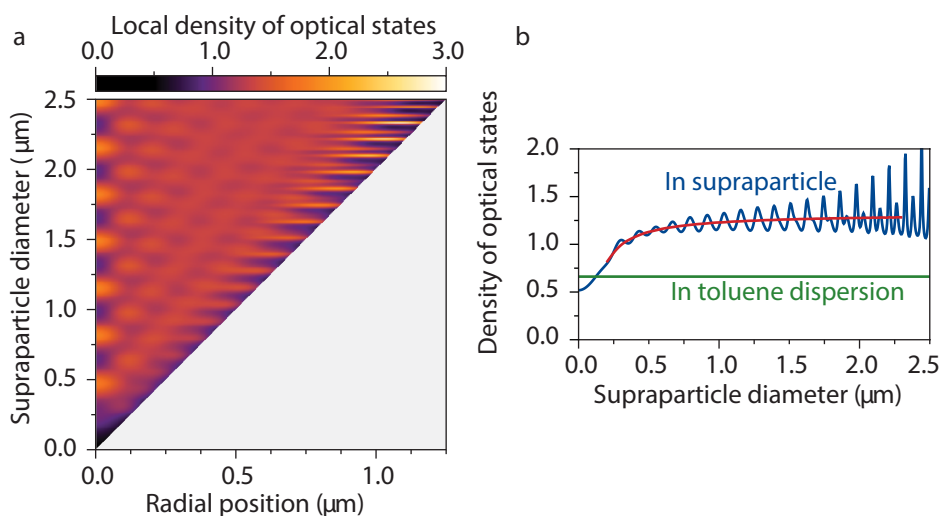


Figure 6.20 • The local density of optical states in a supraparticle. (a) We estimate the local density of optical states (LDOS) experienced by NCs in a SP using a simple model, by approximating the SP as a homogeneous dielectric sphere with a real refractive index. The LDOS in the SP, as a function of SP radius and radial position of the NC, can then be expressed as an expansion in terms of Mie coefficients.⁴⁶ The plot shows the results for a red-emitting NC ($\lambda = 627$ nm) in a SP, averaged over transition-dipole orientation and normalized to the LDOS in vacuum. For the refractive index of the SP we take $n_{\text{SP}} = 1.89$ (= 50% CdS + 50% organic material/water with average $n = 1.4$) and for the environment we assume water ($n_{\text{out}} = 1.33$), as in the experiments of Figs. 4,5 of the main text. The “Mie” LDOS in the sphere is multiplied by a local-field correction factor $[3n_{\text{SP}}^2/(2n_{\text{SP}}^2 + n_{\text{NC}}^2)]^2$ to account for the locally higher refractive index of the NCs. (b) The LDOS averaged over the volume of the SP (blue), compared to the LDOS experienced by a NC in toluene dispersion (green). In large (> 1 μm diameter) SPs the LDOS is approximately twice larger than in toluene dispersion (red); averaging out sharp Mie peaks using a Gaussian SP size distribution with 100 nm standard deviation.

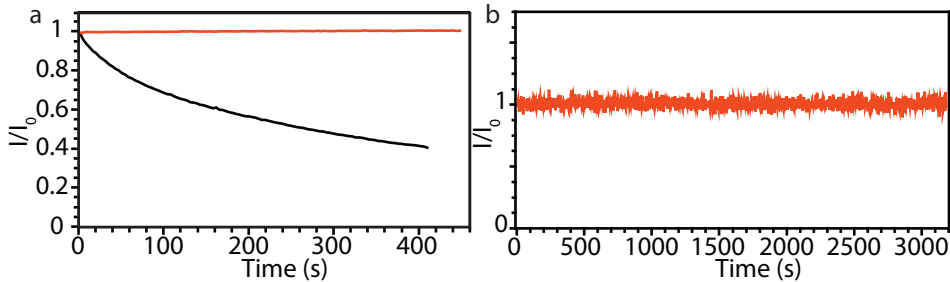


Figure 6.21 • Photobleaching of Si particles filled with RITC compared to SPs. (a) Photoluminescence emission intensity of a dispersion of SPs (red) and Si particles filled with rhodamine isothiocyanate (RITC) (black) over time under continuous excitation ($\sim 0.1 \mu\text{W}$ at 550 nm). The photobleaching of the latter one is evident from the graph; (b) Representative photoluminescence emission trace of a single SP under continuous laser excitation.

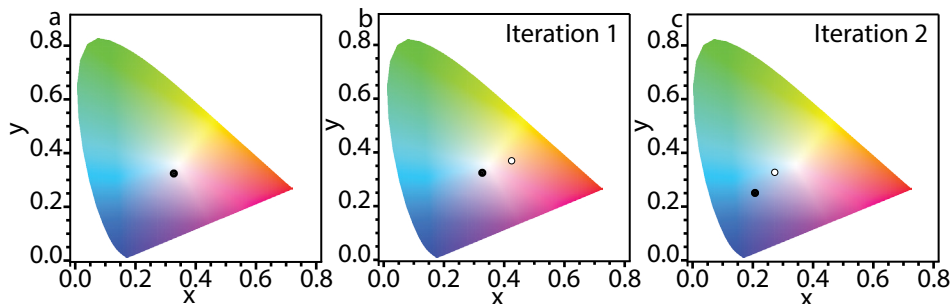


Figure 6.22 • Consecutive adaptations of the composition of the SPs to arrive at a given shade of white light, i.e. a given point in the CIE diagram. (a) We show here how one can approach the “bull’s eye” of the CIE diagram, indicated by the black point. (b) We first prepare a solution of NCs with the target composition (black dot). The solution is then used to make SPs. From the emission spectrum of the SPs we find a considerable shift towards the red (white point). This is due to energy transfer and reabsorption events (see text). (c) Then we prepare a new solution of NCs taking in account the shift of step 1 (black dot). The new adapted solution is used to make SPs. The resulting SPs have CIE coordinates much closer to the target point compared to step 1 (white point). With some iterations, one can fabricate SPs with precisely the desired emission spectrum.

Chapter 7

Lasing supraparticles self-assembled from nanocrystals

Abstract

One of the most attractive foreseen commercial applications of semiconductor nanocrystals (NCs) is their use in lasers. Thanks to their high quantum yield, tunable optical properties, photostability and wet-chemical processability, NCs have arisen as promising gain material. NCs have been already implemented in cavities with different geometries and structures. Electrically-pumped NC-based lasers are now viewed as having the potential to become a game changer, and the first steps towards zero lasing-threshold devices have been achieved. Most of these applications, however, rely on incorporation of NCs in lasing cavities that are separately produced using sophisticated fabrication methods and that are often difficult to manipulate. Here, we present whispering gallery mode lasing in supraparticles (SPs) of self-assembled NCs. The SPs, being composed of NCs, act here both as lasing medium and cavity. Moreover, the synthesis procedure of the SPs, based on an in-flow microfluidic device, allows precise control of the dimensions of the SPs, *i.e.* the size of the cavity, in the micrometer range with polydispersity as low as several %. The SPs presented here show whispering gallery mode resonances with quality factors up to 320. Whispering gallery mode lasing is evidenced by a clear threshold behavior, coherence and exciton decay measurements.

Based on: Lasing Supraparticles Self-Assembled from Nanocrystals. Federico Montanarella, Darius Urbonas, Luke Chadwick, Pepijn G. Moerman, Patrick Baesjou, Rainer F. Mahrt, Alfons van Blaaderen, Thilo Stöferle, and Daniel Vanmaekelbergh
Just Accepted in ACS Nano

*«The good thing about science is that it's true whether or not you believe in it»
(Neil deGrasse Tyson)*

7.1 Introduction

Since the demonstration of amplified spontaneous emission (ASE) and optical gain in systems composed of colloidal semiconductor nanocrystals (NCs),^{1,2} these materials have gained tremendous interest due to their unique, versatile opto-electronic properties and facile processing. In particular, the tunable photoluminescent (PL) emission and high quantum yield, excellent photostability and nearly temperature-independent gain³ are the main features promoting NCs for lasing applications. NCs of different composition (*e.g.* CdSe/CdS, perovskites), and geometries (*e.g.* nanoplatelets, dot-in-rods), have therefore been thoroughly investigated as gain material for lasers during recent years.^{4–10} A major challenge hereby is the non-radiative exciton recombination by the Auger effect. Only recently, suppressed Auger recombination¹¹ and the first NC lasers with continuous wave excitation and “nearly zero” lasing thresholds ($\beta = 1$) through electrical pumping have been reported.^{12–14}

In the quest to realize efficient NCs-based lasers, NCs have been implemented in a large variety of systems and cavities. Today, most optical cavities are realized as distributed Bragg reflectors (DBR), distributed feedback lasers (DFB), or even as waveguide-coupled ring resonators.¹⁵ The combination of NC size control with a high quality cavity generally requires sophisticated and expensive fabrication methods. Importantly, NCs lasing has also been achieved with geometries that are much easier to fabricate, *e.g.* by simple drying of films of the NCs which, under the conditions for which the coffee stain effects are prevented, can be dried as smooth and thin films. However, these systems are operating in the random-lasing regime which lacks essential control over a huge number of lasing modes.^{8,16–18}

Ordered spherical assemblies of NCs, also known as supraparticles (SPs),^{19,20} have recently gained interest due to their collective properties which differ from those of the composing NCs and through new insights obtained on self-assembly in spherical confinement.²¹ For example, recently fabricated SPs can emit pure colors, or can be tailored to allow tunable light emission (*e.g.* white light).²² SPs themselves can be made through self-assembly (SA) inside the spherical confinement induced by slowly drying of oil-in-water emulsion droplets. By controlling the emulsification procedure, SPs can be tuned with a specific diameter between 100 and 10000 nm.^{19,23–25} Furthermore, SPs can be made to be water or oil dispersible, and can be realized as stable dispersions themselves, which strongly facilitates further processing or application of these systems. Additionally, it has been shown that the high effective refractive index that is realizable with SPs made from semiconductor NCs can lead to shape-dependent modulation of their photoluminescence emission (PL) originating from whispering gallery modes (WGMs),²⁶ thus in principle allowing the optical feedback necessary for obtaining lasing. Even though WGMs were observed in SPs, ASE, optical gain or lasing has not been demonstrated for these systems as far as we know.

Here, we report on optically pumped (pulsed laser with pulse duration of a few ps; see Appendix for further details) whispering gallery mode (WGM) lasing from self-assembled SPs composed of luminescent CdSe/CdS NCs, where the SPs act as both lasing cavity and gain medium. For very low excitation densities ($< 58 \mu\text{J}/\text{cm}^2$) we observe resonance peaks superimposed on the PL emission of the SPs, associated with WGMs with a quality factor

of about 320. When the excitation exceeds a certain threshold ($58 \mu\text{J}/\text{cm}^2$) we observe a discrete lasing peak and an effective 20-fold decrease in linewidth, superimposed on the WGMs, which evolves into a multi-mode regime for higher pump pulse fluence. WGM-based lasing is supported by coherence measurements, showing spatial coherence over the entire rim of the SPs for a duration comparable to the pump pulse duration, and by a shortening of the exciton lifetime of almost 3 orders of magnitude.

7.2 Results and Discussion

A scheme of the synthesis of the SPs is presented in Figure 7.1. The building blocks composing the SPs are CdSe/CdS NCs. They have an average diameter of $8.6 \pm 1.0 \text{ nm}$ (average diameter \pm standard deviation, as determined by Transmission Electron Microscopy - TEM), being composed of a 3.6 nm diameter CdSe core and 2.5 nm thick CdS shell (Figure 7.1a). Twice the distance of the interpenetrating layer of ligands adds 3.8 nm to the interparticle spacing in our close packed systems and, because of the monodispersity of the ligand molecules, reduces the total polydispersity of the particles to 8%. A dispersion of these NCs (volume fraction 0.06%) is used to produce SPs through self-assembly of NCs

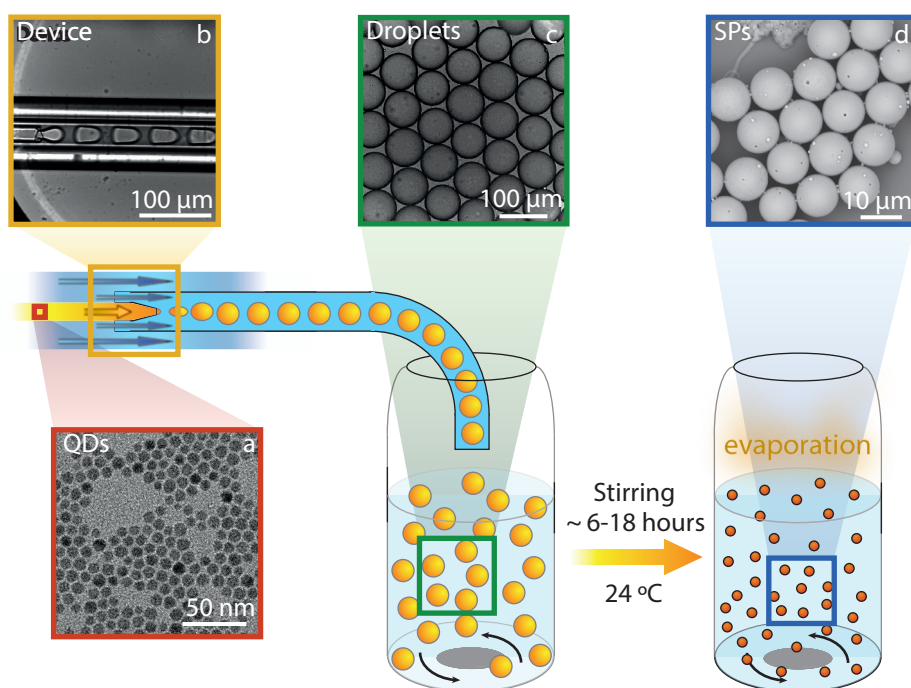


Figure 7.1 • Scheme of the synthesis procedure to make SPs. The synthesis procedure is based on an oil-in-water emulsion method. Cyclohexane droplets containing QDs (a) nearly monodisperse (polydispersity $< 5\%$) (yellow) are made in a microfluidic device (b) through the application of a shear force exerted by the continuous flow of water (blue). The droplets (c) are then stirred in a vial at room temperature for 6 to 18 hours to allow complete evaporation of the cyclohexane. In the end, we obtain monodisperse SPs dispersed in water (d). The insets show: transmission electron microscopy image of NCs (a), optical microscopy images of the device (b) and droplets (c), and scanning electron microscopy image of SPs (d).

enabled by evaporation of the apolar phase of an oil-in-water emulsion (see Appendix for further details).¹⁹ Nearly monodisperse ($< 5\%$) droplets of NCs solution (oil phase) were formed using an in-flow custom-made microfluidic chip (Figure 7.9 in Appendix), which allows precise control of the shear forces and of the relative fluxes of the oil and water phases (Figure 7.1b-c) thus pinching off droplets of a certain size.²⁷ After a certain amount of time (~ 6 -18 hours), which is directly related to the droplet size and many other factors influencing the flux of oil through the system, the oil phase dissolves and finally evaporates out of the water, thus confining the NCs in smaller volumes inducing self-assembly and, when all oil has gone, creates solid SPs (Figure 7.1d). The size of the SPs can be precisely tuned between $5\ \mu\text{m}$ and $15\ \mu\text{m}$ by controlling the size of the droplets and the initial volume fraction of NCs in the oil phase. The SPs used in this experiment have an average diameter of $10.2 \pm 0.5\ \mu\text{m}$, with a low polydispersity ($\text{PD} < 5\%$), and present a smooth spherical shape, as inferred from SEM pictures (Figure 7.1d and 7.5-6 in Appendix).

In Figure 7.2a, absorption and emission spectra of CdSe/CdS NCs (Figure 7.1a) are shown. The photoluminescence (PL) emission is centered at $2.015\ \text{eV}$ ($615\ \text{nm}$) with a full-width at half-maximum (FWHM) of $105\ \text{meV}$. The absorption exhibits the lowest excitonic transition at $2.087\ \text{eV}$ ($594\ \text{nm}$). The PL emission of a single SP under continuous wave excitation (CW) is shown in Figure 7.2. The PL emission of the SPs dispersion is centered at $2.003\ \text{eV}$ ($619\ \text{nm}$) with a FWHM of $102\ \text{meV}$. We observe a small general red shift ($12\ \text{meV}$) of the emission spectrum of the NCs self-assembled in the SPs (Figure 7.2b inset) compared to the NCs freely dispersed in solution. Furthermore, the SPs show whispering gallery mode (WGM) resonance peaks on the low energy side of the emission peak (Figure 7.2b). This phenomenon, previously described in literature for both acoustic waves²⁸ and light waves,²⁹⁻³¹ is based on the difference in refractive index between the material of the SPs ($n_{\text{eff}} \sim 1.7$ for $2\ \text{eV}$ and $27\ ^\circ\text{C}$; see Appendix for details) and the environment ($n_{\text{air}} \sim 1$), which allows total internal reflection of the light inside the SP. The higher the index contrast, the smaller the SP can be without losing the light confinement. WGM are formed when the optical path length of a round trip along the rim of the sphere is a multiple of the

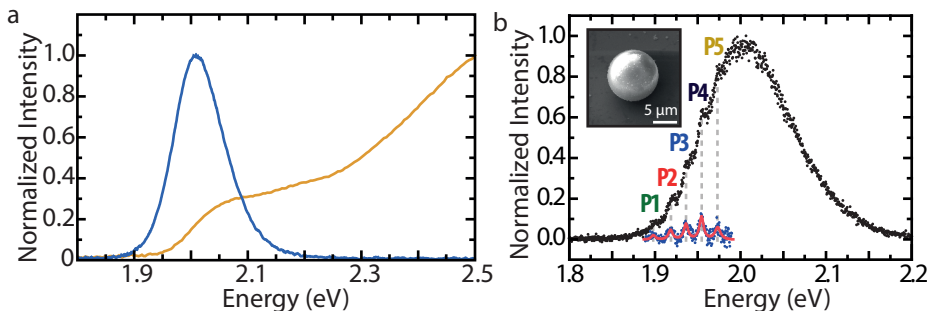


Figure 7.2 • Optical and structural characterization of the NCs in solution and assembled in the SPs. (a) Absorption (yellow) and PL emission (blue) of the dispersed CdSe/CdS NCs. The PL peak maximum is centered at $2.015\ \text{eV}$ with a fwhm of $\sim 105\ \text{meV}$; (b) PL emission of a single SP. The dashed grey lines indicate the position of WGM resonance peaks (numbered P1-5). The PL emission with removed background (blue) allows to highlight these resonance peaks, which are then fitted with multiple Lorentzian peaks (red).

wavelength and they can be observed as modulation of the PL emission spectrum.²⁶ We attribute the absence of WGM resonance peaks on the high energy side and the small general red shift of the PL emission to reabsorption losses deriving from the small Stokes shift typical of semiconductor NCs (Figure 7.1b). The free spectral range (FSR) of the WGM,³² defined as the spacing between two successive maxima, is $FSR = \lambda^2 / (n_{eff} L) = 6.3 \text{ nm}$, where λ is the resonance center wavelength, L is the cavity length ($L = 2\pi R$ for spherical cavities) and n_{eff} is the effective refractive index, is compatible with the radius R measured through SEM ($R = 5 \mu\text{m}$, Figure 7.5-6 in Appendix). Additionally, from the resonance peak width $\Delta\lambda$ in the PL spectra we are able to extract the quality factor $Q = \lambda / \Delta\lambda$ of the cavity, which, in our case, is typically around 320 (Figure 7.2b), and it is probably affected by the surface roughness of the SP and/or other imperfections in their shape.

Figure 7.3a shows PL spectra of a single SP at different excitation fluences. Lasing is observed at the spectral positions of the WGM resonance peaks with thresholds as low as $58 \mu\text{J}/\text{cm}^2$ (pulsed excitation; see Appendix for further details). This threshold fluence corresponds to an average number of excitons per dots of $\langle N \rangle = 2.5$ (using an absorption cross-section $\sigma = 6 \text{ nm}^2$)¹⁴, in agreement with previous observations for similar particles.^{33,34} The necessary modal gain at threshold can be estimated from the cavity Q factor by $\alpha = (2\pi n_{eff} / Q\lambda) = 900 \text{ cm}^{-1}$. The first lasing peak appears at 1.942 eV (P3 in Figure 7.3a), at the same spectral position as one of the modes observed in Figure 7.2b. This particular mode P3 is the first one to reach the lasing threshold as the effective gain of other modes is lower because of increasing reabsorption losses towards the blue side (P4), or lower material gain towards the red side (P2).

Increasing the excitation fluence, the intensity of the lasing peaks increases nonlinearly (Figure 7.3b), typical for optical gain conditions. Furthermore, the appearance of addi-

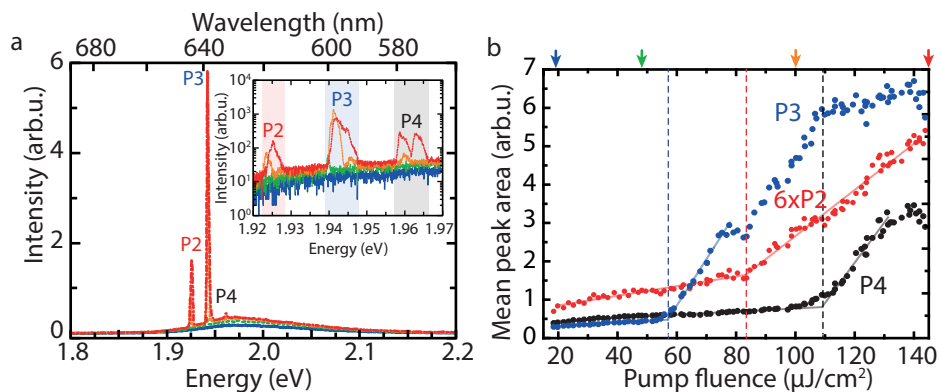


Figure 7.3 • Lasing of a single SP and quantitative analysis. (a) Emission from a single SP at different pump fluence (few ps pulse duration): $18 \mu\text{J}/\text{cm}^2$ (blue), $48 \mu\text{J}/\text{cm}^2$ (green), $100 \mu\text{J}/\text{cm}^2$ (orange) and $145 \mu\text{J}/\text{cm}^2$ (red) at low spectral resolution (300 lines/mm grating); (a inset) high spectral resolution (1800 lines/mm grating), revealing peak substructure (shaded regions denote areas used for analysis in b); (b) Quantitative analysis of the P2 – P4 mean peak areas (vertical dashed lines indicate the pump fluence at which new lasing peaks appear). The colored arrows above the graph indicate the pump fluence at which the respective spectra of panel (a) and (a inset) were taken.

tional lasing peaks, indicating multi-mode behavior (both longitudinal and transversal), is observed (Figure 7.3a). This phenomenon is particularly evident by monitoring the emission with a higher spectral resolution (Figure 7.3a inset), where also peak substructure becomes apparent. Multi-mode behavior is intrinsically associated to spherical cavities and broadband emitters, as several almost energetically degenerate modes exist. For low excitation fluence, only the modes with the highest Q and material gain will be able to lase, while for higher fluence more modes will fulfill the conditions of modal gain necessary to reach the lasing regime.

By quantitatively examining the evolution of the PL emission as a function of pump fluence (Figure 7.3b), the threshold characteristics of the different laser modes can be extracted. We observe that the emission intensity starts increasing superlinearly at a pump fluence of $\sim 58 \mu\text{J}/\text{cm}^2$, corresponding to the lasing threshold, and it keeps increasing with the same slope efficiency except for certain plateau regions. The main plateaus correspond to the appearance of new lasing modes of different longitudinal order that are competing for gain in the same spatial region (Figure 7.3a P2 – P4), thus indicating a multi-mode lasing regime with mode competition. We extracted the lasing threshold for different modes to be: $\sim 83 \mu\text{J}/\text{cm}^2$ for P2 and $\sim 110 \mu\text{J}/\text{cm}^2$ for P4 (Figure 7.3b). For NCs with substantially thicker shells, WGM lasing can be even observed from the blue side of the PL (due to lower absorption at the NC core) and the shell material (Figure 7.10 in Appendix).³⁵ Concerning the peak width, we observe 20-fold decrease in line width above threshold: below lasing threshold, P3 shows a line width of 10 meV, while it has a line width of 0.5 meV slightly above threshold. Further above threshold, the appearance of peak substructure due to onset of lasing from transversal modes (Figure 7.3a inset) increases the effective peak width again. We also note a slight general blue shift of the lasing peaks with increasing pump intensity, which is most likely due to the change of effective refractive index caused by bleaching³⁶ or the plasma dispersion effect.³⁷

In Figure 7.4a, the temporal first-order coherence of the lasing regime is probed by a Michelson interferometer, where the image of the emission is split and recombined at different delay times between the two interferometer arms. The spatial coherence is obtained by spatially inverting the image in one of the arms before recombining the two beams. Below lasing threshold, at $\sim 25 \mu\text{J}/\text{cm}^2$, we observe only interference fringes from PL autocorrelation, lasting for few femtoseconds, *i.e.* no spatially or temporally extended coherence is found. Above lasing threshold, at $\sim 100 \mu\text{J}/\text{cm}^2$, we observe interference fringes extending over the whole outer rim of the SP and lasting for several picoseconds (approximately as long as the pump pulse duration). This temporal and spatial coherence indicates that: (1) the SP is in the lasing regime and that the gain condition lasts, at least, for the pump pulse duration, and (2) that the lasing we are observing is spatially coherent. In the images, the light emission is mainly localized at the rim of the SP, as expected for a WGM. The inhomogeneity along the circumference suggests that it is actually scattered from the SP by local defects as otherwise the wavevectors of WGM in perfectly smooth spheres would be tangential, and therefore light leaking from the WGM could not be detected with our geometry where we image the SP from above. In addition to the well-defined free spectral range between the modes, this extended, ring-shaped spatial and temporal coherence crucially identifies the SPs as both cavity and gain medium, excluding the appearance of

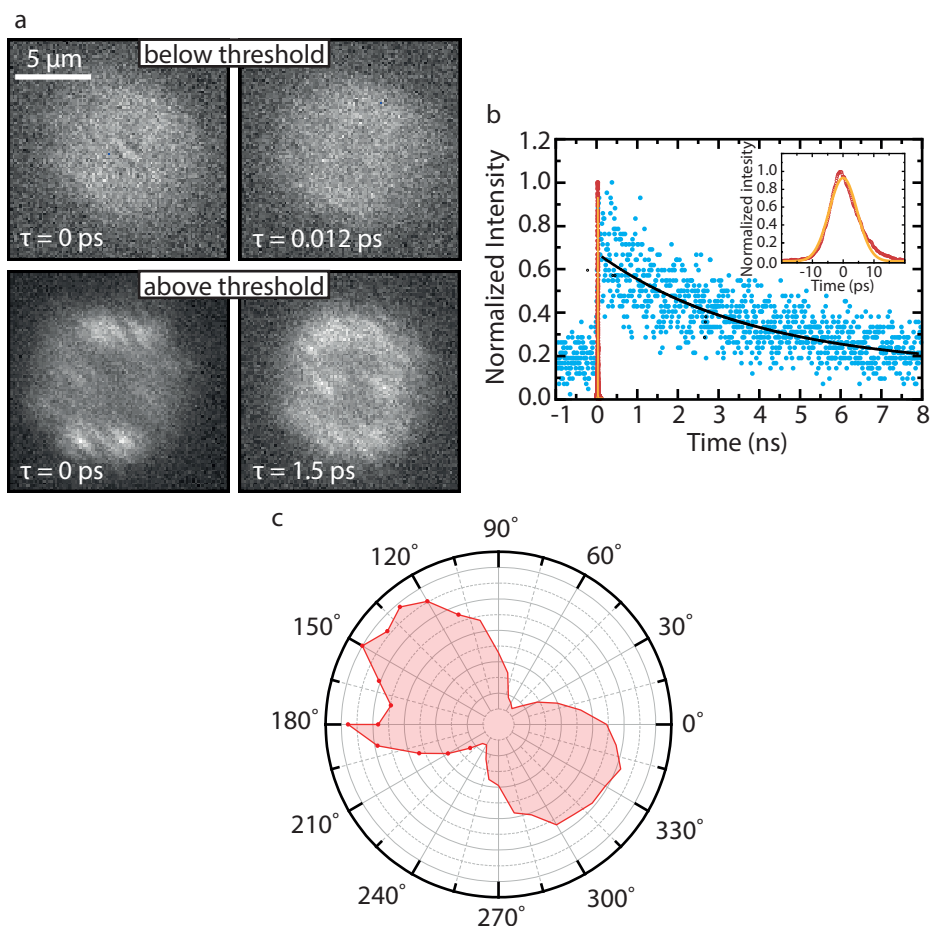


Figure 7.4 • Lasing dynamics and polarization. (a) Coherence measurements performed through a Michelson interferometer where the emission from the sample is split, and spatially inverted and delayed in one interferometer arm, and then recombined on a camera. Below lasing threshold ($\sim 25 \mu\text{J}/\text{cm}^2$ - top row) only very short and localized coherence is observed, lasting for few femtoseconds. Above lasing threshold ($\sim 100 \mu\text{J}/\text{cm}^2$ - bottom row) the spatial coherence extends over the whole outer rim of the SP, lasting for several ps; (b) PL lifetime measurements of a single SP. The lifetime below lasing threshold (in blue, and exponential fit with offset in black) is approximately 4 ns, while above lasing threshold (in red, and Gaussian fit in orange) the lifetime shortens by almost 3 orders of magnitude, leading to a short emission pulse with fwhm of 10.7 ps; (c) Polarization measurement of the emission above lasing threshold. The dumbbell-shaped angular intensity dependence represents a dominantly linear polarization.

random lasing in our NC assembly.¹⁶

Furthermore, we performed time-dependent emission measurements to study the excitation fluence dependent dynamics in the two regimes (Figure 4b). In the low excitation regime below lasing threshold ($\sim 25 \mu\text{J}/\text{cm}^2$), the SPs show an average PL lifetime of 4 ns, in agreement with a decay mainly governed by spontaneous emission. However, for higher

excitation fluence above lasing threshold ($\sim 100 \mu\text{J}/\text{cm}^2$), we observe a dramatic shortening of the emission lifetime by almost 3 orders of magnitude (FWHM of the emitted pulse is 10.7 ps) as a consequence of stimulated emission, further confirming lasing in the SPs. The spectral line width of 0.5 meV is about three times larger than the Fourier-limit of 0.17 meV, suggesting that additional spectral broadening from multi-mode lasing or spectral chirping occurs.

Additionally, we investigated the polarization of the emission of single SPs (Figure 7.4c). Under lasing conditions, the emission shows a dumbbell angular dependency that indicates dominantly linear polarization. In principle, for a WGM propagating perfectly parallel to the substrate, unpolarized emission should be detected in a spatially-integrating detector above the SP. The observed linear polarization, whose axis varies in orientation from SP to SP, could therefore arise from a tilted WGM propagation plane (as supported by FDTD simulations, see Figure 7.8 in the Appendix). Another reason could be the inhomogeneity of scattering around the WGM circumference (see discussion above, the ring in Figure 7.4a is not continuous) that scatters the respective local polarization orientation into the detector. Hence, seemingly linear polarization could be an artifact from the difference in scattering intensities around the circumference of the SP.

7.3 Conclusions

In conclusion, we created an optically-pumped WGM-based laser using self-assembled SPs composed of CdSe/Cds NCs, achieving thresholds as low as $58 \mu\text{J}/\text{cm}^2$. In addition to drastic peak narrowing and nonlinear emission, lasing is confirmed by shortening of the exciton lifetime by three orders of magnitude and by spatially and temporally extended coherence. Our experiments demonstrate that high-quality optical microresonators can be fabricated through controlled self-assembly of colloidal NCs, where the superstructure acts as both laser resonator and gain medium, avoiding the need of a separate lasing cavity fabrication and NCs positioning inside it. Notably, the SPs preserve their properties over many weeks of experiments without showing any significant degradation or stability issues. The applicability of the SP synthesis to every shape of NC (*i.e.*, nanoplatelets, nanorods^{38,39}) and the excellent control over the SP size through microfluidics makes these structures versatile and potentially valuable for several applications. The SP's compatibility with water allows them to be used in microfluidics and bio-compatible sensors. In fact, the sensitivity of WGM to the local environment could be exploited for sensors for biological⁴⁰ or security applications.⁴¹ Such active microlasers provide significant sensitivity improvement over sensors that use passive WGM resonators due to the high nonlinearity and sensitivity to additional absorption near the threshold as well as amplification and line-narrowing associated with the laser process.

7.4 Methods

Chemicals

Sodium dodecyl sulfate (SDS, $\geq 98.5\%$), Cadmium oxide (CdO, $\geq 99.99\%$), Octadecylphosphonic acid (ODPA, 97%), Trioctylphosphine oxide (TOPO, 99%), Trioctylphosphine (TOP, 90%), 1-octanethiol ($\geq 98.5\%$), Dextran from *Leuconostoc mesenteroides* (M_w 670000 g/mol), Hexane (anhydrous, 95%), Cyclohexane (anhydrous, 99.5%), Oleic acid (OA, 90%), Ethanol (EtOH, 99.8%), 1-Butanol anhydrous (BuOH, 99.8%), Methanol (MeOH, anhydrous, 99.8%) and Toluene (anhydrous, 99.8%) were all purchased by Sigma Aldrich and used as received. Selenium (Se, 99.999%) was purchased by Brunschwig Chemie CV.

Synthesis of CdSe NCs

The synthesis of CdSe NCs was performed according to literature.⁴² For this synthesis we first mixed 60 mg of CdO, 280 mg of ODPa and 3 g of TOPO in a 100 mL three neck flask. The mixture was heated to 150 °C and degassed under vacuum for 1 hour. The reaction was then put under nitrogen flow, and the temperature was increased up to 320 °C, where it was kept for 1 hour, until obtaining a colorless clear solution. Then, 1 mL of TOP was added to the mixture, and the temperature was increased to 380 °C, at which temperature a solution of Se-TOP (70 mg of Se in 0.5 mL of TOP) was quickly injected. After 30 s, the reaction was quenched by quickly reducing the temperature through the use of compressed air flow over the glass. The resulting particles were diluted with 1 volume equivalent of toluene and centrifuged at 3500 rpm for 10 min at room temperature. The NCs were extracted from the supernatant, while the precipitate, mainly containing TOPO and unreacted ODPa, was partially redispersed in toluene and centrifuged again in order to extract more NCs. All the collected NCs were then washed through precipitation upon addition of 1 volume equivalent of a mixture of MeOH/BuOH 1:3. This washing procedure was repeated twice and in the end the particles were redispersed in hexane.

Synthesis of CdSe/CdS shell

The synthesis of CdSe/CdS shell was performed according to literature.⁴² A 2 mL hexane solution containing 100 mmol of CdSe NCs was loaded in a three neck flask with 3 mL of ODE and 3 mL of oleylamine. The mixture was then degassed at room temperature for 1 hour under vacuum, and then 30 min at 120 °C in order to remove the hexane, the water and the oxygen. The mixture was then put under nitrogen flow and brought to 310 °C. When the temperature reached 240 °C, two separated solution of 2.5 mL of 0.1M Cd(OA)₂ in 6 mL ODE and 55 μL of 1-octanethiol in 6 mL of ODE (molar ratio Cd(OA)₂:1-octanethiol=1:1.2) were injected dropwise in the reaction mixture at a rate of 3 mL/h with the aid of a syringe pump. At the end of the injection, 1 mL of OA was injected in the mixture, which was then let react for 60 min at 310 °C. The resulting CdSe/CdS NCs were then washed through precipitation upon addition of 1 volume equivalent of a mixture of MeOH/BuOH 1:3. This washing procedure was repeated twice and in the end the particles were redispersed in cyclohexane.

Characterization of CdSe/CdS NCs

The resulting CdSe/CdS NCs had an overall diameter of 12.4 ± 1.0 nm (from TEM analysis), composed of an inorganic core and an organic ligand shell. The inorganic core had a diameter of 8.6 ± 1.0 nm, composed of a 3.6 nm in diameter CdSe core and a 2.5 nm thick CdS shell. The ligand shell was made of oleate ligands with an average length of 1.9 nm. The CdSe core NCs in solution had an emission peak centered at 2.134 eV (581 nm), while the core/shell CdSe/CdS NCs had their emission peak centered at 2.015 eV (615 nm).

Synthesis of SPs

The synthesis was performed in open air adapting a procedure from literature.¹⁹ First, the CdSe/CdS solution of NCs in cyclohexane in a concentration of ~ 1 mg/mL was prepared (volume fraction of ~ 0.0006). Then a water solution made of 10 mL of milli-Q water containing 60 mg of SDS, the surfactant, and 0.4 g of dextran was prepared. The emulsification was performed using a custom-made microfluidic chip (see below for a more detailed description). For this experiment we used 1000 μL/h for the water phase and 200 μL/h for the NCs dispersion, which produced droplets of 109 ± 4 μm of diameter (Figure 7.5a). The so-formed emulsion is collected in a vial containing water solution saturated with cyclohexane (in order to slow down the evaporation). The emulsion is then stirred at room temperature for 6-18 hours (depending on the droplet size) in a cylindrical vial (height of 57.5 mm and diameter of 27.3 mm), which was covered on the top by a layer of parafilm pierced by several 0.8 mm holes, in order to allow all the cyclohexane to evaporate. Through the spherical confinement of the evaporating droplet, the NCs are pushed together to form the SPs. The so-formed SPs have a diameter of 10.2 ± 0.5 μm, which, considering the initial volume fraction and the size of the droplets, is in agreement with our predictions of size, considering conservation of the mass of the NCs during the self-assembly. After the evaporation, the SPs are precipitated by centrifugation (3000 rpm for 20 min) and redispersed in milli-Q water. The SPs show a smooth surface and homogeneous internal distribution of the NCs (Figure 7.6). In order to prepare the samples for the experiment, the water solution of SPs was deposited on a silicon substrate, and then the water phase was evaporated to leave the SPs on the substrate. The same sample was used for the lasing measurements and for the SEM imaging.

Synthesis and characterization of CdSe/(Cd,Zn)S NCs with thick (Cd,Zn)S shell

The synthesis of the NCs was performed in accordance to literature (the “red emitting NCs” described in the SI of ref. ²²). The so-synthesized NCs consist of a 3.1 nm CdSe core with 5 monolayers (ML) of CdS, 1 ML of CdZnS and 1 ML of ZnS. These core/multi-shell NCs are nearly spherical with a diameter of 11.4 ± 1.5 nm (without

considering the oleate capping ligand shell), and the PL emission is centered at 1.977 eV (627 nm).

Optical characterization

The PL emission of a single SP shown in Figure 7.2b was measured using a continuous wave (CW) excitation source at 405 nm wavelength with $\sim 2 \mu\text{m}$ beam diameter and collected through a $100\times$ microscope objective with numerical aperture $\text{NA} = 0.5$. For all lasing measurements, we used a frequency-doubled regenerative amplifier seeded by a mode-locked Ti:sapphire laser, resulting in laser pulses of 100 – 200 fs duration with a repetition rate of 1 kHz. This light was coupled to 1 m-long multi-mode optical fiber with $10 \mu\text{m}$ core diameter in order to achieve a beam which is more homogeneous than a Gaussian beam (it is more similar to a flat-top profile), and pulse stretching to several ps pulse duration. An image of the beam profile and a cross section of the excitation beam on the sample are shown in Figure 7.7. The pump intensity is controlled with a movable gradient filter after the fiber. The excitation beam is focused with a long working distance apochromatic microscope objective ($10\times$, $\text{NA} = 0.26$) to a spot with $\text{fwhm} = 10 \mu\text{m}$ on the sample. The SPs of $\sim 10 \mu\text{m}$ diameter fit completely into the flat-top region of the beam profile.

The emitted light from the SPs is collected through the same objective lens. Suitable long-pass filters are used to block the excitation light. The emission is detected by a fiber-coupled spectrograph (0.5 m focal length monochromator, 300 lines/mm and 1800 lines/mm gratings) equipped with a liquid N_2 -cooled CCD (charge-coupled device) for the spectral measurements. The coherence measurements in Figure 7.4a were recorded using a Michelson interferometer. Here the light from the sample is split with a non-polarizing beam-splitter cube, recombined and focused after the Michelson interferometer on a cooled CCD, resulting in real-space interferograms. At the end of one interferometer arm, a hollow retroreflector is mounted on a motorized linear stage with an additional piezo actuator which inverts the image and provides an adjustable delay. The luminescence lifetimes shown in Figure 7.4b were recorded using a time-correlated single photon counting system with fiber-coupled avalanche photodiode (50 ps time resolution) for measurements below lasing threshold, and a streak camera (2 ps time resolution) for measurements above lasing threshold. The polarization was probed using a linear polarizer (extinction $>10000:1$) on a motorized rotation stage directly after the collecting objective lens.

Definition of polydispersity

All the values of sizes in the article are given with the mean (μ) and the standard deviation (σ) in the form: $\mu \pm \sigma$. Polydispersity of size is defined as $\text{PD} (\%) = (\sigma/\mu) \cdot 100$.

Electron microscopy

SEM images were acquired using a Phenom ProX electron microscope operated at 10 kV. A dual beam FIB (Fei Helios) operated at 30 kV was used for cross sections of the SPs.

Calculation of the refractive index

The refractive index of the SP has been calculated by modeling the SP as composed for the 66% (randomly packed spheres) from NCs and for the 34% by organic material (oleate capping and cyclohexane). The refractive index of the NCs has been calculated considering a core of CdSe of 1.8 nm in radius, covered by a 2.5 nm thick shell of CdS and a 1.9 nm thick ligand shell of oleate. We used the refractive index values for each component at 27 °C at a wavelength of 600 nm: 2.48 for CdSe (ref. ⁴³), 2.52 for CdS (ref. ⁴⁴), 1.46 for oleate (ref. ⁴⁵) and 1.43 for cyclohexane (ref. ⁴⁶). The effective refractive index of the SP is calculated by averaging the refractive indexes of the single component for their volume weight, thus obtaining a value of 1.69.

Acknowledgements

We thank Chris Kennedy for help with the microfluidics.

References

1. Klimov, V. I. *et al.* Optical Gain and Stimulated Emission in Nanocrystal Quantum Dots. *Science* **290**, 314–317 (2000).
2. Vandyshev, Y. V., Dneprovskii, V. S., Klimov, V. I. & Okorokov, D. K. Lasing on transition between quantum-well levels in a quantum dot. *Jetp Lett.* **54**, 442 (1991).
3. Moreels, I. *et al.* Nearly Temperature-Independent Threshold for Amplified Spontaneous Emission in Colloidal CdSe/CdS Quantum Dot-in-Rods. *Adv. Mater.* **24**, OP231-5 (2012).
4. Grim, J. Q. *et al.* Continuous-wave biexciton lasing at room temperature using solution-processed quantum wells. *Nat. Nanotechnol.* **9**, 891–895 (2014).
5. di Stasio, F. *et al.* Single-Mode Lasing from Colloidal Water-Soluble CdSe/CdS Quantum Dot-in-Rods. *Small* **11**, 1328–1334 (2014).
6. She, C. *et al.* Red , Yellow , Green , and Blue Amplified Spontaneous Emission and Lasing Using Colloidal CdSe Nanoplatelets. *ACS Nano* **9**, 9475–9485 (2015).
7. Wang, Y. *et al.* All-Inorganic Colloidal Perovskite Quantum Dots: A New Class of Lasing Materials with Favorable Characteristics. *Adv. Mater.* **27**, 7101–7108 (2015).
8. Yakunin, S. *et al.* Low-threshold amplified spontaneous emission and lasing from colloidal nanocrystals of caesium lead halide perovskites. *Nat. Commun.* **6**, 1–8 (2015).
9. Zhang, Q. *et al.* High-Quality Whispering-Gallery-Mode Lasing from Cesium Lead Halide Perovskite Nanoplatelets. *Adv. Funct. Mater.* **26**, 6238–6245 (2016).
10. Su, R. *et al.* Room-Temperature Polariton Lasing in All-Inorganic Perovskite Nanoplatelets. *Nano Lett.* **17**, 3982–3988 (2017).
11. García-Santamaría, F. *et al.* Suppressed Auger Recombination in ‘Giant’ Nanocrystals Boosts Optical Gain Performance. *Nano Lett.* **9**, 3482–3488 (2009).
12. Wu, K., Park, Y., Lim, J. & Klimov, V. I. Towards zero-threshold optical gain using charged semiconductor quantum dots. *Nat. Nanotechnol.* **12**, 1140–1147 (2017).
13. Lim, J., Park, Y.-S. & Klimov, V. I. Optical gain in colloidal quantum dots achieved with direct-current electrical pumping. *Nat. Mater.* **17**, 42–49 (2017).
14. Fan, F. *et al.* Continuous-wave lasing in colloidal quantum dot solids enabled by facet-selective epitaxy. *Nature* **544**, 75–79 (2017).
15. Xie, W. *et al.* On-Chip Integrated Quantum-Dot–Silicon-Nitride Microdisk Lasers. *Adv. Mater.* **29**, 2–7 (2017).
16. Gollner, C. *et al.* Random Lasing with Systematic Threshold Behavior in Films of CdSe/CdS Core/Thick-Shell Colloidal Quantum Dots. *ACS Nano* **9**, 9792–9801 (2015).
17. Di Stasio, F., Polovitsyn, A., Angeloni, I., Moreels, I. & Krahne, R. Broadband Amplified Spontaneous Emission and Random Lasing from Wurtzite CdSe/CdS “Giant-Shell” Nanocrystals. *ACS Photonics* **3**, 2083–2088 (2016).
18. Zavelani-Rossi, M. *et al.* Self-assembled CdSe/CdS nanorod micro-lasers fabricated from solution by capillary jet deposition. *Laser Photonics Rev.* **6**, 678–683 (2012).
19. de Nijs, B. *et al.* Entropy-driven Formation of Large Icosahedral Colloidal Clusters by Spherical Confinement. *Nat. Mater.* **14**, 56–60 (2015).

20. Montanarella, F. *et al.* Crystallization of nanocrystals in spherical confinement probed by *in-situ* X-ray scattering. *Nano Lett.* **18**, 3675–3681 (2018).
21. Wang, D. *et al.* Interplay between spherical confinement and particle shape on the self-assembly of rounded cubes. *Nat. Commun.* **9**, (2018).
22. Montanarella, F. *et al.* Composite Supraparticles with Tunable Light Emission. *ACS Nano* **11**, 9136–9142 (2017).
23. Wintzheimer, S. *et al.* Supraparticles : Functionality from Uniform Structural Motifs. *ACS Nano* **12**, 5093–5120 (2018).
24. Cramer, C., Fischer, P. & Windhab, E. J. Drop formation in a co-flowing ambient fluid. *Chem. Eng. Sci.* **59**, 3045–3058 (2004).
25. Baroud, C. N., Gallaire, F. & Dangla, R. Dynamics of microfluidic droplets. *Lab Chip* **10**, 2032 (2010).
26. Vanmaekelbergh, D. *et al.* Shape-Dependent Multiexciton Emission and Whispering Gallery Modes in Supraparticles of CdSe / Multishell Quantum Dots. *ACS Nano* **9**, 3942–3950 (2015).
27. Choi, C.H., Weitz, D. A. & Lee, C.-S. One Step Formation of Controllable Complex Emulsions: From Functional Particles to Simultaneous Encapsulation of Hydrophilic and Hydrophobic Agents into Desired Position. *Adv. Mater.* **25**, 2536–2541 (2013).
28. Strutt, John William, B. R. *The theory of sound*. London, MacMillan 2, (1878).
29. Mie, G. Beiträge zur Optik trüber Medien, speziell kolloidaler Metallösungen. *Ann. Phys.* **330**, 377–445 (1908).
30. Debye, P. Der Lichtdruck auf Kugeln von beliebigem Material. *Ann. Phys.* **335**, 57–136 (1909).
31. Chiasera, A. *et al.* Spherical whispering-gallery-mode microresonators. *Laser Photonics Rev.* **4**, 457–482 (2010).
32. Rabus, D. G. *Integrated Ring Resonators: The Compendium*. 127, (2007).
33. Smyder, J. A. *et al.* The influence of continuous vs. pulsed laser excitation on single quantum dot photophysics. *Phys. Chem. Chem. Phys.* **16**, 25723–25728 (2014).
34. Grivas, C. *et al.* Single-mode tunable laser emission in the single-exciton regime from colloidal nanocrystals. *Nat. Commun.* **4**, 1–9 (2013).
35. le Feber, B., Prins, F., De Leo, E., Rabouw, F. T. & Norris, D. J. Colloidal-Quantum-Dot Ring Lasers with Active Color Control. *Nano Lett.* **18**, 1028–1034 (2018).
36. Klimov, V. I., Schwarz, C. J., McBranch, D. W., Leatherdale, C. A. & Bawendi, M. G. Ultrafast dynamics of inter- and intraband transitions in semiconductor nanocrystals: Implications for quantum-dot lasers. *Phys. Rev. B* **60**, R2177–R2180 (1999).
37. Tanabe, T., Notomi, M., Kuramochi, E., Shinya, A. & Taniyama, H. Trapping and delaying photons for one nanosecond in an ultrasmall high-Q photonic-crystal nanocavity. *Nat. Photonics* **1**, 49 (2006).
38. Wang, T. *et al.* Self-Assembled Colloidal Superparticles from Nanorods. *Science*. **338**, 358–363 (2012).
39. Besseling, T. H. *et al.* Determination of the positions and orientations of concentrated rod-like colloids from 3D microscopy data. *J. Phys. Condens. Matter* **27**, 194109 (2015).
40. Haughey, A. M. *et al.* Organic semiconductor laser biosensor: Design and perfor-

- mance discussion. *IEEE J. Sel. Top. Quantum Electron.* **22**, (2016).
41. Rose, A., Zhu, Z., Madigan, C. F., Swager, T. M. & Bulović, V. Sensitivity gains in chemosensing by lasing action in organic polymers. *Nature* **434**, 876–879 (2005).
 42. Chen, O. *et al.* Compact high-quality CdSe-CdS core-shell nanocrystals with narrow emission linewidths and suppressed blinking. *Nat. Mater.* **12**, 445–51 (2013).
 43. Jensen, B. & Torabi, A. Refractive index of hexagonal II--VI compounds CdSe, CdS, and CdSe_xS_{1-x}. *J. Opt. Soc. Am. B* **3**, 857–863 (1986).
 44. Bieniewski, T. M. & Czyzak, S. J. Refractive Indexes of Single Hexagonal ZnS and CdS Crystals. *J. Opt. Soc. Am.* **53**, 496–497 (1963).
 45. O'Neil, M. J. *The Merck index : an encyclopedia of chemicals, drugs, and biologicals.* (Merck, 2001).
 46. Kerl, K. & Varchmin, H. Refractive index dispersion (RID) of some liquids in the UV/VIS between 20°C and 60°C. *J. Mol. Struct.* **349**, 257–260 (1995).
 47. Haase, M. F. & Jasna, B. Tailoring of High-Order Multiple Emulsions by the Liquid-Liquid Phase Separation of Ternary Mixtures. *Angew. Chemie* **126**, 11987–11991 (2014).

Appendix

Glass microfluidics for monodisperse droplet production

The ability to produce monodisperse droplets of a controllable size is an essential first step in the production of monodisperse SPs of tunable size. Here we describe a low-cost and simple microfluidic setup that can nonetheless be used to produce emulsions of a tunable size range between 50 μm and 220 μm in diameter with polydispersities under 5 %. Here, we provide a detailed, stepwise description of the device construction and show results that indicate the droplet size range for which this setup is applicable. The style of microfluidics device described here is referred to in the literature as the coaxial co-flow geometry. The design of the setup is based on earlier studies by Choi and coworkers²⁷ and Haasse and Bruijic.⁴⁷

Device label	Outer capillary	Emulsion outlet	Dispersed phase inlet
1	200 μm square	50 μm square	50 μm round
2	500 μm square	100 μm square	50 μm round in 200 μm square*
3	500 μm square	200 μm square	100 μm round
4	500 μm square	200 μm square	200 μm round

Table 1 • Table of four different types of device designs that can be used to make droplets from 50 μm to 220 μm . The displayed capillary sizes are inner diameters for round capillaries and inner edge lengths for square capillaries. *To ensure that the 50 μm capillary is positioned in the middle of the outer capillary and lines up with the outlet capillary, it is encased in a 25 mm long 100 μm wide square capillary and fixed with ultra-violet-curable glue.

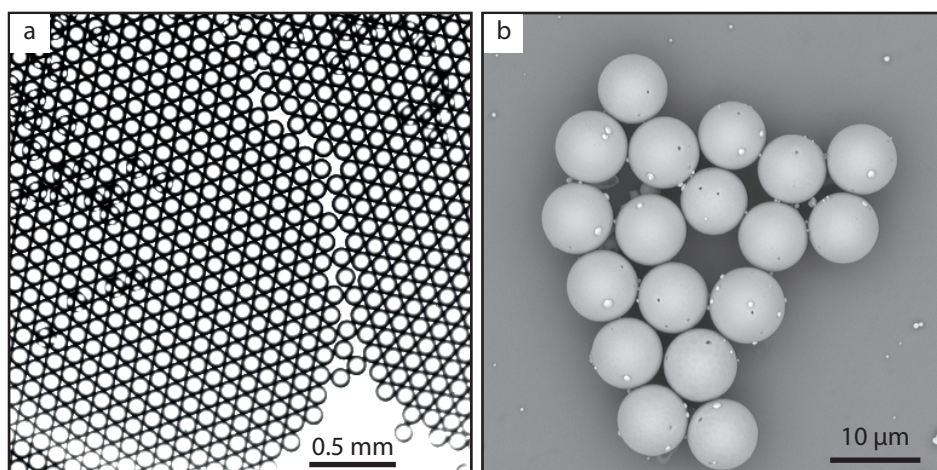


Figure 7.5 • Representative images of droplets and SPs. (a) Optical image of droplets of cyclohexane containing NCs. The average diameter of the droplets is $109 \pm 4 \mu\text{m}$; (b) SEM image of SPs formed from the droplets of panel a. The average diameter of the droplets is $10.2 \pm 0.5 \mu\text{m}$.

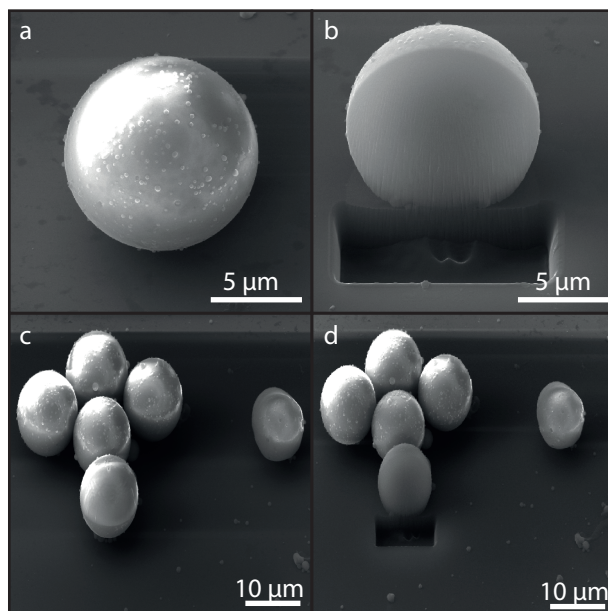


Figure 7.6 • Focused Ion Beam (FIB) SEM images of SPs. (a) SEM image of a single SP; (b) FIB-SEM of the SP of panel a, showing that the SP is close-packed with NCs on the inside; (c) SEM image of a group of SPs; (d) FIB-SEM of one of the SPs of panel c, showing again that the SP is filled on the inside.

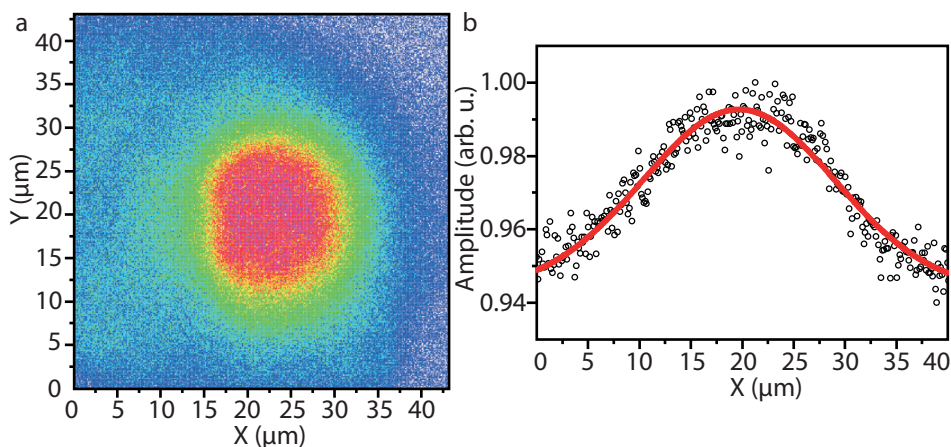


Figure 7.7 • Profile and cross section of the excitation beam. (a) Excitation spot imaged by monitoring the PL from a spin-coated 35 nm-thick luminescent polymer film on a cover slip; (b) Cross section of the excitation beam. In black are the data points, showing a fwhm of 22 μm .

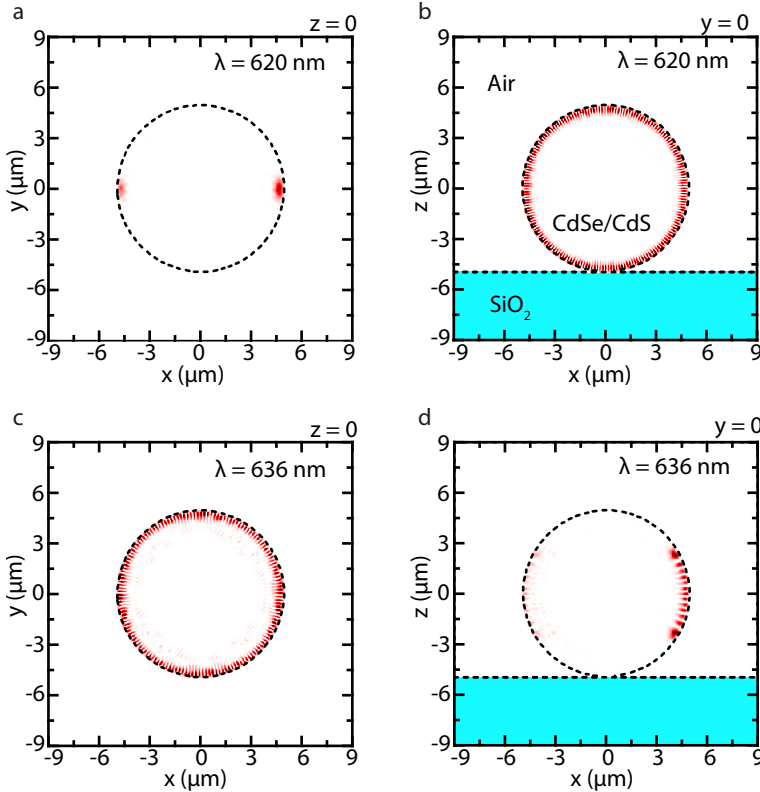


Figure 7.8 • Finite-difference time-domain simulation of WGMs supported by SPs. Dashed lines represent the contours of the SP, the blue colored area shows the SiO_2 substrate, and the normalized electromagnetic field intensity is shown in shades of red where darker color corresponds to higher intensity. (a) Cross section in the xy plane of the SP of a WGM propagating orthogonal to the substrate. When viewed from above, this will appear as linearly polarized light; (b) zx cross section of the same mode presented in a; (c) WGM travelling in the xy plane of the SP. When viewed from above, the rotational symmetry would make it appear as unpolarized light; (d) zx cross section of the same mode presented in c. The seeming asymmetry is an artifact from the cross section where on the left the cut goes through a node and on the right through an antinode of the WGM field. While here the two extreme cases of WGM perfectly normal and perfectly perpendicular to the substrate are shown, WGM with planes at tilt angles in-between are also possible.

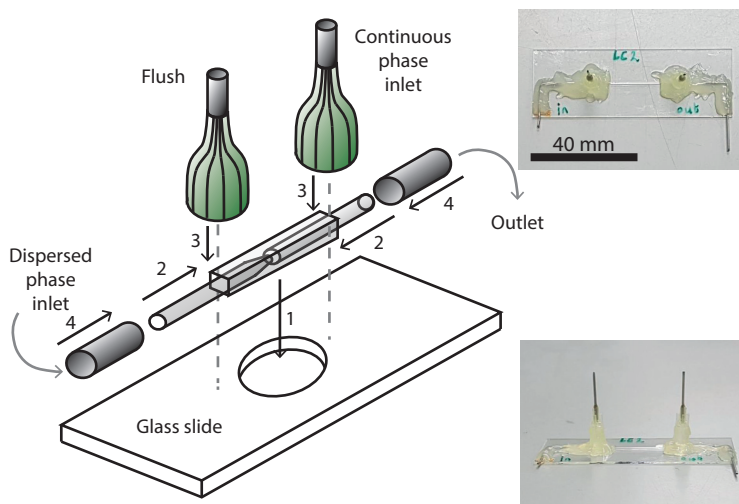


Figure 7.9 • Microfluidic chip design. Transparent shapes represent glass capillaries. Gray tubes represent metal needles from syringe heads. Green shapes represent plastic syringe heads. The numbers indicate the order in which to add parts and correspond to the step number described in the design setup section.

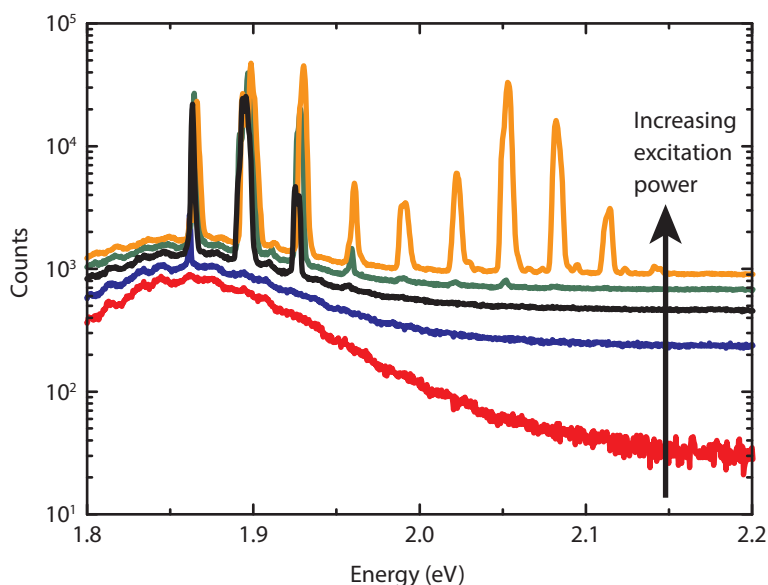


Figure 7.10 • Lasing from SP of CdSe/(Cd,Zn)S NCs with thick (Cd,Zn)S shell. For sufficiently high excitation fluences, we observe lasing from the thick CdS shell of the NCs in the range 1.975 – 2.15 eV. The curves are vertically offset for clarity. To reduce heating from excess pump photon energy, we used pulsed excitation with a wavelength of 500 nm instead of 400 nm (using a travelling-wave optical parametric amplifier instead of frequency doubling of the regenerative amplifier output) focused to a 10× larger spot.

Chapter 8

Summary and Outlook

Abstract

The experiments presented in this thesis have provided insight in the collective phenomena emerging from the self-assembly of colloidal nanocrystals into spherical superstructures called supraparticles. This work has helped to deepen our understanding on (1) the formation of these supraparticles and the structural phenomena of the SP associated to their formation, and (2) the optical properties arising from the interactions between the composing nanoparticles and the surrounding environment. Here we summarize the main results and we draw potential guidelines for future research.

*«I've seen things you people wouldn't believe,
attack ships on fire off the shoulder of Orion,
I watched C-beams glitter in the dark near the Tannhäuser Gates»
(Rutger Hauer - Blade Runner)*

8.1 Introduction

Colloidal semiconductor nanocrystals, with a roughly spherical shape also named quantum dots (QDs) due to their 3D electron confinement, constitute nowadays one of the most investigated fields of nanoscience due to their remarkable size-dependent opto-electronic properties. Thanks to these properties, QDs are already implemented in displays and backlighting applications and their future looks now brighter than ever with forecasted applications such as lasers and luminescent solar light concentrators. In most of the applications QDs are in close-packed arrangements, which, in some cases, triggers the emergence of collective properties. In this thesis we investigated the spontaneous assembly (*i.e.* self-assembly) of colloidal nanocrystals into three dimensional spherical supraparticles (SPs) and the structural and optical phenomena emerging from this configuration. The phenomena here presented are meant to give an example of the potential of these superstructures and, hopefully, trigger the inception of intriguing experiments combining structural and optical properties.

8.2 Structural phenomena

In the first part of this thesis (Chapters 3 & 4) we investigated the structural phenomena emerging from the self-assembly of nanocrystals with different geometries in the spherical confinement of an oil-in-water droplet.

In **Chapter 3**, we showed that two dimensional semiconductor nanoplatelets can be self-assembled in SPs with a general retention of their optical properties (Figure 8.1a). The nanoplatelets in the SPs form small stacks, due to the strong attractive forces between the ligand-covered facets, which are randomly oriented in the supraparticles. Hetero-nanoplatelets with different composition and geometry (*i.e.* core, core/shell and core/crown)

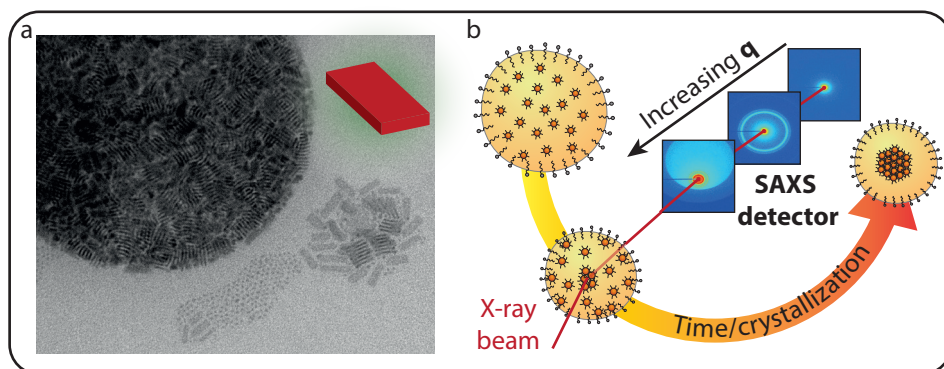


Figure 8.1 • Structural phenomena in nanocrystalline SPs. (a) In Chapter 3, CdSe nanoplatelets with different shape, composition and size have been self-assembled in spherical SPs. Nanoplatelets can be found stacked face-to-face inside the SPs, thus forming small columns randomly oriented in space. The optical properties of the self-assembled nanoplatelets differ only in minor details in comparison to the free suspension configuration. (b) In Chapter 4 we followed the crystallization of FeO/CoFe₂O₄ nanoparticles into SPs inside oil in water droplets by means of X-ray scattering. The wide q range probed in our experiment allowed us to follow the formation process in a large spatial domain, ranging from the shrinking micron-sized droplets down to the positions of the nanocrystals in the droplets after self-assembly with distances a factor 1000 x smaller.

have been synthesized and used as building blocks for the formation of SPs, showing that spherical SPs and/or compact structures could still be formed through the self-assembly process. We also performed a preliminary study on the optical properties of the nanoplatelets in the self-assembled configuration in comparison to the free suspension configuration in order to shed some light on the consequences of the self-assembly on the exciton dynamics.

In **Chapter 4** we performed a thorough study on the mechanism of self-assembly of spherical nanocrystals in an oil droplet in water, which through its surface tension provides a spherical confinement for the self-assembly, *in situ* by means of X-ray scattering (Figure 8.1b). Our results show that the crystallization of the nanocrystals into SPs sets in at a volume fraction of 0.20, suggesting that the attractive forces between the nanoparticles used in this study play an important role in this process. In particular, the fast crystallization process (7.5 min) suggests that the crystallization proceeds through the homogeneous nucleation of several face-centered-cubic (FCC) crystals inside the droplet. The crystals grew in size over time and merged to form SPs composed of a few FCC crystalline domains. Our results are supported by simulations, which gave us further insight into the SP formation process in this case.

8.3 Optical phenomena

In the second part of this thesis (Chapter 5, 6 & 7) we investigated optical phenomena observed in SPs composed of CdSe (core)/ CdS (shell) nanocrystals and arising from either the excitonic interaction between excitons in adjacent nanocrystals, or from the interactions between the nanocrystals and the surrounding environment. These optical phenomena bear particular importance for a future use of QD SPs in applications such as phosphors for displays applications and sensors.

In **Chapter 5** we studied the relation between spontaneous emission, charge carrier trapping and resonant energy transfer in QD assemblies (Figure 8.2a). In particular we showed that reversible charge-carrier trapping slows down the Förster energy transfer between neighboring QDs. While the energy transfer shifts the photoluminescent (PL) emission of the QDs in the SPs towards lower energies in the first 50 ns after excitation, this trend is reversed at later delay times by the release of charge carriers from zero oscillator strength states to the emissive exciton state. This previously “frozen” exciton can then recombine giving rise to PL emission of the same energy as in the initial stage, thus apparently blue shifted with respect to the emission in the intermediate time domain. Our results are supported by Monte Carlo simulations of the exciton dynamics in QD SPs, giving further quantitative insight on the effective role of the charge carrier trapping on the slowdown of the energy transfer.

In **Chapter 6** we presented SPs with tunable emission, composed of Cd(Se,ZnS) core/(Cd,Zn)S shell QDs emitting in different regions of the PL spectrum (Figure 8.2b). These composite SPs were structurally characterized, showing an intrinsic amorphous structure due to the shape and size differences of the composing nanocrystals. By changing the ratio of the composing QDs (emitting in the blue, green and red) in the SPs, we achieved the possibility to fine-tune the emission of the SPs in a wide range of the CIE (Commission

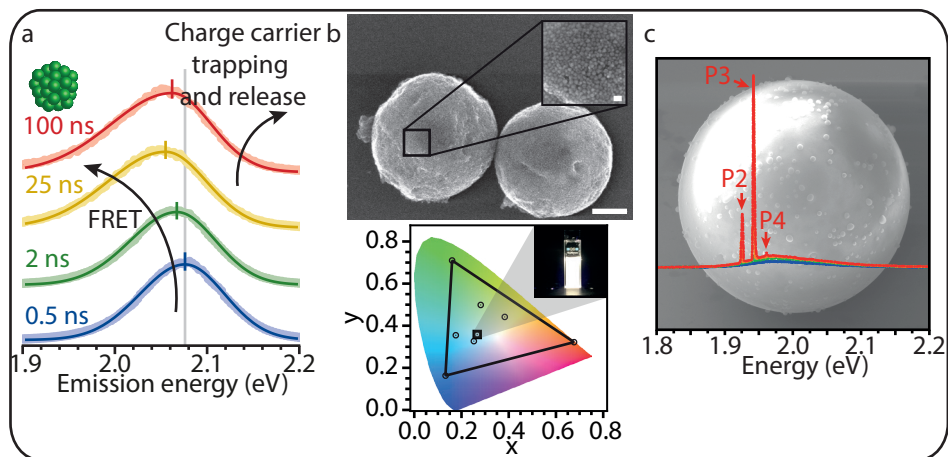


Figure 8.2 • Optical phenomena in nanocrystalline SPs. (a) In Chapter 5 we demonstrated that charge carrier trapping and release reverts the red-shift of the PL produced by Förster resonant energy transfer. (b) In Chapter 6 we produced composite SPs out of three different populations of QDs characterized by emission in different regions of the visible spectrum. The emission of the SPs can thus be fine-tuned in a wide range of the CIE diagram only by changing the ratio between the composing QDs. (c) Monodisperse QD SPs can be used as microresonator due to the presence of whispering gallery modes. In Chapter 7 we showed that, by means of optical excitation, these particles can be used to produced laser light as the single SPs are lasing cavity and gain medium at the same time.

Internationale de l'Éclairage) diagram by means of additive mixing of colors.

In **Chapter 7** we demonstrated the possibility to use CdSe (core) / CdS (shell) QD SPs as lasing cavities (Figure 8.2c). Thanks to the high difference in the refractive index of the SPs compared to the surrounding environment, light can be confined inside the SPs as a standing wave thus producing whispering gallery modes strong enough for lasing if the size and quality of the SP are good enough. We synthesized several micron sized SPs with low polydispersity in size (< 5%) by using a custom-made microfluidic device. By means of optical excitation we generated whispering gallery waves in single SPs and we observed, for the first time, optical gain and lasing. Lasing was confirmed by a drastic reduction of the PL lifetime by three orders of magnitude and by the appearance of spatially and temporally extended coherence. This means that the whispering gallery modes initiate the stimulated emission of resonant excitonic states. Our results demonstrate that SPs self-assembled from colloidal QDs can be used as microresonator, where the SPs themselves act both as lasing cavity and gain medium.

8.4 Outlook

Hopefully, the results presented in this thesis may inspire other researchers to study the collective structural and optical phenomena that may emerge in supraparticles composed of 1D, 2D and 0D semiconductor nanocrystals.

Concerning the structural phenomena, I believe that further experiments could be carried out by means of X-ray scattering in order to investigate the role of the size of the nanocrystal-

tals on the crystallization dynamics of SPs. In particular simulation results show that the size and the composition of the nanocrystal determine the extent of the nanocrystal-nanocrystal van der Waals forces, which, we showed, can play a pivotal role in the determination of the volume fraction at which the crystallization begins.¹ In this sense it would be interesting to repeat the experiment of chapter 4 with nanocrystals of smaller sizes and of different composition (*e.g.* CdSe, Au, Pd), as few reports indicate different crystallization behaviors for other nanoparticle systems.^{2,3}

Concerning the optical phenomena, the results in Chapter 6 suggest for further optical experiments. In particular it would be interesting to investigate the use of these particles as phosphors for lighting applications. In this sense, experiments on the resistance of these objects to optical bleach upon high excitation intensity, and on their resistance to high temperatures over time should be performed to possibly unlock their implementation in LEDs. Furthermore, the possibility to form QD SPs highly monodisperse in size opens the door to the realization of superstructures with structure-dependent optical properties (*e.g.* photonic crystals made of SPs). In this sense, SPs of polymeric spheres with sizes comparable to visible light have shown optical phenomena merely arising from their structure, such as structural coloration.⁴⁻⁶ The use of optically active materials, such as QDs, combined with the structural coloration of the superstructures, would result in materials characterized by peculiar optical properties, such as photonic crystals. Finally, the recent reports on binary SPs,^{7,8} *i.e.* crystalline SPs composed of two nanocrystals, would be an interesting playground for studies aimed to capture the relation between optical properties and the field of plasmonics, whether these binary SPs would be composed of QDs and, for example, gold or silver nanoparticles.

References

1. Evers, W. H. *et al.* Entropy-driven formation of binary semiconductor-nanocrystal superlattices. *Nano Lett.* **10**, 4235–4241 (2010).
2. Marino, E., Kodger, T. E., Wegdam, G. H. & Schall, P. Revealing Driving Forces in Quantum Dot Supercrystal Assembly. *Adv. Mater.* **1803433**, 1–6 (2018).
3. de Nijs, B. *et al.* Entropy-driven Formation of Large Icosahedral Colloidal Clusters by Spherical Confinement. *Nat. Mater.* **14**, 56–60 (2015).
4. Phillips, K. R. *et al.* A colloidoscope of colloid-based porous materials and their uses. *Chem. Soc. Rev.* **45**, 281–322 (2016).
5. Vogel, N. *et al.* Color from hierarchy: Diverse optical properties of micron-sized spherical colloidal assemblies. *Proc. Natl. Acad. Sci.* **112**, 10845–10850 (2015).
6. Goerlitzer, E. S. A., Klupp Taylor, R. N. & Vogel, N. Bioinspired Photonic Pigments from Colloidal Self-Assembly. *Adv. Mater.* **30**, 1706654 (2018).
7. Wang, P., Qiao, Q., Zhu, Y. & Ouyang, M. Colloidal Binary Supracrystals with Tunable Structural Lattices. *J. Am. Chem. Soc.* **140**, 9095–9098 (2018).
8. Wang, D. *et al.* Binary icosahedral quasicrystals of hard spheres in spherical confinement. *Submitted* (2018).

Samenvatting in het Nederlands

Overzicht

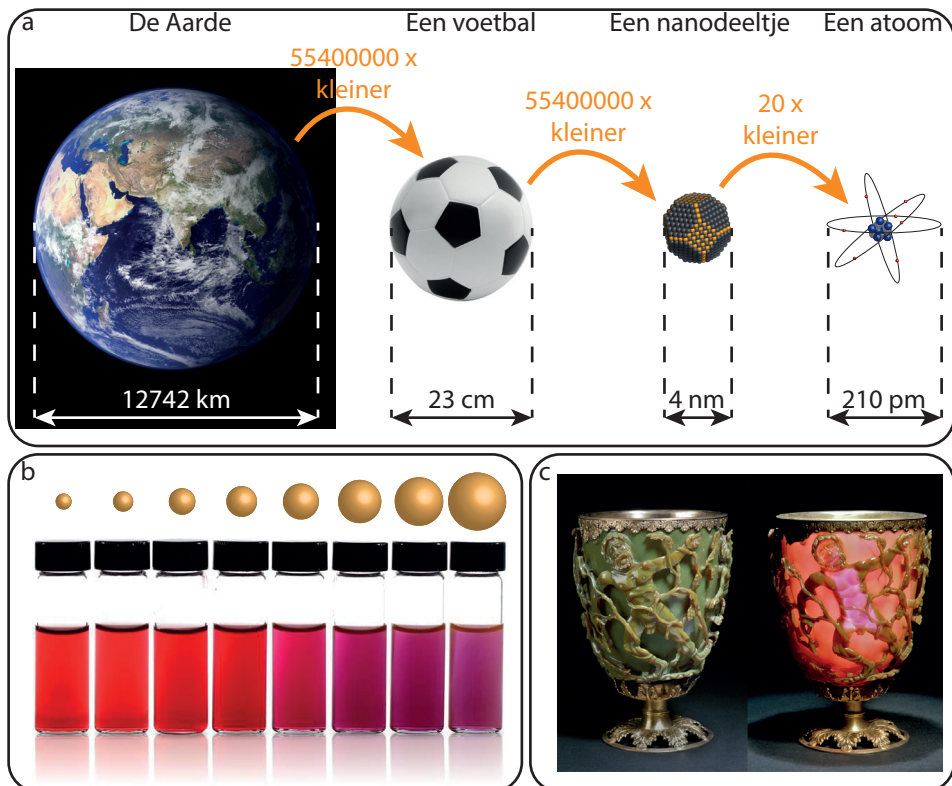
In dit hoofdstuk wordt het onderzoek beschreven in dit proefschrift toegelicht voor een breder publiek. Na een algemene introductie over halfgeleiders en nanokristallen, worden de belangrijkste resultaten die verkregen zijn besproken. Hierna wordt kort voorgesteld wat vervolgstappen kunnen zijn voor verder onderzoek.

*«I speak Spanish to God, Italian to women,
French to men, and German to my horse»
(Charles V)*

I. Introductie

Het onderzoek in dit proefschrift, zoals de titel al suggereert, gaat over de optische en structurele eigenschappen die voortvloeien uit de zelf-organisatie van colloïdale halfgeleider nanokristallen. Uit deze zin kunnen al verschillende vragen naar boven komen: wat is zelf-organisatie? Wat is een halfgeleider? Waar komt het woord 'nano' vandaan? Wat is een kristal? Waarom wordt dit onderzoek überhaupt gedaan? In de komende pagina's probeer ik deze vragen te beantwoorden en geef ik de lezer een kort overzicht van het onderzoek dat ik gedaan heb de afgelopen vier jaar.

Veel technologie is tegenwoordig gebaseerd op het gebruik van halfgeleiders. De smartphones in onze broekzak, de televisie- en computermonitors thuis en de zonnecellen die energie opwekken, zijn allemaal gebaseerd op halfgeleidertechnologie. De meeste van deze apparaten zijn gebaseerd op het materiaal silicium. Materialen kunnen in verschillende groepen worden ingedeeld op basis hun eigenschappen. Als we de mogelijkheid

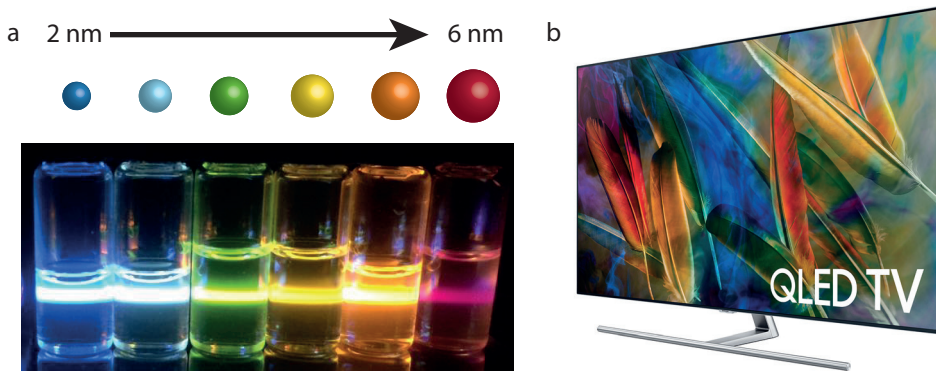


Figuur 1 • Nanokristallen en de nanoschaal. (a) Wanneer we de diameter van de Aarde met een voetbal vergelijken, dan is de voetbal 55 miljoen keer kleiner. Een nanokristal uit dit proefschrift is ruwweg 55 miljoen keer kleiner dan een voetbal, en een atoom is weer 20 keer kleiner dan een nanokristal. (b) Bulk goud is metallisch geel, maar colloïdale oplossingen van goud nanokristallen hebben een kleur die afhangt van de grootte van de kristallen. (c) De beroemde Lycurgus beker, daterend uit de vierde eeuw na Christus, is gemaakt uit glas met goud en zilver nanodeeltjes erin. Dit resulteert in een groene reflectie- en een rode transmissiekleur.

voor het transporteren van elektronen als eigenschap bekijken, kunnen we materialen in drie verschillende groepen opdelen: geleiders, halfgeleiders en isolatoren. Geleiders zijn materialen waarin elektronen gemakkelijk getransporteerd kunnen worden (bijvoorbeeld metalen). Isolatoren zijn materialen waarin elektronen juist niet gemakkelijk getransporteerd kunnen worden (bijvoorbeeld hout of plastic). Halfgeleiders zijn materialen waarin elektronen pas getransporteerd kunnen worden als er een bepaalde hoeveelheid energie aan het materiaal wordt toegevoegd. Deze energie kan op verschillende manieren aan het materiaal worden toegevoegd, zoals door bestraling met licht (zichtbaar, ultraviolet of infrarood licht), of bijvoorbeeld door het aanleggen van een elektrische potentiaal. Deze eigenschap is met name relevant voor halfgeleiders die intrinsiek al de mogelijkheid hebben om met zichtbaar licht een bepaalde wisselwerking aan te gaan. Als een dergelijk materiaal zichtbaar licht absorbeert, worden vrij beweegbare elektronen gecreëerd: er wordt stroom opgewekt, relevant voor bijvoorbeeld in zonnecellen. Of wanneer er extern elektronen worden toegevoegd kunnen deze materialen licht uitzenden, zoals in LEDs. Door al deze eigenschappen hebben halfgeleiders een belangrijke rol in onze maatschappij. Het huidige Tijdperk van Informatie waarin we leven, wordt daarom ook wel de “Silicon Age” genoemd.

Behalve ‘halfgeleider’ is een ander belangrijk begrip van dit proefschrift het woord ‘nanokristal’. Een kristal is een vaste stof waarvan de bouwstenen op een geordende manier in de ruimte geplaatst zitten. Een sneeuwvlokje bestaat bijvoorbeeld uit een regelmatige ordening van watermoleculen. Het woord ‘nano’ geeft aan dat het gaat over lengteschalen van één biljoenste van een meter. Een nanokristal is dus een object waarvan de atomen netjes geordend zijn, en waarvan de afmeting een aantal nanometer is. Om de lezer een idee te geven is er het volgende voorbeeld: als we de Aarde bekijken is deze ongeveer 55 miljoen keer groter dan een voetbal. Als we nu op dezelfde manier een voetbal bekijken ten opzichte van een nanokristal, dan is de voetbal 55 miljoen keer groter, zoals weergegeven in Figuur 1a. Wanneer nanokristallen dergelijke kleine afmetingen hebben, worden de materiaaleigenschappen anders dan wanneer ze veel groter zijn; op de nanoschaal heeft de grootte van een kristal sterke invloed op de eigenschappen. Laten we als voorbeeld het element goud bekijken. In zijn macroscopische vorm heeft puur goud de kleur geel. We kunnen de grootte van een klomp goud veranderen, maar de kleur verandert daarbij niet. Als we nanokristallen van goud maken die in een vloeistof zijn opgelost, ook bekend als colloïdaal goud, dan zal de kleur van deze gouddeeltjes afhangen van hun grootte (zie Figuur 1b). Dit effect was al bekend bij onze voorouders, die goudpoeders langer of korter fijn maalden (wat resulteerde in gouddeeltjes met verschillende groottes) en mengden met ceramische stoffen of glas en zo een gewenste kleur te verkrijgen. Een mooi voorbeeld is bijvoorbeeld de Lycurgus beker uit de laat-Romeinse tijd (Figuur 1c). Voor een halfgeleider is het ook mogelijk om de kleuren die het materiaal opneemt of uitzendt te veranderen door alleen de grootte van de nanokristallen aan te passen.

Colloïdale halfgeleider nanokristallen zijn dus deeltjes van een paar nanometer groot, die in een oplosmiddel zijn gedispergeerd (bijvoorbeeld water of toluen). Omdat de interactie met licht kan worden gestuurd simpelweg door de grootte van de kristallen aan te passen, zijn deze materialen erg aantrekkelijk voor toepassingen in bijvoorbeeld zonnecellen, LEDs en lasers. Tegenwoordig worden colloïdale halfgeleider nanokristallen, beter



Figuur 2 • Colloïdale halfgeleider nanokristallen en hun toepassingen. (a) De emissie van CdSe nanokristallen kan gevarieerd worden over het gehele zichtbare spectrum door de grootte van de nanokristallen tussen 2 nanometer (blauw) en 6 nanometer (rood) te variëren. (b) De eerste LED-telvisies met kwantum dots zijn recentelijk op de markt gebracht.

bekend als kwantum dots, al toegepast in televisies en computer displays (Figuur 2b), en de eerste LEDs gebaseerd op kwantum dots komen waarschijnlijk binnen enkele jaren op de markt. In sommige van deze toepassingen zijn de kwantum dots dicht op elkaar gestapeld, wanordelijk of geordend gerangschikt. In deze configuraties gaan kwantum dots een interactie met elkaar aan, die leidt tot bijzondere collectieve eigenschappen.

Tijdens mijn promotietraject heb ik onderzoek gedaan naar de optische eigenschappen van kwantum dots in oplossing en van kwantum dots in geordende bolvormige structuren genaamd supradeeltjes. De supradeeltjes worden gemaakt door de kwantum dots spontaan te laten zelf-organiseren via speciale experimentele technieken. Simpel gezegd maken we van de nanokristallen (kristal van geordende atomen) een groter kristal (kristal van nanokristallen). Ik heb eerst de structuur van deze kristallen van nanokristallen bestudeerd en vervolgens de optische eigenschappen. De optische eigenschappen ontstaan uit de interacties tussen de nanokristallen in het supradeeltje. Mijn onderzoek heeft geleid tot meer begrip over de vorming van de supradeeltjes en over de gezamenlijke optische eigenschappen van de nanokristallen in de supradeeltjes. Dit leidt, hopelijk, tot meer onderzoek in deze richting, meer kennis in deze tak van nanowetenschappen en wellicht tot meer gebruik van kwantum dots en supradeeltjes in commerciële toepassingen.

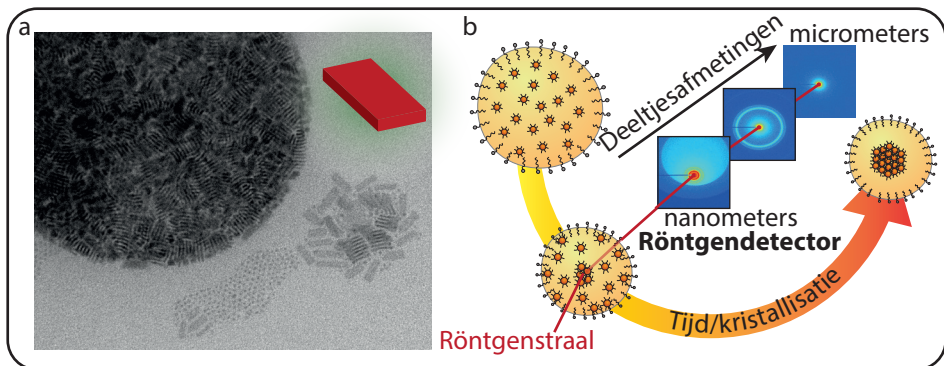
II. Structurele fenomenen

In het eerste deel van dit proefschrift, Hoofdstuk 3 en 4, hebben we de structuren bestudeerd die voortkomen uit de zelf-organisatie van nanokristallen met verschillende geometrieën in bolvormige druppels van olie in water. Oliedruppels met gedispergeerde kwantum dots verdampen langzaam, waardoor de kwantum dots dichter op elkaar gedrukt worden, en uiteindelijk een supradeeltje vormen.

In **hoofdstuk 3** hebben we laten zien dat twee-dimensionale halfgeleider nanoplaatjes gezelf-assembleerd kunnen worden in supradeeltjes met behoud van hun optische eigenschappen (Figuur 3a). De nanoplaatjes vormen rijen van deeltjes door sterke aantrek-

kingskrachten tussen de vlakken (die bedekt zijn met liganden ten behoeve van colloïdale stabiliteit) en deze rijen zijn weer willkeurig georiënteerd in een supradeeltje. Ik heb ook heteronanoplaatjes met verschillende samenstelling en geometrie (kern, kern-kroon, waarbij de schil alleen om de rand zit, en kern-schil deeltjes, waarbij de schil om het gehele nanoplaatje zit) gebruikt als bouwstenen voor de vorming van supradeeltjes. De resultaten laten zien dat we ook ronde supradeeltjes met compacte structuren kunnen maken van nanodeeltjes met een anisotrope vorm of samenstelling. We hebben ook een begin gemaakt aan het bestuderen van de optische eigenschappen van de supradeeltjes gemaakt uit al deze verschillende vormen van nanoplaatjes en deze vergeleken met de vrije nanoplaatjes in oplossing, om de gevolgen van zelf-assemblage voor de dynamica van ladingsdragers in de aangeslagen toestand te begrijpen.

In **hoofdstuk 4** hebben we een onderzoek gedaan naar de dynamica van de zelf-assemblage van nanokristallen in een olie-in-water emulsie. De nanokristallen zijn gedispergeerd in de oliedruppels, die de nanokristallen opsluiten en zorgen dat er ronde supradeeltjes gevormd worden. Het volgen van de zelf-assemblage kan niet met conventionele microscopie met zichtbaar licht, dus we hebben röntgenverstrooiingstechnieken toegepast. De resultaten laten zien dat de kristallisatie van nanokristallen tot supradeeltjes begint bij een volumefractie van 0.20, d.w.z. op het moment dat 20% van het totale volume van een druppel bestaat uit nanokristallen. Dit geeft aan dat attracties tussen de nanokristallen een belangrijke rol spelen tijdens de zelf-assemblage. Wat tevens bijzonder is, is dat het snelle kristallisatieproces (dat ongeveer 7.5 minuten duurt) resulteert in de homogene kristallisatie van verschillende 'vlak-gecentreerde-kubische'-domeinen in één supradeeltje. De experimentele resultaten en conclusies zijn bevestigd en aangesterkt door simulaties die



Figuur 3 • Structurele fenomenen in nanokristallijne supradeeltjes. (a) In hoofdstuk 3 hebben we CdSe nanoplaatjes met verschillende vormen, composities en groottes geassembleerd in ronde supradeeltjes. Nanoplaatjes zitten gestapeld in de supradeeltjes, en vormen kolommen die willekeurig zijn georiënteerd in het deeltje. De optische eigenschappen van de geassembleerde nanoplaatjes verschillen maar een klein beetje ten opzichte van de vrije nanoplaatjes in oplossing. (b) In hoofdstuk 4 hebben we de kristallisatie gevolgd van FeO/CoFe₂O₄ nanodeeltjes naar supradeeltjes in een olie-in-water emulsie door middel van röntgenverstrooiingstechnieken. Het grote bereik van verstrooiingshoeken maakte het mogelijk het vormingsproces te volgen over een groot bereik van lengteschalen; van de krimpende oliedruppels van een aantal micron groot, tot de positie van nanodeeltjes in het supradeeltje, waar de afstanden een factor 1000 keer kleiner zijn.

meer inzicht geven in het vormingsproces van supradeeltjes.

III. Optische fenomenen

In het tweede deel van dit proefschrift (hoofdstuk 5, 6 en 7) hebben we optische eigenschappen bestudeerd van supradeeltjes die bestaan uit CdSe (kern)/CdS (schil) nanokristallen. Deze eigenschappen komen voort uit ofwel interacties tussen ladingen in naburige nanokristallen, of door interacties tussen nanokristallen en hun omgeving. Deze optische eigenschappen kunnen gebruikt worden in toepassingen van de supradeeltjes, bijvoorbeeld als fosforen voor schermen en sensoren.

In **hoofdstuk 5** hebben we de relatie tussen spontane emissie, het vastpinnen van ladingen en resonante energieoverdracht in kwantum-dot assemblages onderzocht. We hebben laten zien dat het reversibele vastpinnen van ladingen in kwantum-dot assemblages energieoverdracht tussen naburige kwantum dots langzamer maakt. De ladingen worden vastgezet in zogenaamde ‘trap’-toestanden, waarin deze ladingen niet kunnen bewegen en geen licht uit kunnen zenden. Terwijl de energieoverdracht de emissiepiek van de kwantum dots naar lagere energie verschuift (het licht verschuift meer naar het rood) in de eerste 50 nanoseconden na excitatie, wordt deze trend omgedraaid op langere tijdschalen (het uitgezonden licht krijgt weer een hogere energie) doordat de vastgepinde ladingen weer worden vrijgegeven (het licht verschuift nu meer naar het blauw). Het reversibel vastpinnen van een lading maakt energieoverdracht kortstondig onmogelijk. Deze resul-

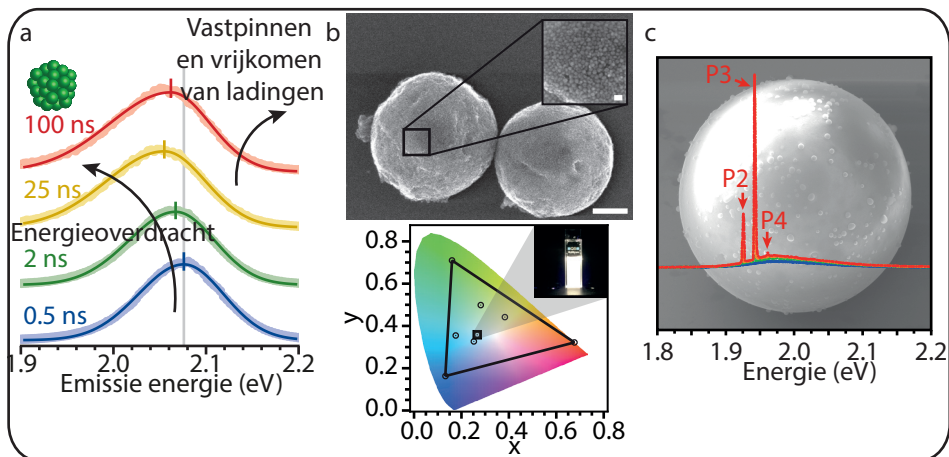


Figure 4 • Optische fenomenen in nanokristallijne supradeeltjes. (a) In hoofdstuk 5 hebben we laten zien dat het vastpinnen en vrijkomen van ladingen van roodverschuiving van emissie door energieoverdracht omdraait. (b) In hoofdstuk 6 hebben we supradeeltjes gemaakt uit blauw-, groen- en rood-emitterende kwantum dots, waarvan de totale emissie gevarieerd kan worden door de verhouding tussen de verschillende kleuren kwantum dots in het supradeeltje aan te passen. De emissie van een supradeeltje kan dus worden aangepast door het gehele zichtbare spectrum. (c) Supradeeltjes gemaakt uit kwantum dots kunnen gebruikt worden als microholtes voor het produceren van laserlicht. Dit komt doordat het licht dat de kwantum dots uitzenden, wordt opgesloten in een supradeeltje en versterkt. In hoofdstuk zeven hebben we laten zien dat we op deze manier laserlicht uit een supradeeltje kunnen halen, waarbij het supradeeltje nu zowel als versterker en holte voor het licht dient.

taten worden bevestigd door Monte Carlo simulaties van de dynamiek van de aangeslagen ladingen. We hebben zo meer inzicht verkregen in de optische eigenschappen van kwantum dots in toepassingen waarbij ze dicht op elkaar gestapeld zijn.

In **hoofdstuk 6** hebben we laten zien dat we supradeeltjes kunnen maken waarvan de emissiekleur aangepast kan worden. Deze supradeeltjes bestaan uit verschillende soorten kwantum dots, die verschillende kleuren licht (blauw, groen en rood) uitzenden. Deze supradeeltjes bevatten een amorfe (wanordelijke) pakking van de kwantum dots. Door de verhouding van de blauw-, groen- en rood-emitterende kwantum dots aan te passen, hebben we laten zien dat het mogelijk is de emissie van een supradeeltjes aan te passen over een breed scala aan kleuren door additieve kleurenmengsels. Op deze manier is het bijvoorbeeld mogelijk om wit licht te maken.

In **hoofdstuk 7** hebben we laten zien dat supradeeltjes die bestaan uit kwantum dots ook gebruikt kunnen worden als holtes waarin laserlicht gemaakt kan worden. Door het grote verschil in brekingsindex tussen de supradeeltjes en de omgeving kan licht dat wordt uitgezonden opgesloten worden in een supradeeltje. Dit licht gaat in rondjes door een supradeeltje heen ('whispering gallery mode') en wordt daarbij versterkt door gestimuleerde emissie. Als de kwaliteit en de grootte van het supradeeltje goed genoeg zijn leidt dit tot lasing. We hebben met behulp van een zelf-ontworpen microfluidische cel supradeeltjes gemaakt van een aantal micron groot en lage polydispersiteit in grootte. Hiermee bedoelen we dat de variatie in grootte van de supradeeltjes maximaal 5% is. Onder excitatie met hoog-energetisch licht hebben we de lasing uit de whispering gallery modes van individuele supradeeltjes kunnen meten. Dat het echt ging om laserlicht, hebben we bevestigd aan de hand van een drastische verandering van de levensduur van de luminescentie en de waarneming van coherentie in ruimte en tijd. Deze resultaten laten zien dat supradeeltjes van kwantum dots als holtes voor lasers gebruikt kunnen worden, waarbij de supradeeltjes zowel de holte als het versterkende medium zijn.

IV. Outlook

Hopelijk kunnen de resultaten uit dit proefschrift gebruikt worden als inspiratie voor andere onderzoekers die onderzoek willen doen naar structurele en optische eigenschappen van supradeeltjes die gemaakt zijn uit halfgeleider nanokristallen.

Wat betreft de structurele eigenschappen denk ik dat meer experimenten gedaan kunnen worden met behulp van röntgenverstrooiingstechnieken. Hiermee kan bijvoorbeeld de invloed van de grootte van de nanokristallen op de dynamiek van de kristallisatie bestudeerd worden. In het bijzonder laten de simulaties zien dat de grootte en samenstelling van de nanokristallen de sterkte van nanokristal-nanokristal vanderwaalskrachten beïnvloeden. Deze zijn belangrijk in het vormingsproces en bepalen met name de volumefractie waarbij de kristallisatie begint.¹ Het zou interessant zijn om de experimenten uit Hoofdstuk 4 te herhalen met verschillende groottes van nanokristallen en wellicht ook met verschillende samenstellingen (zoals CdSe, Au en Pd), omdat er weinig onderzoek is gedaan naar de dynamiek van de kristallisatie van deze systemen.^{2,3}

Qua optische eigenschappen kan er nog een hoop vervolgonderzoek gedaan worden. Het

is bijvoorbeeld van belang om het gebruik van de supradeeltjes als fosfor in verlichtings-toepassingen te onderzoeken. Experimenten kunnen gedaan worden om het uitdoven van de supradeeltjes onder hoge excitatiedichtheden te onderzoeken. Een ander voorbeeld is om de weerbaarheid van de supradeeltjes te onderzoeken bij hoge temperaturen, die relevant zijn voor de toepassing van deze deeltjes in LEDs. Wat verder nog interessant is, is de mogelijkheid om supradeeltjes van kwantum dots te maken die erg monodispers zijn. Hiermee kunnen grotere zogenaamde ‘fotonische’ kristallen gemaakt worden (kristallen van suprakristallen) die sterk met zichtbaar licht interageren als de bouwstenen ongeveer zo groot zijn als de golflengte van licht. Dit is bijvoorbeeld al gedaan met fotonische kristallen van polymeerbolletjes, die verschillende kleuren licht onder andere hoeken reflecteren.⁴⁻⁶ Eveneens interessant is de mogelijk om binaire supradeeltjes^{7,8} te vormen, kristallijne supradeeltjes die bestaan uit twee verschillende soorten nanokristallen, waar bijvoorbeeld plasmonische deeltjes (bijvoorbeeld goud of zilver nanodeeltjes die collectieve oscillaties van elektronen aan hun oppervlak vertonen) en kwantum dots gecombineerd worden.

References

1. Evers, W. H. *et al.* Entropy-driven formation of binary semiconductor-nanocrystal superlattices. *Nano Lett.* **10**, 4235–4241 (2010).
2. Marino, E., Kodger, T. E., Wegdam, G. H. & Schall, P. Revealing Driving Forces in Quantum Dot Supercrystal Assembly. *Adv. Mater.* **1803433**, 1–6 (2018).
3. de Nijs, B. *et al.* Entropy-driven Formation of Large Icosahedral Colloidal Clusters by Spherical Confinement. *Nat. Mater.* **14**, 56–60 (2015).
4. Phillips, K. R. *et al.* A colloidoscope of colloid-based porous materials and their uses. *Chem. Soc. Rev.* **45**, 281–322 (2016).
5. Vogel, N. *et al.* Color from hierarchy: Diverse optical properties of micron-sized spherical colloidal assemblies. *Proc. Natl. Acad. Sci.* **112**, 10845–10850 (2015).
6. Goerlitzer, E. S. A., Klupp Taylor, R. N. & Vogel, N. Bioinspired Photonic Pigments from Colloidal Self-Assembly. *Adv. Mater.* **30**, 1706654 (2018).
7. Wang, P., Qiao, Q., Zhu, Y. & Ouyang, M. Colloidal Binary Supracrystals with Tunable Structural Lattices. *J. Am. Chem. Soc.* **140**, 9095–9098 (2018).
8. Wang, D. *et al.* Binary icosahedral quasicrystals of hard spheres in spherical confinement. *Submitted* (2018).

Sommario in Italiano

Panoramica

La ricerca discussa in maniera estesa in questa tesi é riassunta, in questo capitolo, per un'audience piú ampia. I risultati piú importanti di questa ricerca saranno presentati dopo un'introduzione generale su semiconduttori e nanocristalli. A seguire, un breve paragrafo delinea alcuni spunti per la ricerca futura.

*«Fortune and glory, kid. Fortune and glory»
(Harrison Ford - Indiana Jones)*

I. Introduzione

Il lavoro presentato in questa tesi, come il titolo suggerisce, riguarda i fenomeni ottici e strutturali che emergono dall'auto-assemblaggio di nanocristalli colloidali di materiale semiconduttore. Con questa frase numerose domande possono già prendere forma nella mente del lettore: cosa significa auto-assemblaggio? Cos'è un semiconduttore? Da dove viene il prefisso nano-? Cos'è un cristallo? La parola colloidale ha qualcosa a che fare con la colla? Perché tutto ciò è interessante per la ricerca? Nelle pagine seguenti cercherò di rispondere a queste domande e di fornire al lettore una panoramica generale di che cosa io abbia investigato in questi quattro anni di ricerca e del perché io l'abbia fatto.

Al giorno d'oggi la tecnologia è fortemente basata sui semiconduttori. Gli smartphones nelle nostre tasche, gli schermi della televisione e del computer nelle nostre case e le celle solari che ci forniscono elettricità sono tutti basati su semiconduttori e, in particolare, sul

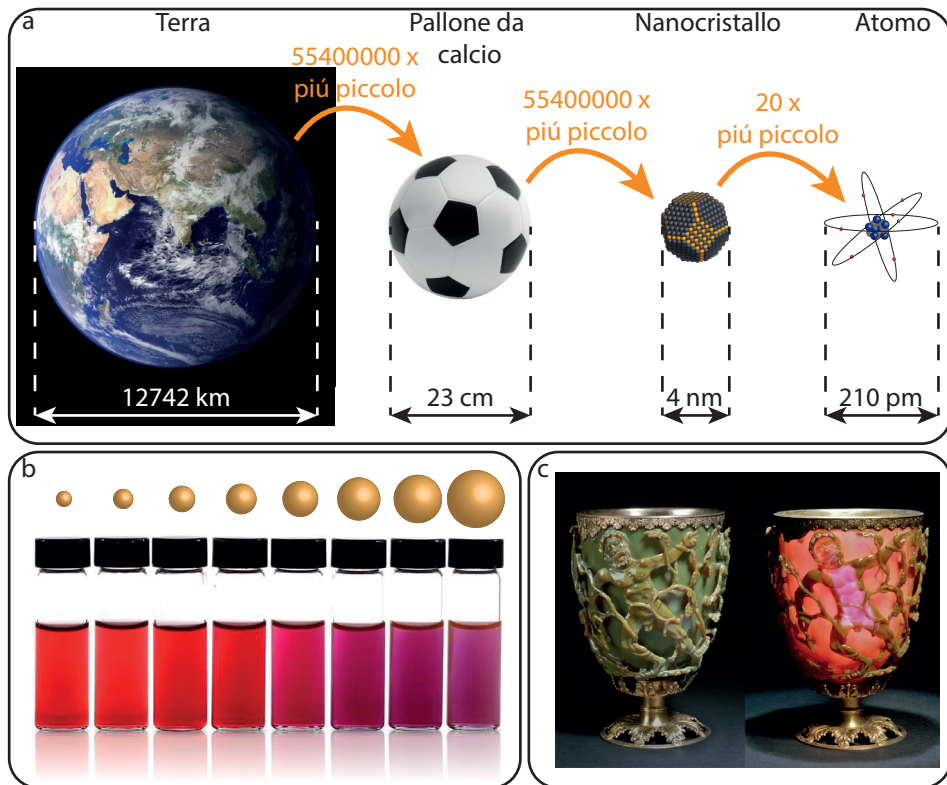


Figura 1 • Nanocristalli e nanoscala. (a) Se confrontiamo il diametro medio della Terra con un pallone da calcio, quest'ultimo è 55 milioni di volte più piccolo del primo. Allo stesso modo, un nanocristallo è 55 milioni di volte più piccolo di un pallone da calcio. Infine, un atomo è circa 20 volte più piccolo di un nanocristallo. (b) Mentre l'oro in forma macroscopica è di colore giallo metallico, sospensioni (o dispersioni) colloidali di nanocristalli d'oro sono caratterizzate da un colore che dipende direttamente dalle loro dimensioni. (c) La famosa coppa di Licurgo, datata al quarto secolo d.C., è fatta di un vetro in cui sono dispersi nanocristalli d'oro e d'argento. Questo risulta in un colore verde in riflessione ed un colore rosso in trasmissione.

silicio. I materiali, in generale, possono essere classificati in diversi modi a seconda della proprietà considerata; se consideriamo la capacità degli elettroni di muoversi nel materiale, allora possiamo classificarli in tre categorie diverse: conduttori, semiconduttori e isolanti. I conduttori sono materiali in cui gli elettroni si muovono molto facilmente (e.g. metalli), gli isolanti sono materiali in cui gli elettroni non si muovono facilmente (e.g. legno o “plastica”), mentre i semiconduttori sono materiali in cui gli elettroni possono muoversi a patto che gli sia fornito un certo quantitativo di energia. Questa energia può essere fornita in forme diverse come, per esempio, sotto forma di luce (e.g. visibile, ultravioletta, infrarossa) o di una differenza di potenziale elettrico. I semiconduttori risultano particolarmente rilevanti nel caso in cui abbiano la capacità intrinseca di interagire con la luce visibile. Questi possono infatti assorbire la luce producendo così elettroni liberi di muoversi (*i.e.* elettricità), per esempio, in celle solari; oppure possono emettere luce quando ricevono elettroni (*i.e.* elettricità) come, per esempio, nei LED. Per questa stessa ragione, i semiconduttori sono oggi parte integrante della nostra società, al punto che l’Età dell’Informazione, nella quale viviamo, è stata anche ribattezzata l’Età del Silicio.

Oltre alla parola semiconduttore, l’altra parola chiave di questa tesi è nanocristallo. Un cristallo è un materiale solido le cui componenti (e.g. gli atomi o le molecole) sono disposte in una struttura ordinata. Un fiocco di neve è, per esempio, un singolo cristallo di acqua. Il prefisso nano-, invece, identifica un fattore di un milionesimo. Un nanocristallo è dunque un oggetto le cui componenti, gli atomi, sono disposti in una struttura estremamente ordinata e le cui dimensioni sono nell’ordine di alcuni nanometri. Per dare un’idea al lettore, se consideriamo la Terra, questa è circa 55 milioni di volte più grande di un pallone da calcio e, allo stesso modo, se paragoniamo un pallone da calcio ad un nanocristallo, quest’ultimo è circa 55 milioni di volte più piccolo del primo (Figura 1a). A queste dimensioni, tuttavia, i materiali si comportano in maniera diversa rispetto a quando essi sono nella loro forma macroscopica/bulk: su scala nanometrica, le dimensioni contano. Prendiamo ad esempio l’oro. Nella sua forma macroscopica, l’oro puro è giallo, e possiamo dargli la forma che vogliamo che il suo colore non cambia. Tuttavia, se consideriamo nanocristalli d’oro dispersi in un liquido, conosciuti anche come dispersione colloidale d’oro, allora essi saranno caratterizzati da un colore che dipende dalla loro taglia (Figura 1b). Questo effetto era già conosciuto dai nostri antenati, i quali mischiavano polvere d’oro macinata per tempi diversi (*i.e.* formando così nanocristalli di dimensione diversa) a ceramica e vetro al fine di ottenere diverse colorazioni. Uno splendido esempio di ciò è la famosa coppa di Licurgo, risalente all’epoca tardo romana (Figura 1c). Tornando ai semiconduttori, è possibile regolare il colore della luce che essi assorbono o emettono (*i.e.* la loro interazione con la luce) semplicemente cambiando le loro dimensioni alla nanoscala.

I nanocristalli colloidali di materiale semiconduttore sono pertanto particelle di materiale semiconduttore, di dimensione di pochi nanometri, e disperse in un solvente (e.g. acqua, toluene). Proprio per la possibilità di regolare la loro interazione con la luce solamente cambiando le loro dimensioni (Figura 2a), queste particelle hanno attratto interesse per una pletora di applicazioni, come celle solari, LED e laser. Al giorno d’oggi, i nanocristalli di materiale semiconduttore, conosciuti anche come punti quantici o quantum dots, sono usati in schermi per televisioni e computer (Figura 2b), e si prevede che i primi LED per illuminazione basati sui quantum dots raggiungeranno il mercato nei prossimi anni. In

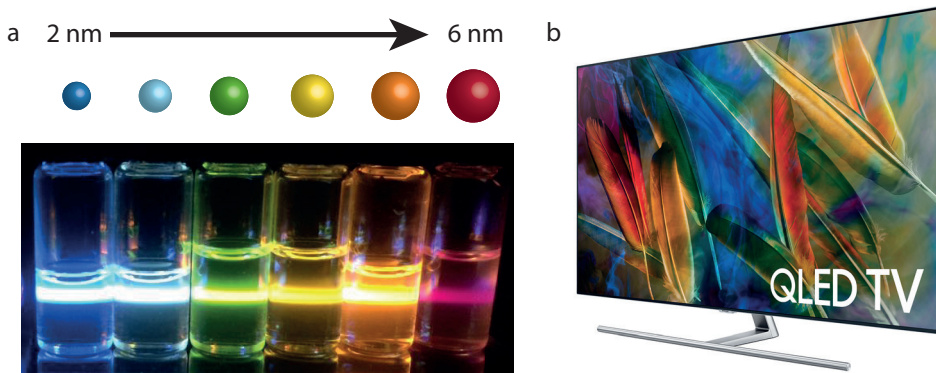


Figura 2 • Nanocristalli colloidali di materiale semiconduttore e le loro applicazioni. (a) L' emissione di nanocristalli di CdSe può essere regolata nell'intero spettro visibile semplicemente cambiando le loro dimensioni tra 2 nm (emissione di luce blu) e 6 nm (emissione di luce rossa). (b) Le prime televisioni con LED basati su nanocristalli di materiale semiconduttore sono recentemente approdati sul mercato, offrendo luminosità e brillantezza del colore ineguagliate.

alcune di queste applicazioni i quantum dots sono molto vicini tra loro, disposti in maniera disordinata o ordinata, in configurazioni compatte. In queste disposizioni, tuttavia, i quantum dots interagiscono tra loro, dando origine a fenomeni collettivi molto peculiari.

Durante il mio dottorato ho investigato le proprietà ottiche dei quantum dots nel caso in cui essi siano dispersi in soluzione e nel caso in cui essi siano ordinati in strutture sferiche chiamate supraparticelle o suprasfere. Le supraparticelle sono ottenute trovando le giuste condizioni sperimentali al fine d'indurre il sistema ad auto-organizzarsi, o auto-assemblarsi, in strutture ordinate. In altre parole, ho investigato le condizioni sperimentali ideali per permettere ai quantum dots di auto-organizzarsi in strutture sferiche e cristalline di dimensioni microscopiche, le quali possono dunque essere viste come cristalli di nanocristalli. Dopo aver investigato i fenomeni strutturali associati a queste supraparticelle, ho investigato i fenomeni ottici emergenti dalle interazioni tra nanocristalli quando questi sono assemblati in supraparticelle. Questo lavoro ha come scopo quello di approfondire la nostra comprensione della formazione delle supraparticelle e delle intriganti proprietà ottiche collettive ad esse associate. Questo potrà, con un po' di fortuna, aprire le porte, in futuro, a ricerca in questa direzione, aumentando le nostre conoscenze in questo ramo della nanoscienza e, forse, accrescendo l'uso dei quantum dots e delle supraparticelle in applicazioni commerciali.

II. Fenomeni strutturali

Nella prima parte di questa tesi (Capitoli 3 & 4) abbiamo investigato i fenomeni strutturali emergenti durante l'auto-assemblaggio di nanocristalli con diverse geometrie in una goccia di "olio" (la soluzione di quantum dots) in acqua, la quale, evaporando nel corso del tempo, confina i nanocristalli in un volume che si riduce nel tempo, spingendoli così ad auto-assemblarsi in strutture complesse (*i.e.* supraparticelle).

Nel **Capitolo 3** abbiamo mostrato come nanoplacchette bidimensionali di materiale semiconduttore possano essere auto-assemblate in supraparticelle con una ritenzione generale

delle loro proprietà ottiche (Figura 3a). Le nanoplacchette nelle supraparticelle si impilano a causa di intense forze attrattive tra i lati delle nanoplacchette (coperti da molecole organiche che ne permettono la dispersione in soluzione). Le nanoplacchette impilate sono orientate in maniera casuale nelle supraparticelle. Etero-nanoplacchette con diversa composizione e geometria (*i.e.* nanoplacchette rivestite interamente, o solo lungo i bordi, da un materiale semiconduttore diverso) sono state sintetizzate e usate come mattoni per la formazione di supraparticelle, dimostrando così che supraparticelle sferiche e/o strutture compatte possono ancora essere formate tramite processi di auto-assemblaggio a partire da costituenti anisotropi. Abbiamo anche effettuato studi preliminari sulle proprietà ottiche delle nanoplacchette in configurazione auto-assemblata e le abbiamo comparate con le proprietà ottiche di nanoplacchette disperse liberamente nel solvente al fine di far luce sulle conseguenze dell'auto-assemblaggio sul comportamento delle cariche elettriche, le quali sono alla base delle proprietà ottiche, nelle nanoplacchette.

Nel **Capitolo 4** abbiamo effettuato uno studio accurato del meccanismo di auto-assemblaggio di nanocristalli sferici in una goccia d'olio in acqua, la quale, attraverso la sua tensione superficiale e l'evaporazione nel corso del tempo, fornisce un confinamento sferico atto all'auto-assemblaggio delle nanoparticelle, in loco e tramite la diffrazione di raggi X (Figura 3b). I nostri risultati mostrano come la cristallizzazione dei nanocristalli in supraparticelle cominci ad una frazione di volume di 0.20 (*i.e.* il 20% del volume totale della goccia è composto da nanoparticelle), suggerendo che le forze attrattive tra le nanoparticelle usate in questo studio giochino un ruolo importante nel processo di auto-assemblaggio. In particolare, il veloce processo di cristallizzazione dei nanocristalli in supraparticelle (7.5 min) suggerisce che la cristallizzazione proceda tramite la nuclea-

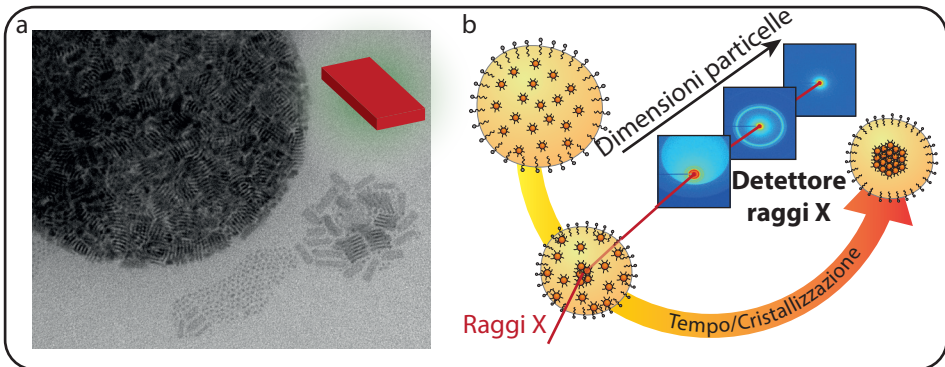


Figura 3 • Fenomeni strutturali in supraparticelle nanocristalline. (a) Nel Capitolo 3, nanoplacchette di CdSe con diversa forma, composizione e taglia sono state auto-assemblate in supraparticelle sferiche. Le nanoplacchette possono essere trovate impilate faccia contro faccia dentro le supraparticelle, formando così piccole colonne orientate in maniera casuale nello spazio. Le proprietà ottiche delle nanoplacchette auto-assemblate differiscono solo in minima parte rispetto alla configurazione in cui le nanoplacchette sono disperse in soluzione. (b) Nel Capitolo 4 abbiamo seguito la cristallizzazione di nanoparticelle di FeO, con un rivestimento di CoFe_2O_4 , in supraparticelle dentro goccioline di olio in acqua tramite diffrazione di raggi X. Le condizioni sperimentali usate nella nostra ricerca ci hanno permesso di seguire il processo di formazione in un ampio dominio spaziale, che va dalle goccioline che si restringono evaporando, di dimensione micrometrica, fino alla posizione dei nanocristalli nelle goccioline dopo l'auto-assemblaggio, con distanze di un fattore 1000 x più piccole.

zione omogenea di diversi cristalli cubici a facce centrate dentro la gocciolina. I cristalli di nanoparticelle crescono in dimensioni nel corso del tempo e si uniscono per formare supraparticelle composte di alcuni domini cristallini cubici a facce centrate. I nostri risultati sono supportati da simulazioni, le quali ci forniscono una maggiore comprensione del processo di formazione delle supraparticelle in queste condizioni.

III. Fenomeni ottici

Nella seconda parte di questa tesi (Capitoli 5, 6 & 7) abbiamo investigato i fenomeni ottici osservati in supraparticelle composte da nanocristalli con CdSe (cuore)/ CdS (rivestimento) ed emergenti o dall'interazione tra le cariche presenti in nanocristalli adiacenti, o dalle interazioni tra i nanocristalli e l'ambiente ottico che li circonda. Questi fenomeni ottici hanno particolare importanza per l'uso futuro di supraparticelle di quantum dots in applicazioni quali fosfori per schermi e sensori.

Nel **Capitolo 5** abbiamo studiato la relazione tra emissione spontanea di luce, intrappolamento delle cariche e trasferimento energetico risonante in supraparticelle di quantum dots (Figura 4a). In particolare abbiamo mostrato come l'intrappolamento reversibile delle cariche all'interno delle nanoparticelle rallenti il trasferimento energetico tra quantum dots vicini. In altre parole, in particolari condizioni, le cariche nei nanocristalli possono essere intrappolate in dei cosiddetti "stati trappola" in cui non possono né muoversi né emettere luce. Questo intrappolamento ha l'effetto pratico di impedire che l'energia delle cariche venga trasferita tra punti quantici vicini mediante un effetto chiamato trasferimen-

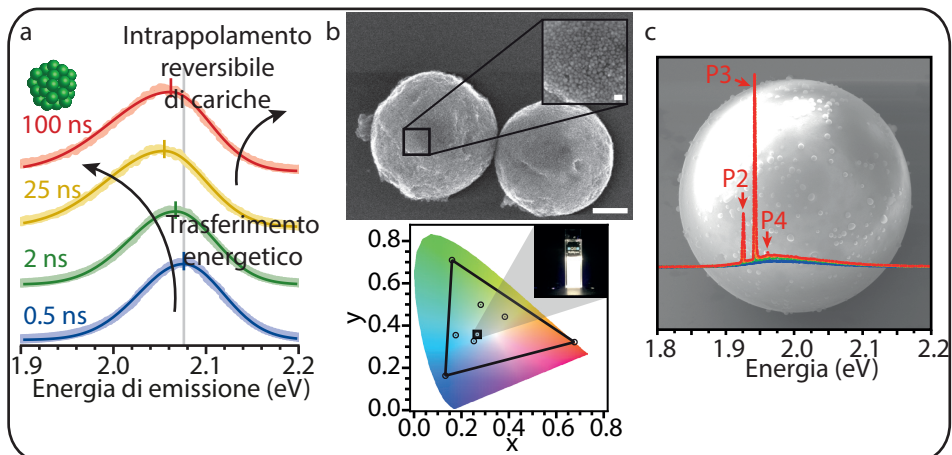


Figure 4 • Fenomeni ottici in supraparticelle nanocristalline. (a) Nel Capitolo 5 abbiamo dimostrato come l'intrappolamento delle cariche e la loro liberazione inverta lo spostamento dell'emissione di luce verso il rosso prodotto dal trasferimento energetico risonante. (b) Nel Capitolo 6 abbiamo prodotto supraparticelle composte usando tre diversi tipi di quantum dots caratterizzati da emissione di luce nel rosso, verde e blu. L'emissione di luce delle supraparticelle può essere regolata precisamente in un'ampia gamma di colori semplicemente cambiando il rapporto tra i quantum dots che le compongono. (c) Supraparticelle di quantum dots, monodisperse in taglia, possono essere usate come microresonatori grazie alla presenza di whispering gallery waves. Nel Capitolo 7 abbiamo mostrato come, tramite illuminazione, queste particelle possano essere usate per produrre luce laser.

to energetico. Mentre il trasferimento energetico ha il tipico effetto di spostare l'emissione di luce dei quantum dots nelle supraparticelle verso il rosso (*i.e.* luce che diventa piú rossa nel tempo) nei primi 50 ns dopo la creazione delle cariche, questo andamento é rovesciato, a tempi piú lunghi, dal liberamento delle cariche che erano state intrappolate, risultando cosí in una emissione di luce verso il blu (*i.e.* luce che diventa piú blu nel tempo). I nostri risultati sono supportati da simulazioni di tipo Monte Carlo della dinamica delle cariche. Le simulazioni ci forniscono una maggiore comprensione, a livello quantitativo, del ruolo dell'intrappolamento delle cariche sul rallentamento del trasferimento energetico. I nostri risultati sono particolarmente rilevanti per l'utilizzo di quantum dots in dispositivi ad illuminazione, dove é necessario predire l'emissione di luce delle nanoparticelle quando queste sono in configurazioni compatte.

Nel **Capitolo 6** abbiamo presentato supraparticelle con emissione regolabile, composte da quantum dots con un cuore di Cd(Se,ZnS) ed un rivestimento di (Cd,Zn)S e caratterizzati da emissione di luce in diverse aree del visibile (*i.e.* rosso, verde e blu) (Figura 4b). Queste supraparticelle composite sono state caratterizzate dal punto di vista della struttura, evidenziando una struttura amorfa (*i.e.* disordinata) dovuta alla diversa forma e dimensione dei nanocristalli che le compongono. Cambiando il rapporto tra i diversi quantum dots che compongono le supraparticelle e che, lo ricordiamo, emettono luce rossa, verde o blu, abbiamo ottenuto la possibilitá di regolare in maniera precisa l'emissione di luce delle supraparticelle in un'ampia gamma di colori mediante semplice mescolanza additiva di colori (*i.e.* mischiando luce rossa, verde e blu in pari quantitá si ottiene, per esempio, luce bianca).

Nel **Capitolo 7** abbiamo dimostrato la possibilitá di usare supraparticelle composte da quantum dots con cuore di CdSe e rivestimento di CdS per produrre luce laser (Figura 4c). Grazie alle proprietá ottiche intrinseche del materiale semiconduttore che compone le supraparticelle, la luce puó essere intrappolata dentro queste ultime producendo quelle che sono chiamate "onde delle camere a sussurro" (*N.d.T.* whispering-gallery wave nell'originale inglese). In altri termini, la luce intrappolata in queste suprasfere si muove in maniera circolare lungo la circonferenza delle sfere stesse con minima perdita di energia. La luce cosí confinata, se le supraparticelle hanno dimensioni e qualitá sufficiente, puó tradursi in emissione laser. Abbiamo sintetizzato supraparticelle di alcuni micrometri di diametro e con una bassa polidispersitá in taglia (*i.e.* il diametro di ciascuna supraparticella varia al massimo del 5% rispetto al diametro medio) usando un dispositivo microfluidico fatto su misura. Illuminando queste supraparticelle possiamo generare whispering gallery waves in singole supraparticelle cosí osservando, per la prima volta, emissione laser. L' emissione laser é confermata da una drastica riduzione del tempo di vita delle cariche nei nanocristalli e da emissione di luce coerente e monocromatica. I nostri risultati dimostrano come supraparticelle auto-assemblate da quantum dots possano essere usate come microresonatori per produrre emissione di luce laser.

IV. Prospettive

Con un po' di fortuna, i risultati presentati in questa tesi possono ispirare altri ricercatori a studiare i fenomeni collettivi strutturali e ottici che possono emergere da supraparticelle composte da nanocristalli di materiale semiconduttore.

Riguardo ai fenomeni strutturali, ritengo che ulteriori esperimenti possano essere realizzati tramite diffrazione di raggi X al fine di investigare il ruolo della dimensione dei nanocristalli sulla dinamica di cristallizzazione delle supraparticelle. In particolare, alcune simulazioni hanno dimostrato come le dimensioni e la composizione dei nanocristalli determinino l'intensità delle forze attrattive di van der Waals tra nanocristalli che, come abbiamo dimostrato, hanno un ruolo cruciale nel determinare a quale frazione di volume delle particelle la cristallizzazione cominci.¹ In questo senso, sarebbe interessante ripetere l'esperimento del Capitolo 4 con nanocristalli di taglia inferiore e diversa composizione (e.g. CdSe, Au, Pd), dal momento che alcuni articoli in letteratura indicano una diversa cristallizzazione per sistemi di nanoparticelle diverse.^{2,3}

Riguardo ai fenomeni ottici, i risultati in Capitolo 6 forniscono lo spunto per ulteriori esperimenti ottici. In particolare sarebbe interessante investigare l'uso di queste particelle come fosfori per applicazioni nell'illuminazione. In questo senso, esperimenti che testino la resistenza di questi oggetti ad intense illuminazioni e ad alte temperature nel corso del tempo dovrebbero essere effettuati al fine di permettere l'uso di queste particelle in dispositivi LED. Inoltre la possibilità di formare supraparticelle di quantum dots altamente monodisperse in taglia apre le porte alla realizzazione di superstrutture le cui proprietà ottiche dipendono direttamente dalla struttura stessa (e.g. cristalli fotonici fatti di supraparticelle). In questo senso, supraparticelle composte da sfere polimeriche con taglia paragonabile alla lunghezza d'onda della luce visibile hanno mostrato di possedere proprietà ottiche meramente dipendenti dalla loro struttura come, per esempio, l'iridescenza, osservata in natura negli opali (i quali, altro non sono, che superstrutture composte da sfere di silice).⁴⁻⁶ L'uso di materiali ottici attivi (che emettono luce o, più in generale, che interagiscono fortemente con la luce), come i quantum dots, combinati con le proprietà ottiche di queste strutture, potrebbe risultare in materiali caratterizzati da sorprendenti fenomeni ottici, come i cristalli fotonici. Infine, i recenti resoconti scientifici su supraparticelle binarie^{7,8}, *i.e.* supraparticelle cristalline composte da due tipi di nanocristalli, potrebbe rappresentare un interessante campo di studi per la ricerca volta a carpire la relazione tra le proprietà ottiche ed il campo della plasmonica (*i.e.* i plasmoni sono oscillazioni coerenti di cariche nei materiali metallici), dove queste supraparticelle binarie sarebbero composte da quantum dots e, per esempio, nanoparticelle di oro o argento.

Riferimenti

1. Evers, W. H. *et al.* Entropy-driven formation of binary semiconductor-nanocrystal superlattices. *Nano Lett.* **10**, 4235–4241 (2010).
2. Marino, E., Kodger, T. E., Wegdam, G. H. & Schall, P. Revealing Driving Forces in Quantum Dot Supercrystal Assembly. *Adv. Mater.* **1803433**, 1–6 (2018).
3. de Nijs, B. *et al.* Entropy-driven Formation of Large Icosahedral Colloidal Clusters by Spherical Confinement. *Nat. Mater.* **14**, 56–60 (2015).
4. Phillips, K. R. *et al.* A colloidoscope of colloid-based porous materials and their uses. *Chem. Soc. Rev.* **45**, 281–322 (2016).
5. Vogel, N. *et al.* Color from hierarchy: Diverse optical properties of micron-sized spherical colloidal assemblies. *Proc. Natl. Acad. Sci.* **112**, 10845–10850 (2015).
6. Goerlitzer, E. S. A., Klupp Taylor, R. N. & Vogel, N. Bioinspired Photonic Pigments from Colloidal Self-Assembly. *Adv. Mater.* **30**, 1706654 (2018).
7. Wang, P., Qiao, Q., Zhu, Y. & Ouyang, M. Colloidal Binary Supracrystals with Tunable Structural Lattices. *J. Am. Chem. Soc.* **140**, 9095–9098 (2018).
8. Wang, D. *et al.* Binary icosahedral quasicrystals of hard spheres in spherical confinement. *Submitted* (2018).

List of publications

This thesis was based on the following publications:

Federico Montanarella, Thomas Altantzis, Daniele Zanaga, Freddy T. Rabouw, Sara Bals, Patrick Baesjou, Daniel Vanmaekelbergh and Alfons van Blaaderen. Composite Supraparticles with Tunable Light Emission. *ACS Nano* **11** (9), 9136–9142, 2017

Federico Montanarella, Jaco J. Geuchies, Tonnishtha Dasgupta, P. Tim Prins, Carlo van Overbeek, Rajeev Dattani, Patrick Baesjou, Marjolein Dijkstra, Andrei V. Petukhov, Alfons van Blaaderen and Daniel Vanmaekelbergh. Crystallization of nanocrystals in spherical confinement probed by *in-situ* X-ray scattering. *Nano Lett.* **18** (6), 3675–3681, 2018

Federico Montanarella, Margherita Biondi, Stijn O.M. Hinterding, Daniel Vanmaekelbergh and Freddy T. Rabouw. Reversible Charge-Carrier Trapping Slows Förster Energy Transfer in CdSe/CdS Quantum-Dot Solids. *Nano Lett.* **18** (9), 5867–5874, 2018

Federico Montanarella^{*}, Darius Urbonas^{*}, Luke Chadwick, Pepijn G. Moerman, Patrick Baesjou, Rainer F. Mahrt, Alfons van Blaaderen, Thilo Stöferle, and Daniel Vanmaekelbergh. Lasing Supraparticles Self-Assembled from Nanocrystals. *Just Accepted in ACS Nano*

Other publications:

Eva Bladt, Relinde J.A. van Dijk-Moes, Joep Peters, Federico Montanarella, Celso de Mello Donega, Daniël Vanmaekelbergh, and Sara Bals. “Atomic Structure of Wurtzite CdSe (Core)/CdS (Giant Shell) Nanobullets Related to Epitaxy and Growth”. *J. Am. Chem. Soc.* **138** (43), 14288–14293, 2016

Jacobine J.H.A. van Hest, A.V. Agronskaia, Jantina Fokkema, Federico Montanarella, Andrés Gregorio Puig, Celso de Mello Donega, Andries Meijerink, Gerhard A. Blab and Hans C. Gerritsen. “Towards robust and versatile single nanoparticle fiducial markers for correlative light and electron microscopy”. *Accepted in Journal of Microscopy*, 2018

Jaco J. Geuchies, Ellenor Geraffy, Carlo van Overbeek, Federico Montanarella, Marlou L. Slot, Oleg Konovalov, Andrei V. Petukhov and Daniel Vanmaekelbergh. “In situ study of the adsorption geometry of PbSe nanocrystals at liquid-air interfaces”. *In preparation*

P. Tim Prins^{*}, Federico Montanarella^{*}, Kim Dümbgen, Johanna C. van der Bok, Jaco J. Geuchies, Stijn O.M. Hinterding, Thomas Zinn, Sander Deelen, Hans L.R. Meijer, Freddy T. Rabouw, Jorick Maes, Kim De Nolf, Yolanda Justo, Narayanan Theyencheri, Andrei V. Petukhov, Celso de Mello Donega, Daniel Vanmaekelbergh and Zeger Hens. “Size Matters, Nucleation and Growth of Colloidal Nanocrystals”. *In preparation*

Federico Montanarella^{*}, P. Tim Prins^{*}, Johanna C. van der Bok, Jaco J. Geuchies, Stijn

O.M. Hinterding, Thomas Zinn, Sander Deelen, Hans L.R. Meijer, Freddy T. Rabouw, Narayanan Theyencheri, Andrei V. Petukhov, Celso de Mello Donega and Daniel Vanmaekelbergh. "In situ study of the formation mechanism of CdSe nanoplatelets". *In preparation*

Federico Montanarella, Maaïke M. van der Sluijs, Michiel Hermes, Patrick Baesjou, Alfons van Blaaderen and Daniel Vanmaekelbergh. "Self-assembly of luminescent CdSe based nanoplatelets in 3D spherical supraparticles". *In preparation*

Conference contributions and presentations

- Nov 2018 **Collective structural and optical phenomena in supraparticles of nanocrystals** (oral)
in the group of Prof. David Norris at ETH Zurich, Switzerland
- Oct 2018 **Whispering Gallery Modes Lasing in Self-Assembled Nanocrystal Supraparticles** (poster)
at the Nanoge FallMeeting18 conference in Malaga, Spain
Prize for best poster, awarded by Elsevier (500 €)
- Oct 2018 **Reversible charge-carrier trapping slows down Förster energy transfer in CdSe/CdS quantum-dot solids** (oral)
at the Nanoge FallMeeting18 conference in Malaga, Spain
- Jun 2018 **Reversible charge-carrier trapping slows down Förster energy transfer in CdSe/CdS quantum-dot solids** (poster)
at the QD2018 conference in Toronto, Canada
- Jun 2018 **Whispering gallery mode lasing in self-assembled nanocrystal supraparticles** (poster)
at the QD2018 conference in Toronto, Canada
- Mar 2018 **The birth of a nanocrystalline supraparticle: crystallization kinetics of nanocrystals in spherical confinement studied with in-situ X-ray scattering** (poster)
at the SyNew meeting in Ghent, Belgium
- Dec 2017 **The birth of a nanocrystalline supraparticle: crystallization kinetics of nanocrystals in spherical confinement studied with in-situ X-ray scattering** (poster)
at the MRS Fall Meeting in Boston, USA
- Dec 2017 **Whispering gallery mode lasing in supraparticles of luminescent nanocrystals** (poster)
at the MRS Fall Meeting in Boston, USA
- Jul 2017 **Composite supraparticles with tunable white light emission** (oral)
at the Nanax8 conference in Braga, Portugal
- Jul 2017 **Whispering gallery mode lasing in supraparticles of luminescent nanocrystals** (poster)
at the Nanax8 conference in Braga, Portugal
- Sep 2016 **White light emitting supraparticles** (poster)
at the Nanoge conference in Berlin, Germany
- May 2016 **White light emitting supraparticles** (oral)
at the QD2016 conference in Jeju, South Korea
- Aug 2015 **Self-assembly of luminescent nanocrystals into supraparticles** (poster)
at the NanoSa15 conference in Dresden, Germany

Acknowledgements

The work presented in this thesis would not have been possible without all the people that helped me during these four years. I will try to thank you all in these few pages.

First of all I would like to thank my supervisors: Daniel, Alfons and Patrick. **Daniel**, thank you for your guidance and support during these four years, for being always available for discussions and advices and, mostly, thank you for making my PhD so enjoyable, not only on a professional level but also on a more personal level. I really enjoyed our daily chats during lunch about Italian cuisine, my waterpolo adventures, your tennis exploits and many other topics. I also really enjoyed the few “social activities” that we had, such as watching the Euro 2016 football match Italy-Belgium together. It was really great to have you as a supervisor and you are one of the main reasons I enjoyed my PhD so much. Thank you. **Alfons**, as for Daniel, thank you for your guidance and your support during these four years. Mainly thank you for sharing your deep knowledge in so many different aspects of science and always being available for advices and suggestions. **Patrick**, I want to thank you for your strong support, especially on a human level. In the first few months of my PhD I truly appreciated your care for my well-being and personal situation as I was settling in the Netherlands. Furthermore our weekly meetings helped me start my PhD with the right pace. To conclude, I am happy and proud to be your “first” PhD student.

To keep on this track, few people strongly contributed to this PhD thesis through discussion of ideas and results, brainstorming sessions and nice collaborations. **Freddy**, your contribution to this thesis was really substantial. Thank you for all the ideas, the Mathematica sessions, the Illustrator tutorials, the text polishing and, more in general, all the help and time that you provided me. Beside the scientific part, I really enjoyed all the social activities and *snoeprisesjes* that we had in these years; to mention just a few: getting lost in Paris with Ward, all the museums we visited together and the board game nights. You are a special person and a friend, and maybe one day you will also finally become “civilized”, you will wear a *toga* and I will finally be able to call you Roman. Until then, I will be proud to consider you my “barbaric” friend. Another great character in most of these adventures is **Ward**. Dear bomber, you already know, I always look at you as a model, and you also substantially contributed to this thesis of mine with ideas and suggestions. I will always keep with me the memories of our trips to South Korea and Japan, to Paris, to Lille to watch the Euro 2016 match Italy vs Ireland and many more. You are a great friend and I was really proud to be your *paranimf*. I can only hope that in future we will keep in touch and you will still consider me your *bombertje*. It’s funny as most of these important people seems to have been seated in the same room, OL158 (maybe it’s the influence of our plant, **Herman**), and indeed also the next two did. **Jaco**, the Greek philosopher Aristotle wrote, in the IV century BC, that a friend is “a single soul dwelling in two bodies”. Now I can think of very few other people that would fit this description for me. I am happy to have found such a great friend like you, and I am proud that you will be my *paranimf*. Along these years we found out to have several common interests and you introduced me to several interests of yours, such as surfing, leaving a kind of legacy to me. On a more scientific point of view, you also introduced me to synchrotron based X-ray scattering experiments, which are, in the end, a substantial part of my thesis. For all this, and much more, thank you. Also from OL158 is my other precious *paranimf*, **Maryam**. At this very moment, while I am writing these few lines, you are despairing over the writing of your thesis (you

are in your last week) and I cannot but think on how far we got since we both started at the beginning of 2015. Dear Maryam, you are sincerely one of the best friend I have and I am really lucky to have met you in my life. Sharing the office and, more in general, working with you was one of the main reasons I enjoyed my PhD so much (even if you were a bit bossy) and I think we really had a great time together. Our daily chats and jokes and your jingling laughter will always constitute, for me, golden memories. Thank you for everything. Another person that strongly contributed to my PhD was **Tim P.** Tim, it was really great working with you and I think our Grenoble project and trips are the perfect example for that. I will always keep very good memories of our trips to ESRF (and also of our holiday in Portugal ;)) and hopefully our setup will leave a legacy of publications to us and to the group. Tim, you are a brilliant scientist and a great person, and I am truly happy to consider you my friend (even though, or maybe especially because, you can be a rascal sometimes).

For the results of this thesis I am also most grateful to all the students I had the privilege of supervising. **Maaïke**, my first student and, later, my office mate in OL158, I was really lucky to have you as my student and it was mainly thank to you that I realized how much I like supervising students. Guiding you, teaching you the synthesis of nanoplatelets in the first weeks of your master research and, soon, observing you making the project your own project was really satisfying. With a little bit of luck we will be able to publish our work soon. **Nolan, Suzan, Evert, Rosalie, Huygen** and **Jelle**, my second year students, it was really great making “quantum dot rainbows” with you guys, and I am proud to use your picture in Chapter 2 of this thesis. **Huygen** was later also my bachelor student. You are smart, diligent, hard-worker and very, very funny and it was really a pleasure to supervise you. With a bit of luck I will continue on your project during my postdoc. I am happy you decided to do your master thesis at CMI again (I think both you and Tim made a great choice) and I hope our roads will cross again in future. **Elena**, my second bachelor student, it was also a pleasure supervising you, as you showed to be very diligent, creative and, mostly, stoic, drilling holes (and thus destroying) your beautiful nanoplatelets for the sake of science. In the end you were so successful that your project was continued by Bas. **Margherita**, nonostante tutto ciò che tu possa pensare, hai fatto un ottimo lavoro e sono molto felice e orgoglioso di come il tuo master project sia andato. Ti voglio ringraziare per il lavoro che hai fatto perché, senza di te, probabilmente il capitolo 5 non esisterebbe. Spero che serberai ricordi felici del tuo periodo a Utrecht ed in bocca al lupo per il tuo dottorato a Toronto. Ti ricordo che quando lo finirai (perché so che lo finirai), ti terrò alla promessa che mi hai fatto questa estate (e di cui ho il video). **Luke**, before meeting you I thought that the famous “luck” of the Irish was just a way of saying. You completely convinced me it was real when you made perfectly monodisperse supraparticles at the first trial! Thanks to your work we are now publishing an article about lasing in supraparticles, which is also chapter 7 of this thesis. You are a hard-worker (maybe not the best organizer) and a very nice guy and I have nice memories of your master project (and I hope you do as well). Thank you for your work, I really wish you all the best for the future. Last but not least, **Nienke**, even though you only did your literature review with me, I really enjoyed working with you, and I can forecast a brilliant scientific future ahead of you.

Many more people contributed to make these four years great, some with bigger and some

with smaller contributions. As for the CMI group, when I first moved to the Netherlands I had a very nice time with **Sergiu**; our daily lunches, the football matches watched together and the swims at the pool are all great memories. I really appreciate all the time we spent together in the last months of your postdoc and the first months of my PhD. Merci, mon ami! **Annalisa**, è stata una lunga avventura da quando abbiamo iniziato insieme nel Febbraio 2015. Mi sembra ieri che eravamo nel coffee corner alle 9h00 del mattino aspettando che arrivasse qualcuno. Nonostante le mie battute riguardo alle tue origini sarde e alla latitudine geografica entro cui un territorio é definibile come Italia, iniziare il dottorato con un connazionale e dividere con te l'ufficio per un anno e mezzo é stato un piacere; grazie per tutto. **Anne**, I can think of many social activities together that I really enjoyed, going from the “90's now” and “00's heroes” nights at Tivoli, to the few *snoepreisesjes*, to our trip to Toronto and Canada, which was absolutely great (beside the heat - I will never complain about Dutch weather again). I really appreciated your company and your good taste for food (especially Greek). **Tim S.**, **Carlo**, **Jacobine** and **Annelies**, you all contributed somehow in making these four years very pleasant, with nice conversations in the lab, in my office or at *borrels*, watching Game of Thrones together in Daniel's office, playing board games and practicing my Dutch language skills. **Bas**, thank you for forcing me to practice my Dutch on a daily basis and teaching me so many funny sayings like “*wat een weertje, koeken peertje*” in exchange for candies. My Dutch would be way worse without you, and my PhD would have been way less fun. **Kelly**, we shared many great candy trips, such as the visit to the Efteling, the movie nights at your place and the trip to Tromsø (maybe not so great for you). Thank you for all these great adventures and memories. **Pedro** and **Pradip**, it was very nice collaborating with you guys; shame that we didn't manage to conclude the project in the end. I will always remember the “Mississippi” synthesis protocol that Pradip and I developed. **Ellenor**, thank you for all the nice and funny moments we shared, such as our trip to ESRF (you're welcome), the Irish tongue-twisters, and Gino's videos about grandmothers and bicycles. **Chenghui**, thank you for all the times that you helped me during these years and for the nice chats and conversations, you are really great. **Serena**, grazie per le risate, le conversazioni e, in generale, per rendere il gruppo piú divertente con la tua personalità. **Ingmar**, **Andries** and **Celso**, thank you for all the help and the advices during these years. **Harold**, thank you for the nice trip to the roman *castellum* of *Fectio* to rediscover my roman origins. Thanks also to all the other PhD and master students, former and current, and staff that contributed to make CMI such a great place: **Jette**, **Naud**, **Pascal**, **Thomas**, **Marlou**, **Christa**, **Joep(ske)**, **Christiaan**, **Elleke**, **Robin**, **Peter J.**, **Saoirsé**, **Joost**, **Thomas G.**, **Rouhollah**, **Winston**, **Allan**, **Wenjin**, **Linda**, **Stephan**, **Onno**, **Pierre**, **Liudmyla**, **Giuseppe**, **Atul**, **Markus**, **Dechao**, **Mathijs**, **Nadine**, **Mark M.** and **Sophia**.

My PhD life was divided between two different groups, one is indeed CMI, whose people I talked about, and the other one is SCM, whose people I want to thank now. When I first started my PhD I was strongly helped by three people: Relinde, Wiebke and Ernest. **Relinde**, thank you for sharing with me your knowledge about chemical synthesis of nanoparticles and being my “lab buddy” in the first months of my PhD. Thanks to your help I could swiftly start doing my own research independently in the lab. Also, thank you for teaching me the first basic principles of Dutch! **Wiebke**, you were also my “lab buddy”, for the confocal microscopy part of my project; thank you for all the help and the training you

gave me. Also thank you for the nice “social activities” (as we like to call them at CMI) together, of which I will keep nice memories, such as, for example, our trip to Berlin, where you were a great guide. **Ernest**, you also helped me a lot with optical microscopy, so thank you so much for all the time you spent assisting me and for all the knowledge you shared with me. All this mixed with a great amount of witty jokes that still cracks me up; did I ever tell you that you are like the Dutch version of Jim Carrey? Beside these three people, I interacted with several other nice people at SCM which greatly contributed to my PhD, both scientifically and personally. **Simone**, bomber, grazie per tutte le risate ed i momenti piacevoli sia a lavoro che fuori. Ricorderò sempre come abbiamo cantato l'inno d'Italia assieme prima della partita Euro 2016 perché tutti gli altri erano in ritardo. Sei un grande. **Da**, thank you for sharing your deep knowledge with me and for discussing my results about supraparticles over the years. **Toni**, thank you for your simulations on forming supraparticles, which are now part of Chapter 4, and for discussing with me the follow-ups, which helped me to get a better understanding of crystallization in spherical confinement. Also thank you for the assistance with designing the PhD thesis cover. Beside the scientific part, thank you for all the nice moments over these years. **Jessi**, cutiepie!, I already knew you were great before we went to Boston together for MRS Fall 2017, but then I really had the proof of it. Our trip to the US was absolutely one of the trips I enjoyed the most during my PhD. You are not only a great scientist, but you are also a very funny, nice and amiable person. I will always remember your judging looks while I ate cookies (I'm the cookie monster after all), the time we went to the stadium to watch the hockey match, how you dropped the cannoli 2 minutes after we bought them, how you laugh when I say *roughly*, and you bullying me (which nobody believes). I am really happy we got to know each other better and that we became friend (even if you stole my student :P) and I really hope we will keep in touch in the future. To the MRS trip is related also **Kanako**; thank you for greatly contributing in making this trip so great. I really enjoyed how we managed to make a perfect Japanese (*konnichiwa*) out of me and sorry if Jessi and I procured you blisters with all the walking. I really wish you all the best for the future, and I hope we'll see each other again, maybe at some conferences. **Stijn**, I really enjoyed working with you and being your colleague, first, when you were a master student at CMI and, later, when you became a *collega* at SCM. Thank you also for coming to Grenoble with Tim and me, thus contributing to the success of the experiment, and for running simulations for the work in chapter 5. **Pepijn** and **Chris**, thank you for your patience in training me and my student with microfluidics, it is really a zen technique and you are really two *gurus*. Pepijn, thank you for your contribution to the work in Chapter 7, which is now close to publication. **Michiel**, thank you for the simulations on the crystallization of supraparticles of nanoplatelets. **Guido**, **Giulia**, **Rama**, **Naveed**, **Massi**, **Carmin** and **Nik**, thank you for all the nice evening spent together during these four years. **Marjolein**, thank you for your contributions to our understanding of the crystallization in spherical confinement. Thanks also to all the other members of SCM, former and current, which contributed in making this PhD so enjoyable: **Arnout**, **Laura**, **Krassimir**, **Marijn**, **René**, **Gabriele**, **Emanuele**, **Frankje**, **Maarten**, **Xiaodan**, **Robin**, **Dnyaneshwar**, **Albert**, **Anna**, **Somil**, **Douglas**, **Henriette**, **Wessel**, **Berend**, **Srivatssan**, **Sid**, **Sina**, **Tom**, **Ravi**, **Harini**, **Nina** and **Xiaobin**.

Most of the work presented in this thesis would not have been possible without the help of the technicians. **Hans Meeldijk** and **Chris Schneijdenberg**, thank you for all the trainings

and all the marvelous TEM, SEM and STEM pictures that you made, or you helped me make, during these years. **Hans Ligthart**, **Peter van den Beld** and **Peter Helfferich** thank you for all the assistance on a daily basis; we would not be able to do research without you guys. **Sander Deelen** and **Hans Meijer**, thank you for making real the setup that Tim and I only thought of.

My PhD project was part of a Marie Curie network, “Phonsi”, which involved at least 2/3 meetings per year in different locations in Europe and Asia with the other members of the network. In particular, within this project, we were 15 PhD students and we used these meetings to grow as scientists, to establish collaborations and, mostly, to enjoy the time together. Above all, I think that the time we spent travelling around in Israel, during and after the meeting, was the one I enjoyed the most: great sightseeing and great people. But also the time we spent together in Nizza and in Torremolinos constitutes great memories. Connected to the Phonsi, I also spent few weeks in Zurich, working with **Darius**, **Michael**, **Thilo** and **Rainer**. Thank you guys for the nice and productive collaboration which resulted in Chapter 7. Especially thank you Darius and Michael for making my time in Zurich so pleasant, during my secondment and during my latest visits. All in all, I would like to thank all the PhDs which contributed in making the Phonsi network so great: **Adam**, **Johanna**, **Niall**, **Darius**, **Bogdan**, **Michael**, **Nayyera**, **Ye**, **Renu**, **Vignesh**, **Ronan**, **Maryam**, **Annalisa** and **Lukas**.

Besides the Phonsi, during my PhD, I had the chance to collaborate with several people around the world which I would like to thank. **Andrei Petukhov**, thank you for sharing your deep knowledge on synchrotron based X-ray scattering experiments which led to the results in Chapter 4 and, hopefully, to two more publications from the work with Tim. Thank you for your advices and your help with interpreting the data, and thank you for accompany us to our latest trip to ESRF. Related to X-ray scattering, **Rajeev Dattani**, **Thomas Zinn** and **Narayan Theyencheri**, thank you all for your help and assistance in performing and analyzing the X-ray scattering data. I am very happy about our productive collaboration, and I hope to come again to Grenoble in future to perform intriguing experiments. Some of the images in this thesis (especially in Chapter 6) were obtained from the Electron Microscopy group in Antwerp. **Sara Bals**, **Thomas Altantzis** and **Daniele Zanaga**, thank you for the amazing images that you were able to obtain. I think I will never cease to be impressed by the marvelous research that you do with electron microscopy. In November 2016 I went to Zurich to perform some studies on formation of nanoplatelets in the deMello group. **Ioannis Lignos** and **Andrew deMello**, thank you for the nice collaboration and for hosting me in your group, showing me all the wonderful things you can do with microfluidics.

Beside the scientific/work environment, I would like to thank all those people, living close-by or far away, that contributed in making these four years special. **Monica M.**, ricordo ancora il nostro primo incontro: in coda, al freddo, sotto la pioggia davanti al palazzo dell'SSH e di come ti sei avvicinata con un pizzino fradicio chiedendomi se quello fosse il posto giusto. Da allora sono diventato un *habitué* del vostro appartamento ed abbiamo passato degli splendidi e divertenti momenti assieme. Con la tua simpatia, semplicità e bontà hai contribuito a rendere speciali i primi mesi dal mio arrivo a Utrecht. Grazie per

tutti i bei ricordi e per aver contribuito a rendere questi quattro anni così speciali. **Ronja**, thank you for contributing to ignite my passion for surfing, for all the funny moments, for the dinners, the witty discussions and for the Talisman nights. **Naomi**, thank you for all the nice moments, the dinners, the visits to museums together and all the nice “philosophical” conversations.

An important part of my life in the Netherlands was spent in the water, and more precisely in de Krommerijn swimming pool, playing in the Heren 6 team of the UZSC club. Waterpolo is one of my deepest passions and I am proud I had the pleasure and the honor to share this passion of mine with my teammates. The first year was a bit tough, as I had to adapt to the Dutch way of playing (I ended up being the second player with the most expulsions; and the first one had only one more than me), but I think I made up for it in the following years. Luckily I had **Jorrit** making fun of me and with me, thus contributing in making these years of waterpolo in the Netherlands real fun; so thank you, my friend. These were years of amusement and I really enjoyed playing with you all guys, so thank you for making it so special: **Emile, Dirk-Jan, Jan Willem, Steven, Ton, René, Rob, Staf, Maurits, Ronald, Bart, Floris, Adrian, Harold, Andre, Mark** and **Nik**. Hartelijk dank ook aan **Maarten**, die altijd in mijn waterpolo vaardigheden heeft geloofd en een belangrijke bijdrage heeft gehad aan mijn geweldige jaren in Nederland.

Few people showed me their affection coming to visit me in the land of the tulips. **Olivier**, bro, merci pour ta vraie amitié et pour tous les moments marrants qu'on a partagé. Je n'ai pas encore accepté que les Killers ont pas chanté Mr. Brightside au Ziggo Dome; il faut qu'on va les revoir. **Emanuela**, bomberina grazie per essere venuta a trovarmi e per avermi fatto sentire il tuo affetto in questi anni. A quest'ora starai probabilmente insegnando la pallanuoto champagne ai thailandesi, sfoggiando le tue innate capacità atletiche. Verrà il giorno in cui ci alleneremo di nuovo assieme, ma fino ad allora sarai principalmente “chiacchiere e cavalletto”. **Lidia**, grazie per tutte le risate ed i bei momenti passati assieme. Serberó sempre con me il ricordo di quando siamo andati a vedere la partita Olanda vs USA e della tua collana di piume arancioni che ha lasciato una scia di piume da qui a Ginevra. **Giulia**, la tua visita a Utrecht é iniziata all'insegna della sfortuna (aereo ritardato per ben due volte in 24 ore penso sia un record assoluto), ma é stata decisamente molto piacevole; soprattutto le nostre scorrazzate in due su una bicicletta, di notte, in giro per Utrecht. Grazie per tutti i tuoi messaggi affettuosi e per farmi sentire a casa ogni volta che torno a Genova. **Andrea**, come ti ripeto spesso, sei stata la sorpresa piú piacevole da quando sono andato a Parigi. Grazie per le tue ripetute visite a Utrecht e per la tua amicizia di lunga data. **Martina**, qualsiasi cosa io possa scrivere in queste poche righe sará sempre riduttiva. Grazie per la tua amicizia onesta e profonda, grazie per farti sentire vicina anche se abitiamo così lontano e grazie per esserci, sempre e comunque.

Ogni volta che sono tornato in Italia alcune persone mi hanno fatto sentire a casa con il loro affetto; come se non fossi mai partito. Grazie a questi amici, con cui sono cresciuto assieme. Grazie **Dario, Monica, Serena, Carlo, Marco, Sara, Valentina, Alice, Livia** e **Mattia**.

Grazie ad **Arturo, Simone** e **Davide**. Per tutte le vite e le avventure che abbiamo vissuto e

per tutte quelle che ancora ci attendono.

Infine grazie alla famiglia, sempre presente a supportarmi ed a sostenermi, con affetto ed orgoglio. Grazie **Zia Silvana, Zio Gianni, Valeria, Andrea, Zio Lino e Paolo.**

Per finire, grazie ai miei genitori, **Nadia e Giacomo**, per aver reso tutto questo possibile, per avermi supportato e sostenuto, con amore e con affetto in tutti questi anni. Questo é per voi. Vi voglio bene.

To really conclude, I would like to thank this wonderful country, the Netherlands, and all its wonderful people, who always made me feel welcome. I wish to conclude citing the French philosopher Voltaire, who profoundly loved the time he spent in the Netherlands and, jokingly, said farewell to this land with these few lines: *“Adieu Hollande, pays de canaux, canards et canailles”*.

Federico, November 2018

About the Author



Federico Montanarella was born in Genova, Italy, on the 24th September 1990. He obtained his high school diploma from Liceo Scientifico G.D. Cassini in Genova in 2009 with a final grade of 100/100. In September of the same year he started a Bachelor degree (BSc) in Materials Science at Università degli Studi di Genova. During his bachelor studies he did a six months internship at ASG Superconductors under the supervision of Mr. Daniele Magrassi and Prof. Marina Putti, where he worked on the characterization of magnesium diboride superconductive components for nuclear magnetic resonant machines. After obtaining his BSc in 2012 *cum laude*, he started a Master degree (MSc) in Materials Science and Engineering in the same year. During his Master, Federico performed an Erasmus exchange period of one year in Paris at the Université Pierre et Marie Curie – Paris 6 (now Sorbonne Université), where he deepened his knowledge on nanostructures. While in Paris, he performed a six months internship at the École Supérieure de Physique et Chimie Industrielle (ESPCI) in the group of Prof. Benoît Dubertret, where he discovered the magic world of nanocrystals and, in particular, where he worked on the synthesis and the optical characterization of colloidal quantum dots and their coupling to plasmonic heterostructures. After returning to Italy, he completed his MSc in December 2014 *cum laude*.

In February 2015 Federico started a PhD under the supervision of Prof. Daniel Vanmaekelbergh (Condensed Matter and Interfaces group), Prof. Alfons van Blaaderen and Dr. Patrick Baesjou (Soft Condensed Matter group) at Utrecht University in Utrecht, the Netherlands. During his PhD, Federico worked on several topics, including the synthesis of semiconductor nanocrystals with different shape, size and composition, the self-assembly of nanocrystals in spherical supraparticles with sizes in the nano- and micrometer range, and the optical and structural characterization of these structures. Most of the results described in this thesis have been published in international peer-reviewed scientific journals and presented at several international conferences. During his PhD, Federico supervised three master students and two bachelor students. Furthermore he supervised several second-year research projects and he was teaching assistant for the “Nanomaterials” course.

Outside of the lab, Federico enjoys playing water polo, which he has been playing since he was 10 years old. His passion for water polo led him to play in Italy, France and, finally, the Netherlands, where he played for one of the UZSC club teams in Utrecht. Only in the last season, Federico scored 29 goals in 17 matches, becoming the top scorer of his team and substantially contributing to the final second place of his team, which resulted in the promotion to the upper league. Besides playing water polo, Federico also enjoys swimming and surfing. Furthermore, because of his great passion for history, Federico is also currently doing a Bachelor (BA) in History at Università degli Studi di Genova.

